Cavity Quantum Electrodynamics with Ion Coulomb Crystals
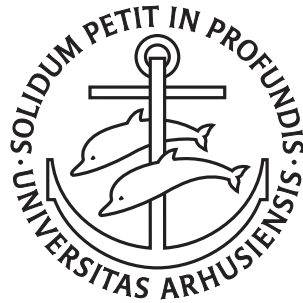
Peter Herskind

PhD Thesis

Preface

This thesis summarizes my work as a PhD-student in the Ion Trap Group of Michael Drewsen at the Department of Physics and Astronomy at the University of Aarhus. The past four years have introduced me to a number of interesting problems and tasks of a diversity ranging from the understanding of ion trapping and quantum information science to basic milling and soldering.

The work presented here could not have accomplished without the help, guidance and support from both colleagues, collaborators, teachers, friends and family.

During the four years I have been involved with this project it has grown from a small, at times one-man effort, to being a full group within the Ion Trap Group. It has been truly amazing to experience a project grow from being drawings on a computer screen to a whole group of colleagues and friends with whom you can enjoy a cold beer with at the end of the day. Not solely because of their pleasant company, the members of the Ion Trap Group, past and present, deserves a great amount of credit for present state of this project.

About five years ago, in the spring of 2003, Anders Mortensen came up to me and asked if I would like to go trap some ions with him. A year and a half later, after I had spent six months in the Ion Trap Group as an undergraduate student and another year abroad, Anders was finishing up his PhD-studies and I returned to the group to pick up where he had left. I am grateful to Anders for trusting me with his project and I feel privileged to have been given the responsibility to continue his work. I am also grateful to my supervisor Michael Drewsen for accepting me as the PhD-student for this project and for introducing me to this exciting field of physics. Our many discussions and his guidance and enthusiasm over the past four years have been invaluable.

After about two years, I was joined in my efforts, toward the construction of a new ion trap, by Aurelién Dantan. I had met Aurelién by chance at a conference in Copenhagen and after a visit to our group he agreed to join as a postdoc after the summer 2006. Today, I do not believe it would have been possible to find a better man for the job. Aurelién immediately added momentum to the project and by Christmas we had trapped the first ions in our new trap. Shortly after, Maria Langkilde-Lauesen started working as a master student, both in the lab and later on simulations for the experiments, which became a great resource to us.

In one of the first experiments we worked on with the new trap we joined forces with Rich Hendricks and David Grant, also from the Ion Group, who were working on loading of ion traps by laser ablation. Rich lead these experiments with great skill and other than the fact that they were very successful I also remember them as being some of the most fun experiments to do.

List of publications

[I] P. Herskind, A. Mortensen, J.L. Sørensen, M. Drewsen, *"Cavity-QED with ion Coulomb crystals"*, in Non-Neutral Plasma Physics Conference IV, AIP Conference Proceedings vol. 862, p. 292 (2006)

[II] P. Herskind, J. Lindballe, C. Clausen, J. L. Sørensen, M. Drewsen, *"Second-harmonic generation of light at 544 and 272 nm from an ytterbium-doped distributed feedback fiber laser"*, Opt. Lett. **32**, 268 (2007)

[III] R. J. Hendricks, D. M. Grant, P. Herskind, A. Dantan, M. Drewsen, *"An all-optical ion-loading technique for scalable microtrap architectures"*, Appl. Phys. B **88**, 507 (2007)

[IV] P. Herskind, A. Dantan, M. B. Langkilde-Lauesen, A. Mortensen, J. L. Sørensen, M. Drewsen, *"Loading of large ion Coulomb crystals into a linear Paul trap incorporating an optical cavity"*, to appear in Appl. Phys. B. (DOI 10.1007/s00340-008-3199-8)

[V] P. Herskind, A. Dantan, J. Marler, M. Albert, M. Drewsen, *Realization of Strong Collective Coupling with Ion Coulomb Crystals in an Optical Cavity*, submitted for publication.

Contents

Til mine forældre.

Chapter 1

Introduction

Quantum electrodynamics establishes the coupling between light and matter at a fundamental level. Even in the vacuum an atom is influenced by the fluctuations of the electromagnetic field, which give rise to well-known effects such as spontaneous emission and the Lamb shift [1]. The effect of spontaneous emission, for instance, arises as the result of the atom being coupled to the vacuum field and in this sense the notion of an isolated atom is fundamentally unphysical. As the vacuum contains an infinity of modes for the atom to decay to, the process is irreversible and the emitted photon is incoherently added to the reservoir of the vacuum. In 1946 Purcell noted that this description of spontaneous emission is only valid *stricto sensu* in the absence of finite boundary conditions for the electromagnetic field. More specifically, he pointed out that if boundary conditions are imposed on the system, e.g. in the form a cavity surrounding the atom, the associated change in the density of states available for the atom to decay through would lead to a change in the spontaneous emission rate of the atom [2]. In 1974 Drexhage reported the first observations of this effect by studying fluorescent organic dyes in the vicinity of a conducting plate acting as a reflecting mirror [3]. He observed changes in the fluorescence from the dyes depending on their distance from the mirror, signifying a change in the coupling between the emitter and the electromagnetic field as a result of modified boundary conditions for the field. In the present context of interactions with a cavity field, we would characterize Drexhage's cavity as only half a cavity and, hence, a very poor one. For this reason no drastic changes in the fluorescence were observed in these experiments. Later studies, with atoms in both microwave [4–6] and optical [7, 8] cavities, have, however, demonstrated dramatic changes in the spontaneous emission rate, both in the form of enhancement as well as inhibition.

Since these pioneering experiments the field has evolved rapidly and is now known as the field of cavity quantum electrodynamics (QED) [9]. Within this field, a fundamentally different regime from the perturbative one to which the above mentioned experiments belong, is the one in which the coupling between the atom and the field mode of the cavity exceeds that of any dissipative processes in the system, such as spontaneous emission and cavity field decay due to the finite quality of the cavity. In this regime, single quanta of excitation may be transferred coherently back and forth between the atom and the cavity field and the emission of a photon by an atom can thus become a reversible process.
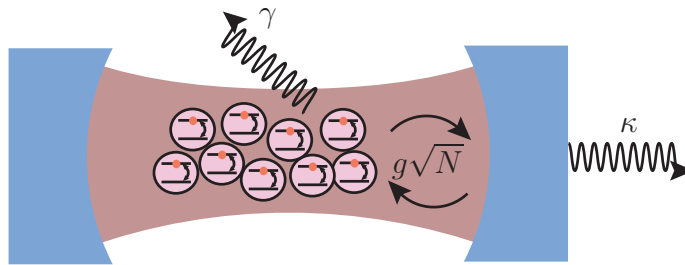
Figure 1.1: Schematic of the generic cavity QED experiment. γ is the decay rate of the atomic dipole, κ is the decay rate of the cavity field, g is the single atom coupling strength to the cavity field and N is the number of atoms.

The generic cavity QED experiment is drawn schematically in fig. 1.1. Here γ denotes the decay rate of the atomic dipole, κ is the decay rate of the cavity field and g is the coupling strength of a single atom to the cavity field. For a collection of N atoms as depicted here, the relevant coupling rate is given by the *collective* coupling strength of $g\sqrt{N}$. If for a single atom, the criterion $g > \gamma, \kappa$ is fulfilled, the system is in what is commonly referred to as the strong coupling regime of cavity QED, in which excitation, as described above, can be coherently mapped from a quantum state of an atom to a quantum state of a photon and vice versa. This regime has been realized by a number of experiments with neutral atoms in Fabry-Perot resonators both in the microwave [10] and the optical regime [11, 12], as well as in more exotic systems, such as single atoms coupled to monolithic resonators [13], quantum dots coupled to micro resonators [14, 15] and superconducting qubits coupled microwave cavities [16]. In systems where $N > 1$ one can define a so-called *collective* strong coupling regime, conditioned upon $g\sqrt{N} > \gamma, \kappa$. This regime was originally studied with clouds of atoms passing through optical Fabry-Perot cavities [17] and has recently been explored with Bose-Einstein condensates for which the combination of optically dense atomic samples and high finesse cavities gave rise to formidable coupling strengths [18, 19].

In general, all of the above systems rely upon the use of a high-Q resonator for the electromagnetic field while at the same time having a low modevolume of the cavity field as compared to the wavelength of the atomic transition. This was exactly what was pointed out by Purcell in his 1946 letter.

The strong coupling regime of cavity QED provides a playground for light-matter interactions, which is interesting to explore from a fundamental physics perspective alone. Furthermore, cavity QED has recently attracted much attention due its potential within quantum information science [20]. The motivation for developing techniques that can be applied in quantum information science is driven by the promises held by this field for realizing communication and computation beyond the limits of classical information science. While quantum communication allows for instance for fundamentally secure transmission of information [21], quantum computation offers the possibility of solving problems that are intractable on a classical computer [22, 23].

At the heart of most applications within quantum information science is an efficient interface between light and matter [24–26]. Whereas photons are excellent entities for transmission and distribution of quantum information [27], stationary atomic systems, such as laser cooled ions or atoms, are well-suited for processing [28,29] and storing [25, 30] of quantum information. Within the framework of cavity QED, neutral single atom systems have made great progress in engineering of quantum interfaces for light [31–33] making the field very active.

Cold trapped ions are currently state-of-the-art in quantum information processing. Examples include quantum gate operations with outstanding fidelities [29, 34], production of highly entangled states [35, 36], realization of small quantum algorithms [37, 38], and the first realizations of teleportation of atomic systems [39, 40]. Also within metrology ions are now an established reference [41] providing precision at the seventeenth decimal place. Combining the fields of cold ions and cavity QED is thus very attractive as it allows the prime techniques developed within ions based quantum logic and cavity QED based light-matter interactions to come together. Furthermore, one avenue for scaling of present day quantum computation capabilities is believed to be through the establishment of quantum networks [24, 26, 42] allowing different processing units, consisting of e.g. few ions, to interconnect. In this respect, an ion-photon interface would be a key element.

In recent years there has been much progress in interfacing single ions with optical cavities [43–47], however, the regime of strong coupling between ions and photons has remained an elusive goal for many years. As mentioned above, the strong coupling regime is realized by the use of very high Q cavities and low modevolumes relative to the wavelength of the atomic transition. In the optical regime this implies that a very short cavity with very low internal losses must be employed. This makes the strong coupling regime an extremely challenging goal to achieve in general. With ions it is further complicated by the influence of the mirror substrates on the confining fields of the ion trap, which may perturb or even impede trapping.

For applications within quantum information science, it has been pointed out that the requirement of single-atom strong coupling can be relaxed for ensembles of atoms [48, 49]. The regime of interest is then the *collective* strong coupling regime, defined as $g\sqrt{N} > \gamma, \kappa$. This allows for the use of a longer and technically less demanding cavity while still allowing strong interaction between the atomic ensemble and single photons. In this regime, the performance of the system is often quantified by the so-called cooperativity parameter $C = \frac{g^2 N}{2\kappa\gamma}$, which, for many applications in quantum information science, is the parameter of interest. For instance, it has been shown that the performance of a quantum memory for light scales as $\frac{2C}{1+2C}$ [50, 51] and with a cooperativity of e.g. 5, quantum states of light can thus potentially be mapped onto the state of the atomic ensemble with more that 90% fidelity.

Recently, there has been much focus on such collective states in neutral atom systems and their interfacing with single photons [25, 33, 52, 53]. For instance, storage of excitation and subsequent conversion to single photons have been demonstrated [52] as well as the full phase-coherent transfer of single quanta of excitation between different atomic ensembles via a cavity photon [53]. These experiments showed excellent capabilities of the atom-photon interface in terms of the efficiency by which conversion between atomic and photonic form of excitation could be achieved. However, as many other experiments based on neutral atoms [25, 54], the storage time of the

coherent atomic excitation was limited to microseconds. Although, progress to fight this issue in neutral atom systems is ongoing, ion trap based systems are still unrivaled, with typical coherence times of milliseconds [55] and even seconds for some schemes [30, 56]. The many orders of magnitude separating the values of this parameter in neutral- versus ion-based experiments represent one obvious motivation for embarking on a campaign to develop an ion-photon interface.

Additional advantages in working with ions are that they can be extremely well-confined spatially [57], and that they are generally easily prepared in a given internal state. As typical densities of ensembles of ions in ion traps are $\sim 10^8 \text{ cm}^{-3}$ absorption effects across the ensemble is negligible in optical pumping for instance.

Inspired by the benefits offered by ions and the potential of the collective regime, we have developed an experiment capable of confining large ensembles of laser cooled ions inside an optical cavity. This has allowed us to achieve the first realization of collective strong coupling with ions. The cooperativity obtained in this experiment is comparable to that used in neutral atom based quantum memories [25, 33, 52, 58, 59], which is very promising for the use of this system as a tool for quantum information science.

The thesis is organized as follows:

- Ch. 2, 3 and 4 are devoted to establishing the theoretical framework for the following chapters. In ch. 2 we put the light-matter interaction sketched in the above on firmer ground and derive equations for the interaction between atoms and laser fields as well as derive expressions for physically observable parameters in the cavity QED interaction. In ch. 3 we describe the ensemble of ions, which in our experiments form so-called ion Coulomb crystals. Special emphasis is made on the physical properties of such crystals that are of particular relevance for a cavity QED type experiment. In ch. 4 we then describe how such ion Coulomb crystals are cooled to millikelvin temperatures by Doppler laser cooling.

- The laser systems used in the experiments are described in ch. 5. Among these is a 272 nm uv laser source that was developed specifically for the production of the ion Coulomb crystals. The system relies on two consecutive stages of frequency doubling and is described in some detail.

- In ch. 6 we describe the experimental setup. This rather technical chapter covers both the design and construction of the ion trap used to confine the ions, as well as the optical resonator and its characterization. Furthermore, the measurement schemes employed in the later study of the cavity QED interaction are also described.

- Ch. 7 describes how ions are loaded into the trap. We present results on loading via two different methods: a "traditional" method using a thermal atomic beam derived from an effusive oven, and a novel method, based on laser ablation of a calcium target, that was recently developed in our group.

- The trap is characterized in ch. 8. The trapping parameters are calibrated using the theory of ch. 3 and the performance of the system for cavity QED type experiments is estimated.

- As the final step in the process toward achieving collective strong coupling, the preparation of the ensemble of ions in a specific state is treated both theoretically and experimentally in ch. 9.

- In ch. 10 we present the first results on collective strong coupling of ion Coulomb crystals and a cavity field at the single photon level. We evaluate quantitatively the performance of the system by a series of measurements of the effect of the coherent coupling between the ion Coulomb crystal and the cavity field.

- Finally, in ch. 11 we conclude and give an outlook for further studies with this system.

Chapter 2

Atom-light interaction

This chapter will review the basic theory of atom-light interaction. We shall begin in ch. 2.1 by considering an ensemble of two-level atoms interacting with a near-resonant single-mode light field. This will later be extended to more complex systems, however, much of the physics in this thesis will be well-described by such a simple two-level model. In ch. 2.2 we introduce the theoretical treatment for the evolution of the field of an empty optical resonator (a cavity). Finally, in ch. 2.3 we consider the interaction of the cavity field and the atomic ensemble. In the actual experiments which will be presented later in the thesis, a so-called ion Coulomb crystal will constitute the atomic ensemble. These crystals will be described in detail in ch. 3. For the purpose of introducing the theory for the interaction of these crystals with a light field, we shall treat them here as simple two-level atoms.

2.1 Interaction of two-level atoms with a light field

The interaction Hamiltonian in the dipole approximation for N atoms interacting with a single mode light field can be written as

$$\hat{H}_{\text{int}}(t) = -\sum_{j=1}^{N} \mathbf{D}_j \cdot \mathbf{E}(t), \tag{2.1}$$

where $\mathbf{E}(t)$ is the electric field and $\mathbf{D}_j$ is the dipole operator for the jth atom, which are given by

$$\mathbf{E}(t) = \mathbf{E} \cos \omega_l t = \mathcal{E}_0 \hat{\epsilon} \hat{A} e^{-i\omega_l t} + \mathcal{E}_0 \hat{\epsilon}^* \hat{A}^\dagger e^{i\omega_l t}, \tag{2.2}$$

and

$$\mathbf{D}_j = \mathbf{d}_{\mathbf{eg}}^j \left| \text{g} \right\rangle_j \left\langle \text{e} \right|_j + \mathbf{d}_{\mathbf{ge}}^j \left| \text{e} \right\rangle_j \left\langle \text{g} \right|_j. \tag{2.3}$$

In the above equations, $\mathcal{E}_0$ is the electric field amplitude, $\hat{\epsilon}$ is the polarization vector, $\hat{A}$ and $\hat{A}^\dagger$ are the annihilation and creation operator for the electromagnetic field, ω_l is the frequency, $\mathbf{d}_{\mathbf{eg}}^j$ ($= \mathbf{d}_{\mathbf{ge}}^j \equiv \mathbf{d}^j$) is the dipole matrix element of the transition and $\left| \text{e} \right\rangle_j \left\langle \text{g} \right|_j$ and $\left| \text{g} \right\rangle_j \left\langle \text{e} \right|_j$ are the atomic raising and lowering operator, respectively. Note that in eq. 2.2 we have absorbed the factor $\frac{1}{2}$ into $\mathcal{E}_0$ to avoid carrying it through all

the equations to follow. This means that the intensity of the light field is defined as

$$I \equiv 2\epsilon_0 c \mathcal{E}_0^2. \tag{2.4}$$

In the rotating wave approximation, that is, omitting non-energy conserving terms, the interaction Hamiltonian reads,

$$\hat{H}_{\text{int}}(t) = -\hbar \sum_j \left[g_j \hat{A}^\dagger \left|\text{g}\right\rangle_j \left\langle\text{e}\right|_j e^{i\omega_l t} + g_j \hat{A} \left|\text{e}\right\rangle_j \left\langle\text{g}\right|_j e^{-i\omega_l t} \right], \tag{2.5}$$

where the coupling strength of the jth atom g_j has been defined as (here assuming linear a polarization such that $\hat{\epsilon} = \hat{\epsilon}^*$ and parallel to $\mathbf{d}^j$),

$$g_j = \frac{\left|\mathbf{d}^j\right| \mathcal{E}_0}{\hbar}. \tag{2.6}$$

Assuming all atoms have equal coupling strength g and defining the atomic coherences:

$$\hat{\tilde{P}} = \sum_{j=1}^N \left|\text{g}\right\rangle_j \left\langle\text{e}\right|_j \;\; ; \;\; \hat{\tilde{P}}^\dagger = \sum_{j=1}^N \left|\text{e}\right\rangle_j \left\langle\text{g}\right|_j, \tag{2.7}$$

the interaction Hamiltonian becomes,

$$\hat{H}_{\text{int}}(t) = -\hbar g \hat{A}^\dagger \hat{\tilde{P}} e^{i\omega_l t} - \hbar g \hat{A} \hat{\tilde{P}}^\dagger e^{-i\omega_l t}. \tag{2.8}$$

As the atomic coherences, the atomic populations are defined as:

$$\hat{\Pi}_k = \sum_{j=1}^N \left|\text{k}\right\rangle_j \left\langle\text{k}\right|_j \;\; ; \;\; k = \{\text{g}, \text{e}\} \tag{2.9}$$

In addition to the interaction Hamiltonian we have the atomic Hamiltonian

$$\hat{H}_{\text{atom}} = \hbar \omega_{\text{eg}} \hat{\Pi}_{\text{e}}. \tag{2.10}$$

Using Hamilton's equation of motion for the time evolution of an operator $\hat{Q}$, $\dot{\hat{Q}} = \frac{i}{\hbar} \left[\hat{H}, \hat{Q} \right]$ (in the Heisenberg picture) [60], we can find the equations of motion for the atomic operators. The full set of equations for the operators are known as the Heisenberg-Langevin equations, from which all properties of the atoms can be calculated. In this thesis we shall only be interested in the mean values of the atomic operators and the resulting set is equations is then given by

$$\begin{aligned}
\dot{\Pi}_{\text{g}} &= ig \left(A^* \tilde{P} e^{i\omega_l t} - A \tilde{P}^* e^{-i\omega_l t} \right) \\
\dot{\Pi}_{\text{e}} &= -ig \left(A^* \tilde{P} e^{i\omega_l t} - A \tilde{P}^* e^{-i\omega_l t} \right) \\
\dot{\tilde{P}} &= -i\omega_{\text{eg}} \tilde{P} - igA e^{-i\omega_l t} \left(\Pi_{\text{e}} - \Pi_{\text{g}} \right),
\end{aligned}$$

where $Q \equiv \left\langle \hat{Q} \right\rangle$ and $Q^* \equiv \left\langle \hat{Q}^\dagger \right\rangle$. Rewriting in terms of slowly varying variables P and P^* defined through

$$P = \tilde{P} e^{i\omega_l t} \;\; ; \;\; P^* = \tilde{P}^* e^{-i\omega_l t} \tag{2.11}$$

and adding the effect of a spontaneous decay rate Γ from the excited to the ground state and the decoherence rate of the atomic dipole $\gamma = \Gamma/2$ the equations of motion for the atomic operators become

$$
\begin{align}
\dot{\Pi}_\mathrm{g} &= \Gamma\Pi_\mathrm{e} + i\left(\Omega^* P - \Omega P^*\right) \tag{2.12a}\\
\dot{\Pi}_\mathrm{e} &= -\Gamma\Pi_\mathrm{e} - i\left(\Omega^* P - \Omega P^*\right) \tag{2.12b}\\
\dot{P} &= -\left(\gamma + i\Delta\right)P - i\Omega\left(\Pi_\mathrm{e} - \Pi_\mathrm{g}\right), \tag{2.12c}
\end{align}
$$

where we have introduced the detuning

$$
\Delta = \omega_\mathrm{eg} - \omega_l, \tag{2.13}
$$

and inserted the Rabi frequency $\Omega = gA$.

Eq. 2.12 are commonly referred to as the optical Bloch equations in the literature. In steady state we find for the atomic coherence:

$$
P = -\frac{i\Omega}{\gamma + i\Delta}\left(\Pi_\mathrm{e} - \Pi_\mathrm{g}\right). \tag{2.14}
$$

Inserting this in the steady state expression for the excited state population Π_e, this can be expressed as

$$
\Pi_\mathrm{e} = \frac{1}{2}\frac{s}{1+s}, \tag{2.15}
$$

where s is the saturation parameter, defined as

$$
s = \frac{2\left|\Omega\right|^2}{\left(\Gamma/2\right)^2 + \Delta^2} = \frac{s_0}{1 + \left(\frac{2\Delta}{\Gamma}\right)^2}, \tag{2.16}
$$

and where s_0 is the on-resonance saturation parameter given by,

$$
s_0 = 2\frac{\left|\Omega\right|^2}{\left(\Gamma/2\right)^2} \equiv \frac{I}{I_\mathrm{sat}}, \tag{2.17}
$$

where $I_\mathrm{sat} = \frac{\hbar\Gamma\omega_\mathrm{eg}^3}{12\pi c^2}$ is the saturation intensity and $\Gamma = \frac{\omega_\mathrm{eg}^3 |d|^2}{3\pi\epsilon_0\hbar c^3}$ [61]. Note that our definition of the on-resonance saturation parameter and, hence, the Rabi frequency differs by a factor 4 and 2, respectively, from what is used in some texts [62–64]. This can be traced back to our definition of the field intensity in eq. 2.4.

2.2 A single mode optical cavity

We consider the case of an empty cavity as depicted in fig. 2.1 and wish to find an expression for the cavity spectrum, that is, a relation between the incoming field $E^\mathrm{in}(t)$ and the outgoing fields $E_1^\mathrm{out}(t)$ and $E_2^\mathrm{out}(t)$ as a function of the frequency of the field and the cavity parameters. The field $E(t)$ after the first mirror is given by

$$
E(t) = t_1 E^\mathrm{in}(t) + \alpha E''(t) r_1 e^{i\pi}, \tag{2.18}
$$

where $e^{i\pi}$ is the phase shift associated with the reflection on the mirror, t_i and r_i are the field transmission and reflection coefficients for the two mirrors ($i = 1, 2$)
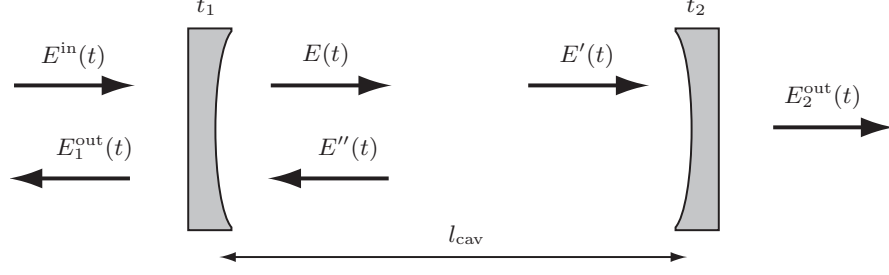
Figure 2.1: Schematic of a cavity of length l_{cav} and with two mirrors with field transmission coefficients t_1 and t_2. $E(t)$ represent the field at different locations. See text for details.

and the factor α accounts for the scattering and absorption losses in a reflection on either of the mirrors. If $\mathcal{L}$ is the total intra-cavity losses per round trip for the field intensity, we can write this as $\alpha = \sqrt{1 - \mathcal{L}/2}$. Likewise, the field intensity coefficients associated with transmission and reflection are related to the amplitudes by $t_i = \sqrt{T_i}$ and $r_i = \sqrt{R_i}$ and for each mirror the intensity coefficients must naturally satisfy $T + R + \mathcal{L}/2 = 1$. The field $E''(t)$ inside the cavity is given by

$$E''(t) = \alpha r_2 E(t - \tau) e^{i\phi} e^{i\pi}, \tag{2.19}$$

where $\tau = \frac{2l_{\text{cav}}}{c}$ is the round-trip time and $\phi = (\omega_l - \omega_c)\tau = -\Delta_c \tau$ is the phase change for a field of frequency ω_l after one round-trip and where ω_c is the resonance frequency of the cavity. Inserting eq. 2.19 in eq. 2.18:

$$
\begin{aligned}
E(t) &= t_1 E^{\text{in}}(t) + \alpha^2 r_1 r_2 E(t - \tau) e^{i\phi} e^{2i\pi} \\
&= \sqrt{T_1} E^{\text{in}}(t) + (1 - \mathcal{L}/2)(1 - T_1/2)(1 - T_2/2)(1 + i\phi)E(t - \tau) \\
&= \sqrt{T_1} E^{\text{in}}(t) + (1 - \mathcal{L}/2 - T_1/2 - T_2/2 - i\Delta_c\tau)E(t - \tau), \tag{2.20}
\end{aligned}
$$

where we have expanded according to the assumption that $\mathcal{L}, T_1, T_2, |\phi| \ll 1$ and retained only first-order terms[1]. The decay rate of the field through the mirrors is given by

$$\kappa_i = \frac{1 - r_i}{\tau} = \frac{1 - \sqrt{1 - T_i}}{\tau} \simeq \frac{T_i}{2\tau}. \tag{2.21}$$

Similarly, we may define a decay rate of the cavity field associated with the intra-cavity losses as $\kappa_{\mathcal{L}} = \frac{\mathcal{L}}{2\tau}$. Rearranging and dividing eq. 2.20 by τ, we get

$$\frac{E(t) - E(t - \tau)}{\tau} = -(\kappa_{\mathcal{L}} + \kappa_1 + \kappa_2 + i\Delta_c)E(t - \tau) + \sqrt{\frac{2\kappa_1}{\tau}} E^{\text{in}}(t),$$

which for $\tau \to 0$ becomes

$$\dot{E}(t) = -(\kappa_{\mathcal{L}} + \kappa_1 + \kappa_2 + i\Delta_c)E(t) + \sqrt{\frac{2\kappa_1}{\tau}} E^{\text{in}}(t). \tag{2.22}$$

---

[1] For the cavity used in our experiments, this is a valid assumption as $\mathcal{L}, T_1, T_2 < 1\%$ and, since we are interested in the cavity spectrum around resonance, the phase shift ϕ will also be close to zero.

This is the equation of motion for the field inside the cavity. It contains the passive losses of the cavity due to the mirrors and a phase shift depending on the cavity detuning Δ_c, as well as a source term originating from the input field $E^{\text{in}}(t)$. Later we shall see how the introduction of ions inside the cavity changes the field evolution.

In steady state the field amplitude becomes

$$E(t) = \frac{\sqrt{\frac{2\kappa_1}{\tau}}}{\kappa_{\mathcal{L}} + \kappa_1 + \kappa_2 + i\Delta_c} E^{\text{in}}(t), \tag{2.23}$$

The output fields can be found from: $E_1^{\text{out}}(t) = t_1\alpha E''(t) + r_1 E^{\text{in}}(t)$ and $E_2^{\text{out}}(t) = t_2\alpha E'(t)$ for the reflected and the transmitted field, respectively. The transmission and the reflection are then described by Lorentzian functions of the form:

$$\text{trans} = \left| \frac{E_2^{\text{out}}(t)}{E^{\text{in}}(t)} \right|^2 = \frac{4\kappa_1\kappa_2}{\left(\kappa_{\mathcal{L}} + \kappa_1 + \kappa_2\right)^2 + \Delta_c^2}, \tag{2.24}$$

and

$$\text{refl} = \left| \frac{E_1^{\text{out}}(t)}{E^{\text{in}}(t)} \right|^2 = \frac{\left(\kappa_{\mathcal{L}} - \kappa_1 + \kappa_2\right)^2 + \Delta_c^2}{\left(\kappa_{\mathcal{L}} + \kappa_1 + \kappa_2\right)^2 + \Delta_c^2}. \tag{2.25}$$

In fig. 2.2 both transmission and reflection has been plotted for the parameters applicable to our cavity.

As a measure of the quality of the optical resonator, we introduce the cavity finesse

$$\mathcal{F} = \frac{\text{FSR}}{\text{FWHM}}, \tag{2.26}$$

where the free spectral range (FSR), given by $1/\tau$, is the frequency spacing between the cavity resonances (i.e. the detuning necessary for the cavity field to acquire a phase shift of 2π) and the full width at half the maximum (FWHM) of the empty cavity is given from the Lorentzian of eq. 2.24 or eq. 2.25 as $2\left(\kappa_{\mathcal{L}} + \kappa_1 + \kappa_2\right)/2\pi$. From
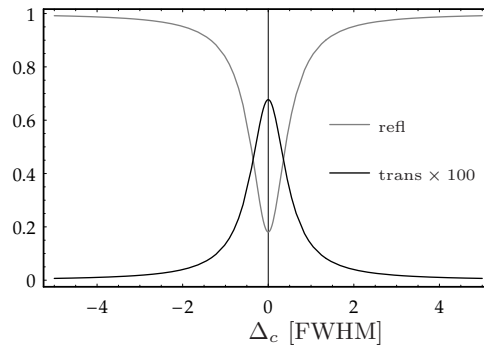
Figure 2.2: Transmission and reflection of the empty cavity for $T_1 = 1500$ ppm, $T_2 = 5$ ppm and $\mathcal{L} = 600$ ppm. The cavity transmission signal has been multiplied by a factor 100 to compensate for the small transmission T_2 of the output mirror and the frequency scale is in units of the FWHM of the cavity.

the relation between the cavity decay rate and the mirror transmission (eq. 2.21) the finesse can thus be written as:

$$\mathcal{F} = \frac{2\pi}{\mathcal{L} + T_1 + T_2}. \tag{2.27}$$

The finesse of the cavity can therefore be found from a measurement of either the FSR and the FWHM (eq. 2.26) or the cavity losses $\mathcal{L}$ (eq. 2.27) if both transmission coefficients are known.

The reflection signal provides a simple way of estimating the losses. Let us define the parameter β as the ratio of the reflection on and off resonance. Then from eq. 2.25,

$$\beta = \frac{\text{refl}(\Delta_\mathrm{c} = 0)}{\text{refl}(\Delta_\mathrm{c} \to \infty)} = \frac{(\kappa_\mathcal{L} - \kappa_1 + \kappa_2)^2}{(\kappa_\mathcal{L} + \kappa_1 + \kappa_2)^2} = \frac{(\mathcal{L} - T_1 + T_2)^2}{(\mathcal{L} + T_1 + T_2)^2}, \tag{2.28}$$

where we have used eq. 2.21 in the last step. Taking the square root on both sides and isolating $\mathcal{L}$ then gives an expression for the losses,

$$\mathcal{L} = \frac{1 \pm \sqrt{\beta}}{1 \mp \sqrt{\beta}} T_1 - T_2, \tag{2.29}$$

where the upper sign is used when the total cavity losses exceeds the input coupler transmission, $\mathcal{L} + T_2 > T_1$, and the lower sign is used in the opposite case, when $\mathcal{L} + T_2 < T_1$. For the reflection signal in fig. 2.2 we would evaluate the losses to be about 600 parts per million (ppm) by use of eq. 2.29.

2.3 Interaction of a two-level atom and a single mode cavity field

In this last section of the chapter we combine the results of the two previous sections to obtain a description of an ensemble of N two-level atoms interacting with a cavity field. This will provide the theoretical framework for our experiments with clouds of cold trapped ions inside an optical cavity that we will describe in ch. 10.

Including an ensemble of ions in the cavity, the field equation (eq. 2.22) is modified by the addition of a term describing the interaction with the atomic medium, which via Hamilton's equation of motion for the mean value of the field operator A can be evaluated to igP. Furthermore, with our definition of the interaction Hamiltonian (eq. 2.8), the field equation can be written in terms of the mean values of the field operators by making the substitutions $E \to A$ and $\frac{1}{\sqrt{\tau}} E^\mathrm{in} \to A^\mathrm{in}$, such that

$$\dot{A} = -\left(\kappa + i\Delta_c\right) A + igP + \sqrt{2\kappa_1} A^\mathrm{in}, \tag{2.30}$$

where, for simplicity, we have substituted $\kappa = \kappa_\mathcal{L} + \kappa_1 + \kappa_2$. Note that with this definition $|A|^2$ is a (dimensionless) of number of photons, whereas $\left|A^\mathrm{in}\right|^2$ is a photon flux (photons/s).

In our experiments we will study the interaction between an atomic ensemble and a light field composed of single quanta. In terms of field strength this corresponds to the low saturation regime ($s \simeq 0$) and the population inversion $\Pi_\mathrm{e} - \Pi_\mathrm{g} \simeq -N$.

Combined with the expression for the steady state atomic coherence (eq. 2.14), the solution to the cavity field equation (eq. 2.30) in steady state becomes:

$$A = \frac{\sqrt{2\kappa_1}}{\kappa' + i\Delta'_c} A^{\text{in}}, \tag{2.31}$$

with

$$\kappa' = \kappa + g^2 N \frac{\gamma}{\gamma^2 + \Delta^2} \tag{2.32}$$

and

$$\Delta'_c = \Delta_c - g^2 N \frac{\Delta}{\gamma^2 + \Delta^2}. \tag{2.33}$$

These represent the effect of absorption and phase-shift of the cavity field due to the interaction with the atomic ensemble. The lineshape is still a Lorentzian but with a half-width κ' and a detuning parameter Δ'_c dressed by the atoms. On resonance (at $\Delta = 0$) the absorption dominates and can be expressed as:

$$\text{Abs}(\Delta = 0) = \frac{\gamma g^2 N}{\gamma^2} = 2\kappa C, \tag{2.34}$$

where we have introduced the cooperativity parameter defined as [65]

$$C = \frac{g^2 N}{2\gamma\kappa}. \tag{2.35}$$

Eq. 2.33 represents the phase-shift due to a dispersive interaction off resonance. It attains its maximal value for $\Delta = \pm\gamma$ where it is equal to κC. The performance of our system may thus be evaluated, in terms of cooperativity, by measurements of absorption or phase shift. We shall return to this in ch. 10. As in the previous section, from the intra-cavity field we can derive an expression for the transmission and the reflection of the cavity. Fig. 2.3 shows a plot of the transmission coefficient for a cooperativity of $C = 10$ as a function of cavity detuning Δ_c and atomic detuning Δ. The effects of atomic absorption around $\Delta = 0$ and large phase-shift around $\Delta = \pm\gamma$ are clearly seen.

It is illustrative to return for a moment to the time-dependent equations for the atomic coherence and the cavity field. Setting the population inversion $\Pi_e - \Pi_g = -N$ as in the above, these follow from eq. 2.12 and eq. 2.30

$$\dot{P} = -(\gamma + i\Delta)P + igNA \tag{2.36a}$$
$$\dot{A} = -(\kappa + i\Delta_c)A + igP. \tag{2.36b}$$

By solving this set of coupled equations we find directly the eigenvalue spectrum of the combined atom-cavity system. An interesting case is that for which the atomic- and cavity detuning are both zero. The eigenvalues then follow straightforwardly from eq. 2.36 as

$$\lambda = -\left(\frac{\gamma + \kappa}{2}\right) \pm \sqrt{\left(\frac{\gamma - \kappa}{2}\right)^2 - g^2 N} \tag{2.37}$$

and the solution to the coupled set of equations for the system is then of the form $e^{\lambda t}$. From this we see that the first term gives rise a to decay of the system excitation as
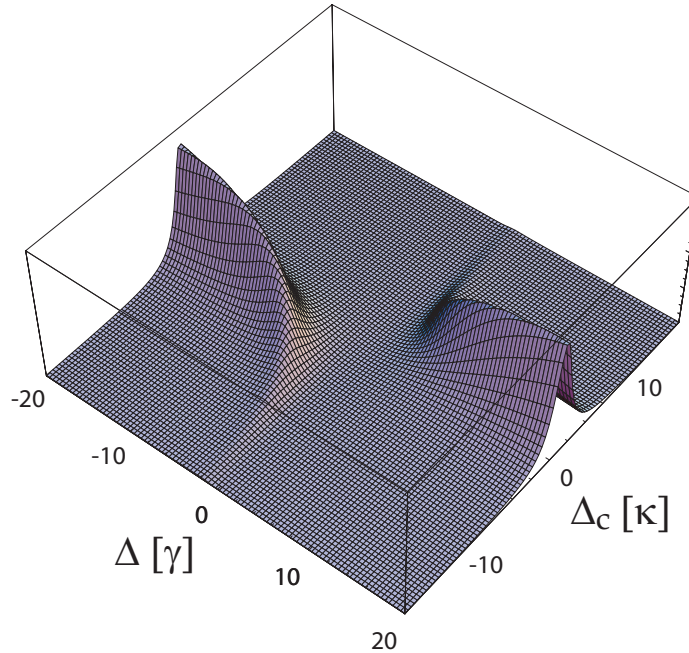
Figure 2.3: Transmission of a cavity for $C = 10$ as a function of cavity detuning Δ_c and atomic detuning Δ in units of cavity half width κ and atomic coherence decay rate γ, respectively. Parameters used are applicable to our experiment.

expected since κ and γ represent the decay rates of the field and atomic coherence, respectively. The square root term can, however, become imaginary and thus give rise to an oscillatory behavior if $g^2 N > |\gamma - \kappa| / 2$. Physically, this can be interpreted as a coherent exchange of excitation between the cavity and the atoms and it is this process that allows for the realization of e.g. quantum memories for light based on cold atomic ensembles [48, 66]. In the context of quantum information science one may think of the collective coupling (at rate $g\sqrt{N}$) as the coherent interaction that transfers information from a photonic to an atomic system and of the decay (at rates γ, κ) as sources of loss of information.

Obviously, the regime in which the coherent evolution is faster than any dissipative evolution is very interesting. Within the field of cavity QED, this is commonly referred to as the strong coupling regime. In our system where a collective interaction is at play, one defines the *collective* strong coupling criterion as [9]

$$g\sqrt{N} > \kappa, \gamma. \tag{2.38}$$

Note that this collective regime is fundamentally different from the single atom strong coupling regime for which $g > \kappa, \gamma$. One obvious difference is that for a single atom to absorb a photon it must be in the ground state and a single photon may thus saturate the transition. This establishes a certain "memory" in the system which is different from the case of an ensemble of atoms. Indeed, in our derivation of the optical Bloch equations (eq. 2.12), when including the effect of spontaneous emission

in the form of a phenomenological rate Γ, we neglected this effect [2]. One consequence of the collective nature of the coupling in our system is that an effect such as photon anti-bunching [32, 68, 69] is not expected.

The collective strong coupling regime does thus not exhibit behavior that is truly quantum, which is also reflected by it being well-described by a semi-classical model. In this respect, the transmission coefficient of fig. 2.3 simply corresponds to the linear susceptibility response of the system. Nevertheless, as pointed out in the introduction, in the context of quantum information science, the collective regime has great potential for producing efficient light-matter interfaces [24, 25, 33, 52, 58]. Indeed, a commonly used figure of merit for such systems is the cooperativity parameter C and for quantum memories and entanglement generation, the fidelity of such schemes often scales as $\frac{2C}{2C+1}$ [50, 51]. A system such as that modeled in fig. 2.3 with $C = 10$ may thus potentially allow fidelities close to 95% in such applications.

The usefulness of the collective interaction for quantum information science illustrates that, although the interaction may be accounted for semi-classically, this does not imply that it does not facilitate coherent interaction with quantum states, e.g. quantum states of light. To treat a system comprised of an atomic ensemble interacting with a single photon, we describe the state of the system in a restricted basis spanned by only two states: $|g, 1\rangle$ and $|e, 0\rangle$. These represent configurations where either all the atoms are in the ground state and there is one photon in the cavity ($|g, 1\rangle$) or one atom is in the excited state, with the remaining atoms in the ground state, and no photons are in the cavity ($|e, 0\rangle$). The atomic basis states are the symmetric, so-called, Dicke states [70]

$$|g\rangle \quad = \quad |g_1, ...g_N\rangle \tag{2.39a}$$

$$|e\rangle \quad = \quad \frac{1}{\sqrt{N}} \sum_{i=1}^{N} |g_1, ...e_i, ...g_N\rangle, \tag{2.39b}$$

which were first introduced by Dicke and have been used e.g. in the context of superradiance [71]. In this picture, the atomic coherence may thus be written as

$$P = |g\rangle \langle e| = \frac{1}{\sqrt{N}} \sum_{i=1}^{N} |g_1, ...g_N\rangle \langle g_1, ...e_i, ...g_N|,$$

which, for N identical atoms, results in

$$P = \sqrt{N} |g_1, ...g_N\rangle \langle g_1, ...e_i, ...g_N|, \tag{2.40}$$

where, once again, the $\sqrt{N}$ factor appears due to the collective interaction with the ensemble.

The quantity $g\sqrt{N}$ will be referred to as the collective coupling strength throughout this thesis and it is the scaling of this parameter with the number of atoms that allows us to enter a regime where single photons can interact strongly with an atomic ensemble. The value of g can be found from eq. C.3 and eq. 2.6 based on the dipole matrix element of the relevant atomic transition and on the mode-volume of the optical cavity. From this, the collective coupling strength can evaluated for a given atomic system and a given cavity geometry. This is done, for our system, in appendix C.

---

[2]this is known as the Markov approximation [67]

Chapter 3

The physics of ion Coulomb crystals in a linear Paul trap

This chapter will provide the basic theoretical tools required for an understanding of the physics of ion Coulomb crystals, both in a general sense and in the context of cavity QED experiments with this form of matter. We begin by a review of the theory of the linear Paul trap used to confine the ion Coulomb crystals and then move on to describe the physical properties of ion Coulomb crystals relevant for this thesis.

3.1 The linear Paul trap

All experiments presented in this thesis have been performed with trapped charged particles confined in a linear Paul trap. This type of trap combines static and radio-frequency (rf) electric fields to create a time-averaged harmonic potential. The use of a time-varying field is necessary as Laplace's law prevents us from obtaining a three-dimensional extremum for the electric potential $\phi(x, y, z)$ using only static electric fields. Specifically, from Laplace's equation

$$\frac{\partial^2 \phi(x, y, z)}{\partial x^2} + \frac{\partial^2 \phi(x, y, z)}{\partial y^2} + \frac{\partial^2 \phi(x, y, z)}{\partial z^2} = 0 \qquad (3.1)$$

it follows that all three terms cannot have the same sign, e.g. positive, which would be necessary to create a potential minimum.

The linear Paul trap is closely related to its predecessor, the quadrupolar mass filter [72], invented by Wolfgang Paul in the 1950's, however, the linear Paul trap in its present form was not invented until 1989 [73]. Other types of related traps include the hyperbolic Paul trap [74], the race-track trap [75] and the Penning trap [76], the later differing from all the former by the use of a static magnetic field instead of the oscillating rf-field. For a comparison of these traps see e.g. [77, 78].

This section will review the basics of the linear Paul trap and introduce some of the concepts and parameters, needed for the remainder of the thesis.
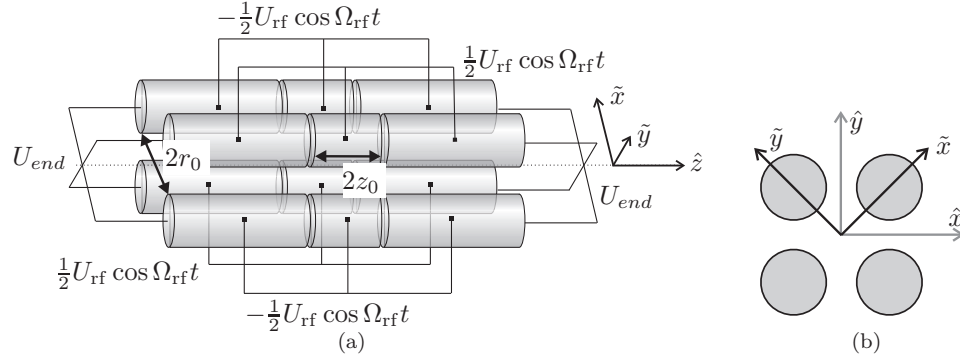
Figure 3.1: (a) Linear Paul trap electrode configuration with applied voltages. We will refer to the $\hat{z}$-axis as the trap axis (dotted line). (b) End-view of the Paul trap with the definitions of the $\tilde{x}$ and $\tilde{y}$ axis (black). The $\hat{x}$ and $\hat{y}$ axis (grey) are used elsewhere.

3.1.1 A single ion in a linear Paul trap

Fig. 3.1 shows a schematic of the linear Paul trap. The trap consists of four sectioned cylindrical electrode rods placed in a quadrupole configuration. Confinement in the radial plane (xy-plane in Fig. 3.1) is obtained by applying time varying voltages $\frac{1}{2}U_{rf}\cos(\Omega_{rf}t)$ and $\frac{1}{2}U_{rf}\cos(\Omega_{rf}t+\pi)$ to the two sets of diagonally opposite electrode rods, where U_{rf} is the peak-to-peak amplitude of the rf-voltage and Ω_{rf} is the rf-frequency. This gives rise to a potential in the radial plane of the form:

$$\phi(\tilde{x},\tilde{y},t) = -\frac{1}{2}U_{rf}\cos(\Omega_{rf}t)\frac{\tilde{x}^2-\tilde{y}^2}{r_0^2}, \tag{3.2}$$

where r_0 is the inter-electrode inscribed radius, defined in fig. 3.1. The sectioning of each of the electrode rods allows for application of a static voltage U_{end} to the end-electrodes, which provides confinement along the z-axis. The electric potential along the z-axis is then well described by

$$\phi(z) = \eta U_{end}\frac{z^2}{z_0^2}, \tag{3.3}$$

where η is a constant related to the trap geometry and $2z_0$ is the length of the center electrodes. A requirement of Laplace's law is that the confinement along the z-axis, provided by this static field, is accompanied by a defocussing effect in the radial plane. The total electric potential in the radial plane is then given by

$$\phi(\tilde{x},\tilde{y},t) = -\frac{1}{2}U_{rf}\cos(\Omega_{rf}t)\frac{\tilde{x}^2-\tilde{y}^2}{r_0^2} - \frac{1}{2}\eta U_{end}\frac{\tilde{x}^2+\tilde{y}^2}{z_0^2}. \tag{3.4}$$

The sectioning of the electrode rods also allows for individual dc-offsets to be applied such that the ion can be shifted radially with respect to the quadrupole minimum. This has been omitted in eq. 3.4 for the sake of simplicity.

From eq. 3.3 it follows immediately that the motion of a single charged particle *along the z-axis* is that of a simple harmonic oscillator. The equations of motion *in the*

radial plane for a single charged particle can be found from eq. 3.4 via Newton's second law but are somewhat more complicated and require a bit more work. Rewriting the resulting second order differential equation in terms of more convenient parameters, the equations of motion in the radial plane can be described by the so-called Mathieu equation, after the French mathematician Emile Mathieu,

$$\frac{\partial^2 u}{\partial \tau^2} + [a - 2q_u \cos(2\tau)] u = 0, \qquad u = \tilde{x}, \tilde{y}. \tag{3.5}$$

Here we have introduced the following dimensionless parameters:

$$\tau = \frac{\Omega_{rf} t}{2}, \qquad a = -4 \frac{\eta Q U_{end}}{M z_0^2 \Omega_{rf}^2}, \qquad q_x = -q_y = 2 \frac{Q U_{rf}}{M r_0^2 \Omega_{rf}^2}, \tag{3.6}$$

where Q and M are the charge and mass of the particle, respectively.

For the particle to exhibit stable motion in the radial plane, the solutions to eq. 3.5 must be non-diverging and the resulting amplitude of its motion must be bounded by some maximum, set by the physical surroundings, e.g. the trap electrodes. The stable (non-diverging) solutions to the Mathieu equation can be found in e.g. ref. [79]; in fig. 3.2a) the regions of stable motion in (a, q)-space have been plotted in accordance to this.[1] In general both positive and negative values of a can result in stable motion in the radial plane. However, from the definition of a (eq. 3.6), it is evident that, once the choice has been made to trap e.g. positively charged particles, a will be limited to negative values only, in order to obtain stable motion along the z-axis. Fig. 3.2b) shows this area in (a, q)-space. More details can be found in ref. [81].

The region of stable motion depends linearly on the charge-to-mass ratio, Q/M, of the trapped particle through the a and q parameters as seen from eq. 3.6. As a result of this and the relatively broad area of stability in (a, q)-space, different atomic species can be trapped simultaneously provided that their charge-to-mass ratio is not too different. For instance, all singly-charged isotopes of naturally abundant calcium, as will be the focus of this thesis, can be trapped simultaneously.

In general the trap is operated such that $|a|, |q| \ll 1$. This allows the equation of motion for the ion (eq. 3.5) to be rewritten as

$$u(t) = u_0 \left[1 - \frac{q_u}{2} \cos\left(\Omega_{\rm rf} t\right) \right] \cos\left(\omega_r t\right), \tag{3.7}$$

by introducing the secular frequency

$$\omega_r = \frac{\sqrt{q^2/2 + a}}{2} \Omega_{\rm rf}. \tag{3.8}$$

The ion's motion is now comprised of two distinct types of motion: A high frequency motion at Ω_{rf} and a low frequency motion at $\omega_r \ll \Omega_{rf}$. Note that the amplitude of the high frequency motion, the so-called *micromotion*, is given by the q parameter, which means that its amplitude is small and, hence, only acts as a jitter superimposed

---

[1] Adding a friction force, as to include e.g. laser cooling, will obviously affect the motion of the charged particle and the stability diagram will be modified accordingly [80]. The effect is quite small, however, and has been neglected here for the sake of simplicity.
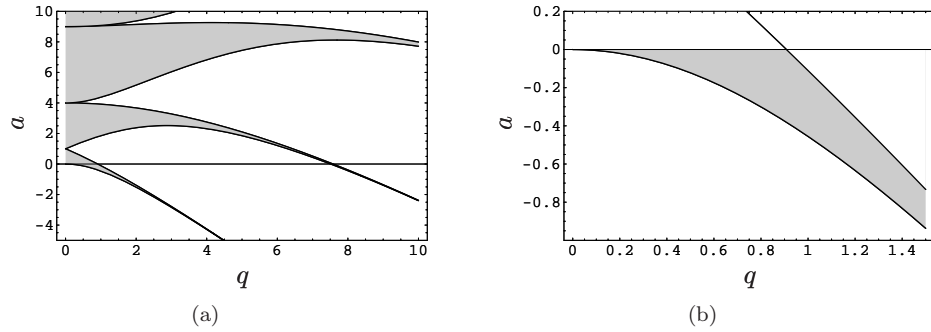
Figure 3.2: (a) Stability diagram of the Mathieu function in the (q, a)-space. Regions with stable solutions are marked with grey. (b) Region of stable motion of a positive particle in the linear Paul trap. Both diagrams also apply to negative q-values, i.e. the stability regions are mirrored in the a-axis.

on the dominant, so-called *secular motion*. When averaging out the fast motion, the secular motion can be described as motion in a harmonic so-called *pseudo-potential*:

$$\Phi_r(r) = \frac{1}{2}M\omega_r^2 r^2, \tag{3.9}$$

where ω_r can be expressed as

$$\omega_r^2 = \frac{Q^2 U_{rf}^2}{2M^2 r_0^4 \Omega_{rf}^2} - \frac{\eta Q U_{end}}{M z_0^2}, \tag{3.10}$$

through eq. 3.6 and eq. 3.8.

Likewise, the harmonic potential along the z-axis (eq. 3.3), may be expressed through the frequency ω_z as

$$\Phi_z(z) = \frac{1}{2}M\omega_z^2 z^2, \tag{3.11}$$

with

$$\omega_z^2 = \frac{2\eta Q U_{end}}{M z_0^2}. \tag{3.12}$$

From eq. 3.9 and eq. 3.10 it is seen that the radial potential depends inversely on the mass of the trapped particle [2], whereas the axial potential, described by eq. 3.11 and eq. 3.12, is independent on the mass. As a result, heavier particles are confined less tightly, radially, an issue we shall return to when discussing the trapping of two-component ion Coulomb crystals later in this thesis.

3.2   Ion Coulomb crystals

When several ions are confined in a linear Paul trap, the individual ions experience not only the electric potential of the trapping fields, but also the Coulomb interaction with the other ions. The system is then best described as a plasma and in terms of

---

[2]This forms the basis for the quadrupole mass filter.

collective parameters such as temperature and density. The ion plasma confined in our linear Paul trap is obviously a non-neutral plasma as its constituents are all of the same sign of charge. Another example of this type of plasma is the valence electrons in a metal. The electrons form a strongly coupled plasma confined in a neutralizing background of positive metallic ions, in the same way as our positive ions are confined in the neutralizing fields of the linear Paul trap.

Before describing ion Coulomb crystals, we begin by introducing a few basic concepts and parameters from plasma theory [82]. First, we shall consider the fundamental time and length scales appropriate for such systems. Here a brief example may be helpful: If we imagine a plasma of some density ρ and consider the effect of displacing a sheet of charge within the plasma by some amount δx, that is, a one-dimensional charge displacement. The sheet then experiences the field associated with its own displacement from equilibrium corresponding to twice the field from a sheet of charge $Q\rho\delta x$. The electric field is then [83]:

$$|\mathbf{E}| = \frac{Q\rho\delta x}{\epsilon_0}.$$

From the force $\mathbf{F} = Q\mathbf{E}$ we can find the potential energy U associated with the charge displacement as,

$$U = \int F dx = \frac{Q^2\rho\delta x^2}{2\epsilon_0}.$$

Approximating the potential by a harmonic potential $U = \frac{1}{2}M\omega^2\delta x^2$, we can extract the frequency of oscillation, the plasma frequency, as

$$\omega_p^2 = \frac{Q^2\rho}{\epsilon_0 M}, \tag{3.13}$$

which is sets the most fundamental time scale for plasma physics. We may interpret the corresponding period as the minimal time scale, on which plasma behavior is observed.

From ω_p a complementary length scale termed the Debye length λ_D can be defined by use of the Virial theorem for a harmonic potential $U = K$ and equating the kinetic energy by $\frac{1}{2}k_\mathrm{B}T$,

$$\lambda_\mathrm{D} = \sqrt{\frac{k_\mathrm{B}T}{M\omega_p^2}} = \sqrt{\frac{\epsilon_0 k_\mathrm{B}T}{\rho Q^2}}. \tag{3.14}$$

There are a number of ways to interpret the physical significance of the Debye length. It is considered the fundamental length scale for Debye shielding, which is the shielding of external fields by rearrangement of the space charge. The electric field of a test charge Q is thus screened out by the rearranging of the particles within the plasma over the distance λ_D.

In general, the collective behavior of a plasma is only observed on length scales larger than the Debye length and the spatial extend of the collection of charged particles must thus be greater than this characteristic length for plasma theory to apply. This is indeed the case for ion Coulomb crystals such as those confined in our linear Paul trap where $\lambda_\mathrm{D} < 1$ μm, which is much less than the inter-ion spacing of several μm.

The last physical quantity that we require from plasma physics for our understanding of ion Coulomb crystals is the plasma coupling parameter Γ_p, which for a one-component plasma of particles of charge Q and at temperature T is defined as[3]

$$\Gamma_p = \frac{Q^2}{4\pi\epsilon_0 a_{\mathrm{ws}} k_{\mathrm{B}} T}. \tag{3.15}$$

Here we have introduced the Wigner-Seitz radius a_{ws}, defined as the radius of a sphere that has a volume corresponding to the volume per particle at zero temperature:

$$\frac{4}{3}\pi a_{\mathrm{ws}}^3 = \frac{1}{\rho_0}, \tag{3.16}$$

where ρ_0 is the zero-temperature density of the ion plasma.

From the coupling parameter, which is essentially the ratio of the Coulomb interaction to the thermal energy, the thermodynamic state of the plasma can be determined. For instance, simulations predict that at $\Gamma_p \simeq 2$, short-range order within the plasma arises and a phase-transition from a gas to a liquid phase occurs [84], while around $\Gamma_p \simeq 170$ a phase-transition to a solid state will occur [85, 86], indicating the onset of long-range order within the plasma. The simulations predict a body-centered cubic (bcc) lattice structure in this crystalline state. Such crystallized structures, termed *ion Coulomb crystals*, are believed to be present in the interior of cooling white dwarfs, as two-component crystals of carbon and oxygen nuclei embedded in a neutralizing degenerate electron gas [87].

In the laboratory, conditions for crystallization can be achieved e.g. in experiments with laser cooled ions in Paul traps [88, 89]. From eq. 3.15 and eq. 3.16 it is seen that the conditions for crystallization are governed by the density and the temperature of the ion plasma. As we shall see later in this chapter and in ch. 4 both parameters can be controlled in the experiment. In our experiments, typical densities are of the order of 10^8 cm^{-3}, corresponding to a critical temperature for crystallization of around 10 mK, which is above the minimum temperature that can potentially be reached by Doppler laser cooling, which for our atomic system of Ca$^+$ is about 0.5 mK (see ch. 4). The plasma coupling parameter has been plotted in fig. 3.3 as a function of temperature for typical trapping parameters of our experiments.

3.2.1   The zero temperature charged liquid model

Two important parameters in our experiments are the density of the ion Coulomb crystal and its shape. In order to quantify the interaction between the cavity field and the ions we need to be able to evaluate the density of the ion Coulomb crystal as well as calibrate our trapping parameters. This section will review the necessary theoretical tools required for this.

Although ion Coulomb crystals are structured forms of matter, many of their characteristics, and specifically those of immediate interest such as shape and density, are well accounted for by a zero temperature charged *liquid* model [90]. For a cylindrically symmetric potential, like that of the linear Paul trap, such a model predicts the

---

[3]This is often denoted by Γ in the literature but to avoid confusion between this and the spontaneous decay rate of an atom we have added the subscript p and otherwise retained the standard notation for both these parameters.
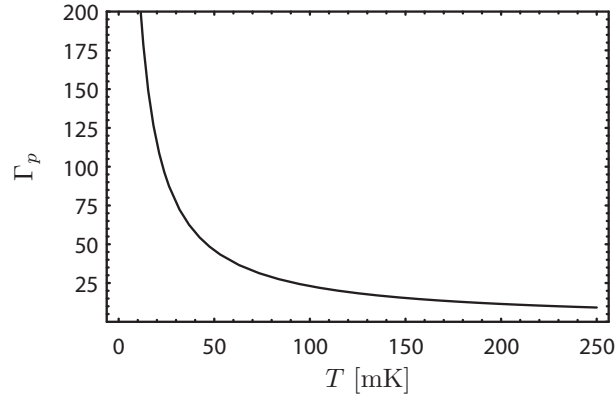
Figure 3.3: Plasma coupling parameter Γ_p versus temperature T for typical trapping parameters ($\rho_0 \simeq 6 \times 10^8$ cm^{-3}).

equilibrium shape to be a spheroid of constant density [91]. In general, the shape of a spheroid can be described by its aspect ratio, defined as the ratio of the crystal radius to its length: $\alpha \equiv 2R/L$. We distinguish between three different shapes (see fig. 3.4): *Spherical* for $\alpha = 1$, *prolate* for $\alpha < 1$ and *oblate* for $\alpha > 1$. Within the zero temperature charged liquid model a relationship between the ratio of the trap frequencies ω_z/ω_r and the aspect ratio of the crystal α can be derived. Following ref. [91] and assuming the electric potential from the charge distribution to vanish at infinity, this electric potential can be written (as a function of r and z inside the crystal) as

$$
\phi_{\text{charge}}(r, z) = \frac{\rho_0 Q}{4\epsilon_0} R^2 L \left[\frac{2}{(R^2 - L^2)^{\frac{1}{2}}} \sin^{-1} \left(1 - \frac{L^2}{R^2} \right)^{\frac{1}{2}} \right.
$$
$$
\left. - r^2 f(R, L) - z^2 g(R, L) \right], \tag{3.17}
$$

(a) Spherical ($\alpha = 1$)   (b) Prolate ($\alpha < 1$)   (c) Oblate ($\alpha > 1$)

Figure 3.4: Possible spheroidal shapes of the ion Coulomb crystal. The aspect ratio is defined as $\alpha \equiv 2R/L$. The z-axis corresponds to the trap axis in the linear Paul trap.

where the functions $f(R, L)$ and $g(R, L)$ are given by

$$f^{\alpha<1}(R, L) \;=\; -\left[\frac{1}{(L^2-R^2)^{\frac{3}{2}}}\sinh^{-1}\left(\frac{L^2}{R^2}-1\right)^{\frac{1}{2}} - \frac{L}{(L^2-R^2)\,R^2}\right]$$

$$g^{\alpha<1}(R, L) \;=\; \left[\frac{2}{(L^2-R^2)^{\frac{3}{2}}}\sinh^{-1}\left(\frac{L^2}{R^2}-1\right)^{\frac{1}{2}} - \frac{2}{(L^2-R^2)\,L}\right],$$

in the prolate case and

$$f^{\alpha>1}(R, L) = \left[\frac{1}{(R^2-L^2)^{\frac{3}{2}}}\sin^{-1}\left(1-\frac{L^2}{R^2}\right)^{\frac{1}{2}} - \frac{L}{(R^2-L^2)\,R^2}\right]$$

$$g^{\alpha>1}(R, L) = -\left[\frac{2}{(R^2-L^2)^{\frac{3}{2}}}\sin^{-1}\left(1-\frac{L^2}{R^2}\right)^{\frac{1}{2}} - \frac{2}{(R^2-L^2)\,L}\right],$$

in the oblate case. The total potential inside the crystal will be given by the sum of the trap potential $\Phi_{\text{trap}}(r, z)$ (eq. 3.9 and eq. 3.11) and the potential from the ion plasma $Q\phi_{\text{charge}}(r, z)$ (eq. 3.17)

$$\begin{aligned}
\Phi_{\text{tot}}(r, z) \;=\;& \Phi_{\text{trap}}(r, z) + Q\phi_{\text{charge}}(r, z) \\
=\;& \frac{1}{2}M\omega_r^2 r^2 + \frac{1}{2}M\omega_z^2 z^2 + \frac{\rho_0 Q^2}{4\epsilon_0}R^2 L \times \\
& \left[\frac{2}{(R^2-L^2)^{\frac{1}{2}}}\sin^{-1}\left(1-\frac{L^2}{R^2}\right)^{\frac{1}{2}} - r^2 f(R, L) - z^2 g(R, L)\right].
\end{aligned}$$

Since the total potential inside the crystal must be constant, it follows that the two terms depending on r must cancel out and likewise for the two terms depending on z. Hence,

$$\frac{1}{2}M\omega_r^2 r^2 \;=\; \frac{\rho_0 Q^2}{4\epsilon_0}R^2 L r^2 f(R, L)$$

$$\frac{1}{2}M\omega_z^2 z^2 \;=\; \frac{\rho_0 Q^2}{4\epsilon_0}R^2 L z^2 g(R, L).$$

Finally, taking the ratio of the two equations we arrive at

$$\frac{\omega_z^2}{\omega_r^2} = \frac{g(R, L)}{f(R, L)} = \begin{cases} -2\dfrac{\sinh^{-1}(\alpha^{-2}-1)^{\frac{1}{2}}-\alpha(\alpha^{-2}-1)^{\frac{1}{2}}}{\sinh^{-1}(\alpha^{-2}-1)^{\frac{1}{2}}-\alpha^{-1}(\alpha^{-2}-1)^{\frac{1}{2}}} &, \text{ for } \alpha < 1 \\[1.5em] -2\dfrac{\sin^{-1}(1-\alpha^{-2})^{\frac{1}{2}}-\alpha(1-\alpha^{-2})^{\frac{1}{2}}}{\sin^{-1}(1-\alpha^{-2})^{\frac{1}{2}}-\alpha^{-1}(1-\alpha^{-2})^{\frac{1}{2}}} &, \text{ for } \alpha > 1 \end{cases} \qquad (3.18)$$

Fig. 3.5 shows a plot of this relation (solid line). For comparison, a plot corresponding to a weakly coupled plasma in thermodynamic equilibrium is shown also (dashed line). In most of our experiments we will be working with prolate crystals of relatively low aspect ratios ($\alpha \sim 0.1$) in order to increase the optical depth of the ion Coulomb crystal along the trap axis. We shall return to this issue in ch. 8.
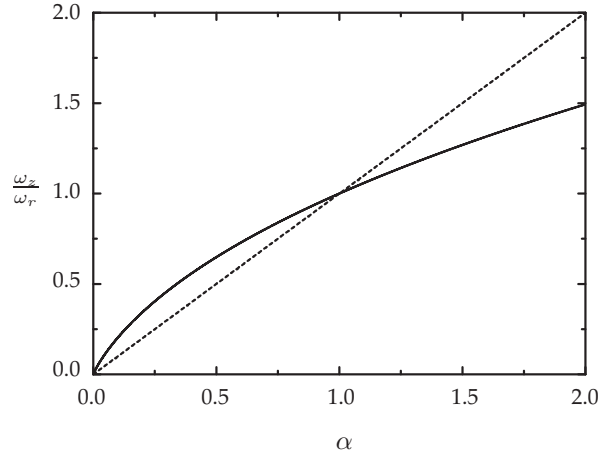
Figure 3.5: Ratio of the axial and radial trap frequencies vs. aspect ratio for a zero temperature charged liquid (solid line) and for a plasma of weakly coupled particles in thermodynamic equilibrium (dashed line).

The second parameter of interest in this section is the (average) density of the ion Coulomb crystal. The equilibrium requirement of a constant potential inside the crystal, also used in the previous derivation, allows us to write the following relation:

$$\phi_{\text{tot}}(r,z) = \frac{\Phi_{\text{trap}}(r,z)}{Q} + \phi_{\text{charge}}(r,z) = \text{constant}$$

$\Downarrow$

$$\nabla^2\phi_{\text{tot}}(r,z) = \frac{\nabla^2\Phi_{\text{trap}}(r,z)}{Q} + \nabla^2\phi_{\text{charge}}(r,z) = 0. \tag{3.19}$$

Inserting Poisson's equation, $\nabla^2\phi_{\text{charge}}(r,z) = -Q\rho_0/\epsilon_0$, then gives:

$$\frac{\nabla^2\Phi_{\text{trap}}(r,z)}{Q} = \frac{Q\rho_0}{\epsilon_0}. \tag{3.20}$$

Finally, by inserting the expression for the trap potential (eq. 3.9 and eq. 3.11) and taking the Laplacian, we get (after some algebra) an expression for the (average) density of the ion Coulomb crystal at zero temperature:

$$\rho_0 = \frac{\epsilon_0 U_{\text{rf}}^2}{M r_0^4 \Omega_{\text{rf}}^2}. \tag{3.21}$$

The density of the ion Coulomb crystal can thus be controlled by varying the rf-voltage applied to the electrodes. For technical reasons the value of the rf-voltage on the trap electrodes is not known as precisely as other parameters for the trap and requires an independent calibration. The relation between the ratio of the trap frequencies and the aspect ratio of the crystal, derived above, provides the basis for such a calibration: Given that the aspect ratio α can be measured with sufficient precision, U_{rf} can be calibrated via eq. 3.18, keeping in mind that $\omega_r \propto U_{\text{rf}}$ (c.f. eq. 3.10). We shall return to this in ch. 8 where we present results on characterization of the trap.

3.2.2   Effects of micromotion

In our discussion of ion Coulomb crystals we have so far ignored the effects of the micromotion and only considered the secular motion in the time-averaged potential. This description has assumed a form of equilibrium for the ion plasma and made use of thermodynamic concepts such as temperature to account for transitions between different thermodynamic phases. This seems somewhat ill defined, however, when considering the fact that the ions themselves are subject to the time-varying forces of the rf-field, causing their kinetic energies to change violently on the time-scale of this field. Here we will not consider an interpretation of this[4] but focus on what physically observable effects arises as a result of this micromotion and on how these might affect our experiments. Primarily, the effect manifests itself in two ways:

- There will be inhomogeneous broadening of the atomic transitions due to the position and time dependent velocity distribution of the ions [93].

- Coulomb collisions within the crystal will couple kinetic energy associated with the driven rf-motion into the secular motion, thus heating the crystal. This effect is also called rf-heating [94].

Fig. 3.6 shows a schematic illustration of the direction of the micromotion. It shows how the micromotion vanishes on the trap axis and increases the further away from the trap axis the ions are located. The fact that the micromotion vanishes at the trap axis, means that this axis holds a favored position in experiments with ions in linear Paul traps since there is no Doppler broadening of the atomic transitions of the ions due to micromotion. Furthermore, if the micromotion is not coupled to the motion along the z-axis, it will only give rise to a second-order Doppler shift when addressing the ions along this direction. This is also true along the x- and y-direction but only for ions located *on* the x- or y-axis, which as seen from fig. 3.6 have their micromotion perpendicular to the respective axes.

From eq. 3.7 it is seen that the micromotion amplitude is in fact non-vanishing even on the trap axis, where it is given by $A_{\mathrm{micro}} = \frac{1}{2}u_0 q$, with u_0 being the amplitude of the secular motion. This type of micromotion is inherent in a linear Paul trap and a consequence of the secular motion carrying the ion back and forth through the nodal line of the rf-field. It can, however, be minimized by cooling the ion which lowers the amplitude of the secular motion; hence the notion of a vanishing amplitude on the trap axis in the above. For ions not in the nodal line of the rf-field, that is ions that have their equilibrium positions off the trap axis, there is an excess micromotion of the same form as that due to the secular motion, but with u_0 replaced by their mean distance from the trap axis. For a single ion, this can be minimized by moving it to the trap axis [93], but for a three dimensional ion Coulomb crystal, where there are always ions off the trap axis, excess micromotion will be present. To minimize this effect, the crystal must be in the minimum of the quadrupole potential, which is ensured by adjusting the radial dc-offsets on the trap electrodes such that the quadrupole potential coincides with the minimum defined by this radial dc-potential. This adjustment is optimized by loading a two-component crystal and making the heavier component appear in equal ratios on both sides of the central core of the lighter isotope. As the

---

[4]For a discussion of this see e.g. [92].

heavier component is confined less tightly by the radial quadrupole potential, a dc-offset will have a larger influence on this and it will not appear symmetrically around the lighter component. In the images of fig. 4.4 the potential has been optimized in this way.

Since the micromotion is dependent on the distance of the ions from the trap axis, rf-heating will predominantly affect crystals of high aspect ratios, where more ions are located further away from the traps axis, than low aspect ratio crystals. By the same line of reasoning, increasing the number of ions within a crystal of a given aspect ratio, will increase the heating rate and ultimately limit the number of ions and the crystal size.

It is obvious that the above mentioned effects, Doppler broadening and rf-heating, will have a major influence on our experiments and we shall return to them several times throughout the thesis, especially in ch. 8.3 when we characterize our trap with the purpose of optimizing the number of ions in the cavity mode.

3.2.3 Aspects of temperature and structure

As mentioned earlier in this chapter, from molecular dynamics (MD) simulations the ions are expected to form a bcc lattice structure when the plasma coupling parameter Γ_p (eq. 3.15) is above 170 [85,86]. These simulations are, however, based on an infinite plasma, where surface effects can be neglected and until recently, such structures had only been observed in Penning traps with large crystals of more than $\sim 5 \times 10^4$ laser cooled ions [95,96]. Simulations on finite sized plasmas have shown that surface effects do contribute to the structure and predict that the crystals should be composed of concentric shells of ions with a two-dimensional hexagonal structure within each shell [97].

In passing, we mention that this shell structure may serve as a means for measuring the crystal density and can thus provide a complementary calibration to that discussed in ch. 3.2.1 based on measurements of the crystal shape. Specifically, MD simulations predict that for infinitely long crystals of more than three shells, the radial inter-shell spacing δr should be constant across the crystal and proportional to the Wigner-Seitz radius as [97]

$$\delta r = 1.48 a_{\mathrm{ws}} \tag{3.22}$$
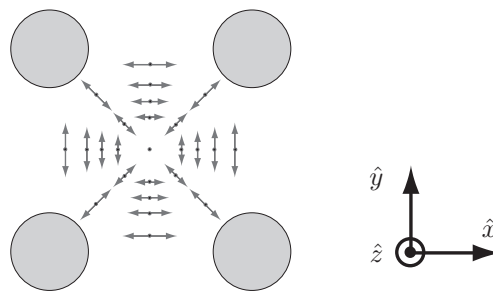
Figure 3.6: Schematic illustration of the micromotion at different locations in the trap. Arrows indicate the changing direction of the force on the ions. The dimensions of the electrodes and arrows are not to scale.

From the expression for a_{ws} (eq. 3.16) the crystal density can thus be found. We shall return to this in ch. 8.

The ordering of ions confined in linear Paul traps into concentric shells have been confirmed experimentally in several experiments [90,98], and, in both simulations [97] and experiments [98], it was found that the ordering into shells could occur at a plasma coupling parameter of only $\Gamma_p \sim 10$, although there was no sign of a phase transition *per se*. Rather, the shell structure became increasingly pronounced, in a continuous fashion, as Γ_p was increased. This means that the observation of shell structure in ion Coulomb crystals does not provide precise information of the temperature, only that it lies below that corresponding to the gas-liquid phase transition at $\Gamma_p \simeq 2$. If we assume the shell structure to occur only for $\Gamma_p > 10$, we get an upper bound for the temperature of $\simeq 230$ mK (c.f. fig. 3.3). For large ion Coulomb crystals, where a considerable number of ions may reside in regions of large micromotion amplitudes, it is then expected that rf-heating may lead to temperatures well above the Doppler limit of 0.5 mK and previous measurements have also found values of the order of a few tens of mK [99]. From the perspective of studying the coupling of ion Coulomb crystals to the cavity field mode, this effect will give rise to Doppler broadening of the atomic transition. Assuming a Maxwell-Boltzmann distribution for the velocity of the ions, the width (FWHM) of the Doppler profile due to the finite temperature of the ions can be expressed as [63]

$$\delta\nu_D = \frac{2}{\lambda}\sqrt{\frac{2k_{\mathrm{B}}T}{M}\ln 2}, \tag{3.23}$$

where λ is the wavelength of the atomic transition and M is the atomic mass. Fig. 3.7 shows this relation for the transition relevant for the cavity QED experiments of this work. The effect of a finite temperature is quite significant even for a few tens of mK, although we will see that it is not a serious limitation for entering a regime of strong collective coupling between the ion Coulomb crystal and the cavity field. In appendix D we calculate the effect of inhomogeneous broadening on the coherent
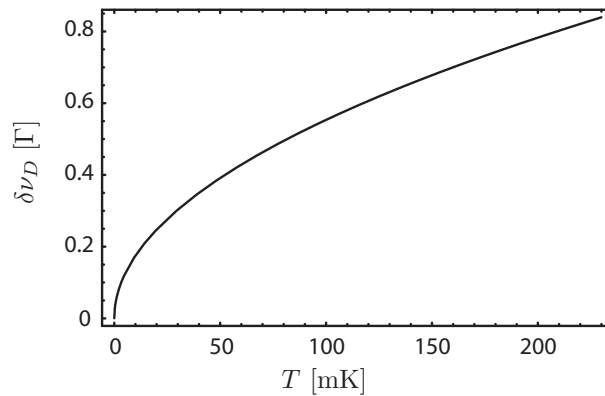
Figure 3.7: Doppler width in units of the natural linewidth $\Gamma = 2\pi \times 22.4$ MHz versus temperature for the relevant transition for the cavity QED experiments with $^{40}\mathrm{Ca}^+$ in this work (the $3D_{3/2} \leftrightarrow 4P_{1/2}$ transition).

coupling strength. Here we find that this can be accounted for by defining an effective decay rate Γ_{eff} which for temperatures below 100 mK is increased by less than 20 %.

It is interesting, however, to turn the issue around and, rather than regarding temperature as a limiting factor in cavity QED experiments with such systems, consider if the light-matter coupling provided by the framework of cavity QED may be utilized as a means to measure the temperature of ion Coulomb crystals. As cavity QED effects within this system are observed at the level of single photons, such a system enables a single photon to act as a temperature probe for a macroscopic ensemble of particles and in this way provide a completely non-invasive scheme for temperature measurements of cold trapped ions. The subject has been treated in appendix D and we shall return to it in ch. 10.

On account of rf-heating, it has not been obvious that three-dimensional long range order would be observed in rf-traps. However, in a recent report from our group it was demonstrated experimentally that three-dimensional long range order could indeed persist in crystals confined in linear Paul traps, even for relatively small crystals of less than 1000 ions where surface effects cannot be neglected [100]. Good agreement with MD simulations was found for low number of ions where the predicted bcc structure was in fact observed.

For higher number of ions a more rectangular pattern in resemblance of an fcc structure was observed and, more recently, experiments with ion Coulomb crystals of two different isotope species have shown highly pronounced periodicity in the rectangular structure of the inner component of the two-component crystal, which was attributed to an effective anisotropy of the inter-particle interaction induced by the rf-field [101]. Fig. 3.8 shows an example of such a crystal where the periodicity is clearly seen. From such periodic rectangular structure one might speculate on new means of engineering the coupling between the crystal and the cavity field. Since the cavity in the experiment is in a standing wave configuration, a periodic density distribution of the atomic medium might allow for an increased (or decreased) overlap between the ions and the anti-nodes of the standing wave cavity field. If the inter-ion distance ($\sim 10~\mu$m), which is controlled by the rf-voltage, can be adjusted such that it becomes an integer value of the anti-node separation of the cavity field ($\sim 0.4~\mu$m), this overlap could be tuned by translating the ion crystal axially via the end-voltage of the trap.
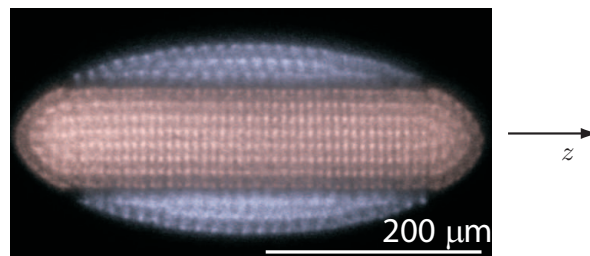
Figure 3.8: Image of two-component crystal consisting ^{40}Ca$^+$ (inner, red component) and ^{44}Ca$^+$ (outer, blue component). The ions are shown in false colors. The three-dimensional shape can be visualized by rotating the crystal around the z-axis (cavity and trap axis in the experiments). Courtesy of Anders Mortensen.

To what extent the structure of the ion Coulomb crystal can be made to match the standing wave field in practice, will depend on the localization of the ions. Previous experiments with single ions in Paul traps have indeed been able to map out the standing wave pattern of the optical resonator [45, 57]. In these experiments the localization of the single ion was extremely high (30-40 nm) as micromotion in single ion experiments can generally be minimized quite efficiently [93]. To estimate the localization of the ions in the Coulomb crystal, we can make use of the Debye length. Given by eq. 3.14 this is effectively the root-mean-square of the amplitude of the ions' motion about their individual "equilibrium" locations [5]. Fig. 3.9a) shows a plot of the Debye length in units of the cavity field wavelength versus temperature for typical trapping parameters of our experiment. If we assume that the ions form a periodic lattice as described above, where they all experience the same phase of the cavity field, we can treat them as being distributed along the cavity axis according to a Gaussian distribution with a width given by the Debye length

$$\rho(z) = \rho_0 \sqrt{\frac{1}{2\pi\lambda_\mathrm{D}^2}} \exp\left(\frac{-z^2}{2\lambda_\mathrm{D}^2}\right). \tag{3.24}$$

The choice of the Debye length as the width is obvious as it was derived in eq. 3.14 as the root-mean-square of the amplitude of the ions motion in a harmonic potential. For typical parameters of our experiments, the period of the plasma oscillation will be around 1 μs. As we shall see later (ch. 6.6.2) we will generally probe the system for longer times and over the measurement time, or at least over several averages of measurements, the ion's position is expected to be smeared out over the Debye length. Furthermore, due to the aforementioned Debye shielding, the motion of the individual ions within the ion Coulomb crystal is completely uncorrelated within this length scale and on this time scale, and for this reason, even measurements on time scales shorter than the plasma oscillation period would be subject to a Gaussian distribution of the ions with a width set by the Debye length.

If we evaluate the convolution of this Gaussian distribution with the standing wave field, $\sin^2(\frac{2\pi}{\lambda} + \phi)$, for different values the displacement of the ions with respect to the nodes of the cavity field, ϕ, we get a measure of how well the standing wave field is mapped onto the collective coupling strength. Fig. 3.9b) shows a few plots of this relation for various temperatures of the ions ranging from the Doppler cooling limit of 0.5 mK to 4 mK. The conclusion is that unless the heating rates in the crystals are very low and the Doppler limit can be approached, effects of the standing wave field and the crystal structure are not expected. Certainly, for crystals not exhibiting such long-range order but rather a shell structure, these structural aspects may largely be ignored. In our treatment of the interaction between the cavity field and the ion crystal later in this thesis, we shall thus simply average out the standing wave pattern of the cavity over the crystal. This calculation of $g\sqrt{N}$ is performed in appendix C.

---

[5]Of cause, again the notion of equilibrium is a bit artificial as the ions may be driven by the rf-field. However, here we are considering motion along the trap axis, where the micromotion amplitude is expected to be quite low.
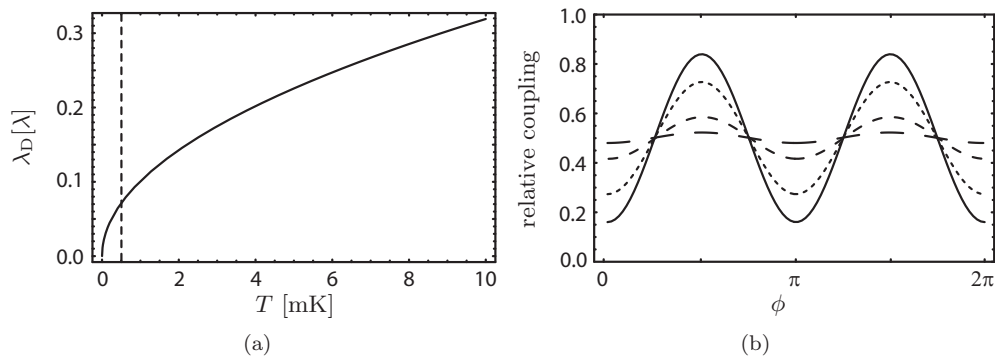
Figure 3.9: a) Debye length in units of the cavity wavelength (866 nm) versus the temperature of the ions for typical trapping parameters of our experiment ($\rho_0 \simeq 6 \times 10^8$ cm^{-3}). The dashed line indicates the limit of Doppler laser cooling. b) Relative coupling strength, assuming all ions see the same phase of the standing wave field, versus their displacement relative to the cavity nodes. The plotted curves are for temperatures, T=0.5 mK, T=1 mK, T=2 mK and T=4 mK in order of decreasing modulation visibility.

Chapter 4

Laser cooling of Ca$^+$

As outlined in the previous chapter, for the ion plasma to crystallize and form an ion Coulomb crystal, thermal energy has to be removed from the system. In our experiments, we make use of Doppler laser cooling to achieve this and the present chapter will review the basics of this technique, with special emphasis on laser cooling of Ca$^+$ ions in a linear Paul trap. For further details about laser cooling see e.g. [62, 64, 102].

4.1 Laser cooling of a two-level atom
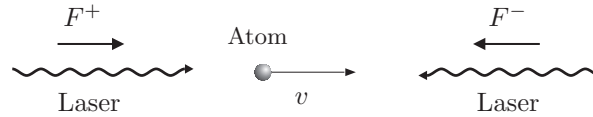
Figure 4.1: Basic principle of Doppler laser cooling. See text for details.

The basic principle of Doppler laser cooling is illustrated in fig. 4.1. The technique relies upon the velocity dependent Doppler shift of an atom (or ion) moving at velocity $\vec{v}$. In the rest frame of the laboratory, the resonance frequency of the atom is shifted according to the Doppler formula: $\omega_A(v) = \omega_A(0)(1 \pm v/c)$, where +/- is used depending on the motion of the atoms being towards (-) or away from (+) the laser beam. By tuning the laser frequency slightly to the red of the atomic transition, atoms moving towards the laser beam are shifted into resonance and will preferentially scatter photons from this beam. As a result of the frequency dependence, the net energy absorbed by the atoms is less than the energy that is emitted. The difference corresponds to a decrease in the kinetic energy of the atoms after the scattering event.

To gain further insight in cooling process, we analyze the force exerted by two counter propagating laser fields on an atom moving at velocity $\vec{v}$ as depicted in fig. 4.1. Each photon transfers a momentum $\hbar k$ with $k = \frac{2\pi}{\lambda}$ being the wave number. The atom scatters photons at a rate given by the product of the spontaneous decay rate Γ and the excited state population Π_e, such that the force (in one dimension) can be

written as

$$F = \hbar k \Gamma \Pi_e = \frac{1}{2} \hbar k \Gamma \frac{s}{1+s}, \tag{4.1}$$

where we have inserted the expression for the steady state population Π_e found in ch. 2 (eq. 2.15). The saturation parameter $s = \frac{2|\Omega|^2}{(\Gamma/2)^2 + \Delta^2}$ (eq. 2.16) depends on the Doppler shift through the detuning Δ and the force can therefore be written as

$$F^+ = \hbar k \Gamma \frac{|\Omega|^2}{(\Gamma/2)^2 + (\Delta + kv)^2} \cdot \frac{1}{1 + \frac{2|\Omega|^2}{(\Gamma/2)^2 + (\Delta + kv)^2}},$$

for a beam co-propagating with the atom, and

$$F^- = -\hbar k \Gamma \frac{|\Omega|^2}{(\Gamma/2)^2 + (\Delta - kv)^2} \cdot \frac{1}{1 + \frac{2|\Omega|^2}{(\Gamma/2)^2 + (\Delta - kv)^2}},$$

for a counter-propagating beam. Combining the two, the total force reads

$$\begin{aligned}
F &= F^+ + F^- \\
&= \hbar k \Gamma \left[\frac{|\Omega|^2}{(\Gamma/2)^2 + 2|\Omega|^2 + (\Delta + kv)^2} - \frac{|\Omega|^2}{(\Gamma/2)^2 + 2|\Omega|^2 + (\Delta - kv)^2} \right].
\end{aligned}$$

Expanding this expression around $v = 0$ to 1st order, the force can be expressed through a friction coefficient [1] β as $F = \beta v$, where

$$\beta = 4\hbar k^2 \frac{\Gamma \Delta |\Omega|^2}{\left[(\Gamma/2)^2 + 2|\Omega|^2 + \Delta^2 \right]^2} = 4\hbar k^2 \frac{s_0 (2\Delta/\Gamma)}{\left[1 + s_0 + \left(\frac{2\Delta}{\Gamma} \right)^2 \right]^2}. \tag{4.2}$$

Fig. 4.2 a) shows a plot of this friction coefficient as a function of the detuning. For the force to work as a friction force, β must be negative, which is seen to happen for $\Delta > 0$. With our definition of the detuning (eq. 2.13) this corresponds to a red detuning in agreement with our qualitative analysis given at the beginning of this chapter. In fig. 4.2 b) the forces from the two cooling beams as well as the total force, has been plotted for a detuning of $\Delta = \Gamma/2$ and $s_0 = 2$.

The cooling process can also be viewed as a result of momentum conservation, in that, the momentum transfer associated with the absorption process is preferentially in the direction opposite to the motion of the atoms. The subsequent re-emission of a photon via the spontaneous decay of the atom, is directionally symmetric with respect to the atom[2] and the momentum transfer associated with this process will thus average out over many scattering events, i.e. $\langle p \rangle = 0$. Though the net momentum transfer due to spontaneous decay averages to zero, this emission process does give rise to a random walk in momentum-space. As a result $\langle p^2 \rangle \neq 0$, which means that the final momentum spread $\langle p^2 \rangle - \langle p \rangle^2$ will have a finite value and, thus, so will the temperature.

---

[1]In general, there will also be terms independent on the velocity, however, for balanced cooling beams these will cancel out.

[2]The exact emission pattern is determined by the induced dipole and, hence, polarization dependent.
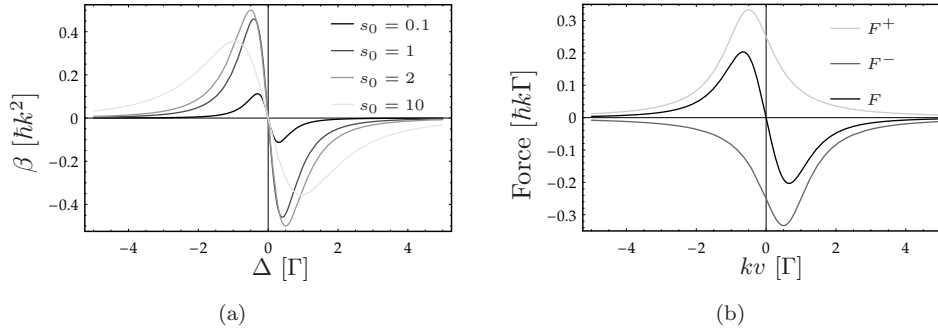
Figure 4.2: (a) Friction coefficient versus laser detuning, Δ (in units of Γ), for various values of the saturation parameter, s_0. (b) Velocity dependence of the laser force on an atom for two counter-propagating lasers (black line), when the detuning is $\Delta = \Gamma/2$ and the saturation parameter is $s = 1$. Gray lines represent the forces of the individual beams.

The final steady state temperature can be found analysis of the diffusion coefficient D [62]. From this it follows that the rate of momentum diffusion can be written as:

$$R_{\text{diff}} = 2D = \hbar^2 k^2 \Gamma \frac{s}{1+s}. \tag{4.3}$$

Basically, the diffusion coefficient stems from a random walk in momentum space with a step size of $\hbar k$ at the scattering rate $\Gamma \Pi_e$. The cooling rate, in terms of momentum, depends on the friction coefficient and the momentum as

$$R_{\text{cool}} = \frac{\beta}{M} \langle p^2 \rangle = \frac{\langle p^2 \rangle}{M} 4\hbar k^2 \frac{s_0 2\Delta/\Gamma}{\left[1 + s_0 + (\frac{2\Delta}{\Gamma})^2\right]^2}, \tag{4.4}$$

where we have inserted eq. 4.2 for the friction coefficient. If we consider the case of low intensity, where we are far from saturating the transition ($s_0 \ll 1$), and optimal detuning of $\Delta = \Gamma/2$, we find

$$R_{\text{diff}} = \frac{1}{2}\hbar^2 k^2 \Gamma s_0, \tag{4.5}$$

$$R_{\text{cool}} = 2\frac{\langle p^2 \rangle}{2M}\hbar k_0^2. \tag{4.6}$$

In steady state $R_{\text{cool}} = R_{\text{heat}}$ and one finds

$$T_{\text{D}} = \frac{\hbar \Gamma}{2k_{\text{B}}}, \tag{4.7}$$

where T_{D} is the so-called Doppler temperature, defined through $\frac{1}{2}k_{\text{B}}T_{\text{D}} = \frac{\langle p^2 \rangle}{2M}$. The minimal temperature that can be reached with Doppler laser cooling is thus set by the width of the transition Γ. At the same time this also determines the capture range of the cooling force, as can be seen from fig. 4.2. A broader transition may allow for cooling at a higher rate and of a wider range of velocities, but the higher scattering rate also increases the diffusion rate and, hence, limits the minimal temperature.

Having established the basic principles of Doppler laser cooling we now turn our attention to laser cooling of calcium ions confined in a linear Paul trap.

4.2   Laser cooling of Ca$^+$

The analysis of the principles of laser cooling given above assumed a free atom, how-
ever, our ions are not free but rather they are confined in a linear Paul trap as described
in ch. 3. Nevertheless, as we shall see in the following, for the parameters of our sys-
tem the assumption may still be valid in regards to Doppler laser cooling. Fig. 4.3
shows the level scheme of Ca$^+$. The thick, colored lines indicate the transitions used
for Doppler cooling, where the main cooling transition is the $4S_{1/2} \leftrightarrow 4P_{1/2}$ transition
(blue). The $3D_{3/2} \leftrightarrow 4P_{1/2}$ transition (red) is also needed to make it a closed scheme.[3]
Since the $4P_{1/2}$-state has a decay rate of $\Gamma_{P_{1/2}} = 2\pi \times 22.4$ MHz the time scale associ-
ated with Doppler cooling $(1/\Gamma_{P_{1/2}})$ is much less than the time scale associated with
the secular motion of the ions in the harmonic trapping potential of the linear Paul
trap. Typical trap frequencies for our trap are ~ 100 kHz (c.f. table 6.1) and the ions
may thus be regarded as free particles on the time scale of the Doppler cooling. From
a frequency point of view, the effect of the ions' motion is to add sidebands to the
absorption spectrum at the trap frequency. But as the cooling transition is orders of
magnitude broader than any of the trap frequencies, these sidebands are not resolved
and we shall pay them no attention in this work.[4]

The use of a fast dipole transition such as the $4S_{1/2} \leftrightarrow 4P_{1/2}$ transition is generally
needed in order to achieve a high scattering rate. The momentum of a single photon

---

[3]We shall use this color code in figures and diagrams throughout the thesis to make the reference
to these transitions obvious.

[4]In cooling schemes where this is not the case and the sidebands can be resolved (the so-called
resolved sideband regime) there exist clever schemes for cooling also the quantized vibrational motion
of the ions to the ground state. This was first demonstrated in 1989 [103] and is termed sideband
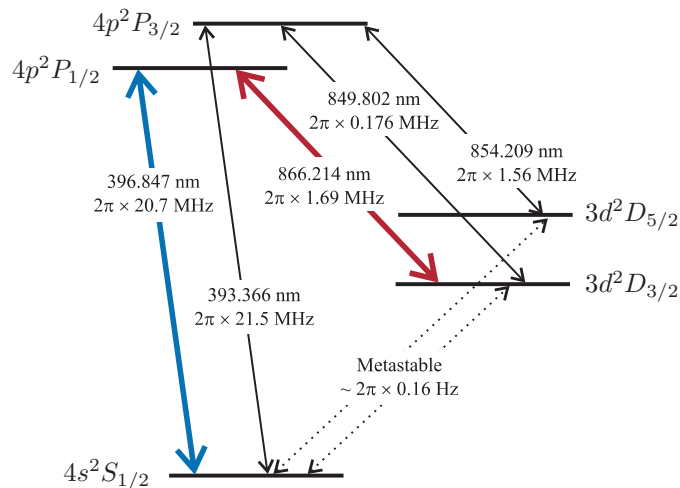cooling.

Figure 4.3: Level scheme for Doppler cooling of Ca$^+$ with wavelengths and partial decay
rates for the dipole allowed transitions (see appendix A). The thick colored lines indicate
the transitions used for Doppler cooling of Ca$^+$. This color coding will be used for the 397
nm and 866 nm throughout the thesis.

is far below that of the ions prior to any cooling and for this reason many scattering cycles are required to cool the ions below the crystallization limit.[5] As mentioned in the previous section, a broad linewidth of the dipole transition also limits the final temperature that can be reached by Doppler laser cooling and for our cooling scheme, using the $4S_{1/2} \leftrightarrow 4P_{1/2}$ transition, the Doppler limit is about 0.5 mK.

In general, to cool atoms in three dimensions requires three sets of counter-propagating beams. In a confining potential, such as that of the linear Paul trap, cooling is only necessary in three directions as the ions reverse their motion with the trap frequency, and can actually be accomplished with a single beam, provided that this beam has a component of its k-vector in all three dimensions.

For the case of ion Coulomb crystals in a linear Paul trap the situation is both more complicated and easier at the same time. The fact that some ions are outside the trap axis, in regions of non-vanishing micromotion amplitude, means that cooling should preferentially be applied axially in order to avoid driving this micromotion. Since the axial and radial degrees of freedom are coupled in a three dimensional ion Coulomb crystal, all motional degrees of freedom will thermalize and cooling only one motional degree of freedom will be sufficient. This is contrary to ions in a string (a one dimensional ion Coulomb crystal) where radial cooling is also necessary. In all experiments with ion Coulomb crystals, we will use two counter-propagating beams along the trap axis. More details will be given in ch. 6.

Finally, we mention that due to the magnetic sub-structure of the $3D_{3/2}$ state, we generally work with a bias magnetic field of a few Gauss perpendicular to the polarization of the 866 nm beam, driving the $3D_{5/2} \leftrightarrow 4P_{1/2}$, to ensure all magnetic sub-states are addressed by this repumping laser.

4.3 Sympathetic cooling and two-component crystals

As mentioned in ch. 3.1.1, different ion species can be trapped simultaneously provided that their relative charge-to-mass ratios are not too different. This is the case, e.g., for different isotopes of a given atomic species, like $^{40}Ca^+$ and $^{44}Ca^+$. When cooled below the critical temperature, both components crystallize to form a two-component ion Coulomb crystal and, as a result of the mass dependence of the radial trapping potential, the two components separate radially. An example of this is shown in fig. 4.4a). The lighter $^{40}Ca^+$ ions form an inner core surrounded by a crystal constituted by the heavier $^{44}Ca^+$ ions. The full three-dimensional shape can be visualized by rotating the crystal around the z-axis (trap axis). In fig. 4.4a) both isotopes are being cooled simultaneously; however, due to their mutual Coulomb interaction, thermal energy is transferred between the two components and it is therefore only necessary to cool one component. Examples of this are shown in fig. 4.4b) and c) where laser cooling is applied only to one of the two isotopes ($^{44}Ca^+$ or $^{40}Ca^+$, respectively). The other isotope is then *sympathetically* cooled via its Coulomb interaction with the laser cooled isotope [105, 106].

Such two-component crystals are appealing as a medium for CQED studies since they allow for laser cooling of the outer, radially separated component, while having the other inner, cylindrical component interacting with the cavity field only.

---

[5]Recently, however, our group has demonstrated Doppler cooling on a dipole-forbidden transition, specifically the $4S_{1/2} \leftrightarrow 3D_{5/2}$ of $^{40}Ca^+$. For details see [104].
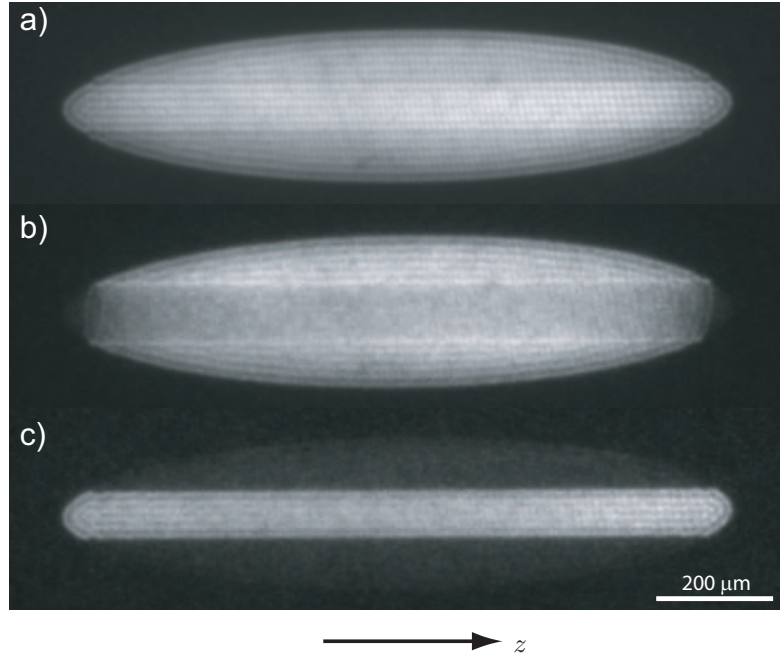
Figure 4.4: a) Image of a two-component crystal consisting of ~ 2000 ^{40}Ca$^+$ ions (inner component) and ~ 13000 ^{44}Ca$^+$ ions (outer component) that are being laser cooled simultaneously. b) ^{44}Ca$^+$ laser cooled, ^{40}Ca$^+$ sympathetically cooled. c) ^{40}Ca$^+$ laser cooled, ^{44}Ca$^+$ sympathetically cooled. The full 3-D shape can be visualized by rotating the crystal around the z-axis (trap axis). Details about the camera system can found in ch. 6.4

The relevant transition for the cavity QED experiments with this system is the $3\mathrm{d}^2\mathrm{D}_{3/2}\leftrightarrow4\mathrm{p}^2\mathrm{P}_{1/2}$ transition of ^{40}Ca$^+$. The isotope shift of this transition, relative to ^{40}Ca$^+$, is 4.5 GHz for ^{44}Ca$^+$, which means that the state of the ^{40}Ca$^+$ ions should not be affected by the cooling lasers when this component is being sympathetically cooled by the ^{44}Ca$^+$ ions. Alternatively one may also choose to work with ^{48}Ca$^+$ instead of ^{44}Ca$^+$ which has an even larger isotope shift of 8.3 GHz. The reason for considering these two isotopes, rather than other naturally abundant isotopes of calcium, is that relatively higher loading rates into the trap can be achieved for these (see ch. 7). The isotope shifts on the various transitions can be found in appendix A

Chapter 5

Laser systems

In the experiments presented in this thesis a number of laser systems have been used. Some had been developed previously in our laboratory while others were developed specifically for the purpose of these experiments. The account within this thesis will naturally reflect this, however, all relevant laser systems will be described, albeit in different detail. References to past thesis' from the Ion Trap Group will provide for further reading if necessary.

In this chapter we will describe the laser systems for production of the following wavelengths:

- **272 nm** used for photoionization of Ca.

- **397 nm** used for Doppler laser cooling and optical pumping of Ca^+.

- **866 nm** used for Doppler laser cooling and optical pumping of Ca^+ as well as a probe laser in the cavity QED experiments.

- **894 nm** used for diagnostics and locking of the experimental cavity for the cavity QED experiments.

In addition, we have a commercial pulsed laser at 1064 nm, which may be used for loading the linear Paul trap by ablation of atomic Ca. This will be described ch. 7.3. In appendix F the specifications on the various laser systems have been summarized.

The wavelength of all lasers can be measured using two home-build λ-meters based on an interferometric setup [107]. These have a 7 digit precision, which is precise enough to achieve a coarse, adjustment of the frequency for e.g. Doppler laser cooling of Ca^+. Furthermore, a setup for optogalvanic spectroscopy [108,109] is available for finding the atomic resonances of Ca^+.

We shall begin this chapter with a description of the 272 nm laser system. It has been described in [110] but in this chapter we shall treat it in more detail. As it relies on second harmonic generation (SHG) the theory behind this will be reviewed briefly, also.

The infra-red diode laser systems for 866 and 894 nm will then be described in the following section. The probe laser used in the cavity QED experiments is essentially the same as the 866 nm laser system used for laser cooling, but as it holds an important

position in these experiments, we shall treat this in some detail. The setup for this laser greatly resembles those of the other diode lasers found in our lab, e.g. a 397 nm and another 866 nm diode laser used for Doppler cooling as well as the 894 nm diode laser used in the experiments with the cavity. For this reason, we will not describe these diode lasers in the same detail as the first 866 nm laser, but merely give their basic characteristics and point out their differences (if any) from this.

Finally, the 397 nm laser systems will be covered, briefly, as well as the stabilized reference cavities used for locking the lasers.

5.1   272 nm laser system

Our ion production scheme, as we shall see in ch. 7, requires a 272 nm coherent light source with a linewidth preferably below 1 MHz. As such a laser system was not commercially available one had to be developed specifically for this purpose. In the past, the Ion Trap Group has relied on an Ar-ion pumped dye laser at 544 nm, frequency doubled to produce light at 272 nm [111]. However, with the increasing complexity of the ion trap based experiments, a laser system offering a higher degree of ease-of-use and reliability was in high demand and, to this end, we decided to develop an all solid-state laser system.

There is a general demand for continuous wave (CW) coherent light sources in the visible and ultra violet (UV) range for applications in both science and industry. Today, the most common sources in the blue-green wavelength range are based on frequency doubling of light from rare-earth element doped solid state lasers [112–114]. Indeed, commercial systems have traditionally been based on Nd-doped solids, which have proved very successful in delivering high power and single frequency light in the green and blue wavelength range through efficient SHG [112]. Furthermore, light from the strong 1064 nm line of Nd:YAG has been converted into 1.1 W at 532 nm with a record holding intra-cavity conversion efficiency of 89 % [113], and a 2.8 W source of 473 nm light based on the 946 nm line of Nd:YAG has also been reported [114].

Sources of this type are at present an obvious choice for further frequency doubling into the UV range, and recently, a record high power of 5 W at a wavelength of 266 nm has been achieved using two stages of frequency doubling of light from a Nd:YVO$_4$ laser [115].

As single mode (SM) rare-earth element doped distributed feedback (DFB) fiber lasers have become commercially available, [116] an alternative to the Nd-based systems has emerged. With a linewidth of a few tens of kHz and an output of several Watts, these lasers constitute an excellent starting point for SHG into the visible part of the spectrum. Given that this can be performed with a high efficiency and without any appreciable distortion of the beam profile, further SHG into the UV range is feasible. For applications in science, these fiber lasers are attractive as their broad gain profile allows for a far broader spectrum to be addressed, as compared to what is at present possible with rare earth doped laser systems using a crystal matrix, such as those based on Nd:YAG. Since laser action can be achieved with Yb doped germanosilicate glass fibers over a wavelength range of $\sim$ 975 to $\sim$ 1200 nm [117], SHG will provide access to a fairly large part of the spectrum around 550 nm and 275 nm. The present chapter describes a 272 nm laser system based on two consecutive SHG processes using light from an Yb doped DFB fiber laser, however, the techniques

involved are fairly general and could easily be extended to other wavelengths.

5.1.1   Second harmonic generation

When an electric field $\mathbf{E}(t)$ propagates inside a non-linear medium it induces a polarization of the form

$$\mathbf{P}(t) = \chi^{(1)}\mathbf{E}(t) + \chi^{(2)}\mathbf{E}(t) \cdot \mathbf{E}(t) + ... \; , \tag{5.1}$$

where $\chi^{(i)}$ is a susceptibility tensor of rank (i+1), implying that the response of the non-linear medium need not be along the same direction as the applied field. Assuming a harmonic input field, $\mathbf{E}(t) = \hat{\epsilon}\mathbf{E}_0 \cos(\omega t)$, the second order response of the medium manifests itself as a time-varying polarization at twice the frequency

$$\mathbf{P}^{(2)}(t) = \hat{\epsilon}_p \chi^{(2)} (\mathbf{E}_0 cos(\omega t))^2 = \frac{1}{2}\hat{\epsilon}_p \chi^{(2)} \mathbf{E}_0^2 \big(1 + \cos(2\omega t)\big) \; , \tag{5.2}$$

where $\hat{\epsilon}_p$ is the polarization vector of the second order polarization, determined by $\chi^{(2)}$ and $\hat{\epsilon}$. From Maxwell's equations we can derive a wave equation for the electric field in the medium

$$\nabla^2 \mathbf{E} - \frac{1}{c^2}\frac{\partial^2 \mathbf{E}}{\partial t^2} = \frac{1}{\epsilon_0 c^2}\frac{\partial^2 \mathbf{P}}{\partial t^2} \; , \tag{5.3}$$

from which it is evident that the non-linear polarization term will act as a source for an electric field oscillating at the second harmonic frequency 2ω. This provides the basis for SHG.

Phasematching
Due to the dispersive properties of the non-linear medium used to generate the second harmonic frequency, the two fields $\mathbf{E}(\omega)$ and $\mathbf{E}(2\omega)$ will in general propagate at different phase velocities, resulting in destructive interference between the second harmonic waves generated at different locations within the crystal. However, as mentioned above, the second order susceptibility tensor allows for the field $\mathbf{E}(2\omega)$ to propagate with its polarization orthogonal to the field $\mathbf{E}(\omega)$, which in conjunction with the birefringence of the medium can be used to keep the two waves in phase. Through the dependency of the refractive index on either the direction of propagation with respect to a certain optical axis in the non-linear medium or on the temperature of the medium, a phase relationship between the two fields can be maintained, such that $\Delta k = k_{2\omega} - 2k_\omega = \frac{2\omega}{c}(n_{2\omega} - n_\omega) = 0$. The two methods (angle- and temperature-based) are commonly referred to as critical and non-critical phasematching, respectively. Finally, one can show that any interference due to phase mismatch Δk will translate into a power dependency of the SHG light field of the form

$$P_2(\Delta k) \propto \left(\frac{\sin(\frac{1}{2}\Delta k l_c)}{\frac{1}{2}\Delta k l_c}\right)^2 \; , \tag{5.4}$$

where l_c is the length of the crystal [63].
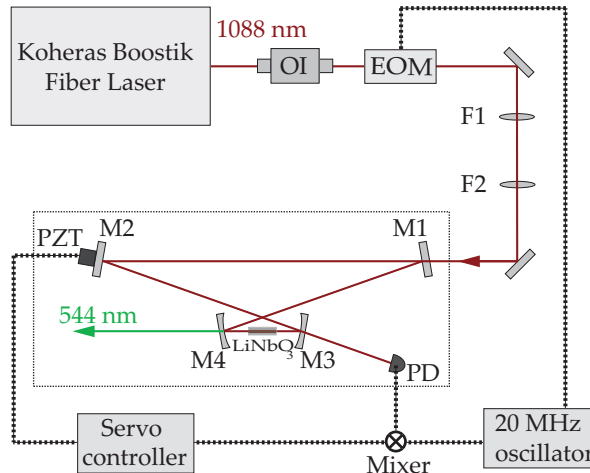
Figure 5.1: Schematic of the setup used for SHG of light from the DFB fiber laser. OI: optical isolator, EOM: electro-optic modulator, F: mode-matching lenses, M: cavity mirrors, PZT: piezo-electric transducer, PD: photo detector.

5.1.2   Production of light at 544 nm

The setup for this first frequency doubling stage is shown in fig. 5.1. The DFB fiber laser (Koheras Boostik[TM]) provides light at 1088 nm, with a linewidth specified to be < 35 kHz (averaged over 125 μs), coupled through a polarization maintaining (PM) fiber [1]. By controlling the length of the fiber laser cavity with a piezo-electric transducer (PZT), the frequency can be tuned over a total range of 5.8 GHz at 1088 nm and through the temperature the it can be tuned about 2.3 GHz/K at 1088 nm. In order to prevent optical feedback from, e.g. the cavity, an optical isolator (OI) with ~ 55 dB optical isolation is inserted immediately after the fiber laser.

For the generation of light at 544 nm from 1088 nm we have chosen $LiNbO_3$ as our non-linear medium.[2] $LiNbO_3$ was chosen instead of e.g. LiB_3O_5 (LBO) due to its higher non-linear coefficient and a 7% Mg-doping was chosen to ensure a low degree of photorefractivity [119]. Furthermore, it allows for type I non-critical phasematching at a temperature of $\sim 157°C$, as can be calculated from the Sellmeier equations for $LiNbO_3$ (see appendix G.1). This is important since the two fields will then be co-propagating and deterioration of the beam profile, common to critical phasematching, where the two beams cannot overlap for the entire length of the crystal, can be avoided. The resulting near-Gaussian beam profile, will serve as an ideal source for further SHG to produce light at 272 nm.

---

[1]This has later been changed to a non-PM fiber. DFB fiber lasers can be very sensitive to stimulated Brillouin scattering in the fiber which causes optical feedback [118]. The use of a PM fiber made this effect more pronounced and changing to a non-PM fiber improved the laser stability. We have found that even with this non-PM fiber the polarization remains stable once the laser has been on for about an hour.

[2]Our crystal was supplied by Castech, www.castech.com.

Phasematching

To achieve phasematching, the crystal is mounted inside a homebuild oven (see fig. 5.2). A series of resistors inside a copper block heats the interior of the oven to $\sim 150°C$ and a PT100 temperature sensor monitors the temperature and a peltier element in a feedback regulating circuit maintains the temperature to fulfill the phasematching condition. In this way the temperature can be tuned and held stable to within a few hundreds of a degree. The oven is isolated by a teflon housing and mounted on a five axis translation stage for alignment purposes. Fig. 5.3 shows the
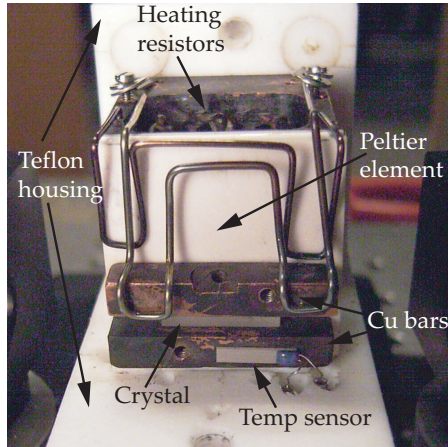
Figure 5.2: Picture of the oven with part of its teflon housing removed.
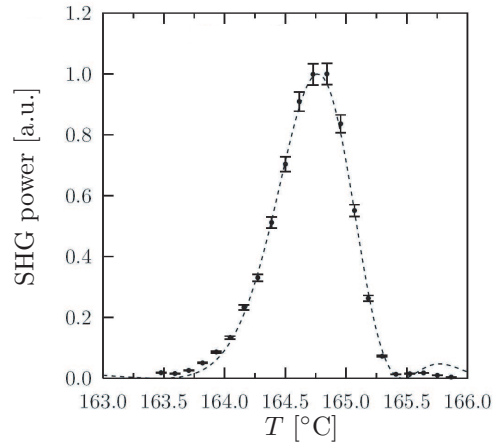
Figure 5.3: Plot of the measured SHG power as a function of temperature. The fit is a sinc-function modified to account for absorption of SHG light (see text).

relative level of SHG power as the temperature is tuned across the phasematching temperature T_{pm}. The asymmetry in the sinc-function predicted by eq.(5.4) can be accounted for by a temperature increase associated with absorption of SHG light. Below T_{pm} this will bring the effective temperature inside the crystal closer to T_{pm} giving rise to a higher power level, whereas above T_{pm} it will push the temperature further away from T_{pm} and result in a lower power level. The fit takes this effect into account to first order and shows nice qualitative agreement. The measurements indicate a phasematching temperature of $\sim 164.7°C$. The discrepancy between this value and the value calculated in appendix G.1 can be ascribed to the lack of calibration of the PT100 thermal sensor and to the empirical nature of the coefficients in the Sellmeier equations used in the calculation.

Optimal focusing

To estimate the optimal focusing and the single-pass conversion efficiency for SHG in $LiNbO_3$, we employ the theory developed by Boyd and Kleinman [120]. In brief, the second harmonic power P_2 is related to the fundamental power P_1 through

$$P_2 = \gamma P_1^2, \tag{5.5}$$

where γ is the single-pass conversion coefficient, depending on both properties related to the crystal as well as the intra-cavity field. To calculate the SHG power, the non-linear crystal is divided into small segments and the second harmonic field generated within each segment is then propagated to the far-field where the Poynting vector is averaged over an optical period to give the power. The final expression for the single-pass conversion coefficient reads (in cgs units):

$$\gamma = \frac{128\pi^2\omega_1^2 d_{eff}^2 l k_1}{c^3 n^2} e^{-\alpha' l_c} h(\sigma, B, \xi) \tag{5.6}$$

where $\alpha' = \alpha_1 + \frac{1}{2}\alpha_2$ is the total absorption and where 1 and 2 indicate whether quantities are related to the fundamental or the second harmonic field. d_{eff} is the effective non-linear coefficient, l_c is the crystal length, n is the refractive index (at phasematching), k_1 is the wave vector of the fundamental field in the crystal, c is the speed of light in vacuum and h is a function that contains all the information about focusing and walk-off through the parameters ξ and B, respectively. These are given by

$$B = \rho\frac{\sqrt{l_c k_1}}{2} \text{ and } \xi = \frac{l_c}{w_0^2 k_1} \ . \tag{5.7}$$

For the special case of non-critical phasematching employed here, $B = 0$ and $\xi = 2.84$ [120], which from eq.(5.7) gives an optimal waist of $\simeq 21$ μm for a crystal length of 15 mm.

Cavity design
The single pass conversion coefficient γ can in principle be calculated from eq. 5.6 if crystal parameters, such as absorption and second order susceptibility, are known. The values given by crystal manufacturers are, however, generally associated with some uncertainty and, in practice, γ is not known until measured. As we shall see later, in this case, it is of the order of 10^{-3} and for this reason it is evident from eq.(5.6) that high conversion efficiencies in continuous wave (CW) SHG can only be achieved if an enhancement cavity is employed to allow for the power to build up. The most common geometry for efficient SHG is the bow-tie resonator, with two plane mirrors (M1 and M2) and two concave mirrors (M3 and M4), as depicted in fig. 5.4. The specific geometry of the cavity was designed to support stable oscillation of a Gaussian TEM$_{00}$ mode with a minimum waist of $\simeq 28$ μm.[3] Using the ABCD-matrix formalism for Gaussian beams [121] we can find a cavity configuration that results in that particular waist at the center of the cavity. The ABCD-matrix for a round-trip in the cavity, starting and ending at the minimum waist inside the crystal, is given

---

[3]This is a little higher than the 21 μm calculated from Boyd-Kleinman theory above. Quite often in SHG the choice of focusing is a trade-off between achieving a high conversion efficiency and a stable output. By choosing a larger waist the conversion efficiency may go down slightly but high intensity effects such as photo-refractivity and thermal effects may be less pronounced.
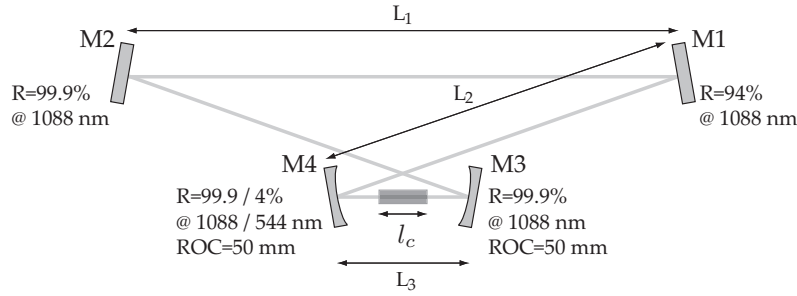
Figure 5.4: Schematic of the cavity used for SHG of light at 544 nm. Relevant lengths are L_1=300 mm, L_2=150 mm and L_3=63 mm (see text below). The folding angle of the cavity is $10°$. The LiNbO$_3$ crystal has a refractive index of 2.22 and a length l_c=15 mm.

by

$$
\begin{bmatrix} A & B \\ C & D \end{bmatrix} = \overbrace{\begin{bmatrix} 1 & l_c/2n_c \\ 0 & 1 \end{bmatrix}}^{\text{cr. center to surf.}} \overbrace{\begin{bmatrix} 1 & 0 \\ 0 & 1/n_c \end{bmatrix}}^{\text{cr. surf.}} \overbrace{\begin{bmatrix} 1 & (l_3 - l_c)/2 \\ 0 & 1 \end{bmatrix}}^{\text{cr. surf. to M4}} \overbrace{\begin{bmatrix} 1 & 0 \\ -2/R & 1 \end{bmatrix}}^{\text{reflection of M4}} \times
$$
$$
\underbrace{\begin{bmatrix} 1 & L_1 + 2L_2 \\ 0 & 1 \end{bmatrix}}_{\text{M4 to M3}} \underbrace{\begin{bmatrix} 1 & 0 \\ -2/R & 1 \end{bmatrix}}_{\text{reflection of M3}} \underbrace{\begin{bmatrix} 1 & (l_3 - l_c)/2 \\ 0 & 1 \end{bmatrix}}_{\text{M3 to cr. surf.}} \underbrace{\begin{bmatrix} 1 & 0 \\ 0 & n_c \end{bmatrix}}_{\text{cr. surf.}} \underbrace{\begin{bmatrix} 1 & l_c/2n_c \\ 0 & 1 \end{bmatrix}}_{\text{cr. surf. to center}} ,
$$

where cr. and surf. abbreviate *crystal* and *surface*, respectively.

The bow-tie cavity has two waists: One minimum waist between M3 and M4 and a larger, auxiliary waist between M1 and M2. It can be can shown that these are related to the elements of their respective ABCD-matrices through the following relation [121]:

$$
w_0 = \left| \left(\frac{\lambda}{\pi}\right)^{1/2} \frac{B^{1/2}}{[1 - (\frac{1}{2}A + \frac{1}{2}D)^2]^{1/4}} \right| . \tag{5.8}
$$

In fig. 5.5 these are plotted as a function of the separation between the M3 and M4, subject to the condition for stability of the resonator mode

$$
-1 \leq \frac{1}{2}(A + D) \leq 1 . \tag{5.9}
$$

The remaining mirror separations in the cavity were chosen to give the smallest possible angle of incidence on the concave mirrors, in order to minimize astigmatism in the beam, while at the same time leaving enough room for the oven. From fig. 5.5 we see that, for $L_3 = 63.2$ mm, the minimum waist is predicted to be 28 μm with a corresponding auxiliary waist of $\simeq 400$ μm. By using a set of two lenses, F1 and F2 in Fig. 5.1, the input beam can be shaped to match this waist and all the light will couple to the TEM$_{00}$ mode of the cavity. When this is achieved, the cavity is said to be modematched.

Once the cavity is properly modematched, the single-pass conversion coefficient can be measured by removing the mirrors M1 and M4 and in this way maintain the focusing used in practice. This gave a value of gamma of 1.62×10^{-3} W^{-1}.
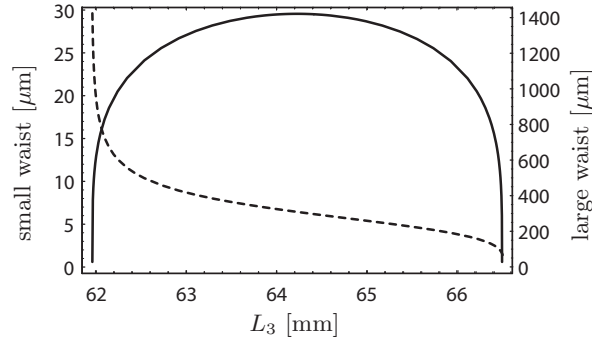
Figure 5.5: Plot of the small waist (solid line) and the large waist (dashed line) as a function of the separation, L_3, between the two concave mirrors M3 and M4.

Optimal input coupler transmission and power build up

In general, the optimal value of the transmission of the input coupler T_{M1} is defined by an impedance matching condition equating T_{M1} with the total intra-cavity losses (see eq. 2.28). When the cavity is perfectly impedance-matched, the reflectivity on resonance drops to zero and all the power is transferred to the cavity. The total intra-cavity losses are comprised of both linear and non-linear losses. The linear losses are associated with scattering on the mirrors and the crystal surfaces, as well as absorption in the crystal and losses due to the finite mirror reflectivities. The three mirrors, M2, M3 and M4, all have a reflectivity of 99.9% at 1088 nm. The output coupler M4 has been anti-reflection (ar) coated for light at 544 nm ($T = 96\%$) to allow for the second harmonic field to exit the cavity. The crystal surfaces have been ar coated to $< 0.2\%$ reflection and in total, the passive losses inside the cavity were measured to be $\mathcal{L} \simeq 1.5\%$ by the method described in ch. 2.2.

The non-linear losses are related to the generation of second harmonic light and depend thus on the intra-cavity power P_c and the single-pass conversion coefficient γ. This can be accounted for by replacing $\mathcal{L} \rightarrow \mathcal{L} + \gamma P_c$ in the equation for the intra-cavity field derived in ch. 2.2 (eq. 2.23). From this we can find an expression for the ratio of the intra-cavity power to the incident power P_1. On resonance ($\Delta_c = 0$) this ratio reads:

$$\frac{P_c}{P_1} = \frac{4T_{M1}}{(\mathcal{L} + T_{M1} + \gamma P_c)^2}. \tag{5.10}$$

As γ is generally only of the order of a percent or less, we can neglect terms of second order in γ and rewrite eq. 5.10 as

$$P_c = \frac{-\mathcal{L}^2 + \sqrt{\mathcal{L}^4 + 32\mathcal{L}T_{M1}\gamma P_1}}{4\mathcal{L}\gamma}. \tag{5.11}$$

The intra-cavity power is plotted in fig. 5.6 as a function of T_{M1} for different incident powers. Typical power levels are 1.0-1.5 W where the optimal transmission is around 0.04. The fact that our transmission coefficient is 0.06 and, thus, a little higher, makes little difference as seen in the plot of fig. 5.6.
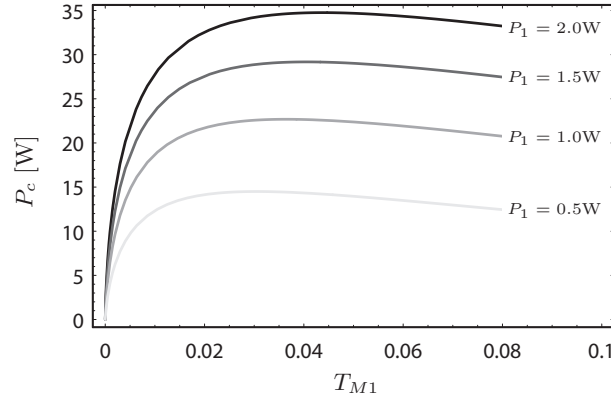
Figure 5.6: Plot of the intra-cavity power P_c as a function of transmission coefficient for the input coupler T_{M1} for various input power levels P_1. The linear and non-linear losses used in the calculation are $\mathcal{L} = 0.015$ and $\gamma = 0.00162$ W^{-1}, respectively.

The aforementioned impedance-matching condition can be understood in qualitative terms as a destructive interference condition. If the incident field, reflected of the input-coupler, and the intra-cavity field, transmitted through, are equal in magnitude and out of phase by π, they interfere destructively. No field is then reflected and all the energy is transferred to the cavity. The former condition (equal in magnitude) led us to an optimum value for input coupler transmission. The latter condition (out of phase by π) leads to the requirement that the total cavity round-trip phase shift must be an integer number of 2π, since a phase shift of π is already there due to the reflections off the mirrors. If the total phase shift is an integer number of 2π the cavity is said to be resonant. To ensure this, the mirror M2 is mounted on a piezo-electric transducer (PZT in Fig. 5.1) and controlled by a servo loop using the Pound-Drever-Hall locking technique [122, 123]. This locking technique requires a phase modulation of the input field, which can be performed with an electro-optic modulator (EOM). The EOM used is homebuilt and based on the same non-linear crystal used for SHG. A 20 MHz rf-signal with an rms amplitude of $\simeq 200$ V is put across the LiNbO$_3$ crystal of the EOM, which produces the required phase modulation. The error signal, used for feedback via the servo loop, is generated by mixing the 20 MHz signal with the signal from the photo detector positioned after the M3 mirror.

Conversion efficiency
From the expression for the intra-cavity power (eq. 5.11) we can find the SHG power as

$$P_2 = \gamma P_c^2 = \gamma \left(\frac{-\mathcal{L}^2 + \sqrt{\mathcal{L}^4 + 32\mathcal{L}T_{M1}\gamma P_1}}{4\mathcal{L}\gamma} \right)^2. \tag{5.12}$$

Fig. 5.7a) shows the measured SHG power P_2 as a function of the fundamental power P_1 incident on the cavity. For a maximum input power of 1540 mW at 1088 nm about 845 mW of usable 544 nm light is generated, corresponding to a conversion efficiency of $\simeq 55\%$. Taking into account a 4 % loss at the output coupler, this gives an internal

conversion efficiency of 57 %, as can be seen from fig. 5.7b).

Also plotted are the theoretical predictions based on eq. 5.12 (solid line) as well as predictions based on a full numerical solution for P_c (dashed line) in which no higher order terms in e.g. γ, have been omitted. As expected, the numerical solution shows better agreement with the measurements for higher powers than the solution in which higher order non-linear losses has been neglected. The remaining discrepancy is not well understood, but could be a result of impaired modematching due to changes in the refractive index of the crystal at higher power levels. With the Mg-doped LiNbO$_3$ crystal used here, photorefractive effects are expected to be quite small [119], although probably not completely negligible. Thermal effects may also be present.

The graph in Fig. 5.8 shows the SHG power measured over a little less than two hours. Over that period of time the power level decreased by $\simeq 2.5$ %. The decrease is mainly caused by limited stability of the temperature controller itself and by adjustment of the temperature setting on the controller at the end of the measurements the power increased back to its initial level.

Beam quality

The beam quality is commonly evaluated by a comparison with a perfect Gaussian beam profile. A quantitative measure of this is the M^2-parameter, which for a perfect Gaussian beam is equal to 1. It is defined as $M^2 = \pi w_0 \theta / \lambda$, where w_0 is the minimal beam waist, and θ is the beam divergence. The most widely accepted method[4] for evaluating M^2 is by focusing the beam and measuring the waist at the focus and the beam divergence beyond the Rayleigh range.

In our measurements we focused the beam with an f = 100 mm lens and measured the waist to be $\simeq 38 \pm 2$ μm in both the vertical and the horizontal direction. The Rayleigh range is about 8 mm and fig. 5.9 show the results of measurements of the divergence angle from which we deduce an M^2 of 1.08 ± 0.5 and 1.05 ± 0.5 in the vertical and the horizontal direction, respectively. As expected for a SHG beam originating from a non-critical phase-matching process, the beam profile is almost a perfect Gaussian, which makes it a good starting point for the generation of light at 272 nm as it can be coupled into an enhancement cavity with high efficiency.

5.1.3   Production of light at 272 nm

The second cavity for frequency doubling of the 544 nm light to 272 nm is shown in Fig. 5.10. This cavity was originally designed and constructed by Jens Lindballe, a former master student of our group, and the setup is well-described in his thesis [124]. Here in brief:

At this wavelength non-critical phase-matching can not be obtained, so type I critical phase-matching in a BBO crystal is employed.[5] The walk-off associated with this process is about 85 mrad and as a result the SHG beam will be non-Gaussian. The crystal is 8 mm long and has been ar coated on both end-faces at the relevant wavelengths, with residual reflections of 0.2 % and 0.6 % at the fundamental and the second harmonic, respectively. The cavity (see fig. 5.10) is in a bow-tie configuration (distance M5-M6, M7-M8: 13.6 cm, folding angle: 6.3°) with mirrors M5 and M6 both being

---

[4]ISO Standard 11146.
[5]This crystal was supplied by Newlight Photonics.
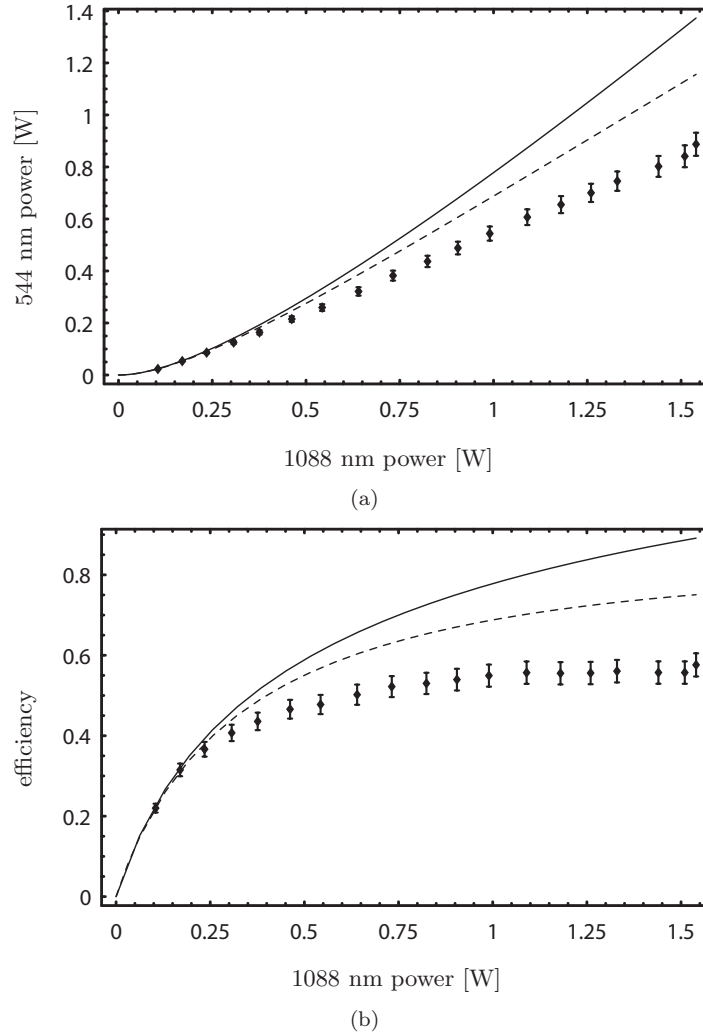
Figure 5.7: a) SHG power vs. incident power. b) Conversion efficiency vs. incident power. Error bars are 5% of data values. The data has been corrected for a 4 % loss at the output coupler M4. The solid line is the theoretical prediction based on eq. 5.12 and the dashed line is based on a full numerical calculation of P_c. Parameters used for the theoretical curves are $T = 0.06$, $\mathcal{L} = 0.015$ and $\gamma = 0.00162$.

plane mirrors with a reflectivity at 544 nm of 99.0 % and 99.9 %, respectively, and the two remaining mirrors M7 and M8 both having a radius of curvature of 10 cm and a reflectivity of 99.9 % at 544 nm. The out-coupling mirror, M8, has a transmission of 85.0 % at 272 nm. Total passive losses amount to $\simeq 1$ %. The crystal is located at the waist ($\simeq 29$ μm) between the two curved mirrors, near the optimum value evaluated from Boyd-Kleinman theory [120]. From the parameters given by the manufacturer, we expect a single-pass conversion coefficient of $\gamma \simeq 18 \times 10^{-5}$ W^{-1}. The cavity is kept
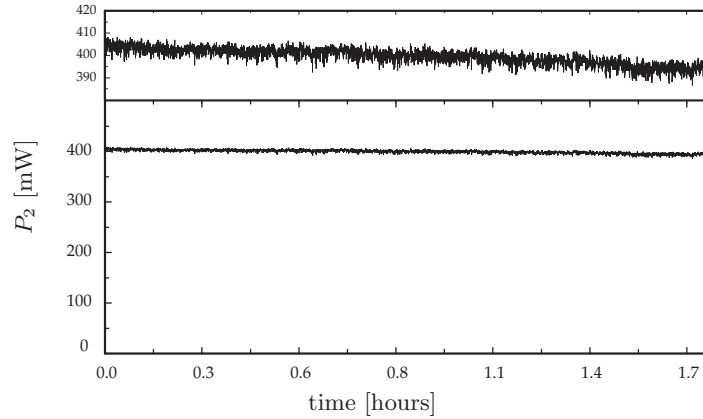
Figure 5.8: 544 nm power versus time.

(a)   (b)
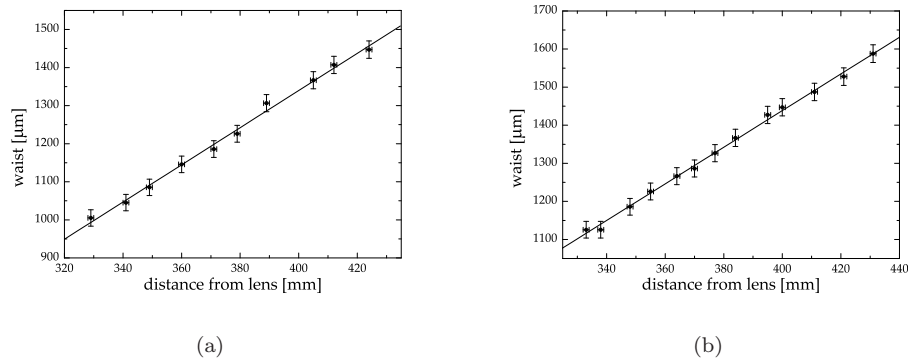
Figure 5.9: Vertial (a) and horizontal (b) beam waists measured versus the distance from the focusing lens. The slopes are measured to be 4.88×10^{-3} and 4.81×10^{-3} for the vertical and horizontal, respectively.

resonant with the 544 nm light by using a Hänsch-Couillaud type polarization locking scheme [125]. The results of this second frequency doubling step are summarized in fig. 5.11. For an input of 730 mW at 544 nm, we achieve a conversion efficiency of 16 %, corresponding to 115 mW at 272 nm. Taking losses at the output coupling mirror of 15 % and imperfect modematching (95 %)[6] into account, the internal conversion efficiency is found to be close to 20 %. The considerably lower conversion efficiency of the second frequency doubling stage is due to several parameters: The input power, which is much lower than for the first SHG stage. The non-linear coefficient of the BBO crystal at 544 nm, which is inferior to that of the LiNbO$_3$ crystal at 1088 nm. And finally, the walk-off due to the critical phase-matching situation, which leads to partial destructive interference of SHG light produced along the crystal. However,

---

[6]This is partly due to the slightly eliptical beam profile of the 544 nm light, as indicated by the difference in the measured M^2-values
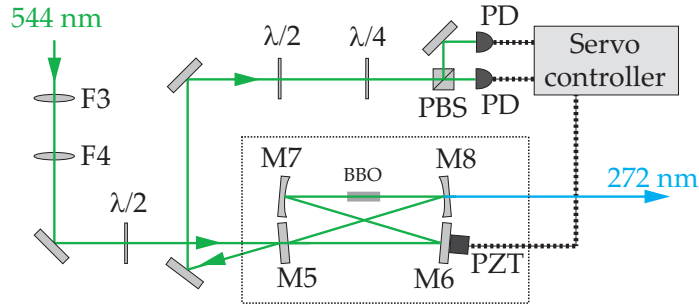
Figure 5.10: Schematic of the setup used for the second frequency doubling stage. F: mode-matching lenses, M: cavity mirrors, PZT: piezo-electric transducer, PD: photo detector, $\lambda/2$: Half Wave Plate, $\lambda/4$: Quarter Wave Plate.

the measured efficiency is far below that predicted by the Boyd-Kleinman theory for the parameters quoted earlier ($T = 0.01$, $\gamma = 18 \times 10^{-5}$ W^{-1} and $\mathcal{L} = 0.01$), which is shown by the the solid line in fig. 5.11. This discrepancy might be due to slightly higher passive cavity losses. Since γ is expected to be about an order of magnitude lower for BBO at 544 nm compared to LiNbO$_3$ at 1088 nm and the fundamental power is about half, non-linear losses are significantly lower in this second SHG process. The impedance matching condition for the input coupler transmission $T = \mathcal{L} + \gamma P_c$ is then mainly determined by the passive losses $\mathcal{L}$ and changes in these will reflect heavily on the intra-cavity power and, hence, the conversion efficiency. The dashed line in fig. 5.11 shows the theoretical prediction for increased losses of $\mathcal{L} = 0.018$ and is in nice agreement with the obtained results. Finally, the non-linear coefficient might also be lower than that specified by the crystal manufacturer.

In terms of input power to usable output power conversion, the overall efficiency (1088 to 272 nm) is 8 %, which is similar to that of a previously reported 175 mW 272 nm source based on a Ti:Sapphire laser operated at 817 nm [126].

The power stability of the UV light reflects that of the 544 nm source. At input powers above 700 mW, changes of up to 20 % are seen over several hours, whereas on a timescale of tens of ms the fluctuations are below 5 %. The frequency stability of system is set by the temperature stability of the DFB fiber laser which results in drifts in frequency at 272 nm of $\sim$100 MHz/K.

5.1.4   Outlook

As mentioned in the introduction of the present chapter, the broad gain profile of Ytterbium ($\sim$ 975 to $\sim$ 1200 nm) makes Yb-based DFB fiber lasers very attractive for frequency doubling into the visible and further into the UV. Other than the laser system presented here, a 275 mW source at 280 nm also based on two consecutive frequency doubling stages of light from a commercial Yb-doped DFB fiber laser has been reported [127], and recently, a 4 W laser source at 546nm also based on SHG of light from a Yb-doped DFB fiber laser, was developed [128]. Furthermore, DFB fiber lasers based on Erbium (emission range $\sim$ 1500 to $\sim$ 1600 nm) [129] and Thulium (emission range $\sim$ 1700 to $\sim$ 2100 nm) [130] may further enlarge the accessible wave-
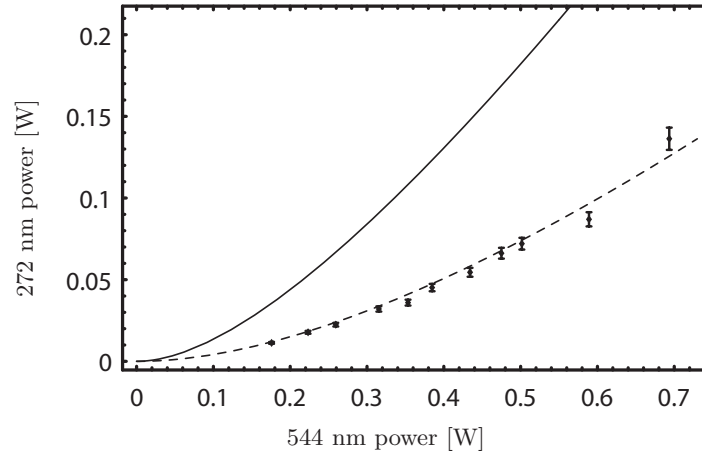
(a)
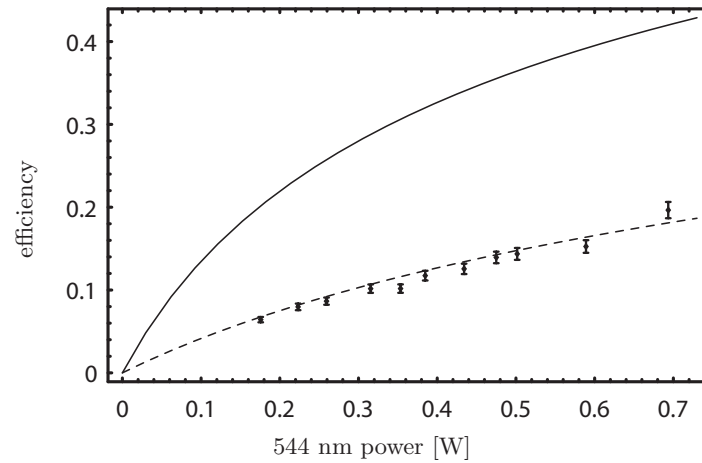
(b)

Figure 5.11: a) Generated second harmonic power at 272 nm as a function of incident light power at 544 nm. b) Internal power conversion efficiency. Error bars correspond to an estimated 5 % uncertainty in the measured powers. The data has been corrected for a 15 % loss at the output coupling mirror, M8, and a modematching of 95 %. The two lines are from a theoretical prediction based on eq. 5.12 for $T = 0.01$, $\gamma = 18 \times 10^{-5}$ W^{-1} and $\mathcal{L} = 0.01$ (solid line) and $T = 0.01$, $\gamma = 1.8 \times 10^{-5}$ W^{-1} and $\mathcal{L} = 0.018$ (dashed line).

length range in the visible and near-UV region. Consequently, we expect rare-earth element doped DFB fiber lasers in combination with SHG to be applied extensively in the future.

5.2   866 nm laser systems

Light at 866 nm is used in laser cooling of all Ca^+ isotopes and in experiments with two-component crystals, such as those presented in fig. 4.4, two laser sources, each one tuned to a different isotopic resonance, were used. Other experiments, that we shall consider later in this thesis, also required the use of two different 866 nm lasers and we thus have two diode laser systems producing light at 866 nm. These are, however, more or less identical. The following is a description of the 866 nm laser used for probing the ion Coulomb crystal-cavity system, specifically. This laser will henceforth be referred to as the 866-1 or the probe laser. The other, mostly used for Doppler cooling and optical pumping of Ca^+, will be referred to as the 866-2, the repumper or the optical pumping laser.

The 866-1 laser is based on an ar-coated diode, as are all diode lasers used in this work. The advantage of using ar coated diodes, rather than Fabry-Perot diodes, is that they have a very broad gain profile and can thus be aligned for lasing over a broad range of wavelengths, if necessary. Feedback to achieve laser oscillation is provided via an extended cavity, where the output coupler is a grating (1800 lines/mm) placed in a Littrow configuration. A drawing of a typical diode laser found in our laboratory is shown in fig. 5.12. The laser diode itself is not seen as it is hidden by the lens which collimates the horizontal beam axis. Frequency tuning can be achieved via the diode current, the temperature, which is controlled by a peltier element under the laser base plate, or by a PZT that controls the angle of the grating and the length of the cavity (See fig. 5.12).
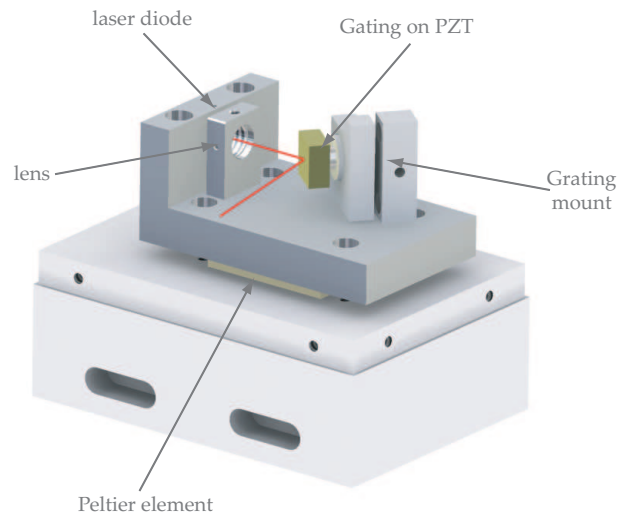
Figure 5.12: Drawing of a typical diode laser used in the experiments. See text for details. Not shown is the cover as well as a styrofoarm housing, which helps the temperature stability.
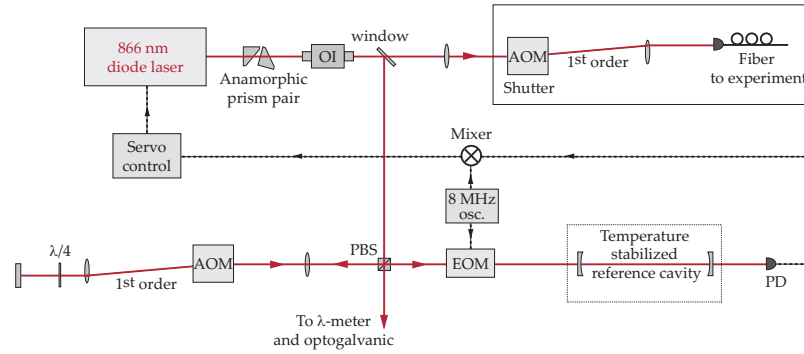
Figure 5.13: Schematic of the 866 nm laser system used for cooling of Ca^+. PBS: Polarizing beam-splitter, $\lambda/4$: Quarter-wave plate, PD: Photo detector. See text for details. There are two such laser systems in our laboratory, which allows for cooling of both $^{40}Ca^+$ and $^{44}Ca^+$ at the same time. Furthermore, the part of the setup in the black frame in the upper right corner, can be duplicated allowing for several beams to be sent to the experiment for different purposes such as optical pumping (ch. 9) and probing the atomic states (ch. 10).

Setup

A schematic of the general setup is shown in fig. 5.13. A pair of anamorphic prisms is used to reshape the otherwise elliptical beam profile at the output of the laser. An OI ensures minimal optical feedback to the laser and frequency stabilization is done by locking the laser to a temperature stabilized reference cavity (see ch. 5.5) using the Pound-Drever-Hall (PDH) locking scheme [122, 123]. The phase-modulation required for this scheme to work is provided by an EOM, which modulates the light at 8 MHz before the reference cavity. For locking, the error signal is divided such that a high frequency, ac-part, is fed back to the laser current, while a low frequency, dc-part, is sent to the PZT, which generally makes for stable, low noise locking over several hours. Once locked, fine tuning of the frequency can be done using an acousto-optic modulator (AOM) inserted in the locking setup. The AOM has a tuning range of ±50 MHz and is placed in a double-pass setup, which effectively, results in a total tuning range of ±100 MHz.

The 866-1 laser actually has two OIs each providing ~ 35 dB attenuation of back scattered light while for most other diode lasers a single OI, as indicated in the drawing of the setup, suffices. The need for such high attenuation arises when the 866-1 laser is used as a probe for the optical cavity, used in the cavity QED experiments. Since this cavity is in a standing wave configuration and is very accurately aligned, it is prone to cause optical feedback to the laser.

Shutters

In some experiments it is necessary to turn the 866 nm light on and off on a very short time scale and with a very high degree of extinction. This is achieved with an AOM in a single-pass setup as shown in the black frame of fig. 5.13. The radio frequency (rf) driving field can be turned on and off with a rise/fall time < 100 ns and with an attenuation of ~ 80 dB. This effectively turns the 1st order beam off. However, even with good optical quality of the AOM crystal and surfaces, there is still some scatter-

ing of the 0th order beam, which ultimately limits the optical attenuation to about 40 dB after the AOM. The optical fiber used as a practical means to guide the light to the experiment then serves a second purpose, namely as a pinhole providing spatial filtering of this scattered light. This usually increases the total optical attenuation to 55-60 dB in our setups. Depending on the experiment, there may be several beams with shutters and fiber couplers as in the setup in the black frame of fig. 5.13.

Linewidth

Finally, the linewidth of the 866-1 laser should be considered. The linewidth of the atomic transition is set by the decay rate of the $4p^2 P_{1/2}$-state to $2\pi \times 22.4$ MHz and as we shall see in ch. 6.6, the cavity linewidth (FWHM) is about $2\pi \times 4.2$ MHz. Since the 866-1 laser is used to probe the interaction between the cavity field and an atomic dipole on this transition, the 866-1 linewidth must be narrower than both of these. Fig. 5.14 shows the result of a linewidth measurement of the 866-1 laser in free running mode (black data points) and when locked to the stabilized reference cavity (red data points). The red and black curves show Lorentzian fits to the data with widths (FWHM) of 458 ± 12 kHz and 214 ± 4 kHz, corresponding to laser linewidths of 279 ± 6 kHz and 107 ± 2 kHz for the free running and locked data, respectively.

The linewidth is measured using a self-heterodyne setup [131], where the laser beam is split into two, and one beam is shifted in frequency by 270 MHz with respect to the other. When re-combining the two beams, a beat node occurs at this frequency with a width reflecting the time correlation between the fields of the two beams. In this measurement, one beam was sent via an optical fiber through a delay line of more than 20 km. This is well beyond the coherence length of the laser itself, which based on
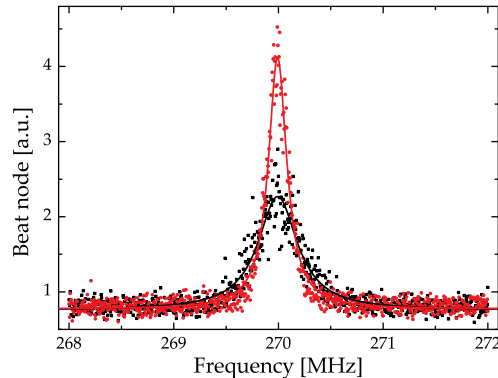
Figure 5.14: Beat nodes obtained by self-heterodyning of the 866 nm laser using a 20 km delay fiber. Black data: Free running. Red data: Locked to reference cavity. The width of the Lorentzian fits are 458 ± 12 kHz and 214 ± 4 kHz, corresponding to laser linewidths of 279 ± 6) kHz and 107 ± 2 kHz for the free running and locked data, respectively. This linewidth is typical for our diode laser (see appendix F over an overview).

our measurement of ~ 100 kHz is $L_{\mathrm{coh}} = \frac{c}{\Delta \nu_{\mathrm{laser}}} \simeq 3$ km. The beat node thus reflects the linewidths of two uncorrelated fields, which assuming a Lorentzian linewidth, is exactly twice the linewidth of the laser. More details can be found in [131].

5.3   894 nm laser system

The 894 nm laser is used in the cavity QED experiments in two ways, which will be described in detail in ch. 6.6:

- To lock the cavity and control the length and, hence, the detuning of this cavity with respect to the atomic transition in the ions.

- To monitor drifts and acoustic noise of the cavity when scanning the cavity.

These two points make this laser a crucial piece of equipment for our experiments. Any noise inherent in this laser will be transfered to the cavity and the quality of our data will degrade as a result thereof.

As already mentioned, this laser system greatly resembles that of the 866-1 laser and for details regarding the general setup and performance we refer to the above section covering the 866-1 laser and appendix F where the specifications have been summarized. As for the 866-1 laser, the fact that the 894 nm laser is used together with the trap cavity means that special precautions must be taken to avoid optical feedback from this. For this reason the 894 nm laser also has two OIs each providing about 35 dB attenuation and with this it performs with low noise and stable output. A quantitative measure of the stability is again the linewidth, which has been measured similarly to the 866-1 laser to 163 ± 8 kHz in the free running case and 89 ± 5 kHz in the locked case.

For the 894 nm laser to function as a locking laser for the cavity and a means of diagnostics for this, three requirements must be met:

- The linewidth of the cavity at 894 nm must not be too different from the linewidth of the cavity at 866 nm.

- The linewidth of the 894 nm laser must be narrow compared to the linewidth of the cavity at 894 nm.

- The 894 laser should have low long-time drifts in frequency.

The first requirement relates directly to the cavity itself and will be considered in ch. 6.6. The second requirement is easily satisfied by the low linewidth of the 894 nm laser and the third is satisfied by locking it to a temperature stabilized reference cavity, provided this does not drift over the time it takes to perform the measurements. This drift has been measured to be ~ 1 MHz/hour (see ch. 5.5), which is low enough for most practical purposes.

5.4   397 nm laser system

We have two laser systems producing light at 397 nm in our laboratory. One is based on a 794 nm Titanium Sapphire (Ti:Sapph) laser and makes use of SHG to produce
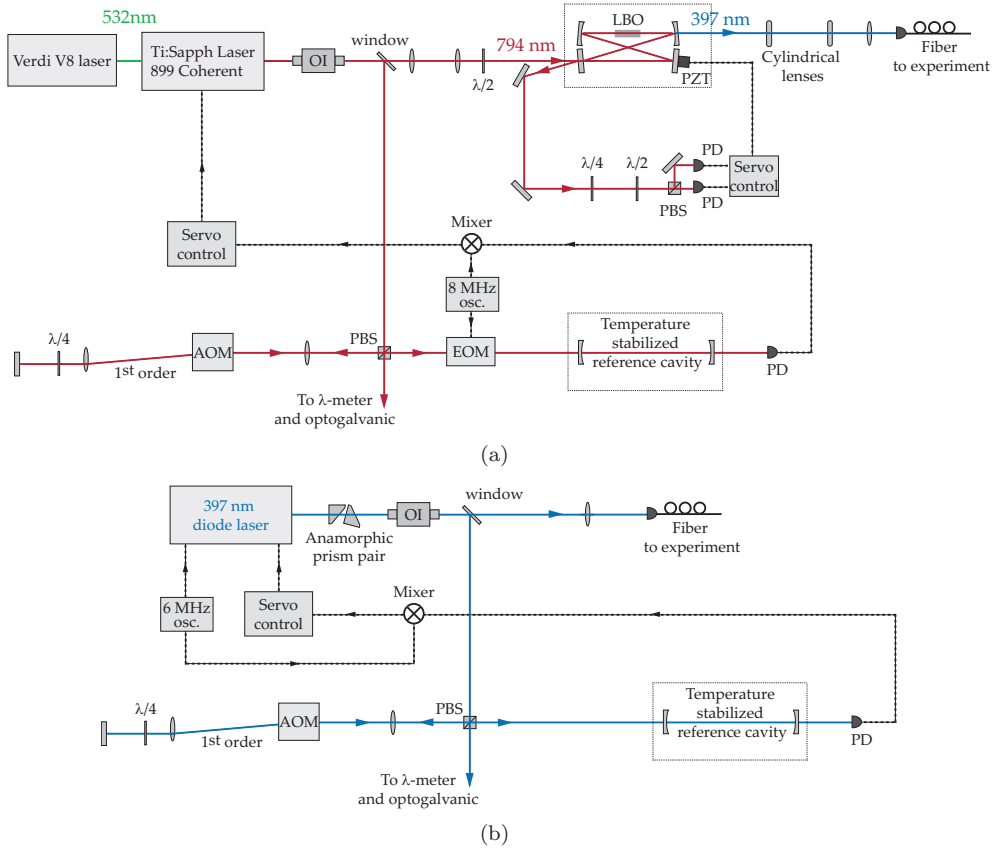
Figure 5.15: a) Schematic of the 397 nm laser system based on SHG of light from a Ti:Sapph laser used for cooling of ^{40}Ca$^+$. b) Schematic of the 397 nm diode laser system used for cooling of ^{44}Ca$^+$. PBS: Polarizing beam-splitter, $\lambda/2$: Half-wave plate, $\lambda/4$: Quarter-wave plate, PD: Photo detector. See text for details.

light at 397 nm. The other is based on a 397 nm diode laser in an extended cavity.

The Ti:Sapph source
The Ti:Sapph based setup is depicted in fig. 5.15a). A Verdi V8 pumps a 899 Coherent Ti:Sapph laser producing light at 794 nm, which is subsequently converted into 397 nm light via SHG in an external enhancement cavity. Immediately after the Ti:Sapph an OI ($\sim$ 35dB attenuation) prevents optical feedback from the SHG cavity. The 794 nm beam is mode-matched to the external enhancement cavity using a set of lenses and converted into 397 nm light in a 12 mm long Lithium Triborate (LBO) crystal. The cavity is in a bow-tie configuration and is kept resonant using a Hänsch-Couillaud polarization locking scheme [125]. This generates an error signal that is fed back to one cavity mirror mounted on a PZT, which controls the length of the cavity. For LBO at this wavelength, the SHG is a type I critical phase-matching process, which implies that the produced 397 nm light has a non-gaussian beam profile due to

walk-off. This is corrected using a set of cylindrical lenses. For more details on this SHG cavity see ref. [132]. Typically, the Ti:Sapph is pumped by 5.5 W producing ~ 300 mW 794 nm light, which gives ~ 40 mW 397 nm light. Of this, about 10 mW is available for the experiment after the optical fiber.

Before the SHG cavity, part of the beam is taken out on a window and used for both wavelength measurement and frequency stabilization. The frequency stabilization is done by locking the Ti:Sapph laser to a temperature stabilized reference cavity (see ch. 5.5) using a PDH locking scheme [122, 123] similar to the 866-1 laser described above. Once locked, fine tuning of the frequency can be done using an AOM inserted in the locking setup. The AOM has a tuning range of ± 50 MHz and is placed in a double-pass setup. Effectively, this corresponds to a total tuning range of the frequency *doubled* 397 nm light of ± 200 MHz.

The linewidth of the Ti:Sapph has been measured previously to be ~ 100 kHz [133], which is sufficiently low for the purpose of Doppler laser cooling and optical pumping of Ca^+, where the linewidth of the transition is 22.4 MHz.

The 397 nm diode source
The 397 nm diode is an ar coated diode. The setup resembles that of the 866-1 laser described above except that phase modulation is achieved through modulation of the laser current at 6 MHz (see fig. 5.15b)). The laser delivers about 10 mW of power, 30% of which is coupled through a PM fiber and sent to the experiment. The linewidth of this laser has not been measured at the time of writing, but is estimated to be below 1 MHz. At any rate, for the purpose of Doppler laser cooling, which has been this laser's primary objective within this work, it has been found to work well.

5.5   Stabilized reference cavities

As mentioned several times throughout this chapter, the frequency stability of the lasers is maintained by locking them to temperature stabilized reference cavities. For the lasers described above, there are three such reference cavities: One for the Ti:Sapph laser at 794 nm, one for the diode laser at 397 nm, and one for the remaining three infra-red diode lasers (866-1, 866-2, 894). Apart from having cavity mirrors with different coatings, the three reference cavities are identical. They consist of a horizontal quartz tube with mirrors at each end forming the optical resonator. The length of the tube is 25 cm, which corresponds to a FSR of about 600 MHz. Quartz has a relatively low, but nevertheless, non-vanishing thermal expansion coefficient $(0.55 \times 10^{-6}$ K$^{-1})$ and the length of the cavity can thus be adjusted through the temperature. The temperature is controlled and stabilized by a PDI-circuit that feeds back to a resistive wire wound around the quartz tube. The cavity itself rests in an evacuated vacuum tube (pressure $\sim 10^{-5}$ mbar), which is also temperature controlled. The stability of the cavity is ~ 1 MHz/hour. For further details see [134].

Chapter 6

The experimental setup

In this chapter we describe the setup that has been developed for the realization of cavity QED experiments with ion Coulomb crystals. We shall detail both the design and construction of the ion trap as well as the integrated cavity. Also covered in this chapter are the ion imaging system, the magnetic field control setup, the cavity detection system and the computer control system. We then conclude and summarize the main points of the chapter.

6.1 The cavity trap

The first cavity trap was originally designed by former PhD-student Anders Mortensen in collaboration with engineer Henrik Bechtold at the Department of Physics and Astronomy at the University of Aarhus. It was designed with the specific goal of implementing a quantum memory for light based on ion Coulomb crystals. Aspects of this as well as theoretical and practical work on the design and construction of the trap are well described in the thesis by Anders Mortensen [66] and we shall refer to it many times throughout this chapter. In early 2005, it was decided that a new trap should be developed and it is this second trap that we will describe in the following. The final version of the new trap, however, is very much inspired by the design of its predecessor and owes its new features largely to the experience accumulated by Anders Mortensen. These features are primarily related to aspects regarding trap- and cavity alignment precision.

6.1.1 Design considerations

For ion Coulomb crystals to enter the regime of strong collective coupling of cavity QED, one must design and implement an experiment where the coherent coupling strength of the crystal to a single photon dominates over all dissipative processes in the system. In ch. 2.3 we formulated this as the strong collective coupling criterion: $g\sqrt{N} > \gamma, \kappa$, where g is the single ion-photon coupling strength, N is the number of ions, γ is the decay rate of the atomic dipole and κ is the decay rate of the cavity field. As described in appendix C the coupling strength of a single ion to the cavity field, scales as $1/\sqrt{V}$, where V is the cavity modevolume. It is therefore appealing to try to make the cavity as small as possible, by positioning the mirrors closely together

so as to achieve the highest possible coupling strength. This has indeed been the approach in experiments with neutral atoms where cavities of only a few tens of μm have been implemented and enabled the fulfillment of the strong coupling criterion even for single atoms [11, 12]. Since the cavity decay rate $\kappa \propto T/l_{\mathrm{cav}}$ (neglecting mirror losses), where T is the mirror transmission and l_{cav} is the cavity length, as the cavity is made shorter to increase the coupling strength, κ is increased unless mirror transmission losses are reduced. For this reason the above mentioned experiments were forced to use extremely high finesse cavities, which are in general technically very challenging both to implement and to operate.

With ions the situation is quite different. The perturbing effect of the dielectric mirrors will be likely to impede trapping of ions when the mirrors are brought very close together and stable confinement thus becomes extremely challenging to achieve. Efforts to overcome this, by use of traps with very small trapping volumes combined with high finesse cavities, are currently made e.g. in the group of Wolfgang Lange at the University of Sussex and may eventually allow single ion experiments to enter the strong coupling regime.

In this work, we choose a different approach which is to scale up the coupling strength by increasing the number of ions interacting with the cavity mode field. As we mentioned already in ch. 2.3, here we are dealing with a collective interaction that in certain aspects is fundamentally different from the single ion/atom systems. However, this type of collective, ensemble-based experiments benefits from the fact that the challenges related to the implementation of short, high finesse cavities can be avoided. Since we do not require single ion strong coupling ($g > \gamma, \kappa$), a longer cavity can be employed, which means that only a moderately high finesse cavity is needed to achieve a sufficiently low value for κ.

For the $D_{3/2} \leftrightarrow P_{1/2}$ transition of $^{40}\mathrm{Ca}^+$ the decoherence rate of the atomic dipole is $\gamma = 2\pi \times 11.2$ MHz. By choosing a cavity with a finesse of about 4000 and a length of about 1 cm the cavity decay rate becomes $\kappa \simeq 2\pi \times 2$ MHz. Since γ is by far the dominant decay rate in the system already, not much is gained by a cavity of higher finesse for the purpose of achieving strong collective coupling. In appendix C we calculate the coherent coupling strength for a 1 cm long cavity, with the parameters of our system, to be around $g \simeq 2\pi \times 0.5$ MHz, which means that about 500 ions are required to enter the regime of strong collective coupling. These numbers will guide us in the following design of the cavity.

At the time when the cavity trap was first designed, only two groups in the world had successfully combined the techniques of ion trapping with small optical cavities to study the interaction between a cavity field and ions. These were the groups of Rainer Blatt [44, 45, 135] in Innsbruck and Herbert Walther in Garching [43, 46, 57] who pioneered the field of cavity QED with ions. Our design has to some extent been guided by their advances, however, in certain aspects, the task of confining ion Coulomb crystals rather than single ions in the mode of an optical resonator imposes further challenges to the design. Here we list some of the main issues that must be considered for the successful implementation of a cavity QED experiment based on ion Coulomb crystals:

- The effect of the mirrors on the motion of the ions, and specifically the effect of

micromotion.

- The trap geometry, which must allow for a large enough number of ions to be confined stably within the cavity mode volume, for the system to satisfy the requirement for strong collective coupling (~ 500 ions).

- Achieving precise alignment of the trap, the cavity, and the trap with respect to the cavity.

- UHV environment and non-magnetic materials, which are necessary to achieve long life- and coherence times of atomic states.

- Avoiding mirror contamination during loading of the trap, which is necessary to maintain the quality of the optical resonator.

We shall address most of these issues in the present section on the design of the trap. In ch. 6.2 we will describe the vacuum chamber and how the UHV environment is achieved and maintained. To minimize stray magnetic fields, we have only used non-magnetic materials, such as titanium, copper, ceramics and glass for the trap and the vacuum chamber and the trap table is made from low-magnetic stainless steel. To address the final issue of avoiding mirror contamination, the trap is loaded via resonant photoionization, which generally provides for clean and efficient loading. This will be described in ch. 7.

The effect of the mirrors
The introduction of cavity mirrors into the trap requires some careful thought. The mirror substrates are made from fused silica, which for static electric fields and the rf-fields of the linear Paul trap has a dielectric constant of $3.78 \times \epsilon_0$ [136]. This will obviously affect the electric field lines of the trap and may cause the rf-fields to have a component along the trap axis. This will give rise to axial micromotion, which as mentioned in ch. 3.2.2, will result in unwanted Doppler broadening of the atomic transitions. The previous experiments combining an optical cavity with an rf-trap have focused on single or few ions [45, 57], where micromotion is less critical as the ions can be positioned in the rf-minimum [93]. For ion Coulomb crystals the situation is different as there will always be some ions that are not in the rf-minimum. Simulations done by Anders Mortensen [66] confirmed that the effect of the cavity mirror substrates could be substantial but also revealed that it is possible to design the mirrors such that the effect would be diminished. The simulations indicated that a viable strategy is to make the mirror substrates flat and extend as far as possible to the electrodes. A simple explanation for this can be found by considering a trap with four infinitely long electrodes in a quadrupole configuration. Everywhere the electric field lines will be perpendicular to the trap electrodes and no component along the trap axis exists. If the region between the electrodes is filled completely with a dielectric medium in one end of the trap, this does not change the electric field since it already fulfills the necessary boundary conditions at the interface of the dielectric and the vacuum. This will not be the case should the dielectric not extend all the way to the electrodes and the rf-field lines will then bend toward the dielectric medium, thus causing axial micromotion.
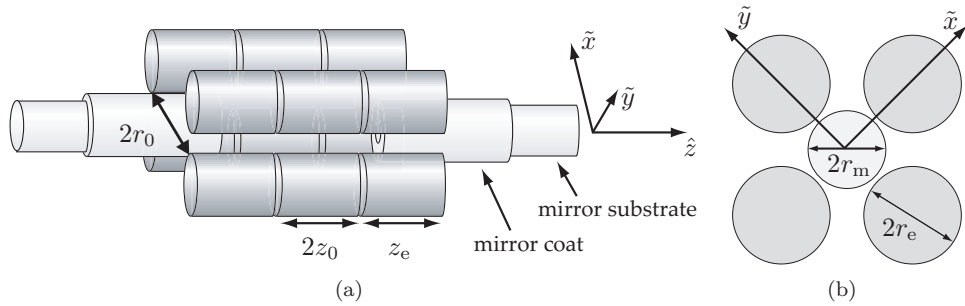
Figure 6.1: (a) Sketch of linear Paul trap with integrated mirrors. (b) End-view of the trap.

Cavity trap geometry

Based on the above analysis, dielectric filling in the form of mirror *coats* are added around the mirror substrates. A schematic drawing can be seen in fig. 6.1. The cavity axis coincides with the trap axis to minimize the effect of radial micromotion. When analyzing which trap geometry would result in the most harmonic potential, the effect of the mirrors was also included in the simulations. The final dimensions for the trap electrodes along with other trap parameters have been summarized in table 6.1. Also guiding the design process was the experience within the Ion Trap Group with similar traps. The final geometry therefore reflects a relatively conservative estimate for what would allow for stable confinement of ion Coulomb crystals of the required density and length. For further details, see [66].

Mirror radius (incl. coat):	$r_\mathrm{m} = 2.08$ mm
Electrode inscribed radius:	$r_0 = 2.35$ mm
Electrode radius:	$r_\mathrm{e} = 2.60$ mm
Center-electrode length	$2z_0 = 5.00$ mm
End-electrode length	$z_\mathrm{ec} = 5.90$ mm
Axial geometrical constant:	$\eta = 0.342$
rf-frequency:	$\Omega_\mathrm{rf} = 2\pi \times 4.0$ MHz
a-parameter(^{40}Ca$^+$):	$a = -0.84 \times 10^{-3}$ V$^{-1} \times U_{end}$
q-parameter(^{40}Ca$^+$):	$q = 1.38 \times 10^{-3}$ V$^{-1} \times U_{rf}$

Table 6.1: Reference table of the trap-parameters. The trap dimensions are shown in Fig. 6.1. Note that the values for the a and q parameters are the theoretical predictions based on the trap geometry (c.f. eq. 3.6) and that the actual values will differ slightly. Measurements of these are presented in ch. 8.2. U_{end} and U_{rf} are typically between 1-15 Volt and 150-400 Volt, respectively.

6.1.2 Alignment and assembly

The final design of the cavity trap is shown in fig. 6.2. The cavity mirror mounts are held by an outer construction, which consists of two end-walls, made from titanium,
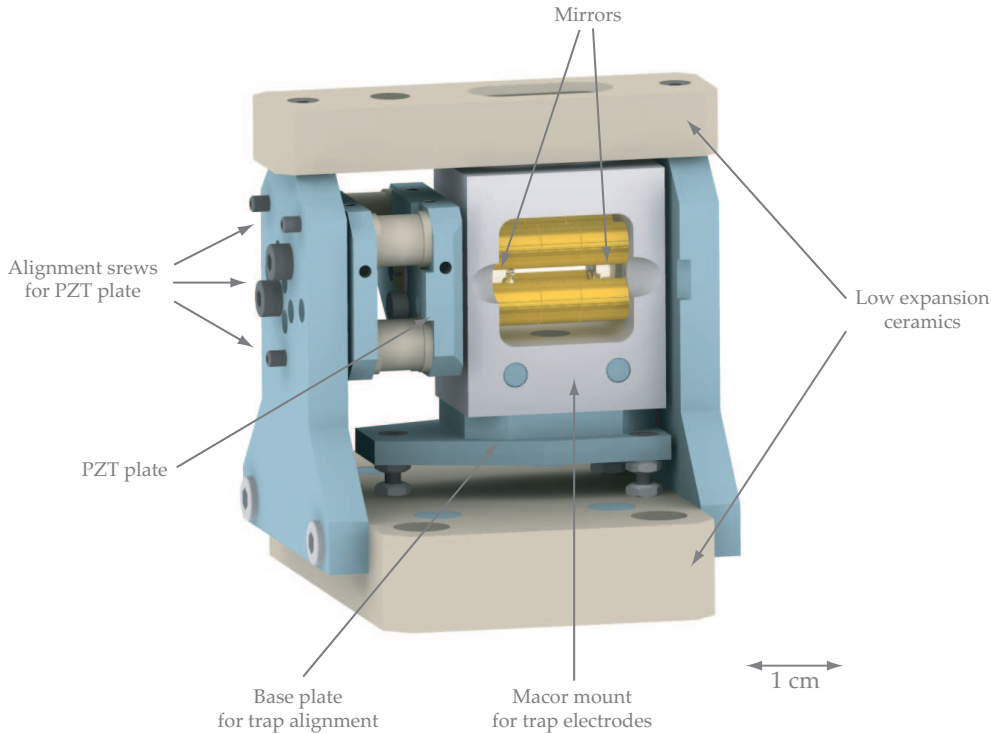
Figure 6.2: Drawing of the new cavity trap. All metal parts are made from titanium or copper to minimize magnetic field effects. See text for details.

separated by two pieces of low expansion ceramics[1] that ensures minimal changes in the cavity length with temperature. One cavity mirror is mounted directly in the end-wall, while the other is mounted on a PZT-plate allowing for control of the cavity length and aligned via the three alignment screws on the PZT-plate (see fig. 6.2). The PZT-plate has three PZTs [2] which in hindsight was an unnecessary complication. The motivation was that it could allow for fine alignment of the cavity, however, in the end it turned out that the PZT-plate was too rigid for this to have any effect. An important feature of the PZT-plate, though, is that electric fields from the PZTs are efficiently shielded by grounding the plate and the outer walls of the PZTs.

The trap electrodes are of gold plated copper and mounted on rods of zerodur[3], which are held in a monolithic macor[4] mount. This construction gives a very high degree of precision, as the final alignment of the electrodes with respect to one another is determined only by the machining accuracy of the zerodur rods and the holes drilled in the electrodes and in the macor mount for these rods. In other words, no tightening or gluing of pieces is required during the assembly of the trap electrodes (see fig. 6.3). All pieces simply slide in together and are then aligned with a precision set by the

---

[1] MC-LD from MarkeTech International Inc.
[2] Ferroperm pz27
[3] an ultra low expansion glass manufactured by Schott.
[4] a machinable ceramic

machining process, which for all parts is better than 10 μm. In their final position the electrodes are fixed by titanium screws that connect the wires for the trap voltages to the electrodes as can be seen in fig. 6.3.

(a)

(b)
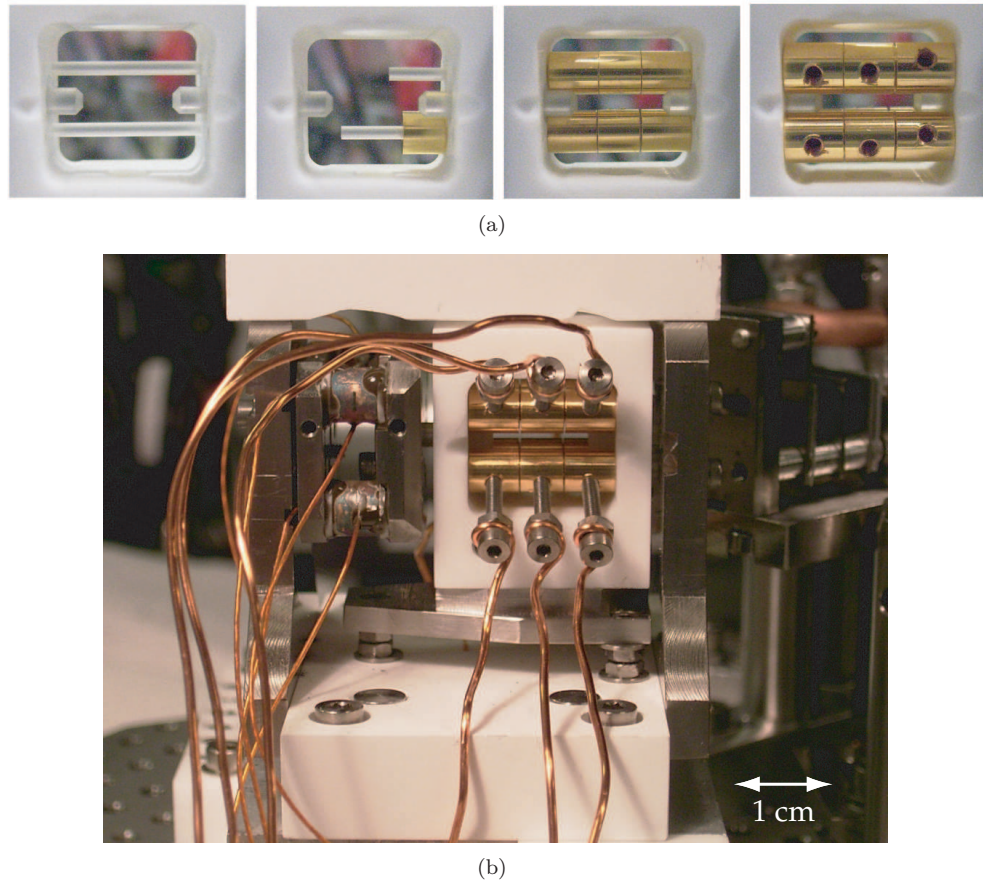
Figure 6.3: a) Pictures of the assembly process. Electrode mount, zerodur rods and electrodes. Also seen are the mirrors (here, without the mirror coats). b) Picture of the fully assembled trap including electrode wires. See text for further details.

Before the electrodes were inserted, the electrode mount was aligned with respect to the cavity axis, using a home made tool consisting of two plates, each with 100 µm diameter holes, mounted on four rods. These rods fitted into the holes in the macor for the zerodur rods that would later hold the electrodes. With the aide of this tool, the electrode mount could be aligned with respect to the cavity axis by adjustment of three screws on the base plate of the electrode mount, such that the cavity mode was not cut by the plates of the alignment tool. This was to ensure that once the electrodes had been inserted, the trap axis would coincide with the optical axis of the cavity. This alignment is critical both to achieve the highest possible number of ions within the cavity mode, but also to ensure that the ions within the cavity mode are those exhibiting the least micromotion and, hence, the least Doppler broadening. We shall

return to this issue in ch. 8 when we present measurements on the characterization of the trap.

6.2   The vacuum chamber

Fig. 6.4a) shows a picture of the trap chamber viewed from above. The dimensions can be seen from the holes in the plate, which are 1 cm apart. Below we will go though the main parts of the trap chamber.

- The trap itself is positioned at the center of the vacuum chamber. Wiring for the trap electrodes and the PZTs is done through two feedthrough flanges and via four macor connector blocks. The wires used for the trap electrodes are 1 mm diameter copper wires without isolation and the wires used for the PZTs are 0.25 mm diameter copper wires isolated by a UHV compatible capton coating.

- Optical access is available through seven view-ports, anti-reflexion coated for the appropriate wavelengths.

- The 397 nm beams for Doppler laser cooling are sent in along the trap axis (z-axis in picture) to avoid driving the radial micromotion. This is possible for the 397 nm beams since the cavity mirrors are transmitting at this wavelength. This is, however, not the case for the 866 nm beams and unless the cavity is held resonant, repumping cannot be done through the cavity. For Doppler laser cooling the angle of the 866 nm repumper is less critical than the 397 nm beam, however, and it can in principle be sent in at $90°$ or $45°$ as shown in fig. 6.4a). By an alternative beam path, however, the angle can be as small as $11°$. This is done via the mirror M1 after which it is reflected off the surfaces of the two mirror coats inside the trap. For alignment purposes, the beam then exits the trap and is reflected by the mirror M2 out of the chamber, where it can be detected.

- 866 nm beams sent in along the trap/cavity axis are used as probe beams for the cavity and the 894 nm beam, likewise sent in along the trap/cavity axis, is used for locking the cavity and monitoring drift and vibrations. This will be described in more detail in ch. 6.6.

- For loading the trap, a 272 nm beam intersects with a beam of atomic calcium at the trap center. A series of skimmers prevents material from this beam from being deposited on the trap electrodes or the mirror substrates. The calcium beam is produced from a small oven and measures about 1.5 mm horizontally and 1.0 mm vertically in the trap center (further details are given in [66]). Alternatively, the calcium beam can be produced by ablating material off a calcium target using a pulsed 1064 nm laser, injected via the mirrors M3 and M4. For further details see ch. 7. Both target and oven as well as a shutter for the oven beam can be seen in the close-up of fig. 6.4b). The shutter consists of an aluminum plate mounted on a rotary motion feedthrough that allows it to be moved in and out of the oven beam.

- For alignment of the optical beams with respect to the trap center, an optical fiber (80 µm diameter) can be moved in and out of the trap. Light scattered

from the fiber is then detected by the imaging system. This is also used for calibration of the imaging system, which will be described in ch. 6.4.

As there is a lot of material inside the chamber, achieving a good vacuum can be difficult and in general requires some time. Prior to assembly, all parts were cleaned in an ultra-sound bath and in a soap solution[5] and baked separately at 150°C, after which they were cleaned again with solvents such as ethanol and isopropanol. Everything was mounted on a stainless steel plate and aligned inside a pre-cleaned box that had a small pump attached to maintain a slightly elevated pressure that would prevent dust and dirt from entering. Access to align the trap was provided through sets of gloves attached to openings in the box. Prior to installation, the plate, along with the entire setup, was baked out at 150°C for a few hours after which the alignment of the cavity was checked. This was repeated several times to ensure the setup would remain aligned during the following bake-out.

Once installed and connected, the entire chamber was baked out for about a week, slowly increasing the temperature to $\sim 150°C$ and then maintaining it there for a few days, while a turbo pump connected to the chamber would pump out. The calcium oven was slowly heated to $\sim 600°C$ over one day to remove oxidized material and air trapped in the porous calcium lumps. To maintain low pressure after the bake-out, an ion pump and a titanium sublimation pump are connected to the trap chamber. These were also degassed during the bake-out and so were the filaments of the ion gauge used to monitor the pressure.

During the entire bake-out procedure we monitored the quality of the cavity inside the trap by measuring its finesse (see ch. 6.6). After degassing the ion pump, we observed that the finesse had dropped by an amount corresponding to additional mirror losses of $\simeq 400$ ppm. Obviously, this is very unfortunate, but for the purpose of most of our experiments, by no means devastating. We shall return to this in ch. 6.6. In the future, we plan to avoid this contamination from the ion pump by inserting a valve between the pump and the main part of the trap chamber. This will allow us to first bake out the entire chamber and degas the ion pump while pumping with the turbo pump. The ion pump can then be valved off and kept under vacuum while the cavity trap is installed in the main part of the chamber. The chamber can then be baked out again and the valve to the ion pump opened after which the effect of degassing should be minimal.

After the bake-out the pressure in the chamber was $\sim 8 \times 10^{-10}$ mbar with the calcium oven turned off. However, when increasing the oven temperature to $\simeq 400°C$, which is the typical temperature in many of our experiments, the pressure would rise to $\sim 3.5 \times 10^{-9}$ mbar. Since then (January 2007), the oven has been on for many hours and the sublimation pump has also been used many times. At the time of writing (August 2008) the pressure has dropped to $\sim 1.5 \times 10^{-10}$ mbar with the oven turned off and only rises to $\sim 3 \times 10^{-10}$ mbar when the oven is heated to $\simeq 400°C$.

---

[5]For all parts except aluminum we used RDS 2%. For aluminum, we used isopropanol.
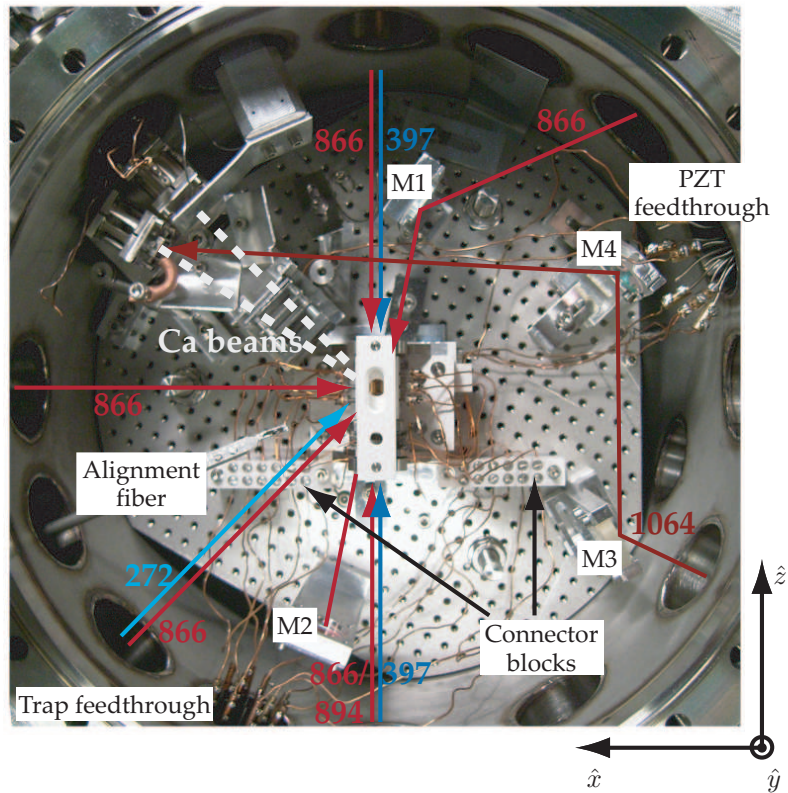
(a)
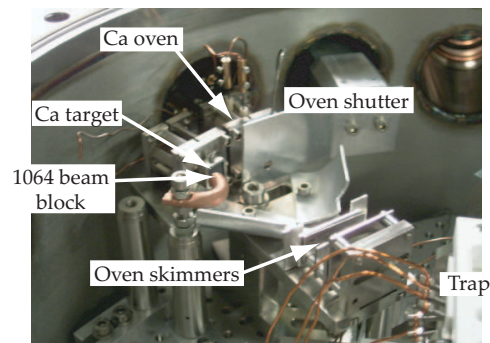
(b)

Figure 6.4: a) Picture of the vacuum chamber with the trap and all the beams used in the experiments. The alignment fiber is glued on to the end of a titanium rod and can be moved in and out of the trap center and used for alignment of the various beams. The dimensions can be seen from the holes in the plate, which are 1 cm apart. b) Picture of the oven setup. See text for further details.

6.3   Trap voltage supplies

The rf-voltage for the trap electrodes is supplied by a frequency generator and ampli-
fied before being transferred to the trap via a resonant circuit. In this circuit the trap
itself acts as the capacitative part of an LRC-circuit which is coupled inductively to
the rf-power supply through a ferrite toroid transformer. A diagram of this circuit for
the voltage supplies (rf and DC) to all trap electrodes is shown in fig. 6.5.[6] It consists
of two separate circuits with opposite phases, which are created from a single rf-input
by winding the output wires in the ferrite toroid transformer in opposite directions.
The two rf-signals are each coupled to a set of six trap electrodes through serial ca-
pacitors (capacitors 2,4,6,8,10,12,14,16,18,20,22,24 in fig. 6.5). Variable capacitors
(capacitors 39 and 52 in fig. 6.5) allow for tuning the two rf-chains with respect to
each other and may also be used to change the overall resonance frequency of the
circuit. Likewise, the capacitors connected to ground immediately before the trap
electrodes (capacitors 40-51 in fig. 6.5) may be adjusted for fine tuning of the voltage
on the individual trap electrodes. However, the entire circuit behaves as one resonant
circuit and any changes in the load on one electrode will affect the coupling of the
rf-voltage into the whole circuit and hence, all electrodes. Similarly, any attempt to
directly measure the voltage on the individual electrodes, will be accompanied by an
additional load, which will alter the resonance condition. Optimization is therefore a
non-trivial process; in practice the only measure of symmetry is provided by the ions
once they have been trapped and cooled. We have the possibility to read out a 100:1
signal of the overall voltage across the two rf-chains via the two monitor outputs in
fig. 6.5, but not the voltage on the individual trap electrodes.

As we shall later return to this rf-circuit to make modifications to the load (see
ch. 8), we give here a short analysis to gain a bit more insight into the behavior of
the circuit. Fig. 6.6a) shows a simplified diagram with a single trap electrode with
some capacitance C_t. Capacitors C_1 and C_2 are the variable capacitors for each phase
and the individual electrodes, respectively, and C_s is the serial capacitor. L is the
inductance of transformer and R_{in} is the input resistance seen by the amplifier. A
resistor R has been included to account for the finite Q-value of the resonator (due
to ohmic losses). An analysis of this simple diagram gives a resonance curve as the
one shown in fig. 6.6b), as expected from a classic LRC-circuit. The actual circuit
is, however, far more complicated than the diagram of both fig. 6.6a) and fig. 6.5.
In reality, there is always some capacitative coupling between the different electrode
circuits and this coupling may change the resonance curve substantially. From the
picture of the trap shown in fig. 6.3b), it seems likely that electrodes on the same
rod will experience some capacitative coupling to their neighbors, thus changing the
capacitative load and, hence, the resonance frequency. Also visible in the picture are
some of the wires for the trap electrodes. These are all fed into the vacuum chamber
through the same flange and there may also be capacitative coupling in between these
wires and, for this reason, the two circuits of opposite phases may be coupled. This
is modeled in the simplified schematic in fig. 6.7a) where a second LRC-circuit is
coupled to the original one of fig. 6.6a) through a coupling capacitor $\tilde{C}_c$. Depending
on the coupling strength, that is, the size of $\tilde{C}_c$, this may give rise to a splitting of
the resonance curve into two as shown in fig. 6.7b). This is not surprising as the

---

[6]This was developed in the electronics department at the institute by Erik Søndergaard.
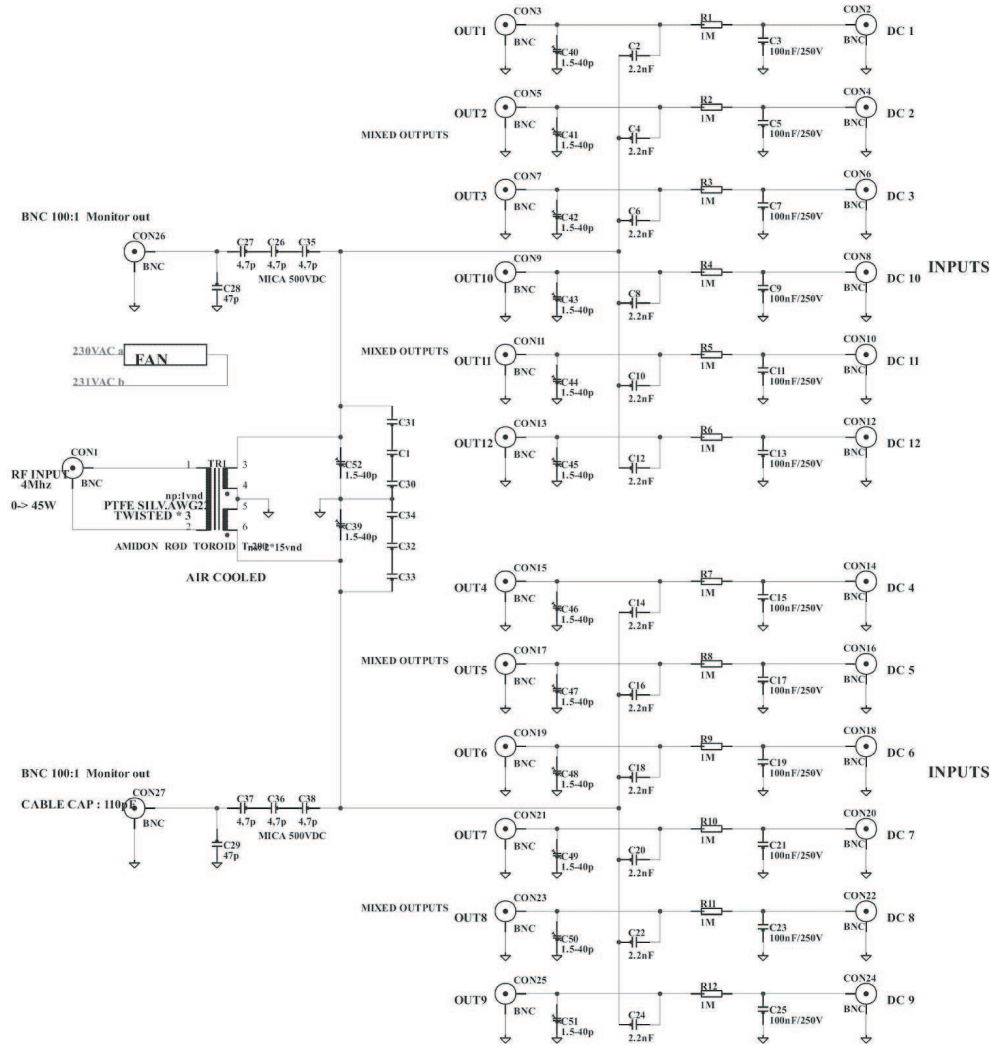
Figure 6.5: Diagram of the voltage supply-trap interface with 1 rf input and 12 DC input. See text for details.

overall circuit can now be considered as two coupled harmonic oscillators, much like a 3-level Λ-system in atomic physics, where a splitting of a resonance line into two is also observed when a third state is coupled to the excited state.

In fig. 6.8 we have plotted the result of a measurement of the circuit frequency response when all electrodes are connected. It clearly shows the predicted splitting of the resonance peak into two. Intuitively, this may seem like a problem, as the Q-value of the resonances and, therefore, the amount of voltage we couple to the electrodes, will be lower. However, even with a lower Q-value, our rf-amplifier is still powerful enough for the voltage on the electrodes to reach the values required for our experi-

(a)   (b)
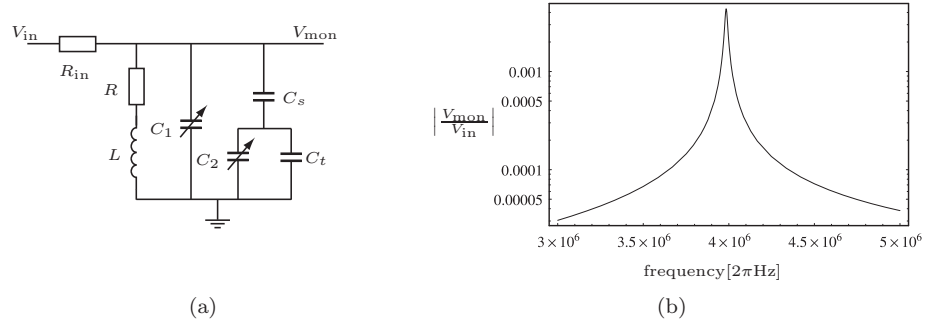
Figure 6.6: a) Simplified diagram of the rf-voltage supply and trap electrodes. C_t is the trap electrode capacitance. V_{in} is the input rf-voltage and V_{mon} is the voltage going to the monitor (capacitors omitted for simplicity). See text for further details. b) Resonance curve for a single trap electrode.

(a)   (b)
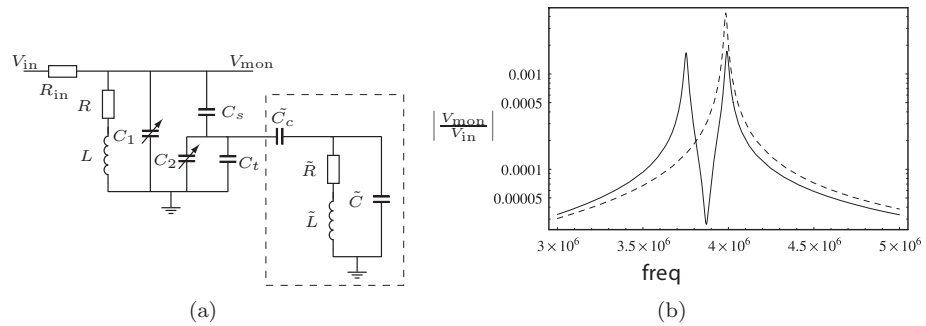
Figure 6.7: a) Simplified diagram of the rf-voltage supply and trap electrodes with capacitative coupling to an additional LRC-circuit (dashed box), through the capacitor C_c. C_t is the trap electrode capacitance. V_{in} is the input rf-voltage and V_{mon} is the voltage going to the monitor (capacitors omitted for simplicity). See text for further details. b) The solid line shows the resonance curve in the case of capacitative coupling to other LRC circuit (of the order of pF). The dashed line shows the case for no coupling.

ments, and the fact that the circuit has two resonances only means that we have more freedom in choosing the rf-frequency. In all experiments within this thesis we have worked at the lower resonance. The exact value may change if the capacitative load on the electrodes is changed, as we shall see later, but in general the trap is operated around 4 MHz.

Finally, DC-offsets can be supplied to all trap electrodes via the inputs on the right hand side in the diagram of fig. 6.5. For each input, a capacitor and a resistor form a low-pass filter which prevents the rf-signal from leaking into the DC-supply. The DC-voltage can be supplied individually to each of the electrodes or to groups of electrodes. For instance, the eight end-electrodes are all connected to the same DC-supply, which allows for adjustment of the end-voltage $U_e nd$ (see fig. 3.1).

Typical values for the end- and rf-voltages are $U_{end} = 1 - 15$ V and $U_{rf} =$
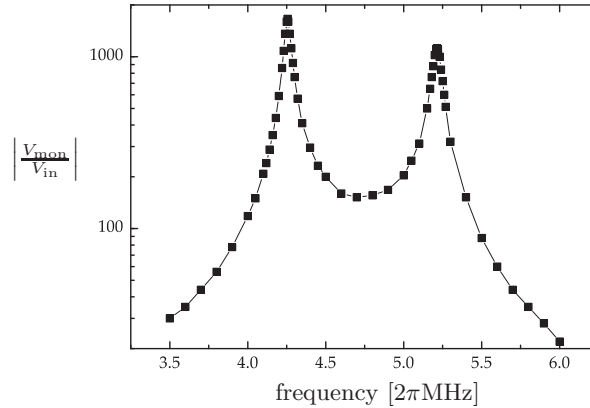
Figure 6.8: Ratio of trap voltage to input voltage versus rf-frequency.

$150 - 400$ V, corresponding to axial and radial trap frequencies in the range of $\sim 2\pi \times 80 - 300$ kHz and $2\pi \times 200 - 800$ kHz, respectively.

6.4 Ion imaging and detection system

The ions are detected by measuring the fluorescence they emit when scattering photons during the cooling cycle. Two camera systems are available to image the ions by collecting this fluorescence and, in this way, we can produce images of the ions from two directions. In addition, a photo-multiplier tube (PMT) produces a signal proportional to the fluorescence rate of the ions, which is very convenient when optimizing e.g. laser detunings for laser cooling. Fig. 6.9 shows a drawing of the entire setup.

The camera system that takes images along the y-axis is the highest resolution imaging system and most of the images presented in this thesis have been produced with it. An achromatic lens with a focal length of 75 mm is located outside the vacuum chamber about 8 cm above the trap center and collects the light scattered by the ions. This is imaged with a $\times 10$ magnification onto an image intensifier and finally onto a charge coupled device (CCD) camera by an objective lens with a magnification of $\frac{1}{2}$, which results in an overall magnification of 5. The CCD camera has a pixel size of 9.9 μm $\times$ 9.9 μm and each pixel thus corresponds to about 2 μm $\times$ 2 μm.

Directly in front of the lens an iris diaphragm is inserted to minimize background light due to Rayleigh scattering from the 397 nm cooling beams passing through the mirror substrates. With a resulting numerical aperture NA $\simeq 0.06$, the iris is the limiting factor in the resolving power of the imaging system, which is then calculated to [137]

$$\text{Res} = 1.22\frac{\lambda}{2\text{NA}} = 1.22 \times \frac{397 \text{ nm}}{2 \times 0.06} \simeq 4 \ \mu\text{m}. \tag{6.1}$$

The pixel size in the recorded images is calibrated from images of the (80 ± 1) μm wide optical fiber, shown in fig. 6.4a). Fig. 6.10 shows such an image where the fiber has been moved into the center of the trap and illuminated with the 397 nm beams.
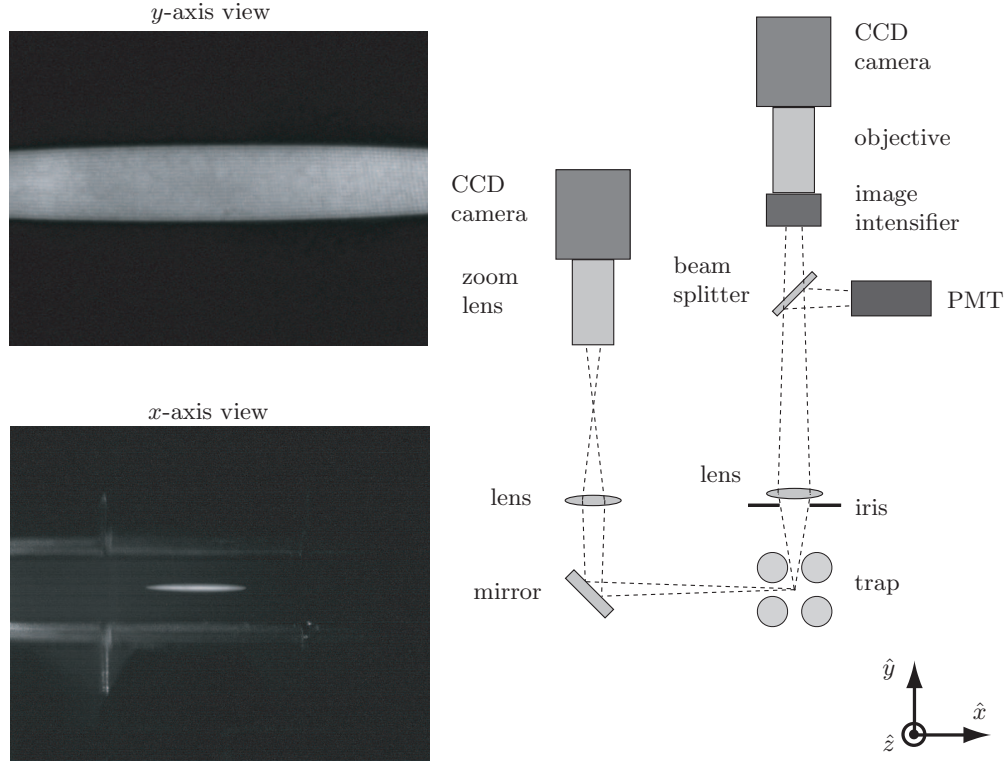
Figure 6.9: Drawing of the camera and PMT setup. The images shows the same crystal viewed along the y-axis with a magnification of 5 and along the x-axis with a magnification that can be varied from 1-3. See text for details.

From this we find a value for the pixel size of (1.98 ± 0.05) μm in accordance with the value expected from the magnification of the imaging system.

A special feature of this imaging system is the image intensifier. It consists of a photocathode, from which electrons are emitted as a result of the incident light. These electrons are then accelerated and amplified through two micro channel plates before producing a fluorescent image on a phosphor screen. It is this image that is imaged by the objective onto the CCD camera. The fact that the signal is dependent on the acceleration voltage after the photocathode means that gating this voltage will allow for production of image sequences of very high time resolution. In this way a time resolution of 20 ns can be achieved.

The camera system that records images from the side along the x-axis is used mainly for determining the length of crystals that exceed the field of view of the first camera system and for determining the location of the crystals in the xz-plane. However, due to geometric constraints imposed by the dimensions of the vacuum chamber and the surrounding optics, the numerical aperture of this imaging system is considerably lower and only low resolution images can be produced. Nevertheless, for determining e.g. the length of mm long crystals it is sufficiently accurate with typical pixel sizes around 10 μm, depending on the magnification set by the zoom
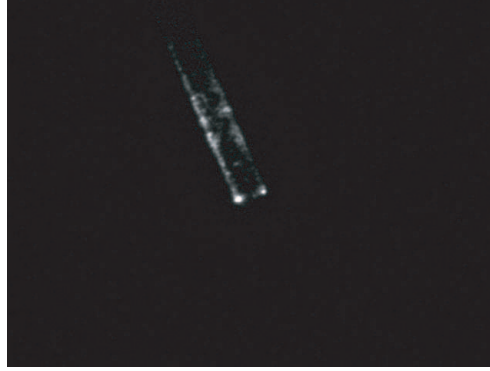
Figure 6.10: Fiber inside the center of the trap (width= 80 μm). This is used for calibration of the pixel size as well as for alignment of the laser beams. The entire image corresponds to the 640×480 pixels of the CCD camera.

lens. Another advantage of having two cameras is that it allows us to take images with a high magnification and a resolution that reveals the crystal structure, while at the same time taking images of the entire trapping region.

6.5 Magnetic field compensation and control

In all experiments it will be important to have a well-defined quantization axis. It is generally chosen to be along the cavity axis, as circularly polarized light will then be a well-defined polarization when propagating in this direction. This quantization axis is defined by an external magnetic field that is created by two current loops in a Helmholtz configuration. However, the earth magnetic field is also present and has a strength of about 0.5 Gauss along the y-axis. This means that in order to define the quantization axis along z better than 1 %, a magnetic field of about 50 Gauss must be applied in this direction. As our magnetic field coils are outside the vacuum chamber (about 30 cm from the ions) this can be a bit demanding from a technical point of view and, in addition, it will lead to a substantial Zeeman splitting of the energy levels, which may not be desirable in all experiments.

Instead, we compensate the magnetic field along the directions perpendicular to the quantization axis using two additional pairs of current coils, also set up outside the vacuum chamber in a Helmholtz configuration. On account of the orientation of the trap with respect to the earth magnetic field, the magnetic field along the x-direction is negligible and we only need to consider the y-direction. We compensate the earth magnetic field along this direction, by trapping and cooling the ions with the 866 nm repumper sent in along the x-axis and polarized along z as shown in fig. 6.11. When the quantization axis coincides with the z-axis, the 866 nm field drives only π-transitions on the $D_{3/2} \rightarrow P_{1/2}$ transition. As a result, the ions accumulate in the $D_{3/2}, m_J = \pm\frac{1}{2}$ states outside the cooling cycle, where they do not scatter any photons, and the fluorescence drops accordingly. Fig. 6.12 shows the result of such a measurement where a magnetic field of about 3 Gauss is applied along the z-direction and the magnetic field along y is varied. The plot shows the fluorescence from the
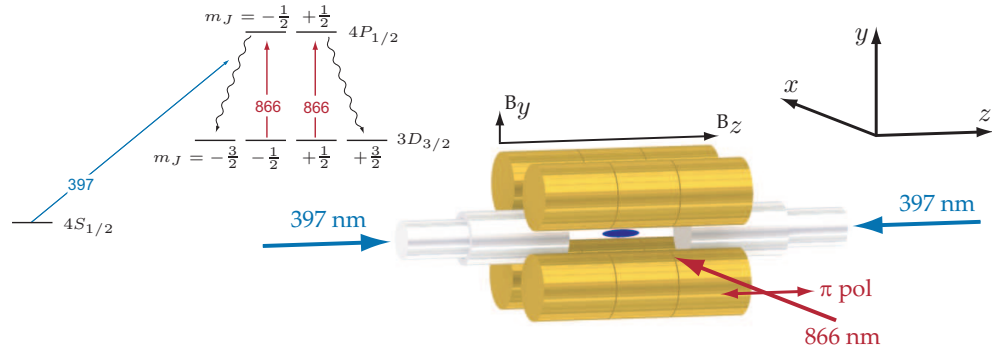
Figure 6.11: Setup for testing compensation of the earth's magnetic field. The magnetic field along y is varied until the quantization axis, defined by the total magnetic field, is along z at which point only π-transitions are driven on the $D_{3/2} \to P_{1/2}$ transition. The ions then accumulate in the $D_{3/2}, m_J = \pm\frac{1}{2}$ states.

ions versus the current in the coils defining the magnetic field along the y-axis and from this we find that the magnetic field along y is most efficiently compensated for $I_y = (-0.10 \pm 0.01)$ Amps, which does indeed correspond to applying a field of about 0.5 Gauss, given the coil configuration.

6.6   The optical resonator

In this section we characterize the cavity in the linear Paul trap and present measurements of its FSR, finesse and intra-cavity losses. The equations derived in ch. 2.2 will serve as the theoretical background for the analysis of these measurements.

Furthermore, we will describe the cavity detection system and the measurement schemes employed in our experiments.

6.6.1   Cavity characterization

Fig. 6.13 shows the spectrum of the trap cavity[7] at 866 nm, when scanning across one FSR using the PZTs. Higher-order transverse modes are barely visible in the scan, and the cavity is mode matched such that 98% of the power is coupled into the fundamental TEM$_{00}$ mode. To measure the FSR of the trap cavity, we scan the frequency of the laser over one FSR of the trap cavity and count the number of FSR of a reference cavity with a known and smaller FSR. The reference cavity we use for this is one of the stabilized reference cavities described in ch. 5.5, which has FSR= 596 MHz, and we count (21.3 ± 0.5) FSR for one FSR of the trap cavity, corresponding (12.7 ± 0.3) GHz. The measurement was repeated by scanning the frequency both up

---

[7]Whenever ambiguity is possible, we shall refer to the cavity incorporated into the trap as the trap cavity to distinguish it from e.g. the stabilized reference cavities.
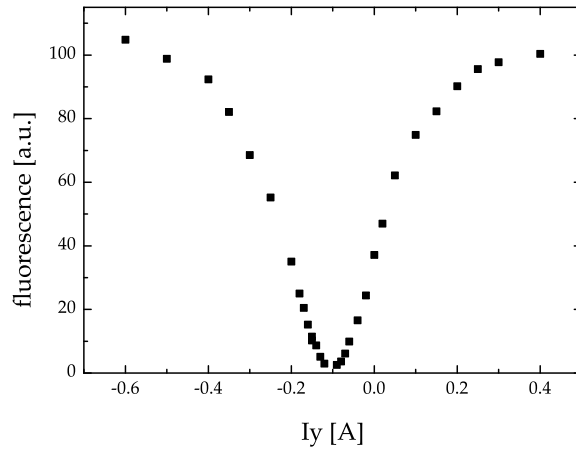
Figure 6.12: Variation in fluorescence with current for magnetic field coils along y A magnetic field of about 3 Gauss is applied along the z-axis which defines the quantization axis. See text for details.

and then down to check if either of the cavities had drifted during the measurement. Relating the FSR to the length via FSR=$\frac{c}{2L}$, we find that the trap cavity is (11.8 ± 0.3) mm long.

Fig. 6.14a) shows a scan around the cavity resonance, when the 866 nm light is modulated at 5.4 MHz with an EOM. The resulting sidebands provide a frequency calibration (see insert fig. 6.14a)) and from a multi-pole Lorentzian fit we deduce a cavity width of FWHM= (3.1 ± 0.1) MHz, corresponding a cavity decay rate of about $2\pi\times1.6$ MHz. From eq. 2.26 the finesse is found to be $\mathcal{F} = 4100\pm100$, which assuming mirror transmissions of 1500 and 5 ppm for the input coupler and the high reflector, respectively, corresponds to intra-cavity losses of (30 ± 30) ppm. This is consistent with the value deduced from the reflection signal (fig. 6.14b)), using eq. 2.29, of about 50 ppm.

As already mentioned in ch. 6.2, during the degassing of the ion pump, the mirrors were contaminated and the finesse was lowered as a result thereof. By an analysis similar to the one given above, the finesse after this incident was found to be ~ 3300 and the losses were evaluated to ~ 400 ppm. Since then, we have observed a slow increase in the losses over time. In terms of hours of running the experiment with the oven turned on, we estimate this increase to be about 0.1 ppm/hour. Fig. 6.15 shows the cavity transmission and reflection at the time of writing. At this time we did not have an EOM available for phase modulation of the input beam and the laser current was modulated instead. Only first order sidebands are resolved, which, nevertheless, this still suffices for a frequency calibration. From the multi-pole Lorentzian fit shown in fig. 6.15a) the width is found to be (4.2 ± 0.2) MHz, corresponding to a cavity finesse of 3000 ± 200. Fig. 6.15b) shows the reflection signal
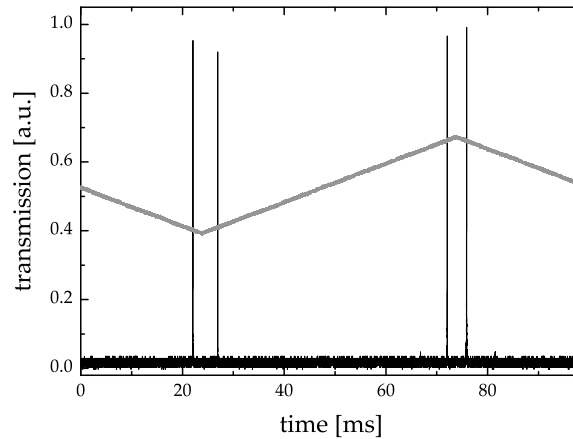
Figure 6.13: Transmission of the cavity when scanning the cavity over more than one FSR. Higher order modes are barely visible and constitute less than 2% of the total power coupled into the cavity. Also shown is the scan signal sent to the PZTs (gray line).

which is seen to extend significantly further towards zero on resonance due to the increased intra-cavity losses. The value for these losses derived from the reflection signal is about 600 ppm, in agreement with the finesse of 3000 found from the cavity width.

Regrettably, the source of the increase in the losses since the bake-out is still unknown to us. As mentioned in ch. 6.2, the background pressure in the vacuum chamber after the bake-out was around $\sim 3.5 \times 10^{-9}$ mbar when the oven was on and has since then dropped by an order of magnitude to around $\sim 3 \times 10^{-10}$ mbar. Although difficult to evaluate, this seems too low to contribute significantly to the increased intra-cavity losses and indeed, no correlation between the pressure value and the contamination rate has been observed. The oven beam might also contribute, although, first, it should in principle be sufficiently narrow to pass through the trap and, second, the mirror coats, seen e.g. in fig. 6.1, provide further protection from the oven beam as they extend further out than the mirrors themselves. Nevertheless, we can not rule this out at present. Finally, there is the possibility that ions lost from the trap during experiments may have contributed to the mirror contamination. In certain experiments performed to characterize the trap, ions were often lost at low axial- and high radial potential, meaning they would preferentially move in the direction of the mirrors when lost. However, no systematic data on the finesse during these experiments is available and the source of the slow increase in losses over time remains an issue for further studies.

The cavity width of FWHM= (4.2 ± 0.2) MHz corresponds to a cavity decay rate of $\kappa = (2.1 \pm 0.1)$ MHz. Although this increase is unfortunate, from the point of view of entering the regime of strong collective coupling, it is by no means critical.
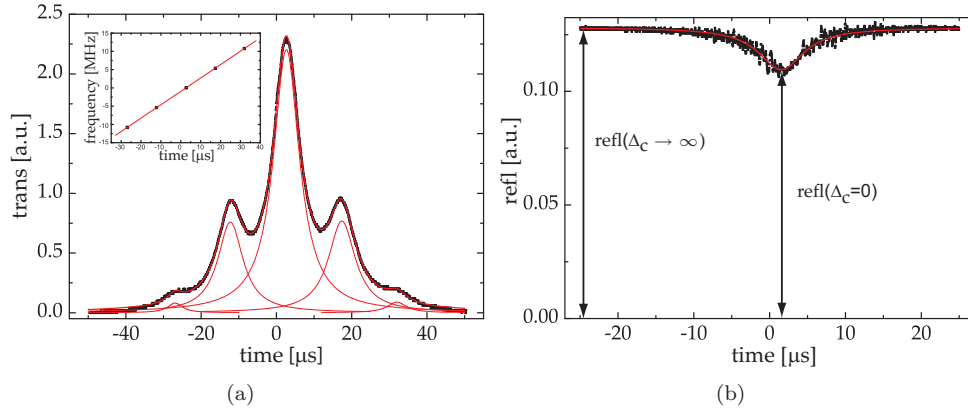
Figure 6.14: a) Transmission signal of the cavity for an input field modulated at 5.4 MHz with an EOM. The insert shows the position of the peaks found from a multi-pole Lorentzian fit. The slope of the linear fit is $\simeq 0.37$ MHz/µs and this is used for a frequency calibration of the scan. The width of the center peak is 3.1 ± 0.1 MHz. b) Reflection signal without modulation. From the ratio of refl($\Delta_c = 0$) and refl($\Delta_c \to \infty$) the intra-cavity losses are found to be 50 ppm (eq. 2.29).

Basically, the result of having 600 ppm losses is that only about 70% of the intra cavity photons will be available for detection (mirror transmission 1500 ppm) and with an overall detection efficiency of $\simeq 16\%$ for the photons leaving the cavity (see ch. 6.6.2), these losses actually makes little difference. This incidentally illustrates how the experiment has been simplyfied by using a longer cavity with a moderate finesse. Had it been necessary to use an extremely high finesse cavity with mirror transmission coefficients of, e.g. 15 and 5 ppm, zero intra-cavity losses would result in a finesse of > 300.000 and we would still get at most 75% of the photons out in one end of the cavity. For such a cavity, 600 ppm losses would be absolutely devastating. The finesse would be lowered to $\simeq 10.000$ and only about 2% of the photons would leak out of the cavity for us to detect.

6.6.2 Cavity detection system

The cavity spectra shown in the previous section (fig. 6.14 and fig. 6.15) were recorded by sending ~ 1 mW power to the cavity and detecting the transmitted and reflected signal with standard silicium photodiodes. In later experiments we will study the interaction of the cavity field and the ion Coulomb crystal at the single photon level and the cavity signal will therefore be significantly weaker. With an average photon number of 1 inside the cavity, the number of photons leaking out of the cavity per second is given by the decay rate of the mirror. We will always be detecting the photons on the side with the higher transmission to get the most signal, both when probing transmission and reflection. When probing e.g. reflection we will thus send in the probe from the partial reflector side. From eq. 2.23 we find that to have on average a single photon in the cavity ($|A|^2 = 1$) on resonance, the number of photons

(a)   (b)
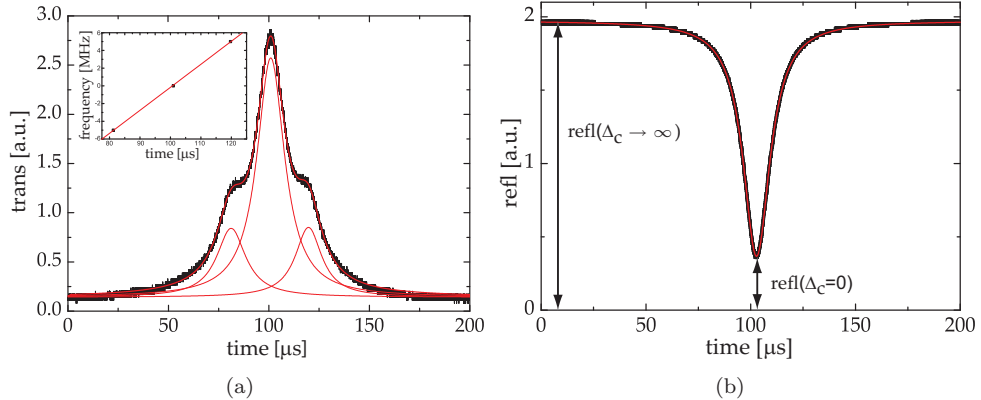
Figure 6.15: a) Transmission signal of the cavity for an input field modulated at 5.0 MHz by modulating the laser current. The insert shows the position of the peaks found from a multi-pole Lorentzian fit (red curve in main graph). The slope of the linear fit is $\simeq 0.26$ MHz/μs and this is used for a frequency calibration of the scan. The width of the center peak is 4.2 ± 0.2 MHz. b) Reflection signal without modulation. From the ratio of refl($\Delta_c = 0$) and refl($\Delta_c \rightarrow \infty$) the intra-cavity losses are found to be 600 ppm (eq. 2.29). Both graph were produced at the time of writing (after $\simeq 2000$ hours of operation) and clearly shows the increase in the intra-cavity losses.

sent to the cavity should be

$$
\begin{aligned}
|A|^2 &= \frac{\left(\kappa_1 + \kappa_2 + \frac{\mathcal{L}}{2\tau}\right)^2}{2\kappa_1} |A|^2 \\
&= \frac{(2\pi \times 2.1 \text{ MHz})^2}{2 \times 2\pi \times 1.5 \text{ MHz}} \times 1 \text{ photon} \simeq 9.2 \times 10^6 \text{ photons/s},
\end{aligned}
$$

which means that off resonance, about 9 million photons are reflected every second, corresponding to a mere 2 *pico*watts at 866 nm for us to detect.[8] Furthermore, if we want a time resolution of e.g. 1 μs, only 9 photons are available for detection and single photon detectors are therefore a requirement.

We use two avalanche photo detectors (APDs) to measure both the transmitted and the reflected photons. In most of the experiments within this thesis, we have coupled the 866 nm light in from the side with the partial transmitter ($T = 1500$ ppm) and measured the reflection signal, as shown in fig. 6.16.[9] As mentioned previously, an 894 nm laser is used to lock the cavity and to monitor its drifts and vibrations. This laser is coupled in along with the 866 nm probe laser and the reflected field thus consists of both 866 nm and 894 nm photons. Since the 894 nm beam is used for locking the cavity, it is much stronger than the 866 nm probe beam and must be

---

[8]In transmission, that is, injecting from the high reflector side and detecting on the partial reflector side, the number of photons, leaving the cavity through the partial transmitter for detection, is about 18.8 million per second, when there is a single photon in the cavity on average.

[9]In the setup as it is drawn in fig. 6.16, the 866 nm beam probes the reflection spectrum of the cavity, however, we also have the possibility of coupling the 866 nm beam in from the side of the cavity with the high reflector ($T = 5$ ppm), and probe the transmission spectrum of the cavity.

filtered out before the 866 nm APD. A half-wave plate for 866 nm, that does not have an effect on the polarization of the 894 nm field, and a polarizing beam splitter (PBS) provides an extinction of the 894 nm photons of about 20 dB. This also allows the 894 nm beam to be sent to a silicium photodetector that is used for locking the cavity (see ch. 6.6.3). After the PBS, a grating (1800 l/mm) then separates the 866 nm and the 894 nm beams, spatially, which in combination with a SM fiber further minimizes the amount of 894 nm photons that reach the 866 nm APD. The fiber coupler and the APD are covered by black plastic and the SM fiber is wrapped in a black rubber tube to avoid detection of room light photons. A symmetrical setup detects the 894 nm photons on the opposite side of the cavity and provides for monitoring of the cavity drift and vibrations. We shall describe how this is done in practice in ch. 6.6.3

As mentioned in ch. 5 we use ar-coated laser diodes for both the 866 nm and the 894 nm lasers. These have gain profiles that are several tens of nm wide and for this reason, there will always be photons at wavelengths far from the laser line due to amplified spontaneous emission. In general, this is not a problem but for the 894 nm laser it means that there are still some photons at 866 nm in the beam and since our detection setup relies on efficiently guiding all the 866 nm photons to the 866 nm APD, the 866 nm photons in the 894 nm beam will also be detected. To prevent the locking laser from interfering with the ions, a grating is set up before the fiber incoupling for the 894 nm laser, similar to the grating setup before the APDs. With this addition, $\sim$mW 894 nm light can be sent to the cavity without being detected by the 866 nm APD.

Table 6.2 summarizes the photon collection budget. In total we detect about 16 % of all 866 nm photons leaving the cavity through the partially reflecting mirror. The losses originate from the optics, the grating used to filter out 894 nm photons, the
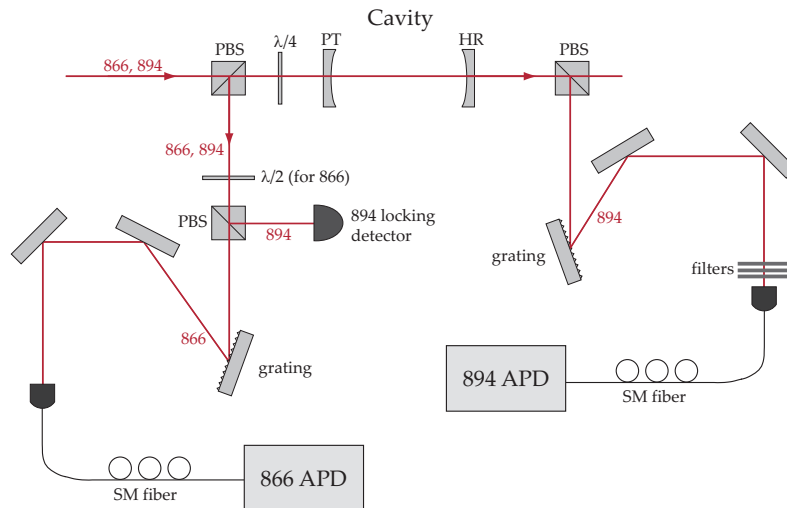
Figure 6.16: Schematic of the setup for single photon detection of 866 nm and 894 nm photons. HR: high reflector ($T = 5$ ppm), PT: partial transmitter ($T = 1500$ ppm). The filters in front of the SM fiber for the 894 nm APD are needed to avoid saturating the APD. See text for further details.

coupling to the SM fiber and the detection efficiency of the APD.

optics	grating	SM fiber	APD	total
90%	63%	65%	44%	16%

Table 6.2: 866 nm photon collection budget.

6.6.3 Locking vs. scanning

We have mentioned several times already that we have the possibility to either lock the cavity to the 894 nm laser or to scan the cavity using the PZTs and then use the 894 nm laser to monitor drifts and vibration of the cavity. In the following we shall describe both schemes.

6.6.3.1 Locking the cavity

Locking scheme

To control the cavity detuning Δ_c with respect to the 866 probe laser we require a scheme for controlling the length of the cavity. The FSR of the cavity is, as we have seen above, 12.7 GHz. Scanning the cavity length across one FSR in a standing wave cavity corresponds to a change in length of $\lambda/2 = 433$ nm and from this we find that the cavity length only changes by $\simeq 0.14$ nm across the 4.2 MHz resonance at 866 nm. Clearly, some form of active stabilization of the cavity length is needed to control Δ_c with a precision better than the cavity width.

To this end we employ the 894 nm laser described in ch. 5.3. The cavity mirrors are still highly reflecting at 894 nm and for this reason the cavity width at 894 nm is still sufficiently narrow. With the additional 600 ppm losses the finesse at 894 nm is around 1800, corresponding to a width of about 7 MHz. At the same time, the wavelength of 894 nm is sufficiently far from the atomic resonance that enough power can be sent into the cavity for the lock to work, without perturbing the Ca$^+$ ions. In practice we only require ~ 10 μW for the cavity lock and with a build-up factor around 1000 at 894 nm this corresponds to a saturation parameter (eq. 2.16) of only $s \sim \frac{\Omega^2}{\Delta^2} \sim 10^{-7}$ at 894 nm for the $D_{3/2} \leftrightarrow P_{1/2}$ transition. The light shift is of the order of $\sim \frac{\Omega^2}{\Delta} \sim 0.1$ MHz, however, if the power is stable, this will only give a constant shift of the resonance and not have any real effect on the experiments. Should the power of the 894 nm field inside the cavity change, the light shift will of cause vary accordingly. However, the shift should be compared with the $\simeq 23$ MHz wide $D_{3/2} \leftrightarrow P_{1/2}$ transition and minor fluctuations will thus have negligible effect.

In an ideal setup the cavity should be locked to an atomic transition. This could in principle be done by locking the 894 nm laser to the D1-line in atomic cesium and then locking the cavity to the 894 nm laser. A problem then arises when tuning the cavity to resonance with the probe at 866 nm: since the frequency of the 866 nm probe is set by the $3D_{3/2} \leftrightarrow 4P_{1/2}$ transition of ^{40}Ca$^+$ it might not be possible to make the cavity resonant with it. In a worst case scenario the two lasers could be

separated by half the FSR of the cavity corresponding to about 6.4 GHz.[10] This is far beyond the tuning range of commercially available AOMs and in our present setup for the 866 and 894 nm lasers these only have a tuning range of ±100 MHz.

To avoid this scenario, we use a temperature stabilized reference cavity (see ch. 5.5) with a FSR of only 600 MHz. This gives us a comb of frequencies separated by 600 MHz to lock the 894 nm laser to. It will then always be possible to find a mode to lock the 894 nm laser to, such that when the cavity is subsequently locked to this laser, the 866 nm laser will be at most 300 MHz out of resonance with the cavity.[11]

By also locking the 866 nm laser to the same reference cavity, the cavity and the 866 nm probe laser are effectively fixed with respect to each other. Relative detuning of the cavity with respect to the 866 nm laser and of the 866 nm laser with respect the $3D_{3/2} \leftrightarrow 4P_{1/2}$ transition of Ca$^+$ is then accomplished through the AOMs in the setup for these lasers (see ch. 5.2). Fig. 6.17 shows a schematic of the entire setup. One drawback of this scheme is that if the reference cavity itself drifts, the two lasers will drift relative to the $3D_{3/2} \leftrightarrow 4P_{1/2}$ transition of ^{40}Ca$^+$. As mentioned previously, this drift has been measured to be < 1 MHz/hour.[12]

Locking the cavity

Fig. 6.18a) show the reflection of the 866 nm probe (black data) when the cavity is locked and the the 866 nm probe resonant with it, as well as the transmission of the 894 nm locking laser (gray data). Both signals are recorded using the APD setup shown in fig. 6.16. Clearly there is a lot of noise and an analysis of the mechanical spectrum of the cavity has revealed several resonances at relatively low frequencies. By scanning the cavity with a sine function and varying the frequency, these me-

---

[10] In principle one has the possibility to shift by the Cs ground state hyperfine splitting of 9.2 GHz, making the worst case scenario ≃ 2.8 GHz.

[11] For the FSR of 12.7 GHz it is actually better than that. Since there are $\frac{12.7}{0.6} \simeq 21.2$ FSR of the stabilized reference cavity across one FSR of the cavity in the trap, the worst case scenario is only 0.2×600 MHz= 120 MHz.

[12] We have recently constructed a 852 nm laser with the purpose of locking the reference cavity to this laser. The 852 nm laser can then be locked to the D2-line of atomic cesium and the 866 nm probe laser and the 894 nm locking laser will then be referenced to an atomic transition via the reference cavity.
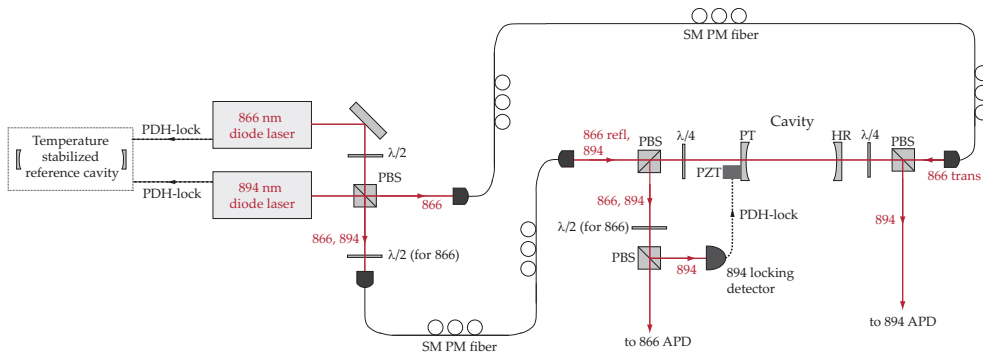
Figure 6.17: Schematic of the setup for locking the cavity and the cavity probe laser to the same reference.
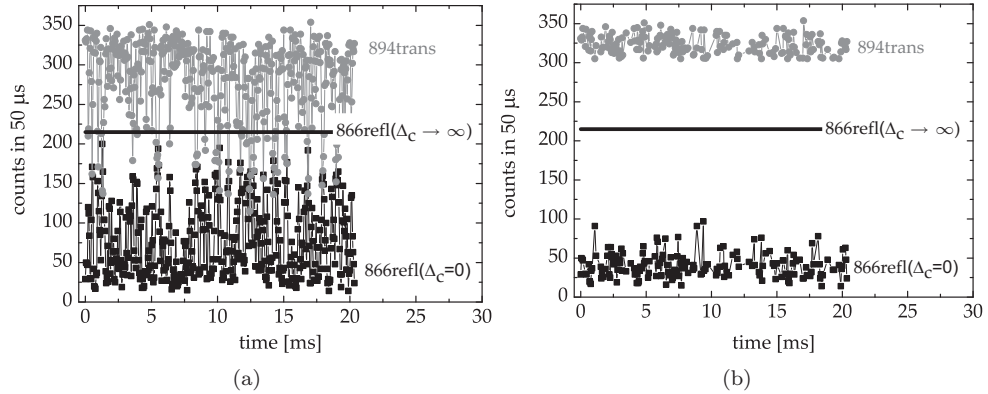
Figure 6.18: a) APD counts pr 50 μs bin when the cavity is locked to the 894 nm laser, the 866 nm laser is resonant with the cavity and both lasers are locked to the temperature stabilized reference cavity. Gray circles are the transmission signal of the 894 nm laser, whereas the black squares are the reflection signal of the 866 nm laser. The black horizontal line at 215 counts pr bin indicates the level of the 866 nm reflection signal when the cavity is off-resonant with it. b) "Cleaned" data. The threshold for the 894 signal is set to 305 counts pr bin.

chanical resonances of the cavity can be mapped out. Their exact locations have been found to vary slightly depending on the position in the PZT-scan, however, we typically observe pronounced resonances around 400 Hz and 2000 Hz in addition to some minor, less critical resonances in between and at higher frequencies.[13] As these resonances are in the acoustic range, background noise from pumps etc. in the laboratory are expected to drive vibrations at these frequencies which due to their resonant nature makes them difficult to compensate by electronic feedback to the PZTs. Feedback is further complicated by the phase-shifts required around the mechanical resonances in order to avoid driving rather than damping the vibrations. In principle compensation is possible if one constructs a feedback circuit that allows for individual adjustment of both phase and amplitude around all resonances, however, in practice it is an extremely difficult task, which is further complicated by the fact that the resonances do not always appear at exactly the same frequencies. The signals shown in fig. 6.18a) are actually the result of an optimized feedback system consisting of a low frequency ($<$400 Hz) and a high frequency feedback as well as high Q filters around the resonances where a carefully tailored feedback is applied.

Even so, the locking signal in fig. 6.18a) is still far from satisfactory and must be improved. One way around the proplem is to make use of the fact that the noise in the two signals (866 probe and 894 reference) originates from the same acoustic noise and is, thus, correlated in time. The signals can then be cleaned as shown in fig. 6.18b). Here the 894 signal is used to to monitor the acoustic noise and when this noise causes the 894 nm level to drop below a certain threshold value (here 305 counts pr. bin) the points in both the 894 and the 866 data are removed. The higher we set

---

[13]These low frequency resonances are suspected to originate from the relatively massive PZT-plate (see fig. 6.2). Plans for a smaller PZT mirror mount as well as passive damping in order to minimize the sensitivity to acoustic noise, in future versions of the trap, are underway.

this threshold, the closer the 866 nm probe signal comes to the on-resonance level, expected from the intra-cavity losses and mirror transmission. For 600 ppm losses and 1500 ppm transmission, this level should be $\simeq 18$ % of the off-resonance level (c.f. eq. 2.29). From fig. 6.18b) we evaluate this to be $\frac{40}{215} \simeq 19$ %. The trade-off inherent in this method is that we get less data points for the same measurement time, which means that a longer measurement time is needed to acquire the same statistics.

In many of our experiments, the parameter of interest will be the cavity width (see ch. 2.3). One way to measure this is by varying the probe detuning Δ when the cavity is locked and recording the reflection level for each value of Δ. Fig. 6.19 shows the results of such measurements for increasing values of the threshold used for the data cleaning. Fig. 6.19a) is a plot of the data for four different threshold values including their corresponding Lorentzian fits. The cavity width (fig. 6.19b)) is seen to approach the dashed line indicating $2\pi \times 4.2$ MHz corresponding to the value deduced from the cavity losses in ch. 6.6.1. The increasing error bars reflect the fact that less points are available for the fit as the threshold is increased.

6.6.3.2   Scanning the cavity

An alternative to the locking scheme described above is to scan the cavity by applying a ramp voltage to the PZTs. Since the amplitude of the acoustic noise is still significant on a kHz scale, the scan should be done considerably faster than a ms and we should allow ourselves at most a few hundred μs to record the cavity spectrum. In many experiments it is even necessary to reduce the probe time, i.e. the bin-time of the 866 nm ADP system, to about 1 μs. As mentioned in the discussion of the cavity detection system (see ch. 6.6.2), with an average intra-cavity photon number of 1, only about 9 photons will be leaving the cavity within a μs and, of these, only 16 % are detected. To produce a cavity spectrum thus requires averaging several scans.

(a)   (b)
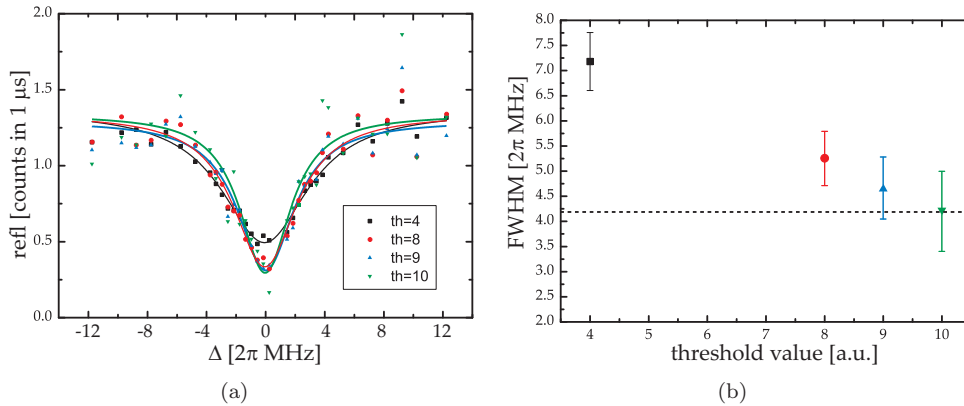
Figure 6.19: a) Reflection spectrum of cavity versus detuning of the probe laser when the data has been "cleaned" as in fig. 6.18. th is the threshold level of the 894 transmission in counts pr. bin. b) FWHM of the reflection signal found from Lorentzian fits to the data in a) as a function of increasing threshold in the data cleaning. The dashed line indicate the value expected the analysis of ch. 6.6.1.

Due to acoustic noise in the system, the spectra recorded at different times are, however, not correlated in the sense that the peak might appear at different times in the scan as the cavity is not locked to a specific length. In other words, the timebase is shifted from one scan to the next. This means that if we try to average over many scans, the peak will be smeared out and the value deduced for the cavity width will be artificially broadened.

This noise induced broadening of the cavity width can be avoided by simultaneously recording a scan for the transmission of the 894 nm beam. As for the cleaning in the locking scheme described above, we may assume that if the two lasers are resonant with the cavity at the same time, the noise in their spectra due to vibrations will be correlated. To obtain a correct average of the 866 nm reflection signal, we therefore compare the location of the 894 nm peak in each scan with the location in the first scan of the data set and shift the time-base accordingly. In a manner of speaking, the locking of the cavity is done post-detection wise: the analysis of the 894 spectrum provides an error signal that shifts the timebase of the 866 spectrum. The basic principle is illustrated in fig. 6.20. After the averaging is done, the timebase in the averaged spectrum is shifted in accordance with the average value of the 894 nm peak position during the entire averaging period.

Note that this referenced averaging can not be accomplished via analysis of the 866 nm signal alone for two reasons. First of all, the resonance of this may be shifted due to the interaction with the ions, and second of all, the 866 signal is too weak to provide any information about the location of the resonance based on a single scan. This is clearly seen in fig. 6.21a) which shows the cavity reflection spectrum when probed at 866 nm after just a single scan. The y-axis displays the counts per bin and, as expected for a single photon detection system, the data only has integer values, which means that for an average value of 2 counts per bin, no structure can be resolved. Fig. 6.21b)-f) shows the resulting reflection spectrum in order of increasing number of averages. 100 scans were averaged to produce fig. 6.21f) which takes about 3 seconds in total.

As a test of the averaging system we evaluate the cavity width for different number
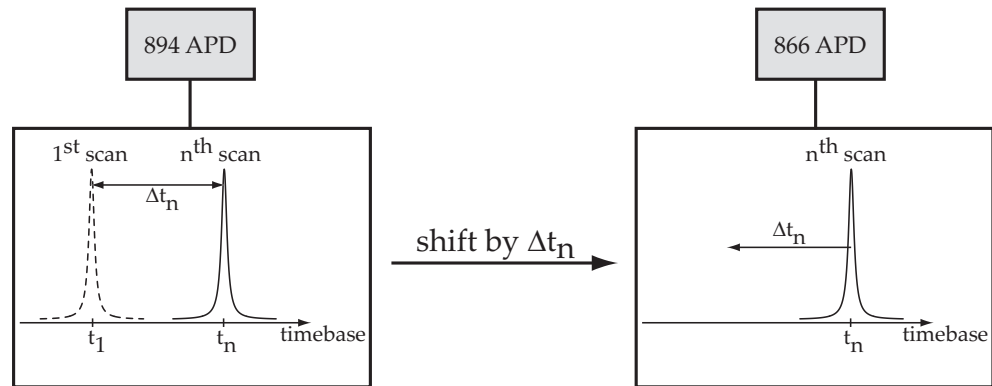
Figure 6.20: Illustration of the principle behind the averaging scheme. Gray peaks correspond to individual scan results while the black curve represents their average. See text for details.
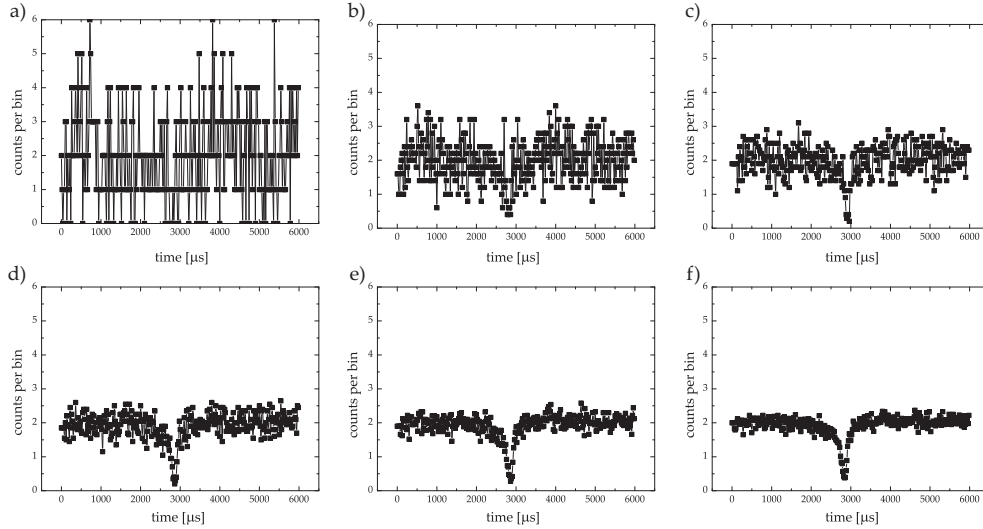
Figure 6.21: Cavity reflection scans after averaging. Number of averages: a) 1, b) 5, c) 10, d) 20, e) 50 and f) 100.

of averages. Fig. 6.22 shows the cavity width (FWHM) versus number of averages found from Lorentzian fits to scans such as those of fig. 6.21. The error bars indicate the uncertainty in the width derived from the fit, which as expected decreases with increasing number of averages.

There is, however, an additional effect that contributes to the final value for the uncertainty. In appendix H we account for the spread in repeated measurements, where we have found that there is a systematic effect on the width that we ascribe to the acoustic noise. In brief, we observe experimentally that the uncertainty in our measurements depends on the time it takes to scan across the peak in the experiment. This uncertainty is included in the evaluation of the data via the methods described in appendix H.

6.7 Experimental control system

The entire experiment is controlled by a LabVIEW software, which handles both acousto-optic shutters and frequency shifters for the lasers, the data acquisition via the PMT and the APDs as well as subsequent averaging and cleaning of the data. Two synchronized counter/timer cards[14] are used to interface the various hardware with the experimental control software for the computer. This allows for control of the various laser beams and the readout of the APD signals with a precision of 0.1 μs (limited by the AOMs rise-time).

A typical experimental sequence is shown schematically in fig. 6.23. It consists of a cooling phase, an optical pumping phase to prepare the ions in the right state (see ch. 9) and a probing phase, which is the actual measurement. The delay between the

---

[14]National Instruments PCI-6602
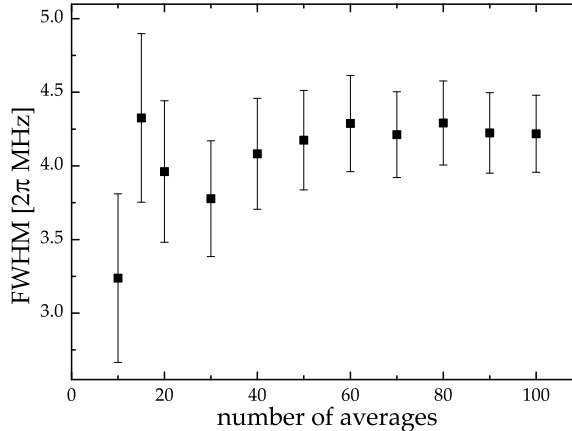
Figure 6.22: Width of the cavity resonance at 866 nm derived from Lorentzian fits to scans such as those of fig. 6.21. The error bars are seen to decrease with increasing number of averages as expected.

probe and the APD is to allow the field to build up and reach steady state inside the optical resonator. We shall return to this in ch. 10. The final result of our measurements is a scan such as those of fig. 6.21 where each point then corresponds to such an experimental sequence.

In our experiments, the cooling and optical pumping time are typically around ~ 10 μs and the probe time ~ 1 μs. We shall return to the experimental sequence and give the exact values in the description of the experiments in ch. 9 and 10.

6.8   Conclusion

This chapter has covered two main aspects of the experimental setup. The design and assembly of the linear Paul trap has been described and in ch. 8 we shall give a characterization of the trap itself based on measurements performed with trapped, cold ions.

The second part of this chapter has revolved around the optical resonator. Two important quantities were measured: the first was the cavity decay rate, which was found to be $\kappa = 2\pi \times (4.2 \pm 0.2)$ MHz. The second was the cavity length of 11.8 ± 0.3 mm from which we can evaluate the single ion coupling strength. From eq. C.12 this is found to be $g = 2\pi \times (0.532 \pm 0.007)$ MHz. These numbers should be compared with the decay rate of the atomic dipole, which for the $D_{3/2} \leftrightarrow P_{1/2}$ transition is $\gamma = 2\pi \times 11.15$ MHz. From the criterion for strong collective coupling $g\sqrt{N} > \kappa, \gamma$ we deduce that about $N \simeq 500$ ions must be confined within the cavity mode volume. We shall examine to what extent this is possible in ch. 8.3.

Toward the end of this chapter we described two different measurement schemes,
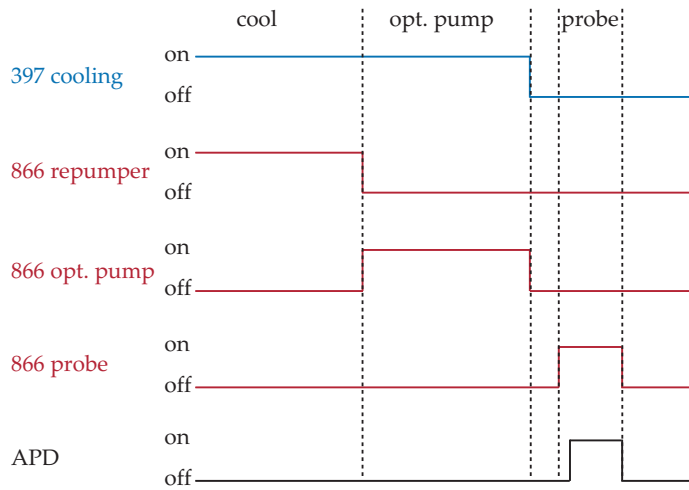
Figure 6.23: Schematic of typical experimental sequence. Opt. pump abbreviates optical pumping. See text for details.

that will both be used in later chapters, along with some methods for circumventing the effects of acoustic noise on the data.

Chapter 7

Loading the trap

In order to efficiently load large crystals into the trap we employ the technique of resonance-enhanced photoionization. Since first demonstrated by our group within this field of physics [111], it has been adopted by many groups, thus expanding the list of ionic atomic species loaded to include Mg^+ [111, 138], Ca^+ [111, 139–142], Sr^+ [143, 144], Cd^+ [145], Ba^+ [146] and Yb^+ [147, 148]. As compared to conventional electron bombardment, this method has several advantages which are all essential to a cavity QED experiment:

- The problem of charging surrounding isolating materials, e.g. mirror substrates, is greatly reduced as only a single electron is produced per ion [111, 143].

- The ionization efficiency can be made much higher, leading to loading rates which are significantly higher than what can be achieved with electron bombardment [142].

- The technique can be extremely isotope selective [149] allowing for loading of different isotopes in well-controlled ratios.

The first point is critical in order to be able to produce nicely shaped crystals that are not perturbed by stray electric fields from locally charged regions in the trap. The second point makes loading at a lower atomic flux practical [139] and thus reduces the risk of contaminating both the trap electrodes and closely spaced delicate objects, such as the mirrors, integrated into the ion trap. Deposition of material on the electrodes is suspected to give rise to heating of the ions [150, 151], which will eventually limit the number of ions that can be confined and crystallized within the cavity mode volume, hence lowering the maximally attainable coupling strength of the crystal-cavity system. Contamination of the mirrors will lower the quality of the resonator and may likewise limit the performance of the system (c.f. ch. 2.3). Finally, the third point must be fulfilled in order to be able to do experiments on two-component ion Coulomb crystals and benefit from the advantages of sympathetic cooling as described in ch. 4.3.

This chapter deals with loading of Ca^+ ions into the cavity trap. The scheme is, as we have already mentioned above, based on resonance-enhanced photoionization of a beam of atomic calcium and we shall begin by a brief review of this scheme in ch. 7.1. A standard loading method employs a small oven, heated to a few hundred degrees

Celsius, to produce the atomic beam and in ch. 7.2 we present results on loading via this method. Recently, we have developed a novel, all-optical loading technique in which the beam of atomic calcium is produced through pulsed laser ablation of a calcium target. This will be the topic of ch. 7.3.

7.1   Isotope selective loading scheme for Ca^+

For production of Ca^+ ions, one strategy has been to use a single UV light source at 272 nm which can lead to two-photon photo-ionization through excitation on the $4s^2{}^1S_0 \rightarrow 4s5p^1P_1$ transition followed by absorption of a second 272 nm photon from either the $4s5p^1P_1$ or the $4s3d^1D_2$ state into the continuum (see fig. 7.1a) [111, 149]. The lifetimes of the $4s5p^1P_1$ and the $4s3d^1D_2$ states are 17-60 ns [152] and 18 ms [153], respectively and the branching ratio for the decay channels of the $4s5p^1P_1$ state is $\sim \frac{1}{54}$ in favor of decay to the metastable $4s3d^1D_2$ state [154]. The three levels form a closed system where, provided that the 272 nm laser is resonant and sufficiently powerful, most of the population will be in the $4s3d^1D_2$ state from where absorption of a second 272 nm photon will ionize the atom.

In an alternative scheme (fig. 7.1b), involving two lasers operating around 423 nm and 390 nm, ionization is achieved via resonant excitation of the $4s^2{}^1S_0 \rightarrow 4s4p^1P_1$ transition (423 nm) followed by excitation to a field ionizing Rydberg state (390 nm) [139, 140]. Originally, this scheme has benefited from using wavelengths which can be provided by commercial violet diode lasers in extended cavities. However, as the production of these lasers has been refined to meet the industrial standard of 405 nm, the 423 nm diodes are no longer commercially available and the simplicity of the
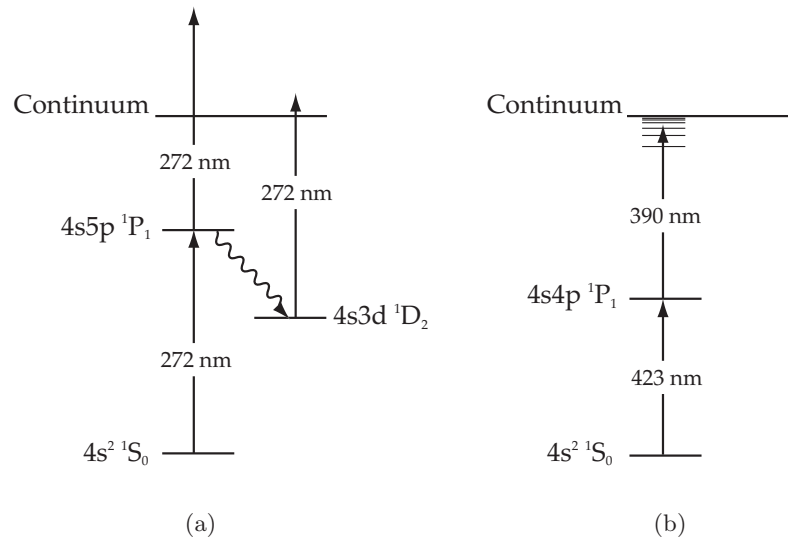
Figure 7.1: a) Two-photon resonant photoionization scheme used in this work. The lifetime of the $4s5p^1P_1$ state is 17-60 ns and the lifetime of the $4s3d^1D_2$ state is about 18 ms. b) Alternative scheme based on diode lasers.

scheme is thus reduced by the addition of frequency doubling of light from diodes operating around 846 nm.

The advantage of using the scheme of fig. 7.1b) over 7.1a) is the higher oscillator strength of the $4s^2{}^1S_0 \rightarrow 4s4p{}^1P_1$ transition as compared to the $4s^2{}^1S_0 \rightarrow 4s5p{}^1P_1$ transition. Combined with the resonant character of the second transition, this gives rise to a higher ion production efficiency.

Both schemes are isotope selective due to the isotope shift on their first transition. However, the degree of selectivity is higher in the scheme of fig. 7.1a) [149] as compared to that of fig. 7.1b) [155], due to a larger isotope shift and narrower linewidth.[1] The enhanced selectivity is highly desired for experiments with two-component ion Coulomb crystals, where the $^{40}Ca^+$ is to be sympathetically cooled by a heavier ionic calcium isotope. In such experiments there should ideally only be enough $^{40}Ca^+$ to fill the cavity mode with the remainder of the ions being of a different isotope that can be Doppler laser cooled.

Ultimately, the ratio in which the various isotopes are produced is limited by the natural abundance of the calcium isotopes (see table 7.1) where ^{40}Ca is by far the most abundant. However, with our loading scheme, the production rate of e.g.

^{40}Ca	^{42}Ca	^{43}Ca	^{44}Ca	^{46}Ca	^{48}Ca
96.941%	0.647%	0.135%	2.086%	0.004%	0.187%

Table 7.1: Natural abundance of calcium. Values are taken from [157].

$^{44}Ca^+$ can still be about three orders of magnitude higher than $^{40}Ca^+$, which is more than adequate in terms of producing two-component ion Coulomb crystals of suitable ratios. Fig. 7.2 shows measurements of the photoionization rate versus the frequency of the 272 nm laser taken in our lab a few years ago [149]. It clearly shows the ability of this scheme to resolve the individual isotopes of calcium. The measurements were done using a laser system based on SHG of light from an Ar-ion pumped dye laser. For the experiments presented in this thesis we have used the 272 nm laser system based on SHG of light from a DFB fiber laser that was described in ch. 5.1.

7.2 Loading the cavity trap I: Oven beam method

7.2.1 Setup

In this section we present results on isotope selective loading of Ca^+ into the cavity trap through photoionization of a beam of atomic calcium produced by a small oven. A picture of the entire setup can be found in fig. 6.4. In fig. 6.4b) a picture of the oven is shown. The thermal beam is produced by resistive heating of metallic calcium inside a small graphite container. Vaporized calcium then effuses through a small aperture in the container and a set of skimmers ensures that the beam occupies a small enough solid angle to pass through the trap without depositing large amounts of calcium. The beam dimensions at the center of the trap are ~ 1.5 mm horizontally

---

[1]Extensions of the scheme of fig. 7.1b) exists, where the second transition from the $4s4p{}^1P_1$ state to the field ionizing Rydberg state at 390 nm is replaced by two or more resonant transitions in the infra-red, which results in even higher isotope selectivity [156].
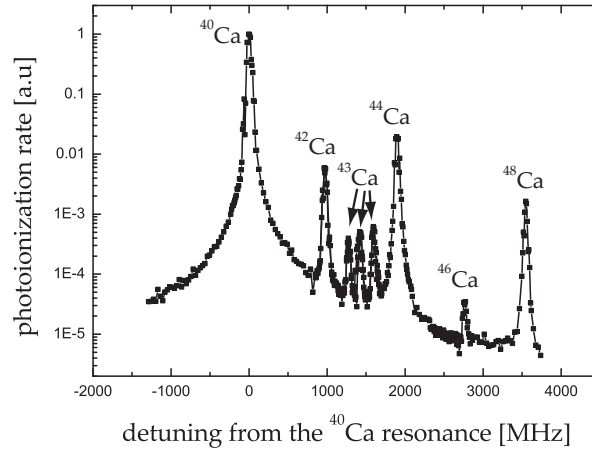
Figure 7.2: Photoionization rate of all naturally abundant calcium isotopes. The three peaks at the ^{43}Ca resonance are due to the nuclear spin of ^{43}Ca of $I = 7/2$ which leads to hyperfine levels of the $4s5p^1P_1$ with total spins $F = 5/2, 7/2$ and $9/2$. The figure is reproduced from the results of [149]. Courtesy of Anders Mortensen.

and ~ 1.0 mm vertically [66]. Here it intersects with the 272 nm beam at an angle of $90°$ in order to minimize Doppler broadening. A schematic drawing of the setup is shown in fig. 7.3

During loading, the 272 nm beam typically has a power of about $10 - 20$ mW and it is focused to a waist of ~ 160 μm at the trap center. The ions produced are then Doppler laser cooled as described in ch. 4.2. Typically, 8-10 mW of 397 nm light detuned by $\sim 20 - 40$ MHz below resonance is used during loading. Both power and detuning are then decreased upon completion of the loading in order to optimize the
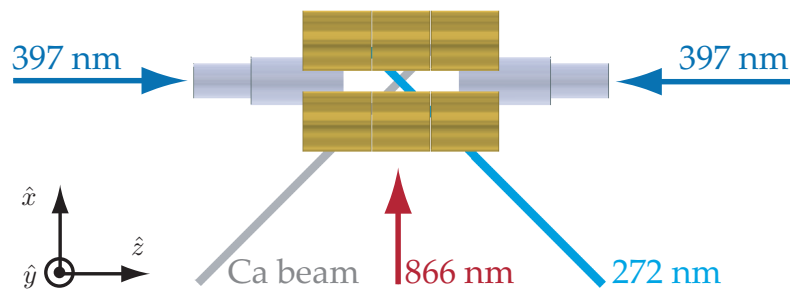
Figure 7.3: Schematic of the setup for loading by photoionization. 397 and 866 nm beams are used for Doppler laser cooling as described in ch. 4.2.

cooling. The number of ions loaded can then be deduced from the recorded images and the trapping parameters. From the recorded images, the crystal volume is found by the method described in appendix B. The density of the ions in the crystal can be evaluated from the results of the zero temperature charged liquid model described in ch. 3.2.1. Specifically through eq. 3.21,

$$\rho_0 = \frac{\epsilon_0 U_{\rm rf}^2}{M r_0^4 \Omega_{\rm rf}^2},$$

the density can be deduced from the value of $U_{\rm rf}$.[2]

7.2.2 Results

Fig. 7.4 shows the number of loaded ions versus time when the frequency of the 272 nm light source is tuned close to the resonance of the $4s^2\ ^1S_0 \rightarrow 4s5p\ ^1P_1$ transition of ^{40}Ca. The end- and rf-voltages were U_{end}=3.9 V and U_{rf}=130 V [3], which corresponds to radial and axial trap frequencies of $\omega_r = 2\pi \times 225$ kHz and $\omega_z = 2\pi \times 160$ kHz, respectively (c.f. eq. 3.10 and 3.12). The oven temperature during the loading sequence was $\simeq 400°$C. As can be seen from the figure, we are able to load in the excess of 3000 ions/s at this relatively low oven temperature. The linear loading rate also shows that even with ~ 50000 ions loaded there is no indication that the trap is saturating and

---

[2]There are various methods for calibrating this density measurement, which will be covered in ch. 8.2.

[3]A relatively low rf-voltage is used during loading to minimize rf-heating, which can make it difficult to crystallize the ions from the thermal beam.
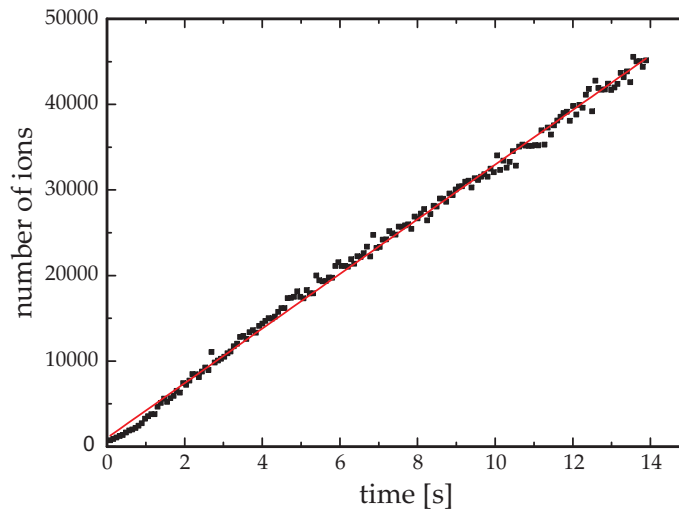
Figure 7.4: Number of ions loaded versus time when the ionization laser frequency is tuned close to the $4s^2\ ^1S_0 \rightarrow 4s5p\ ^1P_1$ transition of ^{40}Ca. The UV-power used for ionization was 20 mW and the oven temperature 400°C. The loading rate deduced from the linear fit is ~ 3200 ions/s.

in principle the line in fig. 7.4 could be extrapolated much further. Due to frequency drifts of the free-running fiber laser, the loading rate was observed to vary on a longer time scale, though. Indeed, under the same conditions as above, the loading rate, when measured every minute for 10 minutes, was found to be 2700 ± 500 ions/s. Active stabilization to e.g. a stable reference cavity, via electronic feedback to either the PZT or the temperature of the DFB fiber laser, should greatly improve the stability in loading. Nevertheless, even without such stabilization, the loading is achieved easily and quickly and with our present system, ion Coulomb crystals with more than 10^5 ions can be produced within a minute. Fig. 7.5 shows an example of such a crystal, where the total number of ions is about 80000 and the density and length of the crystal are 6.1×10^8 cm^{-3} and 3 mm, respectively.

As we have mentioned a few times already, a potentially attractive feature of ion Coulomb crystal based Cavity QED is the possibility to work with two-component crystals since they allow for laser cooling one component (outer, radially separated component) while having the other component (inner cylindrical component) interacting with the cavity field only. By tuning our 272 nm light source to resonance with the respective transitions of specific isotopes of calcium, we have loaded such two-component crystals consisting of ^{40}Ca$^+$ and isotopes of higher mass numbers. When producing ^{M}Ca$^+$, where M $>$ 40, ^{40}Ca$^+$ ions are also created through an electron charge transfer process between atoms in the atomic beam, dominated by ^{40}Ca, and the ions in the trap [66, 149]. This process has the form, ^{40}Ca$+^{M}$Ca$^+ \rightarrow$ ^{40}Ca$^+ +^{M}$Ca$+\Delta E^{M}$ and is nearly resonant in the sense that ΔE^{M} lies much below the energy associated with the thermal collisions leading to the exchange process. The
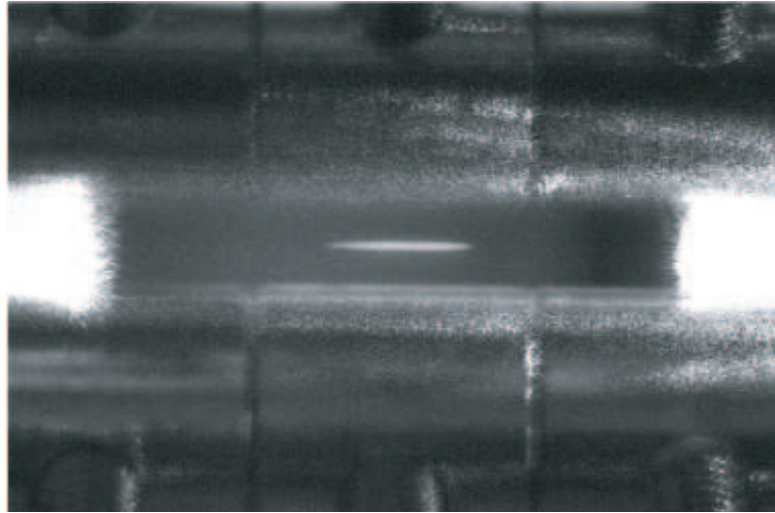
Figure 7.5: Image of a 3 mm long ^{40}Ca$^+$ Coulomb crystal with 80000 ions. The rf-voltage is 300 V corresponding to a density of 6.1×10^8 cm^{-3}. Also visible are the trap electrodes and the mirror substrates, which are slightly out of scale as compared to the crystal due to the fact that they are not in the focal plane. The scattering of the 397 nm light in these are due to Rayleigh scattering in the fused silica mirror substrates.

relative content of ^{40}Ca$^+$ and less naturally abundant isotopes in the crystal can be controlled to a high degree by turning on the atomic beam after the ionization laser has been turned off and thereby converting the outer isotope into ^{40}Ca$^+$ until the desired ratio has been achieved.

By tuning the frequency of the 272 nm laser system via the PZT voltage on the DFB fiber laser, we are able to selectively load specific isotopes of Calcium. The resonances have been found by varying the PZT voltage until the maximum loading rate was obtained. Along with the isotope shifts for the $4s^{21}S_0 \rightarrow 4s5p^1P_1$ transition given in [149], this has been used to calibrate the tunability of the 272 nm laser system. Fig. 7.6 shows a linear relationship between the applied PZT voltage and the detuning from the ^{40}Ca resonance. From the measured slope of 82 ± 2 MHz/V we deduce a total tuning range of the laser system of 16.4 GHz (at 272 nm) over the total PZT-range of 200 V.[4] The inserts in the graph are images of typical two-component crystals loaded into the trap, where an ellipsoid has been superimposed to indicate the boundary of the whole two-component crystal. Missing in fig. 7.6, is ^{46}Ca$^+$, which due to its low natural abundance (table 7.1), is loaded at a comparatively lower rate, even at higher oven temperatures ($> 500°$C). Combined with the before-mentioned drift of the fiber laser, this made it difficult to locate the excact resonance of this isotope. Furthermore, although the graph of fig. 7.6 shows a nice linear dependence in frequency with the PZT voltage, the system does exhibit some degree of hysteresis and all points are taken relative to the ^{40}Ca$^+$ resonance, which was found again after each measurement. The horizontal error bar on ^{40}Ca$^+$ reflects this issue. We note that we confirmed the location of the ^{44}Ca$^+$ isotope by also cooling this isotope and comparing the measured isotope shift on its $3D_{3/2} \leftrightarrow 4P_{3/2}$ transition with the expected value (see appendix A, table A.3).

An important conclusion to draw from fig. 7.6 is that the 272 nm laser system is capable of covering the entire spectrum of naturally abundant calcium and therefore allows for easy loading of a specific isotope, which makes Cavity QED studies with such two-components crystals practical.

As mentioned previously, compared to electron bombardment, the method of resonant photoionization minimizes charging effects as well as trap contamination and formation of patch potentials. From the images presented (e.g. in fig. 7.6) there appears to be no visible perturbation on the shape caused by such effects. In the two-component crystal of fig. 7.7 the upper and lower boundaries of the inner component have been measured to be parallel to within ± 0.1 mrad which also indicates that the introduction of cavity mirrors inside a linear Paul trap does not significantly perturb the trapping of such crystals, even when they are produced directly between the mirrors.

7.3   Loading the cavity trap II: Ablation method

In the loading scheme described in the previous section, the atomic beam was continuous and cannot be switched on and off rapidly, which means that the flux of atoms through the trap is much higher than required. Over time this can lead to accumula-

---

[4]Inferring the frequency shift, from the number of free spectral ranges scanned across over this voltage range, in the two frequency doubling cavities used to generate the light at 272 nm, is consistent with this number to within ± 4 MHz/V.
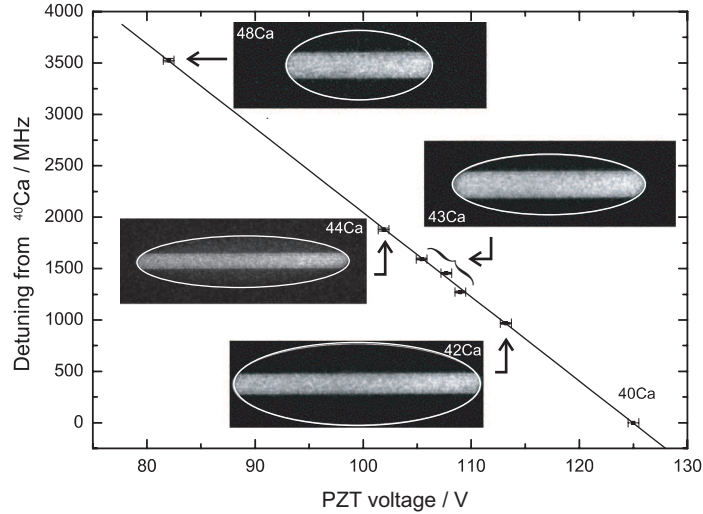
Figure 7.6: Frequency detuning with respect to the ^{40}Ca resonance vs. voltage applied to the fiber laser PZT. The three points around ^{43}Ca correspond to the different hyperfine splitting of the $4s5p^1P_1$ level and the frequency shifts of the various isotopes with respect to the ^{40}Ca resonance are taken from Ref. [149]. The fit indicates a frequency shift of 82 ± 2 MHz/V at 272 nm and the error bars reflect the uncertainty in determining the peak of the ionization resonance. Inserts show typical two-component crystals of the various isotopes, for the same rf-voltage of 220 V, but unequal end-voltages. The dimensions of the black frames are 1.4 mm $\times$ 0.5 mm and the ellipsoids indicate the boundaries of the outer component of the two-component crystals.
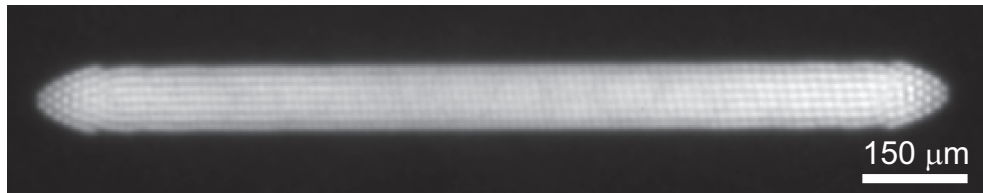
Figure 7.7: Image of a two-component crystal where only ^{40}Ca$^+$ is cooled. The upper and lower boundaries of the inner component have been measured to be parallel to within ± 0.1 mrad. The exposure time was 5 ms.

tion of material on trap electrodes and nearby surfaces such as our cavity mirrors. A cleaner loading technique that would result in contamination is therefore highly desirable both from the point of view of our present context but also for implementations of microtrap architectures [158, 159] where the small trap size makes heating effects extremely pronounced [150]. This heating is attributed to patch potentials due to the presence of contaminants on the trap electrodes, which is indeed often deposited by the atom sources used to load ion traps [151].

We have already emphasized one of the advantages of the photoionization method over electron bombardment being its cleanliness. A key point here is its high efficiency

which leads to a the possibility of working with a lower atomic beam flux. A different philosophy to approach this issue by, is to lower the atomic beam flux altogether. Using an atom source that can be turned on and off more rapidly would allow for having a low average flux during experiments while maintaining a high flux during the loading of the trap.

In this chapter we present a general all-optical technique for loading ion traps that relies on a pulsed laser source to ablate material from a calcium metal target. The atoms produced are directed through the trap, where they are photoionized as in the previous chapter. Through rapid switching of the ablation laser, short pulses can be produced on demand [160]. This reduces the overall amount of material passing through the trap and, hence, reduces risk of electrode and mirror contamination.

7.3.1 Laser ablation

Laser ablation is a broad and complex field and we shall only provide a brief overview here. For further reading we refer to Ref. [161, 162]. Basically, there are two distinct regimes in which nanosecond pulsed laser ablation occurs, distinguished largely by the laser fluence (energy deposited on a surface per unit area by each pulse). Here we are principally concerned with the low fluence regime, in which thermal processes are dominant. If the laser pulse duration is much shorter than the timescale for thermal conduction processes then the region of the target that is irradiated by the laser may be locally heated to high temperatures [163]. This can result in melting, sublimation or desorption of material in the affected region. Laser ablation in this thermal regime has previously been used to reduce the amount of source material required for resonance ionization mass spectrometry [160] and our motivation is therefore similar. As the laser fluence is increased, multi-photon excitation will eventually lead to ionization of material at or near the target surface, resulting in the formation of a plasma phase [164]. This can dramatically increase the rate at which energy is absorbed from the laser beam. In this high fluence regime there are a variety of mechanisms by which material can be ejected from the target surface, some of which occur on a macroscopic scale [161]. For the purposes of loading ion traps the plasma regime may be undesirable because a significant number of atoms can be produced in the excited state. As the isotope selective transition in our scheme is the $4s^2{}^1S_0 \rightarrow 4s5p^1P_1$ transition, the loading will not remain isotope selective for these excited state atoms. In practice this means that ablation should be carried out in the thermal regime, where plasma effects are not observed.

7.3.2 Setup

A pure calcium metal target is placed close to the thermal oven source with an identical set of skimmers leading to the center of the trap (see figure 6.4). The surface of the calcium target is aligned such that it is perpendicular to the path toward the trap center. Due to geometric constraints, this path is aligned at an angle of about 12 degrees relative to the ionization laser.

The ablation laser used in these experiments is a 1064 nm pulsed Nd:YAG laser[5]. The maximum pulse energy is about 80 μJ and remains constant for pulse repetition

---

[5]CrystaLaser QIR-1064-500

rates up to about 3 kHz. For higher repetition rates the maximum energy decreases, and at about 15 kHz it falls as the inverse of the repetition rate. Pulse durations are also dependent on the repetition rate, but are in the region of 30-50 ns for the rates used here. The maximum repetition rate is 200 kHz. The laser is focused onto the calcium target with a waist of about 75 ± 15 μm. In our current setup we are restricted to using an angle between the laser propagation direction and the normal to the calcium surface of approximately 30 degrees. For this reason, the region illuminated by the ablation laser will be slightly larger than the measured beam waist in one direction.

Alignment of the ablation laser is performed by imaging the target with a CCD camera directed parallel to the beam path (see fig. 7.8). With a low pulse energy but large repetition rate, scattered light from the calcium target is clearly visible and allows for accurate positioning of the beam. By placing a filter in front of the CCD camera, this light at 1064 nm is eliminated. The pulse energy can then be gradually increased until light from the calcium target is once again seen on the camera. This light at a wavelength other than 1064 nm is a clear indication of the generation of plasma on the calcium surface. The focusing of the ablation laser beam can then be optimized by finding the point at which plasma is observed with the lowest pulse energy. Once the position of focus has been optimized, we find that plasma can be clearly seen with ablation laser fluences above about 600 mJ/cm^2. In all experiments presented here we have worked at lower fluences to remain in the thermal regime.

To ensure that the ablation beam covers the region of the calcium target that is aligned with the skimmers and the center of the trap, a PZT controlled mirror is used to dither the beam position over a region of about 1 mm^2. We have found that this also helps to keep the ablation rate stable.
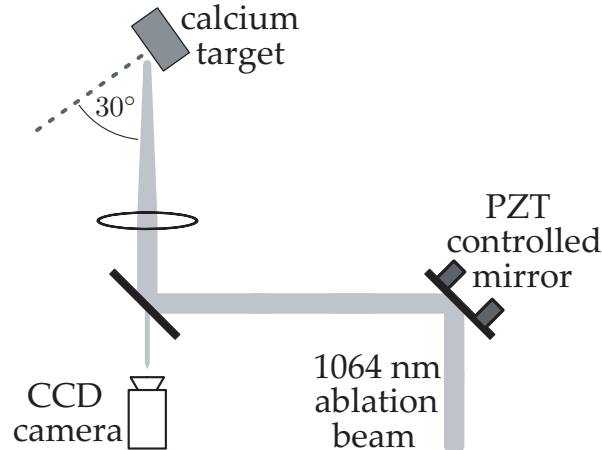
Figure 7.8: Setup for alignment and control of the ablation laser beam. The CCD camera images the target surface, and is used for initial laser alignment. By filtering out light at 1064 nm it can also be used to monitor the extent of plasma formation at the target. The PZT controlled mirror is used to dither the beam position in the vertical and horizontal directions.

7.3.3   Results

In our setup, ions can be loaded into the trap by irradiating the calcium target with the ablation beam whilst the photoionizing laser is operating continuously. Fig. 7.9 shows the calculated number of ions present in the trap as a function of time, whilst the ablation laser is periodically gated with regular 'on' and 'off' periods of nine seconds. The number of ions is seen to increase during the 'on' periods. This increase stops abruptly whenever the laser is switched off, indicating that ion loading is indeed due to ionisation of calcium atoms emitted by the ablation process.

The loading rate is found to be dependent on the ablation laser fluence. Rates as high as 125 ions per second have so far been observed, using a fluence of 240 mJ/cm^2 at a repetition rate of 25 kHz. There are many other parameters that can affect the loading rate, such as the ablation beam positioning and the photoionization laser wavelength and intensity. Furthermore, as mentioned above, geometric constraints prevent the 272 nm beam for photoionization to intersect the atomic beam at a 90° angle. For a thermal beam this can lead to substantial Doppler broadening which will lower the ionization rate. It is expected that with further optimization and a 90° beam configuration even greater loading rates could be achieved, whilst still keeping the ablation laser fluence well below that required to generate plasma.

In order to demonstrate the ability of the ablation loading technique to load individual ions in a controlled manner, which would be relevant for loading of e.g. microtraps for quantum information processing, experiments have been carried out with laser fluences as low as 120 mJ/cm^2. In this regime ions are loaded rather slowly, and it is a straightforward task to shutter the ablation laser once a desired number
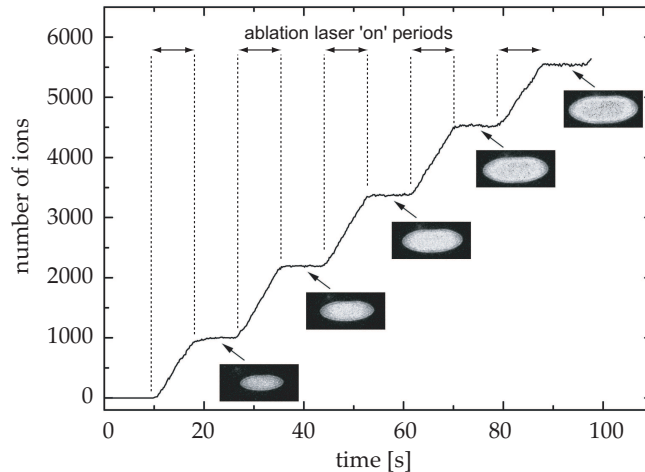
Figure 7.9: Number of ions present in the trap as a function of time, when the ablation laser is periodically gated on and off. The ion number is seen to increase only during the 'on' phase of the gating cycle, indicated by the double-headed arrows. The inset images are examples that show the state of the crystal at the indicated times. The ablation laser fluence used is 240 mJ/cm^{2}and the repetition rate is 25kHz. The 272 nm power used is about 15 mW.

of ions is reached. Fig. 7.10 shows a number of frames taken from a series of CCD images recorded during continuous ion loading at this laser fluence. The number of ions present in the string is clearly apparent in each frame. Also shown in fig. 7.10 is the overall fluorescence as determined by integrating the signal in a fixed area of each of the CCD images. The time at which each of the ions is loaded is clearly marked by a discrete step in the fluorescence level. Brief drops in fluorescence are sometimes observed shortly before a new ion is observed. These transient drops are due to heating of the ions already in the trap by the new, much hotter ion. Drops in signal are sometimes seen at other times, when an ion is excited into a non-fluorescing state through collisions with atoms passing through the trapping region.

Although the rate at which ions are loaded in this example is intentionally rather small, it would be relatively straightforward to implement a loading scheme in which the fluorescence rate is continually monitored and the ablation laser is automatically shuttered when an ion is loaded. With such a system, individual ions could be controllably loaded at higher fluences and hence much more rapidly.

In order to achieve a well controlled loading of the trap, it is important that the loading rate be stable over time. That this is the case is demonstrated in fig. 7.11, which shows the number of ions in an ion crystal during more than fifteen minutes of continual loading. The very slight oscillation in the loading rate can probably be attributed to drifts in the wavelength of the photoionizing laser, which is also observed during loading with the thermal source.

An additional benefit of the laser ablation-based ion-loading technique is that the pressure rise during loading can be kept relatively small. Thermal atom sources must necessarily be maintained at some high temperature during operation. This raised temperature often leads to a significant increase in the background pressure within
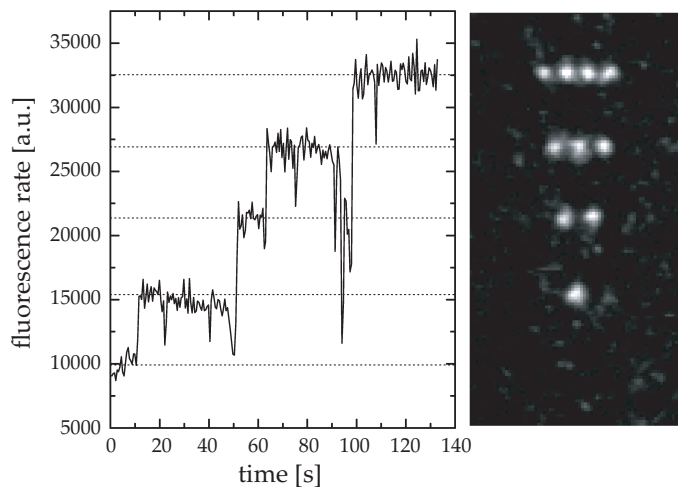
Figure 7.10: Fluorescence detected from the center of the trap as a function of time during continuous ablation with a laser fluence of 120 mJ/cm^2 and repetition rate of 50 kHz. With these parameters the loading rate is extremely small and single ions can easily be loaded. The intensified CCD images show the ion string shortly after each ion is loaded.
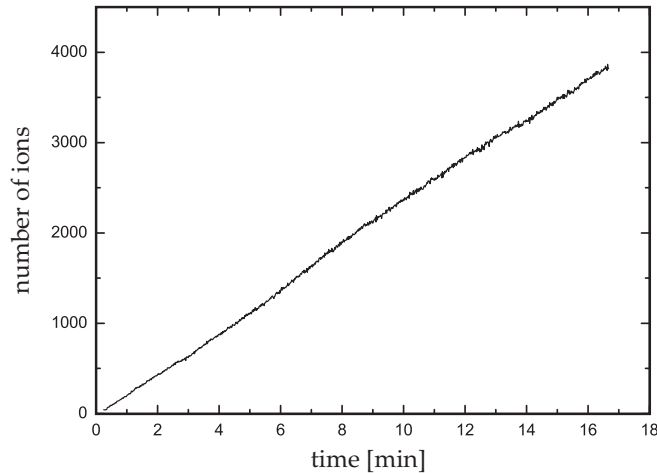
Figure 7.11: Number of ions present in the trap as a function of time during continuous ablation with a fluence of 240 mJ/cm^2 and repetition rate of 25 kHz. The photoionization parameters are set such that the loading rate observed is rather small, but it is seen to be almost constant for a period of more than fifteen minutes.

the vacuum chamber. Even after loading is completed it can take several minutes for the pressure to return to its initial level. During laser ablation, the surface area of the target that is strongly heated is governed by the size of the ablation beam. Since this can be very small, it is possible to avoid large pressure rises during loading and obtain much more rapid recovery times.

Upon first ablating the surface of the calcium target in our ion trap setup, the pressure was observed to rise as high as 10^{-8} mbar. This initial increase is ascribed to evaporation of contaminant material on the surface layer of the target. As ablation continued, much of this contaminant layer was removed and the pressure in the chamber improved.

The typical pressure response during ablation of the calcium target with a relatively large laser fluence of 270 mJ/cm^2 and a repetition rate of 23 kHz is shown in fig. 7.12. The ablation continues for a period of ten seconds, during which the pressure rises to a new equilibrium level that is approximately 1.5×10^{-10} mbar greater than the base pressure. The pressure returns to its initial value within a few seconds of switching off the ablation laser. Although the pressure rise observed during ablation is actually comparable to that expected from a thermal source that has been used for some time, the situation might have been improved by stronger heating of the calcium target to remove contaminants. This could have been achieved by resistively heating the target during bake-out of the vacuum chamber. Even now it is possible that the pressure rise will be reduced over time as more contaminants have been removed from the target surface.
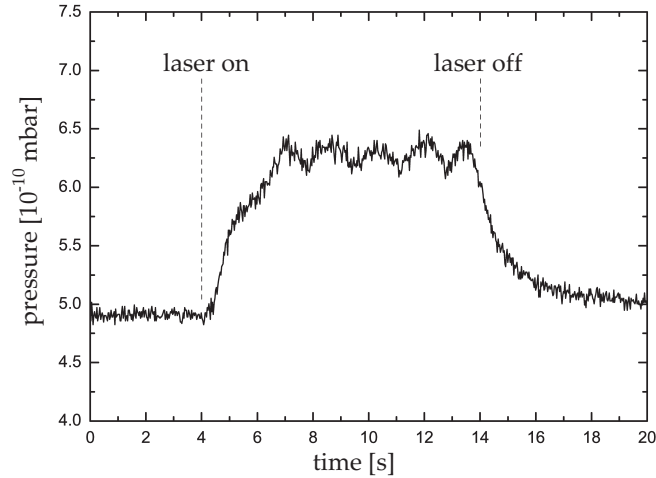
Figure 7.12: Response of ion gauge pressure measurement to a ten second period of ablation loading with a laser fluence of 270 mJ/cm^2 and repetition rate of 23 kHz. An increase in the equilibrium pressure of about 1.5×10^{-10} mbar is observed. The pressure returns to its initial value within a few seconds of switching off the ablation laser.

7.3.4 Photoionization of Rydberg atoms

Besides the trap loading technique described in the previous sections, we have also observed that at relatively high ablation laser fluences ions can be loaded into the trap even *without* the use of the photoionization laser at 272 nm. The loading rates for this process can be as high as 25 ions/s. Although it is not fully understood how the various experimental parameters affect the loading rate we do find that at relatively low fluences it is possible to eliminate this loading process altogether. Indeed, during collection of all the data presented in the previous section no loading was observed without the 272 nm laser.

This loading of the trap without the 272 nm laser is surprising, especially since it occurs even if the 866 nm repumper laser is blocked. This eliminates the laser cooling force and makes it extremely unlikely that an ion generated outside the trap should be captured. It follows that the ions must be generated near the center of the trap as a result of photoionization by the Doppler cooling or repumper lasers. By blocking each of these beams in turn, it has been determined that only the 397 nm cooling beam can be responsible for this photoionization.

Since it takes some time for the ablated atoms to reach the center of the trap, they must necessarily be produced in some long-lived excited electronic state. An obvious candidate could be the metastable 4s3d ^{1}D$_2$ state, but the photon energy at 397 nm is insufficient to ionize from this level (see fig. 7.13c). Alternatively, it is possible that the atoms are produced in bound Rydberg states, from which resonant transitions to some auto-ionizing atomic states exist at 397 nm, but not at 866 nm.

The outer electron in a high-lying Rydberg state atom can be considered as a spectator that does not significantly interact with more tightly bound electrons. The transitions that are available to an atom in such a Rydberg state are therefore very
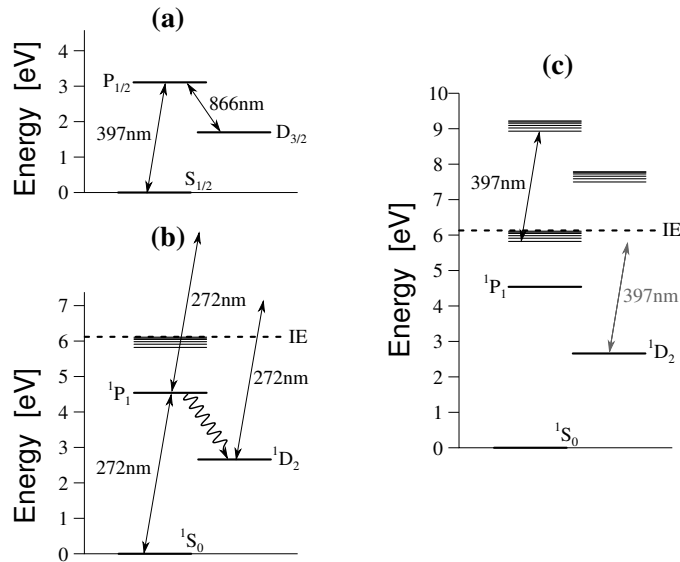
Figure 7.13: a) Partial energy level diagram of Ca^+. b) Partial energy level diagram of atomic calcium. c) By superimposing the ionic energy levels onto each of the atomic Rydberg levels, we obtain approximate values for some of the doubly-excited auto-ionizing states of atomic calcium.

similar to those available to the primary ion. The energy levels of the doubly-excited states can be approximated by superimposing the ionic energy level system onto each of the singly-excited Rydberg levels (see fig. 7.13). It follows that regardless of the exact initial Rydberg state of the calcium atoms there will always be a transition to an auto-ionizing state at close to the 397 nm ion cooling wavelength. The validity of this approximation is confirmed by detailed calculations and measurements of such an auto-ionizing series in calcium [165].

We have studied the rate at which ions are loaded by this process as a function of 397 nm laser power. The results are presented in fig. 7.14. An initially linear relationship is observed which then shows signs of saturation at higher powers.

Since the auto-ionizing resonances are rather broad, this trap loading technique is not expected to be isotope selective and is therefore of more restricted use compared to resonant photoionization of ground state calcium atoms. We note, however, that the same loading effect would be expected for any element that has a rapid Doppler cooling transition available to it in the ionic state. The technique may therefore be particularly useful for elements that only possess one isotope, such as beryllium, or whenever isotope selectivity is not required. The fraction of atoms produced in the Rydberg states, and hence the overall efficiency of this loading process, has yet to be determined.
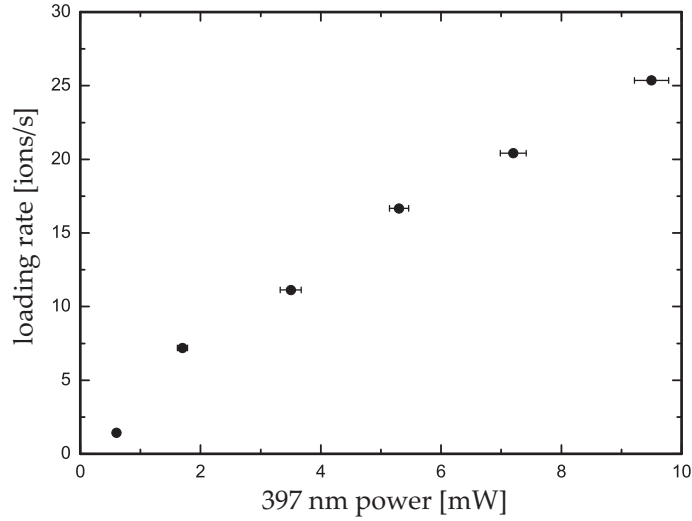
Figure 7.14: Ion loading rate as a function of 397 nm laser power. An initially linear relationship is observed, with possible saturation effects beginning to occur at higher powers. The ablation laser fluence used is 300 mJ/cm^2, with a repetition rate of 20 kHz.

7.4 Conclusion

In this chapter we have presented results on loading of the cavity trap. In the first part of the chapter we demonstrated that by photoionizing a thermal beam of calcium atoms loading rated of more than 3000 ions/s could be achieved. These observations of large loading rates into the trap are encouraging for the perspectives of producing large ion ensembles inside the cavity and, hence, enter the regime of collective strong coupling of cavity QED.

We furthermore demonstrated the ability of the 272 nm laser system that we described in ch. 5.1, to load specific isotopes of Ca$^+$ into the trap. At the same time this conveniently provided a frequency calibration of this laser system.

In the second part of the chapter we described a novel method for loading via ablation of material off a calcium target. Although considerably lower loading rates were observed by this method, the study demonstrated the method as a viable technique for ion trap loading. For our present experiments with highly reflective mirrors integrated into the trap the possibility of working with a substantially lower average atomic flux is obviously highly desirable and it is possible that with further optimization experiments with larger crystals, such as those needed to achieve collective strong coupling, might become practical. In particular, the effect of Doppler broadening is believed to cause lower loading rates and a setup in which the atomic beam produced by ablation and the 272 nm beam can intersect at 90° is thus expected to lead to improvement in the loading rate. Furthermore, Doppler broadening will deteriorate the isotope selectivity of the scheme dramatically and, indeed, we have not been able to achieve isotope selective loading by this method thus far.

Chapter 8

Characterization and optimization of the cavity trap

In this chapter we will focus on optimization of the trap from the point of view of maximizing the number of ions in the cavity mode. The motivation for this comes from the scaling with the number of ions of the collective coupling strength $g\sqrt{N}$, where g is the single ion coupling strength and N is the number of ions interacting with the cavity field. Maximizing N is thus crucial to achieve a high coupling strength and to potentially satisfy the criterion for strong collective coupling, which as we saw in ch. 6.8 should be possible for $N > 500$.

We begin by describing a general method for moving the minimum of the quadrupole potential in the radial plane of the trap, such that it can be made to coincide with the cavity mode. We then present experiments aimed at characterizing the trap. Special attention will be given to the calibration of the density of the trapped ion Coulomb crystals, as knowledge about this parameter is a prerequisite for extracting the number of ions interacting with the cavity field from the recorded images of the crystals. Finally, an empirical study of various effects limiting the maximal attainable number of ions is presented. Based on these observations, we draw conclusions about the optimal trapping parameters for the trap.

8.1 Cavity mode - ion crystal overlap

In ch. 6.1 we described how the cavity trap was designed, and later assembled and aligned. The aim there was to achieve an alignment with a precision in the overlap between the center of the cavity mode and the geometric center of the linear Paul trap of ± 10 μm. To measure the final overlap, a crystal is loaded and cooled by sending in the 397 nm beam along the trap axis and the 866 nm repumper at 90° from the side as shown in e.g. fig. 7.3. By subsequently turning off the 866 nm beam from the side and instead coupling it into the resonant cavity, only the ions within the cavity mode are cooled, while the remaining ions are being sympathetically cooled by these. From the recorded images the location of the cavity mode with respect to the ion crystal can be found. To ensure that this is in fact in the minimum of the quadrupole potential, a two-component crystal is loaded and the radial dc-offsets on the trap electrodes are adjusted such that the heavier component appears in equal ratios on both sides of the

central core of the lighter isotope, as described in ch. 3.2.2.

Fig. 8.1a) shows such a two-component crystal in the quadrupole minimum, where only the central ^{40}Ca$^+$ component is being laser cooled. From fig. 8.1b), where the 866 nm repumper is coupled into the cavity, we estimate that the cavity mode is offset with respect to the center of the trap by $\simeq 90$ μm in the xz-plane. From images taken with the side camera (not shown here) we estimate the offset in the $y'z$-plane to be $\simeq 80$ μm.
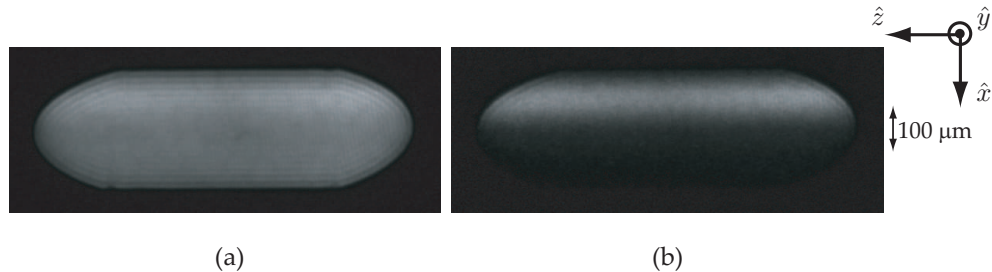
Figure 8.1: Two component crystal in the quadrupole minimum, where only the ^{40}Ca$^+$ component is being directly laser cooled. a) 866 nm repumper sent in from the side (along x). b) 866 nm repumper coupled into the cavity mode (along z). The cavity mode is offset by $\simeq 90$ μm with respect to the center of the crystal.

The discrepancy between this measurement and our initial estimate, based on our method of alignment, is at present not well understood, but nevertheless the resulting poor overlap of the cavity mode and the ions is an issue that must be addressed before pursuing experiments with the interaction between the cavity field and the ions. For typical crystal sizes this imperfect overlap can result in a substantial reduction in the collective coupling strength and a method for moving the ions into the cavity mode must therefore be developed.

8.1.1   Moving the quadrupole potential minimum

Moving the ions requires that special attention be paid to micromotion. In particular, it is crucial that it is the minimum of the quadrupole potential that is moved. Simply "pushing" the ions by applying static dc-offsets will move the ions into regions of large micromotion amplitudes and thereby induce heating as described in ch. 3.2.2. The basic principle of this is shown schematically for one dimension in fig. 8.2. From this illustration we are guided to seek for means to either lower the rf-voltage on one electrode or to increase it correspondingly on the other; both will cause the potential minimum to be shifted towards the electrode of lower rf-voltage, as shown in fig. 8.2c). Before proceeding to the practical implementations of this, we give a more rigorous justification of the method.

Again, we consider the one-dimensional situation, as depicted in fig. 8.3. Here the two electrodes, A and B, can give rise to different field amplitudes. The zero-point on the x-axis indicates the location of the geometric center at a distance r_0 from both electrodes (c.f. fig. 3.1). The potential from either electrode falls off with the inverse
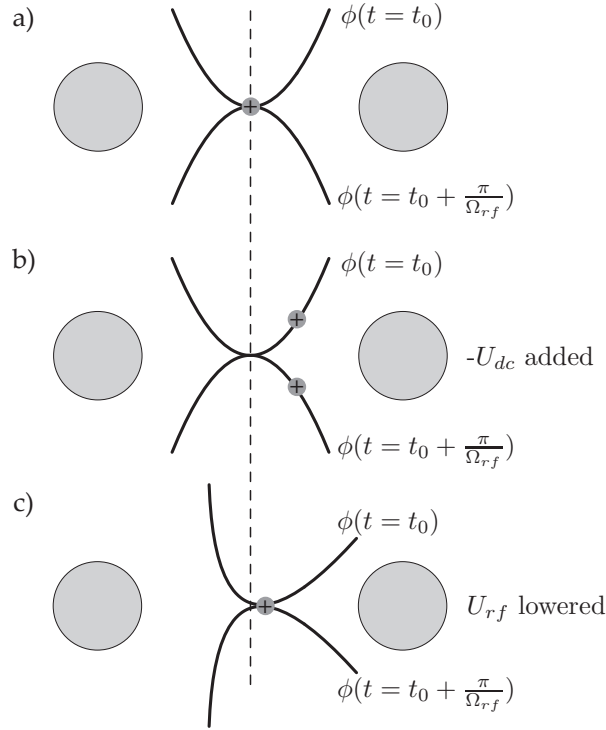
Figure 8.2: Illustration of the basic principle behind moving the ions with respect to the geometric center of the trap. The curves illustrate the rf-potential at two different times in the rf-cycle (out of phase by π). a) Ions in the minimum of the quadrupole potential at the geometric center. b) Ions moved with respect to the geometric center by application of a static dc-potential into a region of large micromotion amplitude. c) Ions moved with respect to the geometric center by lowering the rf-amplitude on one electrode with respect to the other.

of the distance and the total potential at x may thus be written as:

$$\begin{aligned}
\phi(x) &= \frac{A}{r_0 + x} + \frac{B}{r_0 - x} \\
&\simeq \frac{A + B}{r_0} - \frac{A - B}{r_0}\frac{x}{r_0} + \frac{A + B}{r_0}\frac{x^2}{r_0^2},
\end{aligned} \tag{8.1}$$

where we have only retained terms to second order in x in the expansion, based on the assumption that $x \ll r_0$. This is justified by the fact that the inter-electrode inscribed radius $r_0 = 2.35$ mm (table 6.1), is significantly larger than the 80-90 μm shift required for the quadrupole minimum to coincide with the cavity. To find an expression for the location of the minimum x_0 we set the derivative of ϕ with respect

to x equal to zero and solve for x_0,

$$\frac{d}{dx}\phi(x)\Big|_{x=x_0} = -\frac{A-B}{r_0^2} + 2\frac{A+B}{r_0^3}x_0 = 0$$

$$\Downarrow$$

$$x_0 = \frac{A-B}{A+B}\frac{r_0}{2} = \frac{U_{rf}^A - U_{rf}^B}{U_{rf}^A + U_{rf}^B}\frac{r_0}{2}, \tag{8.2}$$

where we have used the fact that A and B are proportional to the rf-voltages to rewrite the expression in terms of these. If we consider a situation where the voltage amplitudes on A and B differ by some attenuation factor $\delta < 1$, such that $U_{rf}^B = \delta U_{rf}^A$, then

$$x_0 = \frac{1-\delta}{1+\delta}\frac{r_0}{2}, \tag{8.3}$$

which for a small attenuation ($\delta \approx 1$), applicable to the situation here, means that $x_0 \propto 1 - \delta$.

Finally we check that the resulting potential is still harmonic around the shifted minimum x_0. If we make the substitution $x \to x + x_0$ in eq. 8.1 we find

$$\phi(x) = \frac{A+B}{r_0} - \frac{A-B}{A+B}\frac{A-B}{4r_0} + \frac{A+B}{r_0^3}x^2, \tag{8.4}$$

which is indeed a harmonic potential.

Based on this analysis our strategy will be to lower the amplitude of the rf-voltage on the electrodes in the direction where we wish to move the ions. In ch. 6.3 we described the electric circuit used to transfer the rf-voltage on to the trap electrodes (see fig. 6.5). This circuit is a resonant circuit where the rf-signal, for all electrodes of both phases, is derived from the same frequency generator. This has the advantage that the phase of the rf-field on the individual electrodes is not subject to relative changes over time but it also means that the rf-voltage can not be adjusted on the individual electrodes independently, without modifying the circuit.

The basic principle behind our method for adjusting the individual voltages on the electrodes can be illustrated by considering the circuit corresponding to a single trap electrode, as shown in fig. 8.4a). There are 2×6 such circuits in parallel in the whole circuit. C_s is the series capacitor of 2.2 nF and C_2 is the variable capacitor (1.5-40 pF) both present in the main diagram of fig. 6.5 and discussed in the analysis given in ch. 6.3. The individual trap electrodes typically has a capacitance of some
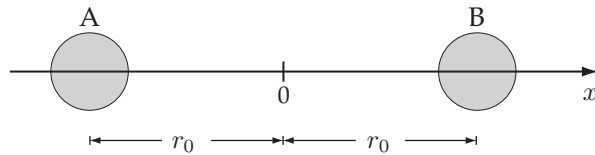
Figure 8.3: Two electrodes used in the derivation of the location of the shifted potential minimum. See text for details.

tens of pF including wires. An analysis of the circuit of fig. 8.4a), which is basically a voltage divider, gives the following expression for the voltage on the electrode:

$$V_e = \frac{V_{\text{in}}}{1 + \frac{C_2 + C_t}{C_s}}.$$ (8.5)

From this relation, the reason for the comparatively high value for C_s is quite obvious, in that the amplitude on the electrode becomes less dependent on the exact value of the trap capacitance C_t and for $C_s \gg C_2, C_t$ we find $V_e = V_{\text{in}}$. From our present purpose of lowering the voltage, eq. 8.5 also shows that this can be achieved either by increasing C_t or by decreasing C_s and in the following we will describe how this is done experimentally in both cases. To move the ions radially, we will make identical changes to the capacitive load on all three electrodes of a given electrode rod (e.g. electrodes 1–2–3 in fig. 8.6). Here we only analyze a single electrode and the situation is of course more complicated when all 12 electrodes are coupled to the same resonant circuit.

8.1.1.1   Parallel load

Increasing C_t can be achieved simply by adding a load $\tilde{C}_p$ in parallel as shown in the diagram of fig. 8.4b) such that $C_t \rightarrow C_t + \tilde{C}_p$ in eq. 8.5. This method is easily implemented by inserting BNC cables of various lengths [1]. Increasing the variable capacitor C_2 will have the same effect but its variation is limited to 40 pF. The attenuation factor δ in eq. 8.3 is given by the ratio of the resulting to the initial gain (eq. 8.5) and may thus be written as:

$$\delta_p = \frac{1 + \frac{C_2 + C_t}{C_s}}{1 + \frac{C_2 + C_t + \tilde{C}_p}{C_s}} \simeq \left(1 + \frac{C_2 + C_t}{C_s}\right)\left(1 - \frac{C_2 + C_t + \tilde{C}_p}{C_s}\right) \simeq 1 - \frac{\tilde{C}_p}{C_s},$$

where we have expanded the expression and neglected terms according to $C_s \gg C_2, C_t, \tilde{C}_p$. From this, we will expect the quadrupole potential minimum (eq. 8.3) to

---

[1]Capacitance: 110 pF/m.
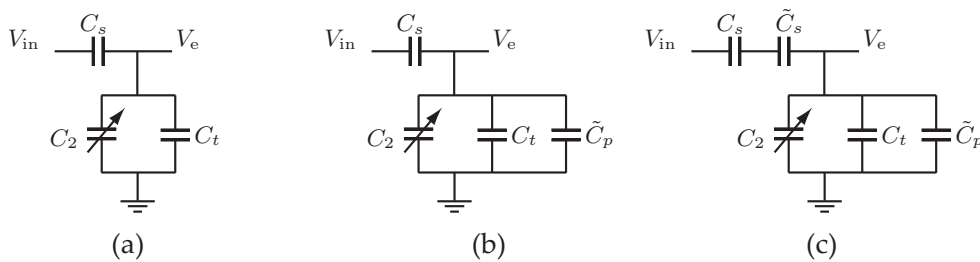
Figure 8.4: Simplified diagram of a single trap electrode. C_s and C_2 refer to the capacitors introduced in ch. 6.3. C_t is the capacitance of the trap electrode. a) No changes to the load. b) Added load $\tilde{C}_p$ in parallel. c) Added load $\tilde{C}_s$ in series. In practice this will always be associated with the addition of a small, parasitic parallel load $\tilde{C}_p$. See text for further details.

move linearly with increasing value of $\tilde{C}_p$ as

$$x_0 \propto \frac{\tilde{C}_p}{C_s}. \tag{8.6}$$

This is shown in fig. 8.5a) where this minimum is moved in the xz-plane by as much as ± 100 μm. The capacitance $\tilde{C}_p$ was added to either electrodes 1–6 or to electrodes 7–12 as defined in fig. 8.6. The red line is a linear fit to the data.

    This method works well in terms of moving the ions, however, the increased capacitance results in a substantially lower resonance frequency of the rf-circuit. Qualitatively, the resonance frequency is given by $\omega = \frac{1}{\sqrt{LC}}$, where L is the circuit inductance and C is the capacitance of the entire circuit. Since we are increasing C the resonance frequency will decrease as $\frac{1}{\sqrt{L(C_{\text{other}}+\tilde{C}_p)}}$, where C_{other} represents the other capacitors in the circuit. Fig. 8.5b) shows measurements of the resonance frequency for both resonances of the circuit (c.f. ch. 6.3) for various values of $\tilde{C}_p$. As for the displacement, the effect is symmetric with respect to adding capacitance on either side of the trap. The solid lines represent fits to the data of the form $\frac{1}{\sqrt{C_{\text{other}}+\tilde{C}_p}}$, which are seen to agree well with this.

    In practice, lowering the resonance frequency is not ideal. For instance, as Ω_{rf} is lowered and becomes comparable to the radial trap frequency ω_r (eq. 3.10), the description of the motion as comprised of secular motion and micromotion becomes inadequate. Furthermore, the experience in our group with similar traps suggests that an rf-frequency of around 4 MHz should result in more stable trapping, and we thus sought an alternative method for lowering the rf-voltage on these electrodes.

8.1.1.2   Serial load

The alternative method consists in adding a capacitor $\tilde{C}_s$ in *series*, as shown in fig. 8.4c), thus changing the serial capacitance as $C_s \to \frac{C_s \tilde{C}_s}{C_s + \tilde{C}_s}$. In practice there will always be some coupling to ground associated with this, which is accounted for by the parallel capacitor $\tilde{C}_p$ ($\sim$ 10 pF).[2] The resulting attenuation factor may now be written as,

$$\delta_s = \frac{1 + \frac{C_2 + C_t}{C_s}}{1 + \frac{C_2 + C_t + \tilde{C}_p}{\frac{C_s \tilde{C}_s}{C_s + \tilde{C}_s}}} \simeq 1 - \frac{C_2 + C_t + \tilde{C}_p}{\frac{C_s \tilde{C}_s}{C_s + \tilde{C}_s}} \simeq 1 - \frac{C_2 + C_t + \tilde{C}_p}{\tilde{C}_s}, \tag{8.7}$$

where as before, in the expansion, we have neglected terms according to $C_s \gg C_2, C_t, \tilde{C}_p, \tilde{C}_s$. The resulting displacement is then inversely proportional to the added capacitance:

$$x_0 \propto \frac{C_2 + C_t + \tilde{C}_p}{\tilde{C}_s}. \tag{8.8}$$

    The advantage of this method is that it has a smaller effect on the resonance frequency of the circuit. The effect of the added capacitances may be viewed as

---

[2]To allow the dc-voltages, e.g., U_{end} to go through to the trap electrodes there is also a 3.3 MΩ resistor added in parallel to the series capacitor $\tilde{C}_s$, which has been omitted here for the sake of simplicity
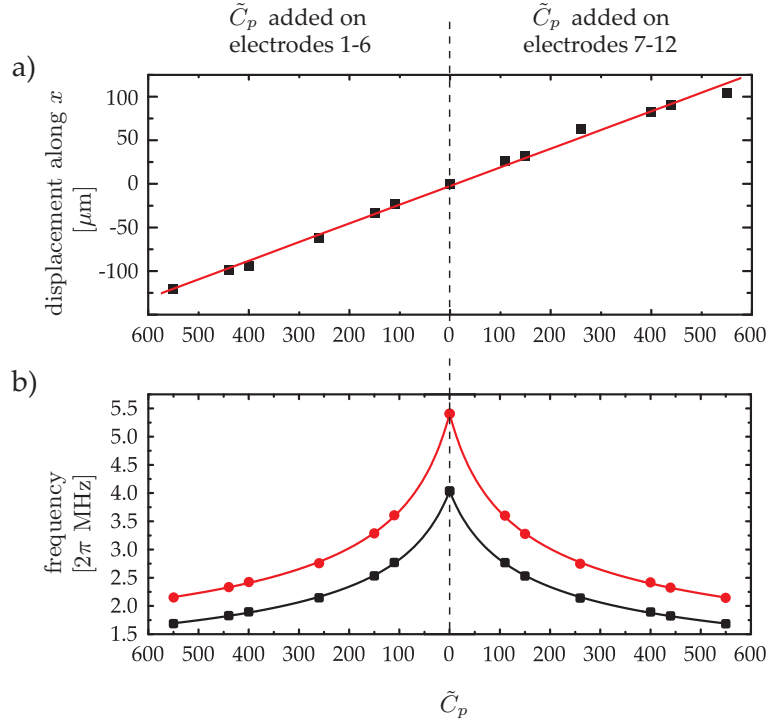
Figure 8.5: Moving of the quadrupole by adding a capacitive load $\tilde{C}_p$ in parallel either on the left- of right-hand side electrodes (when viewed along the z-axis). The dashed line indicates the division with respect to this. a) Displacement along the x-axis versus added load and linear fit. b) Resonance frequencies of the circuit versus added load. The red data is for the higher frequency resonance while the black data is the lower frequency resonance used in our experiments (c.f. ch. 6.3). Solid lines are from fits of the form $\frac{1}{\sqrt{C_{\text{other}}+\tilde{C}_p}}$.

giving rise to an effective trap capacitance,

$$C_t \rightarrow C_t^{eff} = \frac{C_t + \tilde{C}_p}{1 + \frac{C_t + \tilde{C}_p}{\tilde{C}_s}} \simeq \left(C_t + \tilde{C}_p \right) \left(1 - \frac{C_t + \tilde{C}_p}{\tilde{C}_s} \right) \simeq C_t + \tilde{C}_p. \qquad (8.9)$$

Provided the serial capacitor $\tilde{C}_s$ can be inserted without the addition of significant parasitic parallel capacitance $\tilde{C}_p$ then the resonance frequency will not be changed significantly. This is indeed what we observe and fig. 8.7 shows the resulting displacement of the crystal for various values of $\tilde{C}_s$. Black points correspond to the displacement in the xz-plane where $\tilde{C}_s$ is added to electrodes 1–6 while the red point are for displacement in the yz-plane where $\tilde{C}_s$ is added to electrodes 1–2–3 and 7–8–9. The solid line is of the form $\frac{1}{\tilde{C}_s}$, based on the simple model of eq. 8.8 and shows nice qualitative agreement.

These measurements indicates that the necessary displacement of 80–90 μm in the two planes can be achieved for $\tilde{C}_s \simeq 170$ pF added to electrodes 1–9. In the final configuration we have added a capacitive serial load of 120 pF only to electrodes
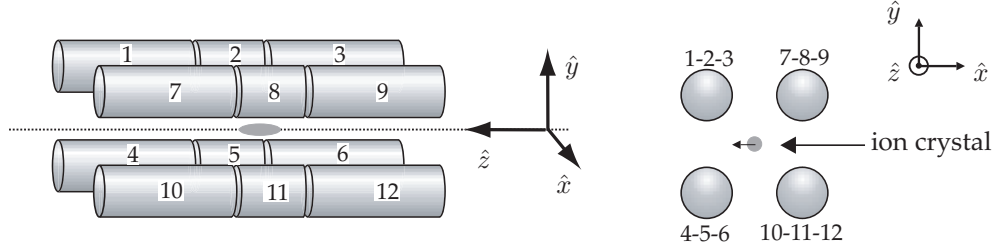
Figure 8.6: Overview of the Paul trap electrode numbering and a sketch of the crystal displacement when the rf-voltage is attenuated symmetrically on electrodes 1–2–3 and 4–5–6.
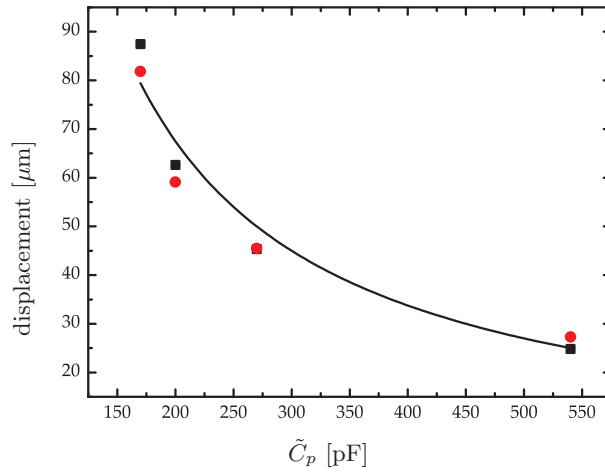
Figure 8.7: Moving the quadrupole by adding a capacitative load $\tilde{C}_s$ in series. Black points correspond to the displacement in the xz-plane (added $\tilde{C}_s$ to 1–6) while the red point are for the $y'z$-plane (added $\tilde{C}_s$ to 1–3 and 7–9). The solid line is of the form $\frac{1}{\tilde{C}_s}$.

1–3, which results in an identical displacement at $45°$ in the xy-plane. Note that this load is exactly a factor $\frac{1}{\sqrt{2}}$ of the 170 pF, as expected from a displacement at $45°$. Further fine adjustment can be facilitated through the capacitors C_2 and fig. 8.8 shows the crystal in its final position in the xz-plane. Here the mode-crystal overlap is only off by 15 μm in along y and 3 μm along x. For typical crystal sizes this will result in a reduction in the coupling strength of at most a few percent (c.f. appendix C). When evaluating the coupling strength in ch. 10 we shall take this into account. The trap frequency has not changed significantly and is still 4.0 MHz in this final position as expected from our simple analysis.
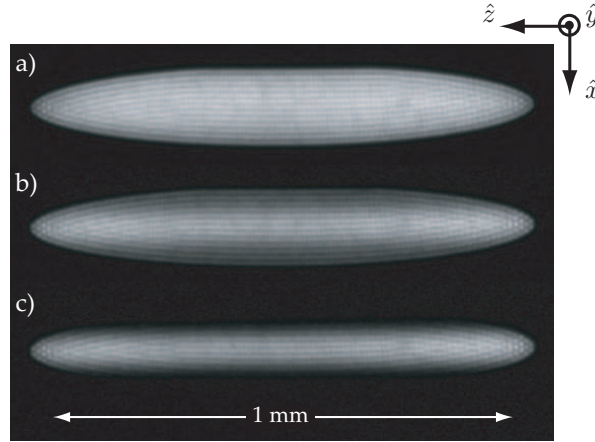
Figure 8.8: Final position of the crystal with respect to the cavity mode. From image a)-c) the 866 nm repumper is shifted from the beam illuminating the entire crystal from the side (along x) to the cavity mode (along z).

8.2 Trap calibration

The objective of the study within this section is in two parts: First, to check that the trap behaves as expected, which means that the trapped ion Coulomb crystals are well-described by the zero temperature charged liquid model of ch. 3.2.1. Secondly, as knowledge of the exact number of ions interacting with the cavity field is important for a cavity QED experiment, we require some form of calibration of the density of the ion Coulomb crystals.

In ch. 3.2.1 we derived the following expression for the density:

$$\rho_0 = \frac{\epsilon_0 U_{\mathrm{rf}}^2}{M r_0^4 \Omega_{\mathrm{rf}}^2}.$$

Here, for the purpose of achieving an accurate calibration of the density, we are principally concerned with the rf-voltage U_{rf}. As described in ch. 6.3 the electronics for the transfer of the rf-voltage onto the trap electrodes, has a 1:100 monitor output, but as we have seen in the previous section, the exact voltage on the electrodes will be dependent on their capacitance, which might not be identical for all electrodes. By all accounts, the changes made to the circuit in order to move the quadrupole minimum, will have rendered the initial 1:100 calibration of the monitor output faulty and some form of calibration is thus required. With the analysis of the previous section in mind, it is clear that a direct measurement is not possible as it will inevitably add some load to the electrodes and change the circuit response altogether. Instead, an obvious probe for the calibration of the trapping parameters is the ion crystals themselves. In practice this means that we should measure quantities that can be compared with predictions made by the zero temperature charged liquid model.

8.2.1   Trap frequencies

In our initial treatment of ion Coulomb crystals and the zero temperature charged liquid model, we derived a relation between the ratio of the trap frequencies $\frac{\omega_z}{\omega_r}$ and the crystal aspect ratio α (c.f. eq. 3.18 and fig. 3.5). In our characterization of the trap, we first verify that this relation provides a good description of the crystals by measuring α for a broad range of trapping parameters in the configuration where no additional load has been applied to any of the electrodes. From α we deduce $\frac{\omega_z}{\omega_r}$ via eq. 3.18, which we then compare with the value predicted by the expression for the trap potentials derived in ch. 3.1.1. From these the ratio of the trap frequencies is given

$$\frac{\omega_z}{\omega_r} = \sqrt{\frac{-a}{q^2/4 + a/2}}, \tag{8.10}$$

where a and q are given by (eq. 3.6):

$$a = -4\frac{\eta Q U_{end}}{M z_0^2 \Omega_{rf}^2} = a' U_{end} \tag{8.11a}$$

$$q = 2\frac{Q U_{rf}}{M r_0^2 \Omega_{rf}^2} = q' U_{rf}, \tag{8.11b}$$

where a' and q' are both constants.

In the experiment we trap and cool ion Coulomb crystals of ^{40}Ca$^+$ and deduce their aspect ratios from the recorded images by measuring their radius and length, as described in appendix B. This is done for trapping voltages in the range $U_{rf} = 150 - 300$ V and $U_{end} = 2 - 20$ V. From the measured values for α we calculate $\frac{\omega_z}{\omega_r}$ via eq. 3.18 and this data is then fitted to the expression of eq. 8.10. Using a' and q' as free parameters their values can be deduced from the fit.

In practice the data is fitted to the following expression:

$$\frac{\omega_z}{\omega_r} = \sqrt{\frac{-(U_{end} - U_{off})}{\frac{q'^2}{a'}\frac{U_{rf}^2}{4} + \frac{1}{2}(U_{end} - U_{off})}}, \tag{8.12}$$

where U_{off} has been included to account for any voltage offsets in the end-voltage. Writing the expression in this way shows that a' and q' are dependent variables in this equation and a fit can therefore only give us information about the ratio $\frac{q'^2}{a'}$, which is given by (c.f. eq. 3.6),

$$\frac{q'^2}{a'} = \frac{q^2}{a}\frac{U_{end}}{U_{rf}^2} = \frac{-Q z_0^2}{M \eta r_0^4 \Omega_{rf}^2}. \tag{8.13}$$

From the fit we find $U_{off} = 0.92 \pm 0.05$ V and $\frac{q'^2}{a'} = -(2.311 \pm 0.016) \times 10^{-3}$ V^{-1}. Using these values we then calculate $\frac{\omega_z}{\omega_z}$ and plot this versus α. The result is shown fig. 8.9a) and is seen to agree well with the theoretical prediction of eq. 3.18 based on the zero temperature charged liquid model (solid line), which confirms the validity of this model and hence the fit result. The fact that $U_{off} \neq 0$ can be ascribed to charging effects caused by the UV laser during loading or the trap. Finally, the value for $\frac{q'^2}{a'}$, obtained from the fit, agrees well with the theoretical prediction of

$-(2.29\pm0.06)\times10^{-3}$ V^{-1}, based on the trap parameters quoted in table 6.1, where the uncertainty comes from the machining and alignment precision of the trap structure (±10 μm).

These measurements thus show that the aspect ratio of the trapped ion Coulomb crystals follows very accurately the predictions based on the zero temperature charged liquid model, which indicates that the trap is working as expected. This leads us to the conclusion that the dielectric mirror substrates have been integrated into the trap without significantly perturbing the trapping fields.

Furthermore, the nice agreement between the prediction based on the trap dimensions and the fit result for $\frac{q'^2}{a'}$, signifies that the reading of the rf-voltage on the 1:100 monitor output is correct, as expected for this case, where no additional load has been applied to the trap electrodes. This measurement may thus be used as a reference for calibration of the rf-voltage when the loads on the electrodes are altered.

Fig. 8.9b) shows the result of a similar measurement after the quadrupole potential minimum has been moved through the addition of a 120 pF serial load on electrodes 1–2–3. Again, nice agreement with the zero temperature charged liquid model is seen, which supports our arguments in the previous section that the trap potentials should not be distorted by any appreciable amount from their initial harmonic form. From the fit we find $U_{off} = (0.99 \pm 0.05)$ V and $\frac{q'^2}{a'} = -(1.991 \pm 0.014) \times 10^{-3}$. Since only the rf-voltage is modified by our scheme for moving the quadrupole potential minimum, it is expected that the offset in the end-voltage is unchanged and that the ratio $\frac{q'^2}{a'}$ is modified as a result of the attenuation of the rf-voltage. By comparison with the value found without any additional load, we deduce that the reading on the 1:100 monitor output of the rf-circuit must be scaled by a factor 0.928 ± 0.007.

Alternatively, we may rewrite the expression for the density (eq. 3.21) in terms of

(a)   (b)
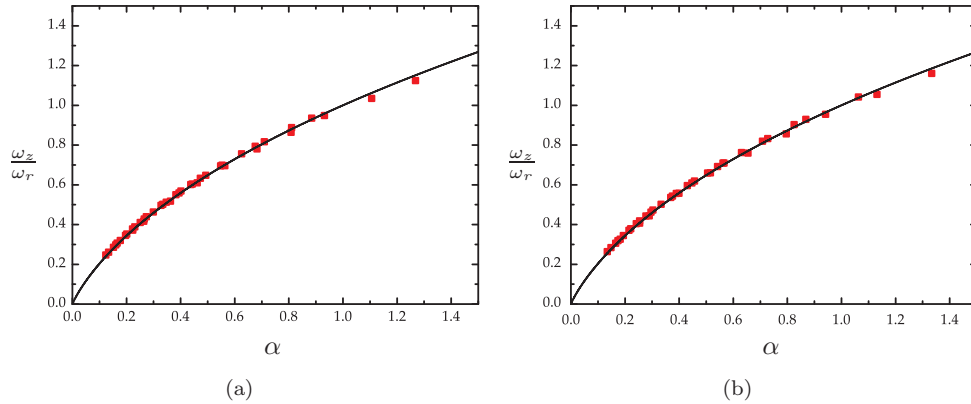
Figure 8.9: Ratio of trap frequencies versus crystal aspect ratio. a) For no additional load on the trap electrodes. b) For 120 pF load on electrodes 1–2–3. The solid black line is the theoretical curve based on the zero temperature charged liquid model (eq. 3.18) and the red points are data where α has been measured directly from images of crystals and $\frac{\omega_z}{\omega_r}$ has been deduced from a fit to eq. 8.12. See text for further details. The errorbars are within the point size.

the $\frac{q'^2}{a'}$ ratio as

$$\rho_0^{\mathrm{cal}} = \frac{\epsilon_0 \eta}{Q z_0^2} \frac{q'^2}{a'} U_{\mathrm{rf}}^2 \tag{8.14}$$

and use the reading on the 1:100 rf-voltage monitor output directly. In the two cases, without additional load and with 120 pF load on the three electrodes, the density of the trapped ion Coulomb crystals is then:

$$\rho_0^{\mathrm{cal}} = \begin{cases} (6.92 \pm 0.12) \times 10^3 \ \mathrm{cm}^{-3} \times U_{rf}^2 [\mathrm{Volt}] & ; \text{for no load,} \\ (6.01 \pm 0.09) \times 10^3 \ \mathrm{cm}^{-3} \times U_{rf}^2 [\mathrm{Volt}] & ; \text{for 120 pF load,} \end{cases} \tag{8.15}$$

where we have included an uncertainty of ± 10 μm in the geometric constants of eq. 8.14.

8.2.2 Inter-shell spacing

In ch. 3.2.3 we mentioned how measurements of the radial inter-shell spacing of the ion Coulomb crystals may be used to deduce the crystal density. Combining eq. 3.16 and eq. 3.22, the inter-shell spacing can be expressed through the density as

$$\delta r = 1.48 \times \left(\frac{3}{4\pi\rho_0} \right)^{1/3}. \tag{8.16}$$

The pre-factor of 1.48, which is based on MD simulations of infinitely long crystals [97], has previously been determined experimentally by our group to be 1.35 ± 0.15 [98]. To this author's knowledge, no experiments has since been reported which has found agreement with the theoretical prediction with a lower uncertainty in the measurements. In the previous section, we found very good agreement between experiment and theory in our measurements of the crystal aspect ratio, in the configuration where no load had been added to the electrodes. Using the value we deduced for the density based on those experiments (eq. 8.15), we should thus be able to produce a better bound on the pre-factor of eq. 8.16.

Fig. 8.10 shows the result of measurements of the inter-shell spacing δr for different values of the rf-voltage. To mimic the notion of "infinitely long" in the MD simulations we used very prolate crystals of 1.5-2 mm length. δr is determined from the recorded crystal images as described in appendix B and the red line shows the result of a fit to the data of the form

$$\delta r = x \times \left(\frac{3}{4\pi\rho'} \right)^{1/3} \times \frac{1}{U_{rf}^{2/3}}, \tag{8.17}$$

where we have used the value for the density factor found in the previous section of $\rho' = (6.92 \pm 0.12) \times 10^3 \ \mathrm{cm}^{-3} \mathrm{V}^{-2}$ (c.f. eq. 8.15). The fit gives a value for the pre-factor of $x = 1.484 \pm 0.010$, which is indeed quite an improvement in the determination of this factor and which strongly supports the MD simulations of ref. [97].

If we instead assume that 1.48 is the correct value and deduce the density from the fit, we find $\rho' = (6.88 \pm 0.13) \times 10^3 \ \mathrm{cm}^{-3} \mathrm{V}^{-2}$, which agrees well with what we found from the measurements of the trap frequencies.

As a cross-check of the density calibration in configuration where the additional load, required to move the quadrupole minimum, is applied, we perform the same
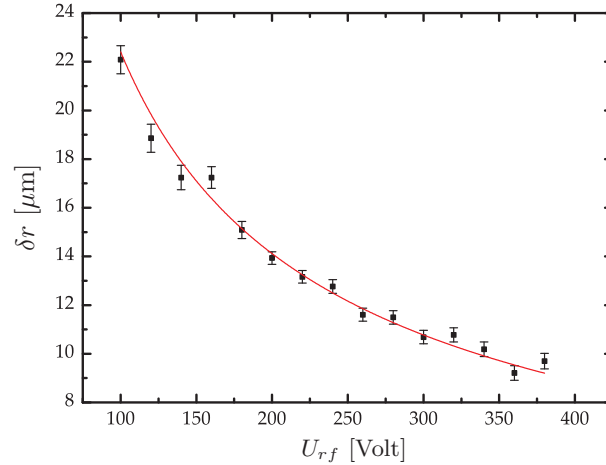
Figure 8.10: Intershell spacing δr measured as a function of the rf-voltage U_{rf} when no additional load is applied to the electrodes. The red line is a fit based on eq. 8.17 from which the pre-factor is determined to be $x = 1.484 \pm 0.010$.

experiment in this configuration. Fig. 8.11 shows the result, where this time the pre-factor is fixed to $x = 1.48$ and using ρ' as a fit parameter. This gives $\rho' = (6.09 \pm 0.14) \times 10^3$ cm^{-3}V^{-2}, which also agrees well with the value deduced from the trap frequencies in the previous section.

Combining our results for the density calibration of ch. 8.2.1 and those of the present section, assuming the pre-factor in eq. 8.16 may be fixed to 1.48, we find the
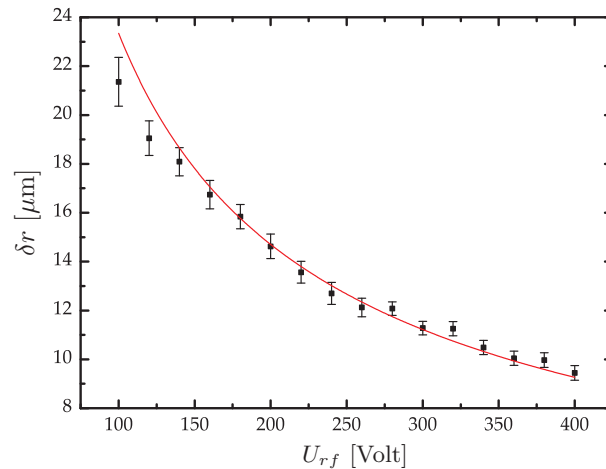
Figure 8.11: Intershell spacing δr measured as a function of the rf-voltage U_{rf} when a 120 pF load is applied to electrodes 1–2–3. The red line is a fit based on eq. 8.17 with $x = 1.48$ from which the density is found to be $\rho' = (6.09 \pm 0.14) \times 10^3$ cm^{-3}V^{-2}.

following for the density of the ion Coulomb crystal as a function of rf-voltage:

$$\rho_0^{\text{cal2}} = \begin{cases} (6.90 \pm 0.09) \times 10^3 \text{ cm}^{-3} \times U_{rf}^2[\text{Volt}] & \text{; for no load,} \\ (6.03 \pm 0.08) \times 10^3 \text{ cm}^{-3} \times U_{rf}^2[\text{Volt}] & \text{; for 120 pF load,} \end{cases} \qquad (8.18)$$

which represents our final calibration of the density and, hence, that used in the remainder of the thesis.

8.3   Maximizing the number of ions in the cavity mode

As mentioned in the introduction, one of the main challenges for the realization of a cavity QED experiment with ion Coulomb crystals is to confine a large number of ions within the cavity mode to enhance the collective atom-light coupling. For our trap, with the optical cavity axis coinciding with the trap axis, the highest number of ions in the cavity mode is achieved when the product of the crystal length and the density ρ_0 is maximized. The length is controlled by both the end- and rf-voltage, whereas the density is determined solely by the rf-voltage (c.f. eq. 3.21). Ideally, we would therefore wish to work at a very low U_{end} and a very high U_{rf}, so as to produce crystals of very low aspect ratio α and high density ρ_0. However, due to the complex interplay between the trapping fields and the heating and cooling rates of the three-dimensional ion Coulomb crystals, the optimal parameters for the system are *a priori* not known and must be determined experimentally. The results presented in the remainder of this chapter have all been obtained with the trap operating without any additional load on the electrodes and any reference to e.g. densities are thus based on the calibration applicable to this configuration. At the time of writing, a similar study has not been conducted for the configuration where the quadrupole minimum is moved, but our experience with the trap in that configuration does not suggest any significant deviations.

We first investigate the dependence of the minimal attainable aspect ratio $\alpha_{\min}$ on the cooling power. This is done by loading crystals of a fixed density and number of ions and then lower the end-voltage U_{end} until the trapping becomes unstable and ions are lost from the trap. Fig. 8.12 shows the aspect ratio as a function of the end-voltage, for three different values of the 397 nm cooling power, all other parameters being kept constant. To the right are shown images of crystals corresponding to the 7 mW data. For each curve, the point furthest to the right corresponds to the crystal right before it is lost and, hence, to $\alpha_{\min}$ for that particular level of cooling power. The conclusion we draw from this graph is that increasing the power helps in trapping crystals of lower aspect ratios.

   As the aspect ratio is lowered toward it's minimal value, we usually observe one of two scenarios by which the ions are lost. In one, the crystal heats up instantaneously (explodes) and all ions are lost, whereas in the other, the crystal shrinks in size, but remains crystallized. In qualitative terms, we interpret the first scenario, as being governed principally by rf-heating in the crystal. As we discussed in ch. 3.2.2, the cooling light at 397 nm is only supplied along the trap axis to avoid driving the radial micromotion of the trap (see e.g. fig. 7.3), and Doppler cooling therefore only cools the axial degree of motion leaving cooling of the radial motion to be achieved solely
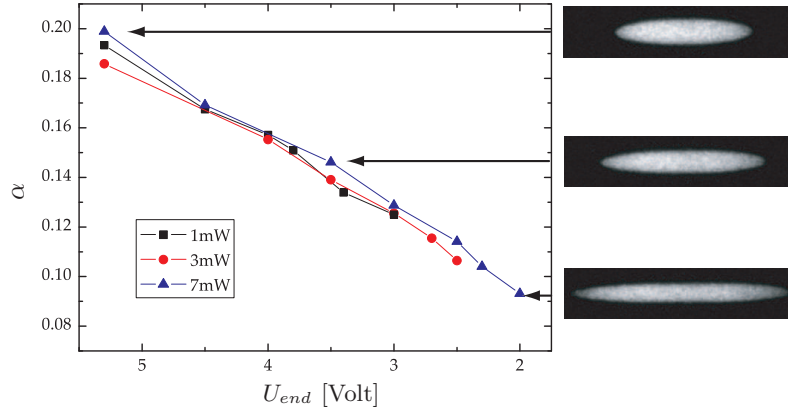
Figure 8.12: Aspect ratio as a function of the end-voltage U_{end} for different powers of the 397 nm cooling laser (total power of both beams) and for a fixed detuning of ~ 20 MHz. To the left are shown images of crystals corresponding to the 7 mW data. The rf-voltage is $U_{rf} = 300$ V ($\rho_0 \simeq 6.2 \times 10^8$ cm^{-3}) and the number of ions is ~ 65000. For this crystal size, the range of aspect ratios corresponds roughly to crystal lengths ranging from 2–3 mm.

via the Coulomb interaction within the crystal. The coupling between axial and radial motion, that this interaction facilitates, is weakened as the aspect ratio is lowered and compensation of rf-heating, which drives the radial motion of the ions, is thus less efficient for low aspect ratios.

The second scenario is usually observed when the number of ions is quite low. In this case there will be less ions in regions of large micromotion amplitudes and therefore less rf-heating to be compensated for by cooling. Stable confinement of low aspect ratio crystals are thus easier achieved, however, ultimately the finite depth of axial trap potential will limit α_{min}. As the end-voltage is lowered, and with it the axial potential (c.f. eq. 3.3), the finite temperature of the ions will allow them to escape from the trap. Since rf-heating influences the temperature, α_{min} is also dependent on the rf-heating within this scenario.

To study the dependence of α_{min} on crystal size we load crystals of various number of ions and let them expand axially until they become unstable and are lost. α_{min} is then determined for each number of ions from the last stable crystal image as in the previous experiment. Fig. 8.13 shows the results for two different power levels of the 397 nm cooling laser beams. Initially, as the number of ions in the crystal increases, α_{min} increases slowly until a threshold is reached and it suddenly jumps to a much higher value, beyond which the slow increase is continued. The observation of an increase in α_{min} is a strong indication that rf-heating is at play. Increasing the number of ions for a given aspect ratio will result in more ions in regions of large micromotion amplitudes and, hence, more rf-heating. It is therefore expected that the crystals become unstable at a higher aspect ratio when the number of ions is increased.

The points before and after the threshold represent two different regimes. Below threshold the ions are lost at very low end-voltages via the scenario interpreted as
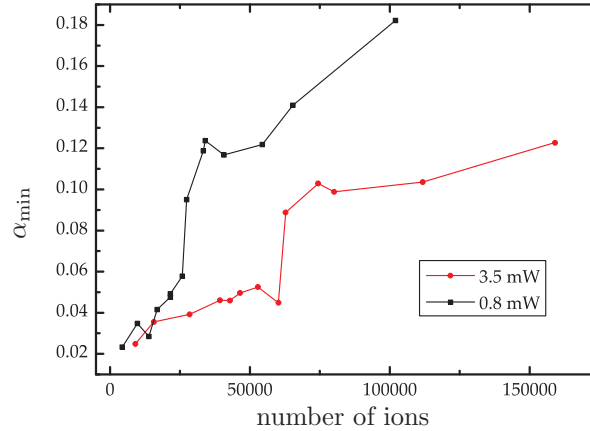
Figure 8.13: Minimal attainable aspect ratio versus the number of ions in the crystal for two different powers of the 397 nm cooling laser (total power of both beams) and for a fixed detuning of ~ 20 MHz. The rf-voltage is $U_{rf} = 300$ V corresponding to a density $\rho_0 \simeq 6.2 \times 10^8$ cm^{-3}.

a result of a low trap potential in the above analysis, whereas above threshold the ions are lost via the scenario interpreted as a direct result of rf-heating. Presumably, the appearance of a threshold may be accounted for as a result of a runaway heating process (hence the sudden loss of all ions), due to the rf-heating, although these simple qualitative arguments does not provide a deeper understanding of this threshold and it remains a subject for further studies.

At any rate, from our analysis of the effect of cooling power, it is not surprising that a lower value of $\alpha_{\min}$ is found at higher power (red curve in fig. 8.13) and that the threshold is shifted to a higher number of ions when the cooling power is increased.

The final parameter that is studied is the rf-voltage, which, as it determines the density via eq. 3.21, is an important parameter to optimize. In this experiment the cooling power is kept constant and $\alpha_{\min}$ is again found for different crystals sizes but this time for various values of the rf-voltage. As seen in fig. 8.14, for most values of the rf-voltage we find the same type of behavior as in the previous experiment. The location of the threshold is seen to depend strongly on the rf-voltage, which also points toward rf-heating as the primary limitation for $\alpha_{\min}$ in this system.

The 400 V data shows an entirely different behavior, where the minimum in $\alpha_{\min}$ does not occur at the lowest number of ions. However, at this high voltage the crystals are generally less stable and a less systematic behavior might therefore be expected. Nevertheless, the 350 V data also shows some signs of deviation from the general trend similar to the 400 V data, although far less pronounced. These observations illustrate that although there are regions for the trapping parameters where general trends can be identified, these do not apply to the entire parameter space and one should be careful about making predictions based on extrapolations for this type of trap.
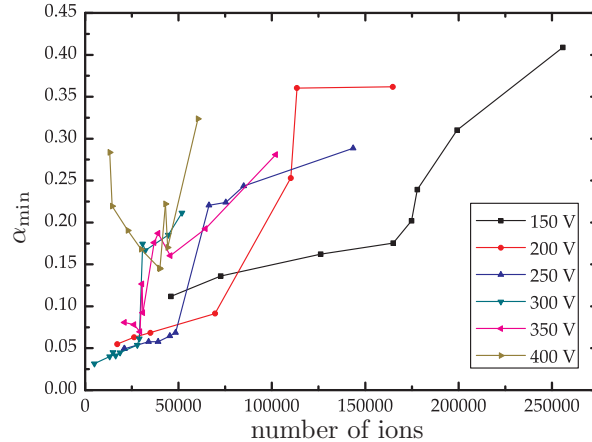
Figure 8.14: Minimal attainable aspect ratio versus the number of ions in the crystal for different different rf-voltages.

From the above measurements of $\alpha_{\min}$, we can estimate the number of ions within the cavity modevolume from eq. C.17 For each value of the rf-voltage the optimal settings are generally those corresponding to the region preceding the appearance the threshold. Fig. 8.15 shows the maximal attainable number of ions in the cavity modevolume $N_{\max}$ as a function of rf-voltage U_{rf}. The number of ions in the cavity modevolume is found to be maximal for rf-voltages near 350 V ($\rho \simeq 8.5 \times 10^8$ cm^{-3}). Here, more than 2000 ions are in the cavity modevolume, which in principle corresponds to a collective coupling strength of $g\sqrt{N} \simeq 2\pi \times 24$ MHz (c.f. eq. C.12). The dashed line in the figure indicates the level above which the number of ions becomes large enough to satisfy the strong collective coupling criterium.

8.4 Conclusion

This chapter has addressed issues regarding the optimization of the trap in order to maximize the number of ions interacting with the cavity field. We have presented a general method for moving the quadrupole minimum of a linear Paul trap in the radial plane and shown results achieved via two different implementations of the general scheme. Both methods allowed us to move the quadrupole minimum with respect to the cavity mode by as much as ± 100 μm and facilitated a near perfect overlap between the ions and the cavity field mode. As this method is quite general it may find use in other experiments; e.g. cavity QED experiments with single ions or in rf-traps where design constraints allows only limited room for adjustments via dc-offsets.

In the second section of this chapter we presented results on the characterization of the trap. Here we found excellent agreement with the theoretical prediction for crystal aspect ratio as a function of the ratio of the trap frequencies. These observations leads us to conclude that the integration of the optical cavity into the linear Paul trap has been accomplished without perturbing the trapping fields.
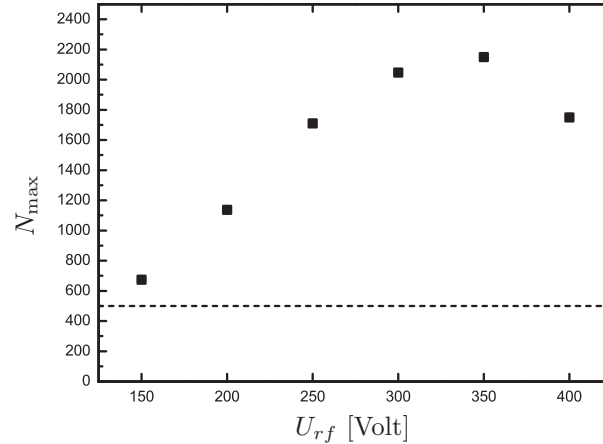
Figure 8.15: Number of ions in the cavity mode volume versus rf-voltage. The interval from 150 V to 400 V corresponds to ion densities between $1.6 \times 10^8 - 1.1 \times 10^9$ cm^{-3}. The dashed line indicate the level above which the criterion for strong collective coupling is potentially satisfied.

Furthermore, based on the trap characterization, the relative uncertainty in our determination of the crystal density is below 2 %, which combined with our present precision in measuring the crystal volume (see appendix B) results in a relative uncertainty in the number of ions of only $2 - 4$ %. For typical crystal sizes this precision is better than $1/\sqrt{N}$. More details can be found in appendix B. In this respect we have not yet considered two-component crystals, where under certain trapping conditions the structure can be strikingly regular and simply counting the ions in the images might lower the uncertainty in the number of ions even further. Fig. 3.8 shows one example of such a crystal.

During the course of this characterization we were also able to confirm, with very high accuracy, a prediction made by MD simulations on the structure of ion Coulomb crystals [97]. With these measurements we can give the following experimental bound on the expression for the inter-shell spacing in an ion Coulomb crystal: $\delta r = (1.484 \pm 0.010)a_{\rm ws}$, where $a_{\rm ws}$ is the Wigner-Seitz radius (c.f. eq. 3.22).

Finally, we conducted an experimental study on the various limiting parameters for achieving the highest possible number of ions in the cavity mode. This allowed us to deduce the optimal trapping parameters for our experiments. The optimal rf-voltage for maximizing the number of ions was found to be around 350 V, although for most of the experiments described in the following chapters we have used an rf-voltage of 300 V as we generally find the long term trapping to be more stable at this value.

For all values of rf-voltage ranging from 150-400 V, we found that the criterion for strong collective coupling (eq. 2.38) could be met and collective coupling strengths of up to $2\pi \times 24$ MHz was predicted. In terms of cooperativity for our system, this would correspond to $C \simeq 12$.

During the optimization of the trap, we observed the appearance of a threshold-like behavior in the maximally attainable number of stably confined ions, which we

ascribed to a complex interplay of the heating and cooling rates within the system. Although not fully understood at present, we suspect this feature to be governed principally by rf-heating.

Chapter 9

State preparation

This chapter deals with the state preparation of the ensemble of the trapped cold ions. This represents an important step in the experiments on the coherent coupling between the ion Coulomb crystal and the cavity field that will be the focus of the succeeding chapter. We begin in ch. 9.1 by a theoretical analysis of the optical pumping scheme employed to realize efficient state preparation. Supplementary information can be found in appendix E. In ch. 9.2 we describe the experimental setup and in ch. 9.3 we present measurements on the optical pumping efficiency achieved by this scheme. In ch. 9.4 we discuss the lifetime of the prepared state and the coherence time of our system. Finally, in ch. 9.5 we conclude on the state preparation.

9.1 Optical pumping of $^{40}\text{Ca}^+$

Fig. 9.1 shows the level scheme of Ca^+ including the magnetic sub-levels of the $4S_{1/2}$, $4P_{1/2}$ and the $3D_{3/2}$ states. The objective of the state preparation considered in this chapter is to accumulate as many ions as possible in the $3D_{3/2}$, $m_J = +3/2$ state in the shortest amount of time. This is motivated by the following:

- The $3D_{3/2}, m_J = +3/2 \leftrightarrow 4P_{1/2}, m_J = +1/2$ transition at 866 nm has the highest Clebsh-Gordan coefficient (see appendix A) and will hence give rise to the largest coupling strength to the cavity field.

- It is highly desirable to have as many ions as possible in this state due to the scaling of the collective interaction strength $g\sqrt{N}$ between the ions and the field (see ch. 2.3).

- The time-issue is especially critical in experiments where the cavity is scanned. Each point in the cavity spectrum is the result of an experimental sequence (see ch. 6.7) which consists in cooling, state preparation and probing. To avoid excess acoustic noise, the scans have to be taken at a high rate, while at the same time, there should be enough points within a scan to do a proper Lorentzian fit to the data and extract e.g. the width with enough accuracy. This means that only a limited amount of time is available to record each point in the spectrum.

9.1.1   Theory and simulations

To achieve efficient state preparation, we employ the technique of optical pumping. As indicated in fig. 9.1 a σ_+- and a σ_--polarized field at 397 nm drives the $4S_{1/2} \leftrightarrow 4P_{1/2}$ transition, while a σ_+- and a π-polarized field at 866 nm drives the $3D_{3/2} \leftrightarrow 4P_{1/2}$ transition. The $3D_{3/2}$, $m_J = +3/2$ state is not coupled to other states and the ions will thus accumulate here.

The Hamiltonian describing the dynamics of this 8-level system is given by:

$$H = H_{\text{atom}} + H_{\text{L}} + H_{\text{B}}. \tag{9.1}$$

The state populations Π_i and the coherences P_{ij} are defined as in eq. 2.9 and eq. 2.11. With these definitions, the atom Hamiltonian H_{atom} is given by,

$$H_{\text{atom}} = \hbar\omega_{\text{sp}} \left(\Pi_2 + \Pi_3 \right) + \hbar \left(\omega_{\text{sp}} - \omega_{\text{dp}} \right) \left(\Pi_4 + \Pi_5 + \Pi_6 + \Pi_7 \right), \tag{9.2}$$

with ω_{sp} and ω_{dp} being the frequency of the $4S_{1/2} \leftrightarrow 4P_{1/2}$ transition and the $3D_{3/2} \leftrightarrow 4P_{1/2}$ transition, respectively. The interaction with the laser fields is described via

$$
\begin{aligned}
H_{\text{L}} = & -\hbar \left(\Omega_+^{\text{sp}} P_{30} + \Omega_+^{\text{sp}\dagger} P_{03} \right) - \hbar \left(\Omega_-^{\text{sp}} P_{21} + \Omega_-^{\text{sp}\dagger} P_{12} \right) \\
& -\hbar \left(\Omega_{+1}^{\text{dp}} P_{24} + \Omega_{+2}^{\text{dp}} P_{35} + \Omega_{+1}^{\text{dp}\,\dagger} P_{42} + \Omega_{+2}^{\text{dp}\,\dagger} P_{53} \right) \\
& -\hbar \Omega_0^{\text{dp}} \left(P_{25} + P_{52} + P_{36} + P_{63} \right),
\end{aligned} \tag{9.3}
$$

where Ω is the Rabi frequency with the superscript indicating the transition and the subscript indicating the polarization ($+$/-: circular, 0: π). The additional subscript 1,2 is added to account for the different Clebsch-Gordan coefficients on the two circular $3D_{3/2} \leftrightarrow 4P_{1/2}$ transitions (c.f. appendix A). In all of our experiments an external magnetic field along z defines the quantization axis for the system. We shall assume that the magnetic field along x and y has been efficiently minimized as described in ch. 6.5 and only treat the effect of the magnetic field along z, which results in a Zeeman splitting of the energy levels accounted for by the final term in eq. 9.1,

$$
\begin{aligned}
H_{\text{B}} = & \frac{1}{2} g_{\text{s}} \mu_B B \left(\Pi_1 - \Pi_0 \right) + \frac{1}{2} g_{\text{p}} \mu_B B \left(\Pi_3 - \Pi_2 \right) \\
& + \frac{1}{2} g_{\text{d}} \mu_B B \left(3\Pi_7 + \Pi_6 - \Pi_5 - 3\Pi_4 \right),
\end{aligned} \tag{9.4}
$$

where μ_B is the Bohr magneton, B is the magnetic field strength and $g_{\text{s,p,d}}$ is the Landé factor, with the subscript indicating the state (see appendix A).

The equations governing the time evolution of the atomic state populations in this eight-level system are derived from the above Hamiltonian H using Hamilton's equation of motion in the rotating wave approximation and including the effect of spontaneous emission, as done for the simple two-level system in ch. 2.1. The result is given in appendix E. Including the coherences, there are 64 coupled first order differential equations which we propagate in time using a classic Runge-Kutta algorithm. Fig. 9.2 shows the time evolution of the atomic population for typical parameters of our experiment where all of the ions are pumped into the right state within 12 μs (dashed, blue line). For technical reasons, that are accounted for in appendix E, the Rabi frequencies of the various polarizations of the 866 nm fields are related via
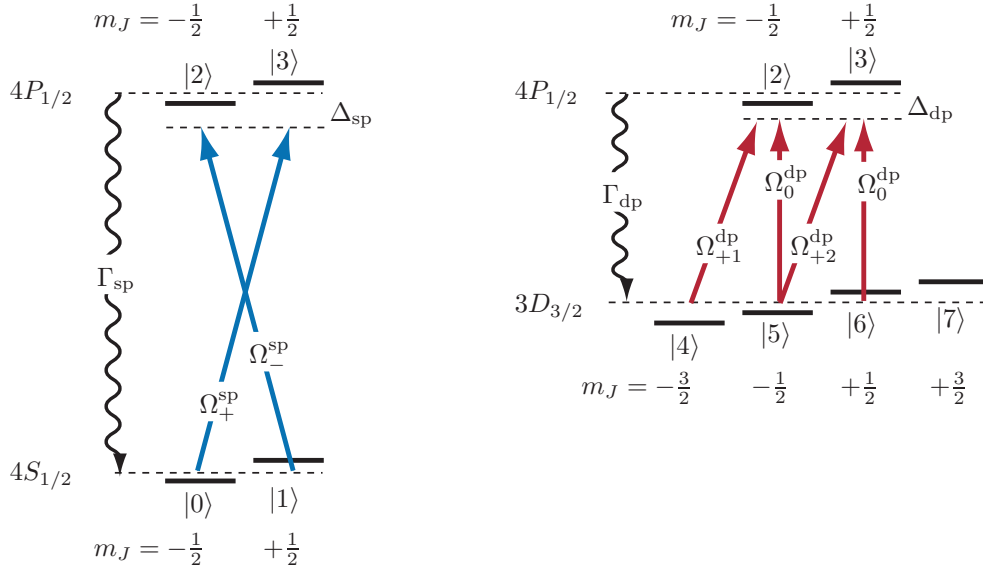
Figure 9.1: Level scheme of the relevant levels and transitions for optical pumping of ^{40}Ca$^+$. Due to the Zeeman effect, the levels are shifted from their unperturbed configuration (dashed lines). Ω denotes the Rabi frequencies of the various transitions, Δ the detunings with respect to the unperturbed transitions and the decay rates Γ are distributed among the magnetic substates according to the Clebsch-Gordan coefficients of those transitions (see appendix A). Γ_{ds} is set equal to zero due to the long life time ($\simeq 1$ s) of the $3D_{3/2}$ state. The state designation $|i\rangle$ where $i = 1, 2, 3, 4, 5, 6, 7$ is used in the equations of motion (see text).

$\Omega_0^{\mathrm{dp}} = \Omega_{+2}^{\mathrm{dp}} = \sqrt{\frac{1}{3}}\Omega_{+1}^{\mathrm{dp}}$ and for simplicity we shall therefore define $\Omega^{\mathrm{dp}} \equiv \Omega_{+1}^{\mathrm{dp}}$, which is the quantity we will be refering to in the following.

In practice there are several factors making the actual experimental conditions different from the idealized scenario modeled here, and deviations from the theoretical predictions are naturally expected. Nevertheless, the simulations may still serve as a useful guide for optimizing the various parameters. To this end, we study the dependence of the optical pumping efficiency on parameters such as Rabi frequencies and detunings. In the simulations, optical pumping is on for 12 μs after which the population in the $3D_{3/2}$, $m_J = +3/2$ state (Π_7) is measured. Fig. 9.3a) shows the dependence of the optical pumping efficiency on the Rabi frequencies of the fields for $\Delta_{\mathrm{sp}} = 2\pi \times 28$ MHz, $\Delta_{\mathrm{dp}} = 0$ MHz, which are the typical detunings used for Doppler cooling of the ion Coulomb crystals. The first thing to notice is that the optical pumping efficiency does not vary much with Ω^{dp} and, for Rabi frequencies on the $4S_{1/2} \leftrightarrow 4P_{1/2}$ transition above $\Omega^{\mathrm{sp}} = 2\pi \times 10$ MHz, a plateau close to 100% is found. Fig. 9.3b) and c) show the the dependence of the optical pumping efficiency on the detunings of the fields for $\Omega^{\mathrm{sp}} = 2\pi \times 15$ MHz and $\Omega^{\mathrm{sp}} = 2\pi \times 7$ MHz, respectively. In both figures $\Omega^{\mathrm{dp}} = 2\pi \times 14$ MHz. The conclusion is that the optical pumping does not depend very strongly on Δ_{dp} and that only for low values of Ω^{sp} does Δ_{sp} become critical. Given the relative strength of the two transitions ($\Gamma_{\mathrm{sp}}/\Gamma_{\mathrm{dp}} \simeq 12$) it is not surprising that the $4S_{1/2} \leftrightarrow 4P_{1/2}$ transition should be the critical one and that, in
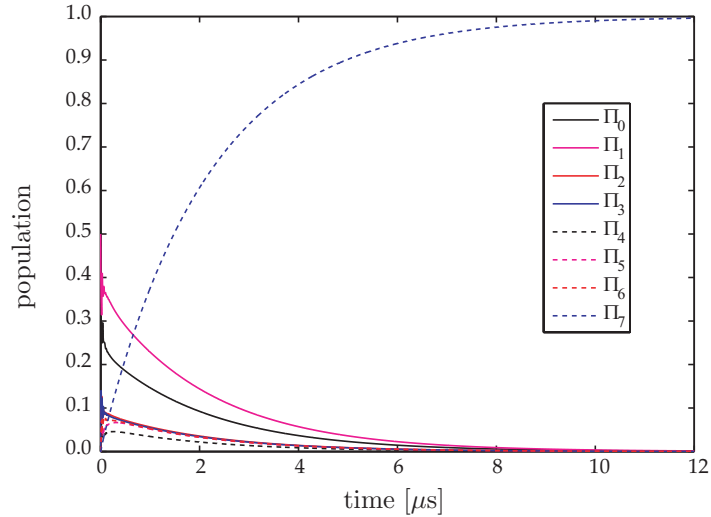
Figure 9.2: Time evolution of the atomic population starting from 50% in each of the two $4S_{1/2}$ states (Π_0 and Π_1) and resulting in 100% accumulation in the $3D_{3/2}, m_J = +3/2$ state (Π_7) after 12 μs. Perfect coherence is assumed between all fields and the parameters used in the simulation are $\Omega^{\mathrm{sp}} = 2\pi \times 15$ MHz, $\Omega^{\mathrm{dp}} = 2\pi \times 14$ MHz, $\Delta_{\mathrm{sp}} = 2\pi \times 28$ MHz, $\Delta_{\mathrm{dp}} = 0$ MHz and $B = 3$ G.

order to achieve efficient optical pumping, this transition should be driven strongly.

9.1.2 Limiting effects

In all simulations we have assumed perfect coherence between all the fields. In reality the two lasers at 397 nm and 866 nm are locked to different reference cavities and can not be expected to exhibit perfect phase coherence over longer times. The effect can be included in the equations of motion by adding a phenomenological decay term in the optical coherences between the $4S_{1/2}$ and the $3D_{3/2}$ states. For decay rates up to $\sim$MHz the effect seen in the simulations is still quite small and has thus been omitted here.

The fields driving the σ and π transitions on the $3D_{3/2} \leftrightarrow 4P_{1/2}$ transition are, as we shall see below, derived from the same laser and may thus be expected to exhibit good phase coherence on the timescale of the optical pumping. From measurements of the linewidth of this laser (see ch. 5.2) we expect coherence times of ~ 10 μs which is indeed comparable to the optical pumping time. Stimulated Raman processes might thus be expected to be driven by the Ω_+^{dp} and Ω_0^{dp} fields, giving rise to dark states and coherent trapping of population [166] in the states $|4\rangle, |5\rangle, |6\rangle$ (c.f. fig. 9.1). To avoid this, and, hence, a lower optical pumping efficiency, it is critical that a magnetic field is applied to Zeeman shift the magnetic sub-states and, thereby, destroy the otherwise perfect two-photon resonance between the Ω_+^{dp} and Ω_0^{dp} fields. Our simulations show that the effect is significantly diminished at magnetic field strengths around 1 G, for typical Rabi frequencies and detunings, and at a magnetic field of 3 G, which we commonly use, the effect can safely be neglected.
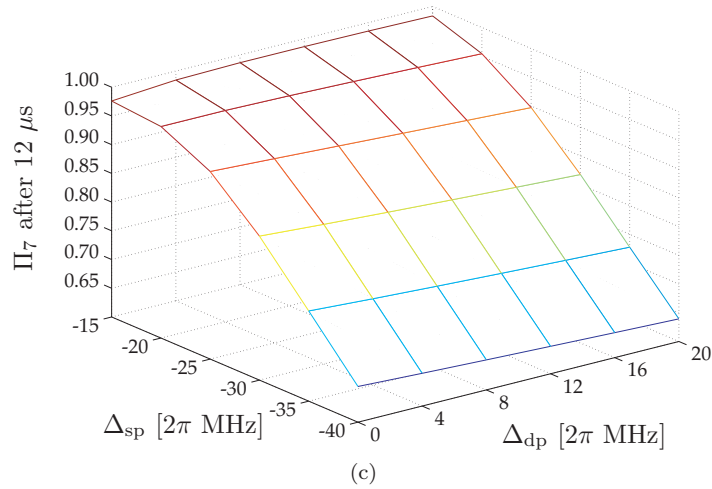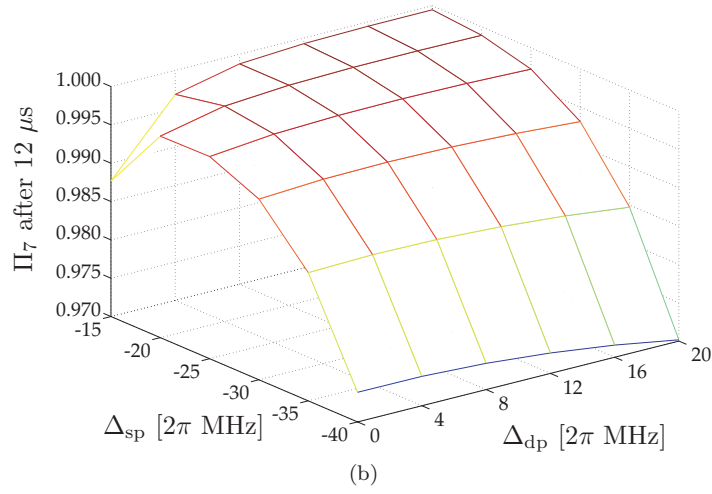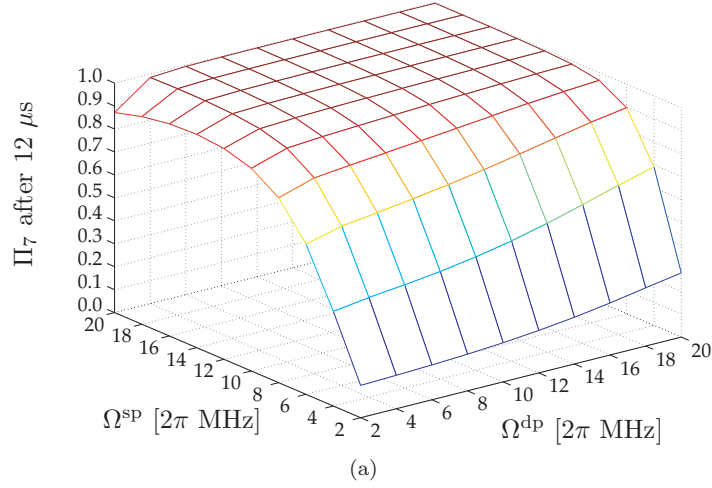
Figure 9.3: Population in $3D_{3/2}$, $m_J = +3/2$ state (Π_7) after 12 μs of optical pumping (a) as a function of Rabi frequencies for $\Delta_{\text{sp}} = 2\pi \times 28$ MHz, $\Delta_{\text{dp}} = 0$ MHz, (b) as a function of detunings for $\Omega^{\text{sp}} = 2\pi \times 15$ MHz, $\Omega^{\text{dp}} = 2\pi \times 14$ MHz and (c) as a function of detunings for $\Omega^{\text{sp}} = 2\pi \times 7$ MHz, $\Omega^{\text{dp}} = 2\pi \times 14$ MHz. In all simulations $B = 3$ G and perfect coherence is assumed between all fields.

Finally, there is the effect of imperfect polarization of the 866 nm optical pumping field, which may lead to a non-vanishing σ_- component. This will depopulate the $3D_{3/2}$, $m_J = +3/2$ state ($|7\rangle$) and lower the optical pumping efficiency. Fig. 9.4 shows how the population accumulated in the $3D_{3/2}$, $m_J = +3/2$ state after 12 μs of optical pumping decreases as the Rabi frequency Ω_-^{dp} is increased. At a Rabi frequency of $\Omega_-^{\mathrm{dp}} = 0.02\Omega_+^{\mathrm{dp}}$, the optical pumping efficiency has dropped below 90%. This means that to stay above 90%, the power in the different polarization components has to be controlled to the level of 4×10^{-4}. The simulations also reveal that the result of an imperfect polarization of the optical pumping beam at 866 nm is that more population is left in the $4S_{1/2}$ state. To some extent, the effect can therefore be compensated by increasing the Rabi frequency Ω^{sp} on the $4S_{1/2} \leftrightarrow 4P_{1/2}$ transition.

9.2   Setup

Fig. 9.5 shows a drawing of the setup used for optical pumping. The quantization axis is defined by a magnetic field along the trap axis as described in ch. 6.5. Cooling is done as discussed previously with the 397 nm beams counter propagating along the trap axis with σ_+/σ_- polarization and the repumper along the x-axis linearly polarized along y. In appendix E.1 we show that a single 866 nm beam at $45°$ with a specific polarization can be used to drive the σ_+ and π transitions necessary for optical pumping. The scheme is then achieved by turning off the repumper and turning on another 866 nm beam at $45°$ (866 OP in fig. 9.5). An alternative scheme would be to use two independent beams, one propagating along the x-axis, polarized along z, driving the π transitions and one propagating along the z-axis, circularly polarized, driving the σ_+ transitions. Implementing the latter beam is complicated in practice however, as it requires the optical resonator in the trap to be resonant with this beam,
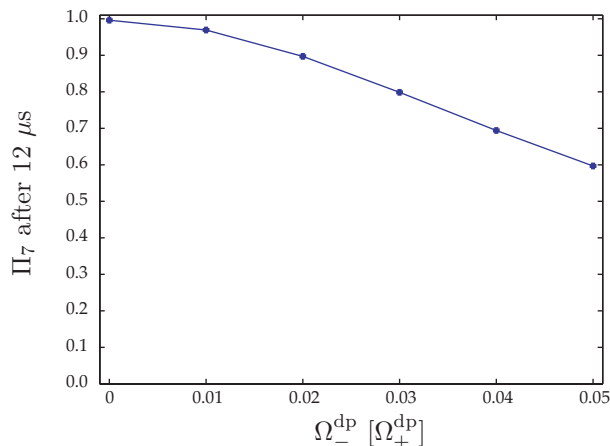
Figure 9.4: Population in $3D_{3/2}$, $m_J = +3/2$ state (Π_7) after 12 μs of optical pumping as a function of Ω_-^{dp} in units of Ω_+^{dp}. Perfect coherence is assumed between all fields and the parameters used in the simulation are $\Omega^{\mathrm{sp}} = 2\pi \times 15$ MHz, $\Omega^{\mathrm{dp}} = 2\pi \times 14$ MHz, $\Delta_{\mathrm{sp}} = 2\pi \times 28$ MHz, $\Delta_{\mathrm{dp}} = 0$ MHz and $B = 3$ G.
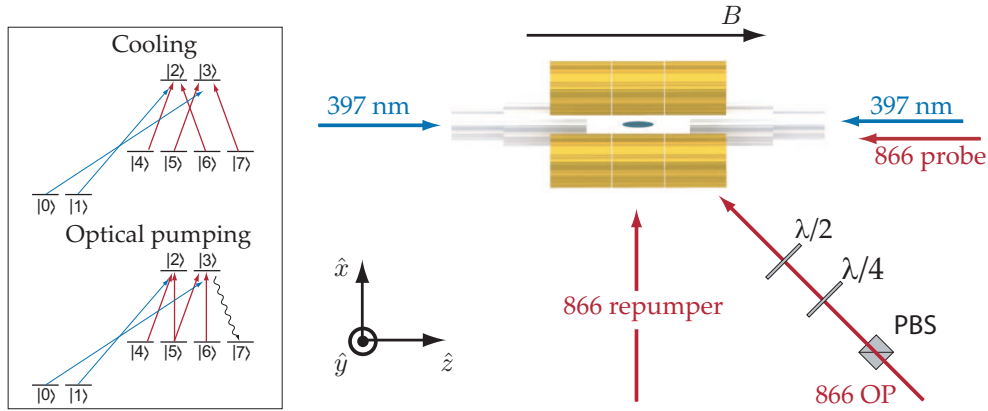
Figure 9.5: Setup for optical pumping. The insert shows the cooling and the optical pumping scheme, respectively. See text for details.

which is not possible in all experiments.

A problem with using a beam at 45° to the trap axis is that the transitions are Doppler broadened due to the radial micromotion of the ions. This results in a lower effective Rabi frequency as well as in the detuning not being well defined in neither time nor space. However, the conclusion from our simulations on the optical pumping efficiency is that neither the Rabi frequency nor the detuning of the 866 nm laser are particularly critical. At least for the ions within the cavity mode volume, we do not expect the 45° geometry to be a problem. The reason is that these ions exhibit the least amount of micromotion due to their proximity to the nodal line of the rf-field, contrary to the outer ions of the crystal.

To ensure the right polarization of the 45° optical pumping beam, a $\lambda/2$-plate and a $\lambda/4$-plate are set up following a PBS. The PBS ensures near-perfect horizontal polarization which is subsequently turned into an elliptical polarization by the $\lambda/4$-plate, by an amount calculated in appendix E.1. The $\lambda/2$-plate is there to compensate for imperfections in the optics and birefringence in e.g. the viewport of the vacuum chamber. When the polarization is such that the beam only drives the σ_+ and the π transitions and the 397 nm beams are on, the ions are optically pumped into the $3D_{3/2}$, $m_J = +3/2$ state. As a result they no longer scatter photons and the fluorescence drops. This effect is seen in fig. 9.6 which shows the measured fluorescence from the ion Coulomb crystal for various orientations of the $\lambda/4$-plate. The horizontal axis is calibrated with respect to the optimal value such that this is at 0°. Here the ions are lost due to heating as a result of the low scattering rate.

9.3 Optical pumping efficiency

The measurements presented in fig. 9.6 were steady state measurements of the scattering rate. This rate is proportional to the exited $4P_{1/2}$ state population and does not provide any information about the population in the desired $3D_{3/2}$, $m_J = +3/2$ state or about the optical pumping time. For such measurements we make use of the
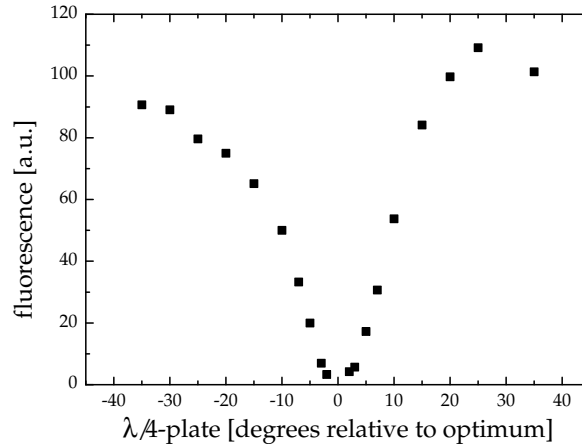
Figure 9.6: Fluorescence vs. wave plate orientation.

PMT (see fig. 6.9) to detect the fluorescence in time and probe the $3D_{3/2}$, $m_J = +3/2$ state by injecting an 866 nm σ_--polarized probe into the trap cavity, resonant with the ions. The full sequence is drawn in fig. 9.7 and, throughout the entire sequence, the fluorescence is monitored with the PMT, which then provides time resolved data. Also indicated is a time-delay between the end of the optical pumping and probe. This is used in measurements of the population lifetime (see ch. 9.4) and is set to zero, otherwise.

Fig. 9.8 shows examples of such measurements. In a) and b) the cooling lasts for the first 5 μs, corresponding to the level around 2 counts per bin, after which the 866 nm repumper is turned off. The optical pumping beam is then on for 12 μs during which the fluorescence level decreases as ions are pumped into the $3D_{3/2}$, $m_J = +3/2$ state. The optical pumping beam is then turned off along with the 397 nm beams which causes the fluorescence to drop to zero. At time t=20 μs the probe is turned on and pumps the ions back into the $4S_{1/2}$ state. The fluorescence at 397 nm collected during the probing is a measure of the population in the magnetic sub-state addressed by the probe. The inserts in the upper right corner of each graph shows which states are probed and how the population is expected to be distributed based on the optical pumping. The fact that the signal recorded by probing with σ_--polarized light (a) is significantly higher than the signal for σ_+ (b) indicates that the optical pumping scheme is working well.

Fig. 9.8c) and d) are based on measurements where the optical pumping beam was not turned on [1] and the ions are then distributed evenly among the four magnetic sub-states due to the relative branching ratios of the decay channels between the $4P_{1/2}$ and the $3D_{3/2}$ state (c.f. appendix A). This means that both the σ_- and σ_+ probe

---

[1] The non-zero fluorescence count rate of about 0.25 pr. bin during this time corresponds to the background level of the 397 nm beams, due to Rayleigh scattering in the mirror substrates.
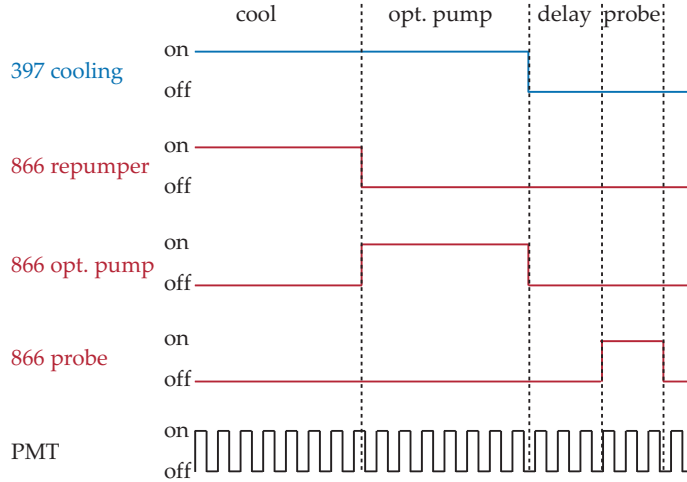
Figure 9.7: Experimental sequence. The delay is only used in measurements of the population life time and is otherwise set to zero.

should produce a signal corresponding to half the ions. By comparing the height of the signals generated by the probe in all four graphs, we can give an estimate for the optical pumping efficiency. If we denote the height of the fluorescence signal due to the probe by $\Pi(i)$ with $i = $ a, b, c, d corresponding to each of the four graphs, then we can express the optical pumping efficiency as either

$$\eta_{\mathrm{OP}} = \frac{\Pi(a)}{\Pi(a) + \Pi(b)}, \text{ or} \qquad (9.5a)$$

$$= \frac{\Pi(a)}{\Pi(c) + \Pi(d)}. \qquad (9.5b)$$

Note that these expressions actually overestimates the efficiency, though, as ions in the $3D_{3/2}, m_J = +1/2$ state also contributes to $\Pi(a)$, which should ideally only have contributions from the $3D_{3/2}, m_J = +3/2$ state. A way around this would be to apply a strong magnetic field to split the magnetic sub-states such that they can be resolved by the probe. However, as the width of the transition is $\Gamma = 2\pi \times 22.4$ MHz this would require a magnetic field stronger than what can be achieved in the present experimental setup. Alternatively, one can probe with a π-polarized field to measure the population in the two $3D_{3/2}, m_J = \pm 1/2$ states, however, since the quantization axis coincides with the cavity axis, it requires probing with a beam that is perpendicular to the cavity. This means that it does not probe the exact same ions as the $\sigma_\pm$ probe, making this method non-ideal for comparison of the different probe signals. Nevertheless, to provide an estimate, we have performed measurements with a π-polarized field. By comparing signals obtained with and without prior optical pumping, we find that the population in the $3D_{3/2}, m_J = \pm 1/2$ states is around 2%. From this and from measurements similar to those of fig. 9.8 we typically find optical pumping efficiencies of $(97^{+3}_{-5})\%$. Increasing the optical pumping time beyond the
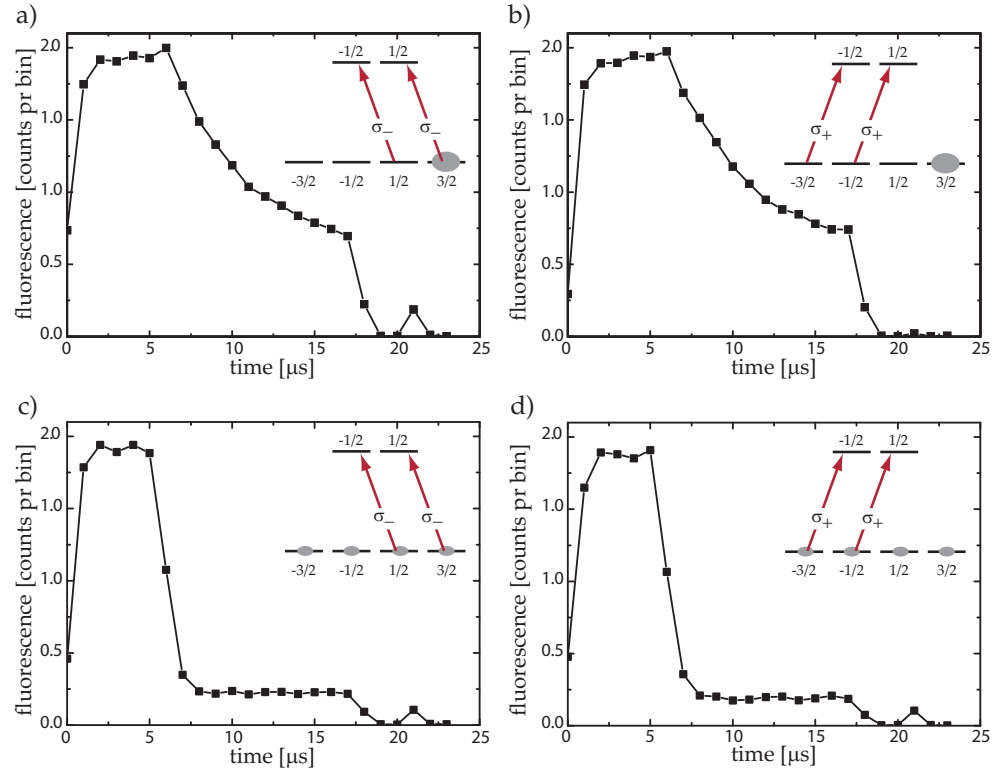
Figure 9.8: Fluorescence measurements during optical pumping sequence based on an average of 100 sequences. The inserts show the probing scheme in each experiment. a) and b) are from measurement with optical pumping whereas c) and d) are based on measurements without optical pumping. All graphs are based on an average of 100 experimental sequences. The parameters during the experiments were, $\Delta_{\mathrm{sp}} = 2\pi \times 28$ MHz, $\Delta_{\mathrm{dp}} = 0$ MHz, $\Omega^{\mathrm{sp}} = 2\pi \times 15$ MHz, $\Omega^{\mathrm{dp}} = 2\pi \times 14$ MHz and $B = 3$ G. The Rabi frequencies are calculated based on the formulas in appendix E.2.

12 μs is not found to increase the efficiency further, which indicates that the system has reached steady state and that there is some competing process depopulating the $3D_{3/2}, m_J = 3/2$ state. This could originate from imperfect polarization of the optical pumping beam as discussed in ch. 9.1.2.

The main contribution to the uncertainty in the above measurements is the relatively low signal strength. To ensure that we are probing the ions that will later interact with the cavity field, we only probe through the cavity and for this reason at most a few thousand ions can contribute to the signal. With the small numerical aperture of our imaging system (see ch. 6.4) the collection efficiency is quite low and we are detecting less than a photon on average during the PMT bin time of 0.5 μs.

9.4   Lifetime and coherence time of the $3D_{3/2}$ states

An interesting parameter to measure is the lifetime of the population in the $3D_{3/2}$, $m_J = +3/2$ state after the optical pumping has been completed. This is commonly referred to as the T_1 time and is closely related to the T_2 time, which describes the coherence time of the system, here the coherence between magnetic sub-states of the $3D_{3/2}$ state [167]. If the experiment is perfectly shielded from external perturbations, T_1 is set by the spontaneous decay rate of the state, which for the $3D_{3/2}$ state makes it about 1 s. Likewise, if external perturbations results in only homogeneous broadening, signified by Lorentzian lineshapes of the atomic transitions, the T_2 time will be equal to the T_1 time.

In reality, effects such as stray magnetic fields and collisions may potentially limit the life- and coherence times. These effects contribute in different ways to the time evolution of the atomic population and we shall give an estimate of their effect and relevance for the experiment in the following.

- **Magnetic fields** can give rise to oscillatory motion between the different magnetic sub-states due to Larmor precession induced by magnetic field components perpendicular to the quantization axis. Furthermore, stray magnetic fields can not be expected to be perfectly homogeneous across the ~ 1 mm crystal and different ions will thus have their states precess at different rates, eventually redistributing the atomic population evenly among all four magnetic sub-states of the $3D_{3/2}$ state. This will be observed as a decay of the $3D_{3/2}, m_J = +3/2$ state toward a steady state value of $1/4$.

  For the $3D_{3/2}$ state, the Larmor frequency is ~ 1 kHz/mG, however, with a strong magnetic field defining the quantization axis, the effect can be suppressed further. With a bias field of ~ 1G and stray fields of the order of $\sim$mG the effect should be significantly diminished, as least to the level of the ~ 1 Hz spontaneous decay rate of the $3D_{3/2}$ state.

  The effect of stray magnetic fields has indeed previously been estimated to a level around or below 1 mG and with gradients below 0.1 mG/mm for this experiment [66]. It was, however, only based on measurements of magnetic fields and gradients arising from local magnetic sources and from fields induced by the currents of the rf-voltage for the trap and has not yet been confirmed by spectroscopic measurements on the trapped ions. It should the pointed out that the effect of fluctuating magnetic fields, e.g. induced by the rf-fields of the trap, will impose limitations on the T_2 time that are not compensated by the bias magnetic field. Basically, it gives rise to fluctuating energy levels, which dephase the atomic dipoles, resulting in a loss of coherence. We expect this to be the main source of decoherence in our system [55].

- **Collisions** may occur either between ions within the crystal or via background gas collisions. As the ions are confined in a crystal lattice, the former type is expected to be very low. For inelastic collisions, which will be dominant in this case, the effect will primarily act as a dephasing of the atomic dipole, hence lowering T_2 [167]. Inelastic background collisions will depend on the background pressure as well as on the composition of the background gas and

have been studied extensively for the case of Ca$^+$ ions confined in ion traps [168, 169]. These studies have focused on two types of collisions, either so-called quenching collisions, resulting in population transfer to the $4S_{1/2}$ state, or J-mixing collisions, transferring population to the $3D_{5/2}$ state.

In our present setup we do not have a background gas analyzer and no quantitative analysis of the effect of background gas collisions can thus be made. Experiments measuring the metastable D-states' lifetimes generally find the effect to be of the order of $10^{-2} - 10^{-4}$ Hz [170–172] depending on background gas composition and pressure. Our experiments have been performed at a pressure of $\sim 3 \times 10^{-10}$ mbar, which is generally comparable or about an order of magnitude larger than in those experiments. By comparison, it seems reasonable to assume that the effect of both J-mixing and quenching collisions will be negligible compared with the 1 Hz spontaneous decay rate, in our experiments.

Background collisions may of cause also result in mixing within the J-manifold, transferring population between different m_J sub-states of the $3D_{3/2}$ state. As with the quenching and J-mixing collisions, this is not expected to contribute significantly on a $\sim s$ timescale. Indeed, experiments on a single ^{40}Ca$^+$ ion in an ion trap at a similar background pressure as in our experiments and where optical pumping also prepared the ion in a specific magnetic sub-state, have found background gas collisions to have a negligible effect on the lifetime of that state [135].

9.4.1   Lifetime of the $3D_{3/2}, m_J = +3/2$ population in the cavity mode

To perform measurements of the lifetime of the $3D_{3/2}, m_J = +3/2$ state we employ an experimental sequence similar to that used for the measurements of the optical pumping efficiency (fig. 9.7) but, this time, varying the delay between the optical pumping and the probing. Similarly, we probe with σ_- and σ_+ polarized light to measure both the population in the $m_J = +1/2$ and $m_J = +3/2$ states (blue data points in fig. 9.9) as well as the population in the $m_J = -1/2$ and $m_J = -3/2$ states (red data points in fig. 9.9). Both sets of data have been normalized to a total population, which we define to be the average value of the data where no optical pumping was done (smaller, green and brown data points). As only one measurement can be taken in each experimental run, the signals are not correlated and will not necessarily add up of 1 due to fluctuations as a result of low count rates.

The data taken by probing without prior optical pumping (green and brown data), shows that the total population in the $3D_{3/2}$ state remains constant on the timescale of the 5 ms of the graph and shows no indication of a decay on a ~ 10 ms timescale. This confirms our assumption that neither quenching nor J-mixing collisions are relevant on this time scale.

Since the population in the $3D_{3/2}$ state is conserved, any decay of the population in the $m_J = +1/2$ and $m_J = +3/2$ states, measured by the σ_- probe (blue points), must be accompanied by an increase in the population in the $m_J = -1/2$ and $m_J = -3/2$ states, measured by the σ_+ probe (red points). Although the data is quite noisy, this is in fact observed and from exponential fits we deduce a rate of 12 ± 8 ms for the
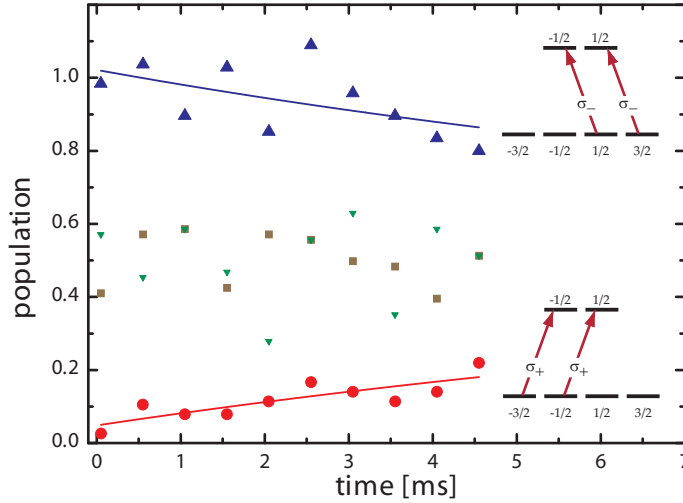
Figure 9.9: Population versus time after optical pumping was completed. Blue data are for a σ_- probe and red data are for a σ_+ probe, both after optical pumping. Exponential fits to both the data sets gives $T_1 = (13 \pm 3)$ ms. Green data are for a σ_- probe and brown data are for a σ_+ probe, both measured without prior optical pumping. These are used to normalize the data.

decay of the blue data and 13 ± 3 ms for the growth of the red data, which combined gives an overall rate of 13 ± 3 ms.

Based on the analysis, given in the introduction of ch. 9.4 of possible limitations in the system, it is surprising to observe a decay on this short a time scale. One effect that could potentially be a problem (and the reason for only taking data up to 5 ms) is the fact that as the delay was increased the ions would begin to heat up. The reason for this is that once a relatively large part of the experimental sequence consists of a delay, the average cooling power applied over the sequence becomes too small to compensate the heating rates within the system and typically we begin to loose the ions after approximately 5 ms. Although this heating might give rise to an increase in the elastic collision rate within the crystal, hence lowering T_2, the inelastic collision rate should still be very low and there is no reason to expect that this should effect the T_1 time.

On possible explanation could be that what we are observing is in fact radial diffusion within the ion Coulomb crystal. If we assume that optical pumping is less efficient further away from the trap center, which could be due to the radial micro-motion of the ions, then as the delay is increased we will be probing a larger fraction of these less efficiently pumped ions, as they diffuse into the cavity mode. In this case the notion of a T_1 time is a bit misleading and diffusion time is then the correct term. This remains to be confirmed, however, given the expected influence of other possible limiting effects, as we have discussed above, it seems highly probable that the decay we have measured is in fact due to diffusion of the ions in the crystal.

9.4.2   Coherence time

At the time of writing no measurements on the coherence time T_2 has been performed. For all coherent processes and e.g. for the purpose of using the ensemble as a quantum memory [48,49,173] T_2 is the parameter of interest. The coherence properties of single ^{40}Ca$^+$ ions have been studied by the Innsbruck group, where the coherence time of a qubit based on the $4S_{1/2} \leftrightarrow 3D_{3/2}$ transition has been measured [55]. Coherence times of $\simeq 1$ ms were found and magnetic field- and laser frequency fluctuations were identified as principal limitations. Indeed, experiments on Bell states of two ^{40}Ca$^+$ ions that are insensitive to magnetic field fluctuations have reported coherence times that were essentially limited by the $\simeq 1$ s lifetime of the $3D_{5/2}$ state [56]. Furthermore, the (first order) magnetic field insensitive systems, such as the hyperfine clock states of ^{43}Ca$^+$ [174, 175] and ^{9}Be$^+$ [30], have demonstrated coherence times of $1 - 10$ s.

As described in ch. 6.5 the earth's magnetic field is compensated via external field coils, but no passive shielding, e.g. by μ-metal, or active stabilization, by e.g. a Hall probe and feedback setup, is installed at present (see e.g. [55, 176]). We may thus expect fluctuating magnetic fields to impose limitations on the coherence times as found in [55], although this remains to be investigated.

The issue of heating found for our lifetime measurements described above could potentially impose limitations to coherence time measurements. For instance, measurement schemes relying on longer time sequences, such as decay of either Rabi oscillations or contrast of Ramsey fringes as done in e.g. Ref. [55], will also be subject to heating effects during the measurements. An electromagnetically induced transparency (EIT)-type experiment [177], on the other hand, may be able to provide direct information about the decoherence rate between two magnetic sub-states of the $3D_{3/2}$ state since the absorption at two-photon resonance depends on this quantity.

9.5   Conclusion

In this chapter we have presented the scheme used for the state preparation of the ensemble of ions. The scheme was first analyzed through numerical simulations and then tested to find that about 97% of the ions can be optically pumped into the $3D_{3/2}, m_J = +3/2$ state within 12 μs. This will serve as the starting point for the experiments to follow where we will study the interaction of such an ensemble of optically pumped ions with the field of an optical resonator in the framework of cavity QED.

We have also presented measurements of the lifetime of the population in the $3D_{3/2}, m_J = +3/2$ state. We stress that the obtained data is quite preliminary and further investigations should be conducted to clarify if the observations stem from diffusion within the crystal. For this reason, the value of 13 ± 3 ms can only be interpreted as the lifetime of $3D_{3/2}, m_J = +3/2$ population within the cavity mode. The actual T_1 time is expected to be much higher and, in the ideal case, given by the 1 Hz spontaneous decay rate of the $D_{3/2}$ state. Further studies, e.g. using a two-component crystal that would allow for continuous cooling during the experiments, as described in ch. 4.3, would be advantageous in this respect. This would enable measurements with considerably longer delay times and ensure a constant diffusion rate by having the cooling independent of the delay time.

Chapter 10

Cavity QED with calcium ion Coulomb crystals

In this chapter we will study our system of ion Coulomb crystals in the context of cavity QED. We begin in ch. 10.1 by a theoretical analysis to justify the treatment of our multi-level ^{40}Ca$^+$ ions as simple two-level systems. Following this, we briefly sketch the experimental setup in ch. 10.2 after which, in ch. 10.3, we present results on the observation of collective strong coupling of ion Coulomb crystals in the context of cavity QED. Here we evaluate the system and measure parameters such as the single ion coupling strength and the cooperativity parameter. In ch. 10.4 we measure the optical pumping efficiency - this time through the collective interaction between the ions and the cavity field. Finally, in ch. 10.5 we conclude.

10.1 Reduction to a quasi- two-level system

In ch. 2.3 we established the theoretical framework for a collection of two-level atoms interacting with a cavity field. However, ^{40}Ca$^+$ ions are not ideal two-level systems but contain a much richer level structure, as can be seen, e.g., in fig. 9.1. To mimic the two-level scenario, we prepare our ensemble of ions in the $3D_{3/2}, m_J = +3/2$ state as described in ch. 9 and probe on the $3D_{3/2}, m_J = +3/2 \leftrightarrow 4P_{1/2}, m_J = +1/2$ transition with the cavity field. The level scheme applicable to this scenario is shown in fig. 10.1. We shall consider the $3D_{3/2}, m_J = +3/2$ state, denoted by $|g\rangle$, as the ground state, which is a meaningful designation as the ~ 10 ms decay time measured in the previous chapter is still orders of magnitudes longer than all other time scales in the system. The excited $4P_{1/2}, m_J = +1/2$ state, denoted $|e\rangle$, can decay back to the ground state at a rate Γ' or to any of the other states in ^{40}Ca$^+$, such as the remaining magnetic sub-states of the $3D_{3/2}$ state or the $4S_{1/2}$ state (see e.g. fig. 9.1 of the previous chapter). This occurs at a rate Γ_{other}. With a single photon in the cavity, the Rabi frequency on the $3D_{3/2}, m_J = +3/2 \leftrightarrow 4P_{1/2}, m_J = +1/2$ transition is given by g for each ion[1]. In the theoretical framework for the cavity QED interaction that we established in ch. 2.3, we assumed a steady state situation in which N ions were in

---

[1]In reality the ions are coupled with different strengths to the field depending on their location in the standing wave TEM$_{00}$ mode of the cavity. We account for this by weighting the number of ions N by the cavity mode function. See appendix C for details.
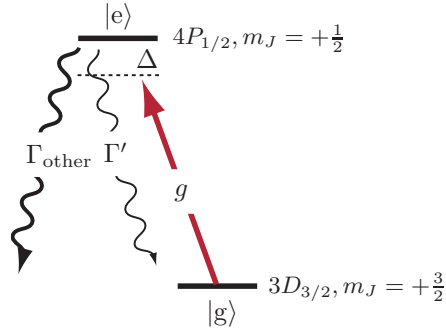
Figure 10.1: Quasi two-level scheme of $^{40}\text{Ca}^+$ prepared by optical pumping to the $3D_{3/2}, m_J = +\frac{3}{2}$ state. Γ' is the spontaneous decay rate on the $3D_{3/2}, m_J = +3/2 \leftrightarrow 4P_{1/2}, m_J = +1/2$ transition, wheras Γ_{other} represent the decay to all other levels.

the ground state and could thus derive measurable parameters such as a transmission or a reflection coefficient. However, due to the irreversible coupling to states outside the two-level system, the long-term steady state solution will be one in which no ions are in the $3D_{3/2}, m_J = +3/2$ state and the coupling to the cavity field will thus vanish on longer time scales. This prompts a study of the different time scales in the system to examine if one may identify a time domain in which a form a quasi-steady state exists that allows the use of the two-level steady state formalism of ch. 2.3.

10.1.1   Quasi-steady state probing scheme

We begin by recalling the equations for the atomic population and coherence (eq. 2.12) and the cavity field (eq. 2.30), which now read (neglecting the effect of the magnetic field):

$$
\begin{aligned}
\dot{\Pi}_{\text{g}} &= \Gamma' \Pi_{\text{e}} + i \left(g A^* P - g A P^* \right) \\
\dot{\Pi}_{\text{e}} &= -\Gamma \Pi_{\text{e}} - i \left(g A^* P - g A P^* \right) \\
\dot{P} &= -\left(\Gamma/2 + i\Delta \right) P - i g A \left(\Pi_{\text{e}} - \Pi_{\text{g}} \right) \\
\dot{A} &= -\left(\kappa + i\Delta_c \right) A + i g P + \sqrt{2\kappa_1} A^{\text{in}},
\end{aligned}
$$

where $\Gamma = \Gamma' + \Gamma_{\text{other}}$. As for the ideal closed two-level system, for a weak probe, almost all the population will be in the ground state. In this low saturation regime the populations evolve slowly and the atomic coherences follow these adiabatically. The condition for this to be valid is that $\Gamma \gg R_{\text{d}}$, where R_{d} is the depopulation rate of the ground state due to the probe. By inserting the steady state solution for the atomic coherence into the equation of motion for the ground state population and assuming that the excited state population can be neglected, we find a rate equation for Π_{g}:

$$
\dot{\Pi}_{\text{g}}(t) = -R_{\text{d}}(t)\Pi_{\text{g}}(t), \text{ with } R_{\text{d}}(t) = \frac{\Gamma \left| g A(t) \right|^2}{(\Gamma/2)^2 + \Delta^2}, \tag{10.1}
$$

where we have included the time dependence implicitly to remind ourselves that the cavity field and, hence, the Rabi frequency $gA(t)$ are not constant. However, as for

the atomic coherences, in the low saturation regime, A evolves much faster than the atomic populations if $\kappa \gg R_d$, and will therefore also follow these adiabatically. To justify our assumption that the depopulation rate R_d is low compared to all other rates, we consider the case where it attains its highest value, namely for $\Delta = 0$. Typically, we will probe the cavity with a field of about one photon, i.e. $|A|^2 = 1$, and with a coupling strength of $g = 2\pi \times 0.53$ MHz we find $R_d = 2\pi \times 0.05$ MHz, which is well below both $\kappa = 2\pi \times 2.1$ MHz and $\Gamma = 2\pi \times 22.4$ MHz for our system.

Fig. 10.2 shows the result of a numerical simulation, which models exactly the above scenario of a single ion resonantly coupled to a cavity field ($\Delta = \Delta_c = 0$), where the input field has been adjusted such that it corresponds to a single photon on average in an empty resonant cavity. It clearly shows the relative time scales for the different processes. The population (dashed blue line) decays as expected on a time scale of $1/R_d \simeq 3$ μs and the cavity field (red solid line) builds up on a time scale of $1/\kappa \simeq 0.1$ μs. Since $\Gamma \gg \kappa$, the atomic coherence (blue solid line) initially follows adiabatically the cavity field, while the ground state population is constant. Then, as the cavity field reaches the 1 photon level and the population begins to decay, the atomic coherence follows the atomic population, as expected. Note that we have only plotted the imaginary part of the atomic coherence, since the real part is zero on atomic resonance.

The results of fig. 10.2 shows that it is difficult to define a quasi-steady state regime on a μs time scale. However, the simulation was performed for a single ion for which a single photon field induces a significant depopulation on this time scale. If more ions are interacting with the cavity field, the effect is reduced as a single photon can only remove one ion at the time and so, for the collective regime that we wish to study, one can expect the population to remain at the initial value for long enough time to probe the interaction.
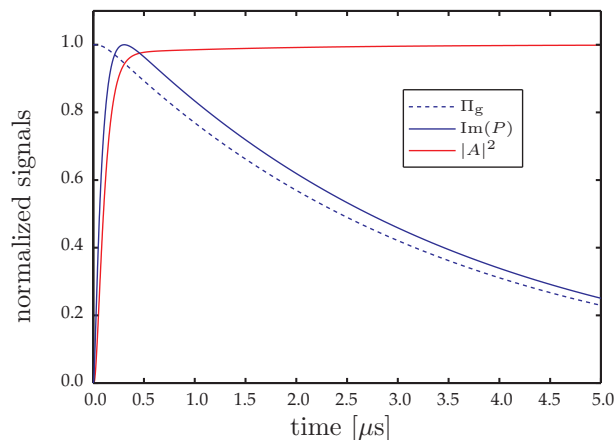
Figure 10.2: Time evolution of the ground state population Π_g, the imaginary part of the atomic coherence P and the cavity photon number $|A|^2$. All parameters have been normalized to their maximal values. Parameters used in the simulation are: $N = 1$, $\Delta = \Delta_c = 0$, $g = 2\pi \times 0.53$ MHz, $\Gamma_{\text{other}} = 2\pi \times (20.7 + 1.7/2)$ MHz, $\Gamma' = 2\pi \times (1.7/2)$ MHz and $\kappa = 2\pi \times 2.1$ MHz.

Fig. 10.3 shows a similar simulation to that of fig. 10.2 but, this time, for an ensemble of $N = 100$ ions. Three time domains can be identified: As in the above, at short times (< 0.1 μs) the cavity field builds up (first frame of fig. 10.3), however, the interaction with the ions now damps the field. The atomic coherence follows the cavity field as before, and both reach a form of steady state after this initial build-up. P and Π_g remain close to constant during the second time domain (second frame of fig. 10.3), which lasts until around 2 μs after the sequence started. It is this second time domain that we identify as the quasi-steady state. Due to the lower cavity field, the atomic population decreases slowly with respect to the 1 ion simulation. However, it still decays over longer time scales allowing the field to build up, hence causing a more rapid decay (c.f. eq. 10.1). This self-reinforcing process eventually leads to a complete depletion of the population, at which point the cavity field reaches a value corresponding to a single photon (third frame of fig. 10.3).

The conclusion from the simulations is that in order to probe the quasi-steady state regime, the measurement should be taken with a short (~ 0.1 μs) delay following the probe and last for at most 2 μs. This will give the field the necessary time to reach quasi-steady state, while at the same time, the probe is short enough, not to cause significant depopulation of the state prepared by the optical pumping. In the experiments to follow, we will use a delay of 0.1 μs and a probe time of 1.4 μs. The average population in the ground state during this time is plotted in fig. 10.4 as a function of the number of ions initially in $|g\rangle$ and confirms that for ensembles of a few hundred ions, the effect of a 1 photon probe field on the population is negligible. Since this analysis has been carried out for the resonant case, the conclusion will be valid when probing in the dispersive regime as well, and we will use this probe time in our sequence for all of the measurements to follow.

10.2 Experimental setup and sequence

The setup for probing and detection as well as the experimental sequence has already been described in ch. 6.6.2, 6.6.3 and 6.7. A drawing of the setup with the optical beams can be found in fig. 9.5 and the experimental sequence is shown in fig. 10.5.
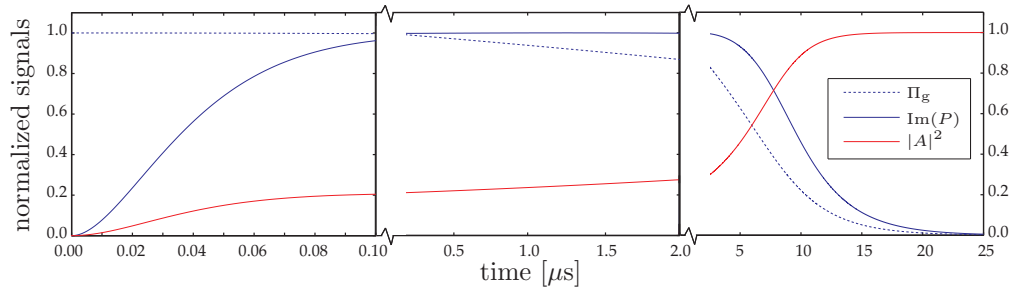
Figure 10.3: Time evolution of the ground state population Π_g, the imaginary part of the atomic coherence P and the cavity photon number $|A|^2$. All parameters have been normalized to their maximal values. Parameters used in the simulation are: $N = 100$, $\Delta = \Delta_c = 0$, $g = 2\pi \times 0.53$ MHz, $\Gamma_{\text{other}} = 2\pi \times (20.7 + 1.7/2)$ MHz, $\Gamma' = 2\pi \times (1.7/2)$ MHz and $\kappa = 2\pi \times 2.1$ MHz.
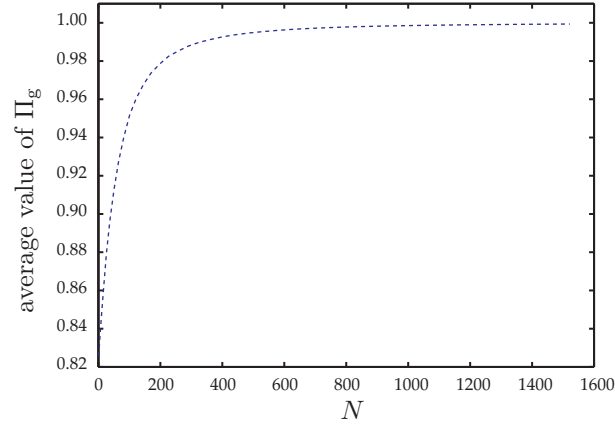
Figure 10.4: Average population Π_{g} during the probe time $[0.1; 1.4]$ μs versus number of ions initially in $|g\rangle$ for a cavity field at the "single photon" level.

The cooling here lasts for 5 μs, followed by 12 μs of optical pumping. As described in ch. 9 this prepares the ensemble of ions in the $3D_{3/2}$, $m_J = +3/2$, typically with 97% efficiency. The probe is then turned on and after a delay of 0.1 μs the APD is turned on for 1.4 μs. The sequence is repeated continuously every 20 μs. In all experiments presented in the following, the 866 nm probe was measured in reflection and the 894 nm laser was used as a reference to process the data and filter out effects of acoustic noise as described in ch. 6.6.3.
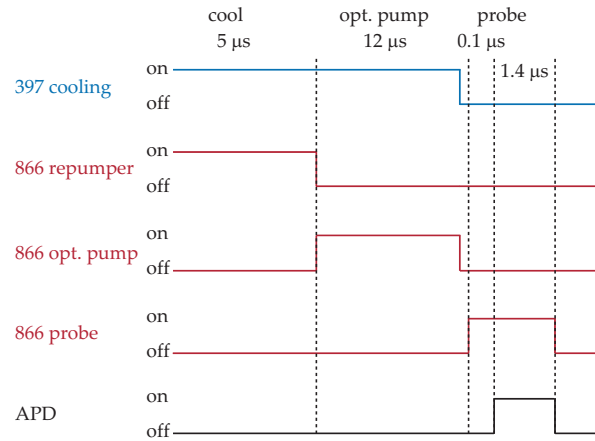
Figure 10.5: Schematic of the experimental sequence. opt.pump abbreviates optical pumping. See text for details.

10.3   Collective strong coupling with an ion Coulomb crystal

10.3.1   Absorption and phase shift

Having identified a quasi-steady state regime in the above, we can make use of the theory of ch. 2.3 for the steady state interaction between an ensemble of two-level ions and a cavity field. When the cavity is scanned across resonance (varying Δ_c) in the presence of the ions we found that the interaction retains the Lorentzian lineshape of the empty cavity but with a half width at half the maximum (HWHM) κ' and a detuning parameter Δ_c' dressed by the ions. Specifically, we found

$$\kappa' = \kappa + g^2 N \frac{\gamma}{\gamma^2 + \Delta^2} \tag{2.32}$$

and

$$\Delta_c' = \Delta_c - g^2 N \frac{\Delta}{\gamma^2 + \Delta^2}, \tag{2.33}$$

where $\gamma = \Gamma/2$ is the decay rate of the atomic coherence. The modifications of κ' and Δ_c' with respect to their unprimed values correspond physically to the absorption and phase shift of the intra-cavity field, respectively. Fig. 10.6 shows the result of a numerical calculation comparing an empty cavity reflection spectrum with one that has 500 ions interacting with the cavity field at an atomic detuning of the probe of $\Delta = \gamma$. Both the effects of absorption and phase shift are clearly seen. In this section we will present results on measurements of both these parameters.

Fig. 10.7 shows images of a typical crystal used in these measurements. In fig. 10.7a) cooling is performed with the 866 nm repumper perpendicular to the cavity axis, illuminating the whole crystal, whereas, in fig. 10.7b) repumping is performed via the cavity field. The images show that the crystal is located at the center of the cavity mode, and that the ions within the crystal exhibit a high degree of localization. The observed shell-structure with emerging long range order effects is an indication that the Doppler cooling is working well. The number of ions in the crystal used
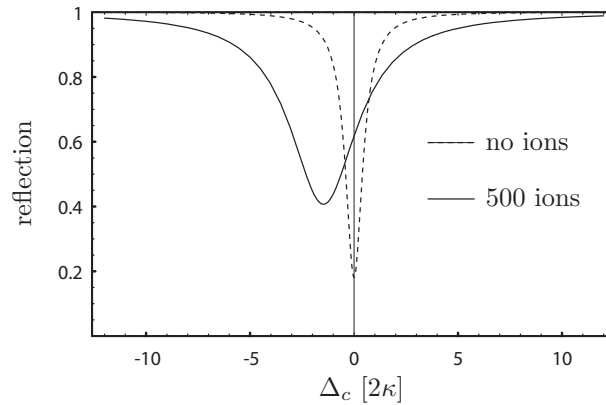
Figure 10.6: Cavity reflection signal for an empty cavity (dashed line) and for 500 ions at $\Delta = \gamma$ (solid line).

in the experiment is evaluated as described in appendix B to about 6400 and the number of ions within the cavity mode is evaluated as described in appendix C to be $N = 536 \pm 18$ and should thus be sufficient to reach the regime of collective strong coupling as described in previous chapters.

Absorption

We will first measure the effect of absorption. For this, we probe in reflection by scanning the cavity (varying Δ_c) and recording the cavity spectrum for different atomic detunings Δ. When varying the probe laser detuning Δ, the frequency of the 894 nm laser is varied accordingly to ensure that they are both resonant with the cavity at the same time. If this is not the case the referenced averaging method described in ch. 6.6.3 is less efficient as the two signals (886 nm and 894 nm) are not perfectly correlated in time and acoustic noise is not filtered out properly.

Fig. 10.8 shows examples of the spectra obtained by this method. The reflection level when the cavity is off-resonant is about 2 counts per bin, with a bin-time is 1.4 μs. The detection efficiency for the photons reflected off the cavity is 16% (see table 6.2), which means that this count rate corresponds to about 8.9 photons/μs. Based on our previous calculation in eq. 6.2 this means that the average photon number in the cavity on resonance is just below 1. Each point in the spectra corresponds to an experimental sequence (fig.10.5) and the entire spectrum is the result of an average of 100 cavity scans. For each scan, a Lorentzian lineshape is obtained and the effect of absorption is clearly observed in the broadening of the lineshape as the atomic resonance is approached.[2]

For every value of Δ we perform a Lorentzian fit to extract the HWHM of the cavity resonance κ'. Fig. 10.9 shows a plot of κ' versus Δ where each point is based on an average of the widths of 5 spectra such as those of fig. 10.8 for a total of 500

---

[2]The induced absorption can also be extracted from this data by evaluating the increased intra-cavity losses via eq. 2.29.
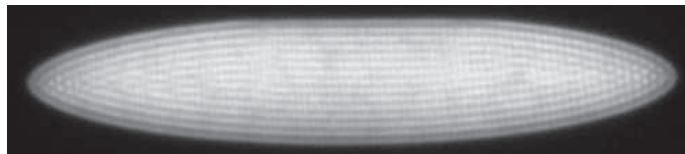
(a)
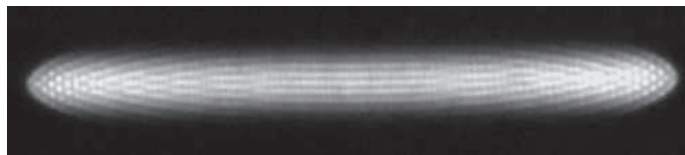
(b)

Figure 10.7: Images of crystal similar to that used in the experiments described in ch. 10.3.1 and 10.3.2. In (a) cooling is performed with the 866 nm repumper perpendicular to the cavity axis, illuminating the whole crystal. In (b) repumping is performed via the cavity field, hence, showing the overlap with the cavity mode.
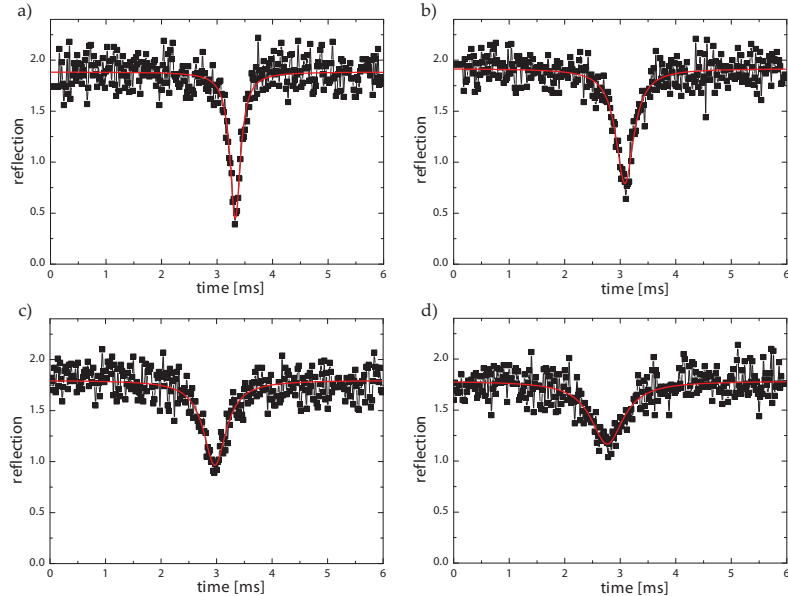
Figure 10.8: Cavity scans of the reflection signal for various values of the atomic detuning Δ, with the detuning approaching atomic resonance from a)-d). The red lines are Lorentzian fits to the data from which the width $2\kappa'$ is extracted. The time axis is calibrated by a measurement without ions by changing the probe frequency with an AOM. This gave 39.7 ± 0.3 MHz/ms. Based on this calibration the widths can be converted to a frequency.

cavity scans. As expected from eq. 2.32 we find a Lorentzian lineshape. The red line is a fit to the data based on this equation, which gives $g\sqrt{N} = 2\pi \times (12.2 \pm 0.2)$ MHz, $\gamma = 2\pi \times (11.9 \pm 0.4)$ MHz and $\kappa = 2\pi \times (2.2 \pm 0.1)$ MHz. With $N = 536 \pm 18$ and correcting for an optical pumping efficiency of 97^{+3}_{-5} % this corresponds to a value for the single ion coupling strength of $g = 2\pi \times (0.530 \pm 0.018)$ MHz in perfect agreement with the expected value of $g = 2\pi \times (0.532 \pm 0.007)$ MHz (see appendix C, eq. C.12).

The system thus satisfies the requirement for collective strong coupling, namely $g\sqrt{N} > \gamma, \kappa$, as expected for a crystal of about 500 ions. In terms of cooperativity this corresponds to a value of $C \simeq 2.8$.

The slightly higher value of γ compared with the expected value of $\gamma = 2\pi \times (11.2 \pm 0.3)$ MHz based on Ref. [178] could be due to the finite temperature of the ions giving rise to a non-negligible Doppler broadening. Based on the treatment of this given in appendix D (specifically by comparison with fig. D.3) this would translate into a temperature of $T = 24^{+20}_{-14}$ mK assuming $\gamma = 2\pi \times 11.2$ MHz, exactly. From our discussion on temperature in ch. 3.2.3 and from previously reported measurements of a few tens of mK [99] it is not surprising if the final temperature of the three-dimensional ion Coulomb crystal is above the Doppler cooling limit for a single ion of 0.5 mK. Furthermore, as discussed in ch. 3.2.2, micromotion may also contribute to the additional broadening that we observe.
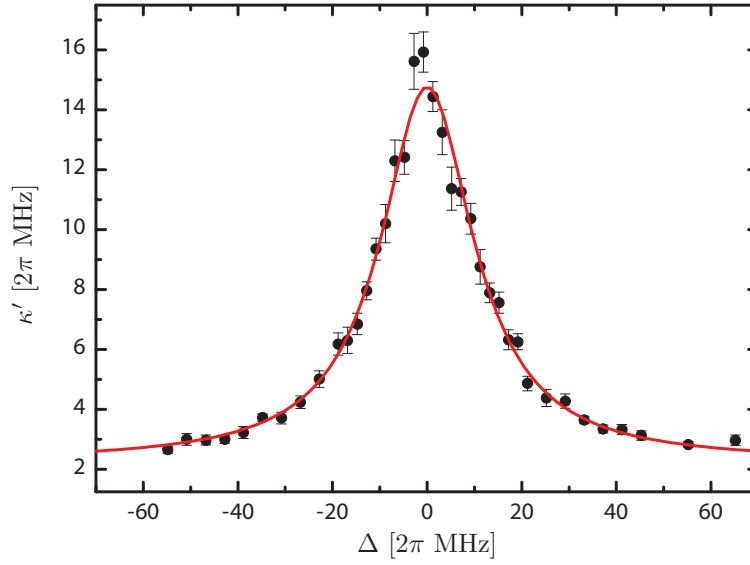
Figure 10.9: Measured cavity HWHM κ' versus atomic detuning Δ for a crystal with $N = 536 \pm 18$ ions interacting with the cavity field. The red line is a fit to the data based on eq. 2.32. The values derived from the fit are: $g\sqrt{N} = 2\pi \times (12.2 \pm 0.2)$ MHz, $\gamma = 2\pi \times (11.9 \pm 0.4)$ MHz and $\kappa = 2\pi \times (2.2 \pm 0.1)$ MHz.
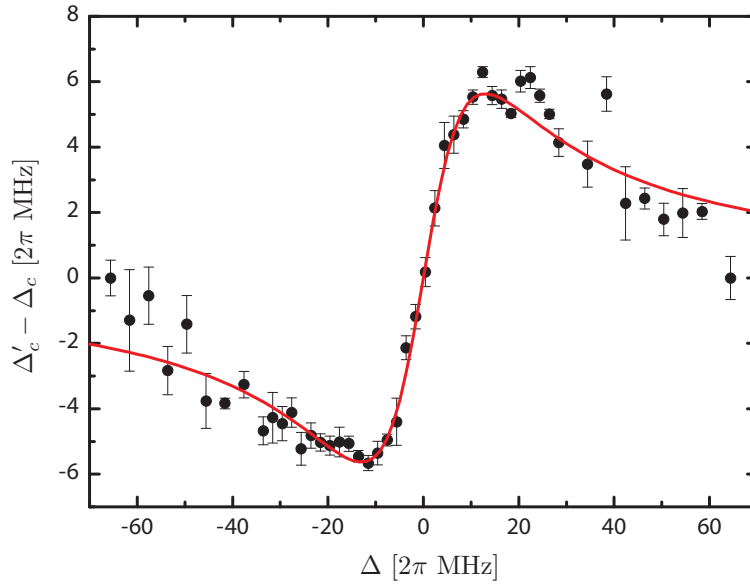
Figure 10.10: Measured phase shift $\Delta'_c - \Delta_c$ versus atomic detuning Δ for the same crystal as in fig. 10.9. The red line is a fit to the data based on eq. 2.33. The values derived from the fit are: $g\sqrt{N} = 2\pi \times (12.0 \pm 0.3)$ MHz and $\gamma = 2\pi \times (12.7 \pm 0.8)$ MHz.

Phase shift

The phase shift induced by the crystal is evaluated by an experiment conducted in the same way as for the absorption except that we maintain the detuning of the 894 nm reference laser constant with respect to the cavity resonance. This allows us to measure the phase shift induced by the interaction with the ions, as predicted by eq. 2.33, by comparing the location of the 866 nm probe resonance with the location of the resonance of the 894 nm reference. This method makes our measurements insensitive to drifts of the cavity during the time it takes to perform the measurement series.

Fig. 10.10 shows the results. As for the absorption, each point is the result of an average of 5 cavity spectra. For every 100 averages a Lorentzian fit was done to find the location of the probe resonance with respect to the reference, which would correspond to the empty cavity resonance. The values from the five Lorentzian fits were then averaged to give the final value plotted in the graph as a single point. The red line is a fit to the data based on eq. 2.33, which gives $g\sqrt{N} = 2\pi \times (12.0 \pm 0.3)$ MHz and $\gamma = 2\pi \times (12.7 \pm 0.8)$ MHz, consistent with the previous measurements. We generally observe slightly higher values for γ and slightly lower values for $g\sqrt{N}$ when measuring the phase shift and the data is also more noisy. We ascribe this to the fact that when the probe and the reference laser are not resonant at the same in the scan, the time correlation between the acoustic noise in the two signals becomes imperfect, thus lowering the accuracy of our referenced averaging method (c.f. ch. 6.6.3). This is also seen in the raw data (not shown here) by the occurrence of additional broadening of the probe resonance at large phase shifts, where the time separation between the resonances of the probe and the reference are the largest.[3]

10.3.2   Vacuum Rabi splitting

Finally, we have studied the interaction between the crystal of fig. 10.7 and the cavity field in the regime where the two are resonantly coupled, such that $\Delta = \Delta_c$. In the low-saturation regime, the system is then described by

$$\dot{P} = -(\gamma + i\Theta)P + igNA \qquad (10.2)$$
$$\dot{A} = -(\kappa + i\Theta)A + igP + \sqrt{2\kappa_1}A^{\text{in}}, \qquad (10.3)$$

where $\Theta = \Delta = \Delta_c$. We have already treated the resonant case of $\Theta = 0$ in ch. 2.3 where we found the eigenvalues for the combined ion-cavity system (eq. 2.37). The system can be viewed as two coupled harmonic oscillators, one being the atomic dipole P, the other being the cavity field A. In the low-saturation regime where the cavity field and the atoms exchange at most one quanta of excitation, the basis states are made up of only three possible states: $|g,0\rangle$, $|g,1\rangle$ and $|e,0\rangle$, where $|g\rangle$ and $|e\rangle$ are the Dicke states defined in eq. 2.39 and $|0\rangle$ and $|1\rangle$ corresponds to the cavity field state of zero and one photon, respectively. In the absence of any coupling between P and A ($g\sqrt{N} = 0$) the states $|g,1\rangle$ and $|e,0\rangle$ will, in the resonant case $\Delta = \Delta_c$, be degenerate and only a single resonance line is observed when the two oscillators are probed. If, however, the two are coupled as in eq. 10.3, the coupling will give rise to a splitting of

---

[3]This could be remedied, e.g., by modulating the reference beam with an EOM to create sidebands. The carrier can then be used as the constant reference, while one of the sidebands can be used for the referenced averaging. Alternatively, an AOM can be used as well.
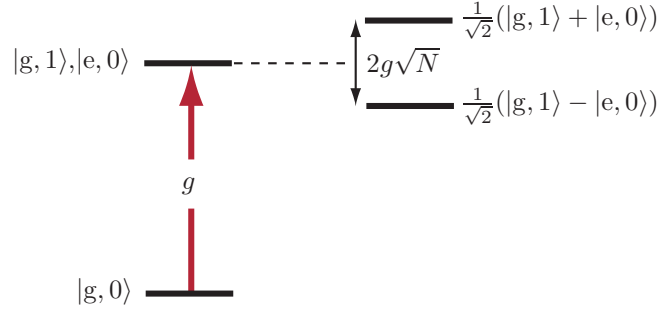
Figure 10.11: Level diagram explaining the effect of the coupling in a "dressed" state picture.

the degeneracy and a double resonance can be observed, depending on the strength of the coupling relative to the unperturbed linewidths γ, κ. This is shown schematically in fig. 10.11 and can be interpreted as the ions being "dressed" by the cavity field or vice versa. In this sense it is analogous to a light shift induced by a strong light field on an atomic transition [64]. However, in cavity QED, the effect arises already at the level of a single photon. For this reason the splitting is often referred to as the vacuum Rabi splitting.

Solving eq. 10.3 in steady state, the expression for the cavity field reads:

$$A = \frac{\sqrt{2\kappa_1}}{\kappa'' + i\Theta''} A^{\text{in}}, \tag{10.4}$$

with

$$\kappa'' = \kappa + g^2 N \frac{\gamma}{\gamma^2 + \Theta^2} \tag{10.5}$$

and

$$\Theta'' = \Theta - g^2 N \frac{\Theta}{\gamma^2 + \Theta^2}. \tag{10.6}$$

This is analogous to the expressions for the absorption and phase shift (eq. 2.32 and 2.33), however, here the phase shift (10.6) gives rise to a splitting of the resonance line rather than a shift of the resonance as measured above.

An expression for the reflectivity of the cavity versus the detuning Θ can be derived from the above equations (eq. 10.4, 10.5 and 10.6) as was done for the empty cavity in ch. 2.2. This gives:

$$\begin{aligned}
\text{refl}(\Theta) &= \left| \frac{2\kappa_1 - \kappa'' - i\Theta''}{\kappa'' + i\Theta''} \right|^2 \\
&= \frac{\left[(\kappa_1 - \kappa_{\mathcal{L}})\left(\gamma^2 + \Theta^2\right) - g^2 N \gamma \right]^2 + \left[\Theta\left(\gamma^2 + \Theta^2\right) - g^2 N \Theta \right]^2}{\left[(\kappa_1 + \kappa_{\mathcal{L}})\left(\gamma^2 + \Theta^2\right) + g^2 N \gamma \right]^2 + \left[\Theta\left(\gamma^2 + \Theta^2\right) + g^2 N \Theta \right]^2}. \tag{10.7}
\end{aligned}$$

Fig. 10.12 shows the cavity reflection, comparing the spectra for no ions and for 500 ions. The splitting of the resonance line into two is clearly seen and increases with the coupling strength $g\sqrt{N}$.
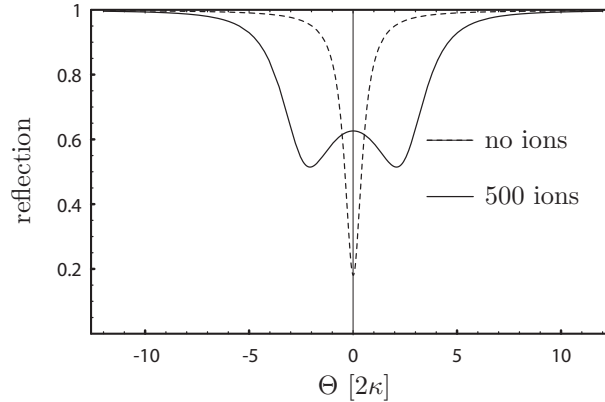
Figure 10.12: Cavity reflection signal for an empty cavity (dashed line) and for 500 ions for $\Theta = \Delta = \Delta_c$ (solid line). The graph is produced based on the expression given in eq. 10.7 for $\gamma = 2\pi \times 11.2$ MHz, $\kappa = 2\pi \times 2.1$ MHz and $g = 2\pi \times 0.53$ MHz.

To perform the measurement, the cavity is locked on atomic resonance and the reflection is recorded for different values of the detuning of the probe laser. Each point in the resulting spectrum is based on 20.000 experimental sequences (each of 20 μs length) and the data is subsequently processed to filter out acoustic noise as described in ch. 6.6.3.

The resulting spectrum is shown in fig. 10.13. As expected it is split into two peaks. The red line is a fit to the data based on eq. 10.7. To make the fit converge, we had to keep the decay rates of the atomic coherence γ and the cavity field κ fixed to the values derived from the absorption curve shown in fig. 10.9 above. This gives a value for the collective coupling strength of $g\sqrt{N} = 2\pi \times (12.1 \pm 0.2)$ MHz in agreement with the previous measurements. As mentioned above, a spectrum such as that of fig. 10.13 is commonly referred to as the vacuum Rabi splitting in the literature and is often considered as the hallmark strong coupling in cavity QED.

10.3.3 Scaling with number of ions

We have also examined the variation of the collective coupling strength with the number of ions in the cavity modevolume. The number of ions in the cavity modevolume can be varied by adjusting the trapping parameters, specifically, the end-voltage U_{end} and the rf-voltage U_{rf} as we did for the trap characterization in ch. 8.3. Alternatively, the number of ions can be gradually increased by loading more into the trap.

In one type of measurements we have studied the effect of absorption on resonance, where from eq. 2.32 the cavity HWHM is related to the cooperativity parameter via

$$\kappa' = \kappa(1 + 2C) \tag{10.8}$$

with

$$C = \frac{g^2 N}{2\gamma\kappa}. \tag{2.35}$$
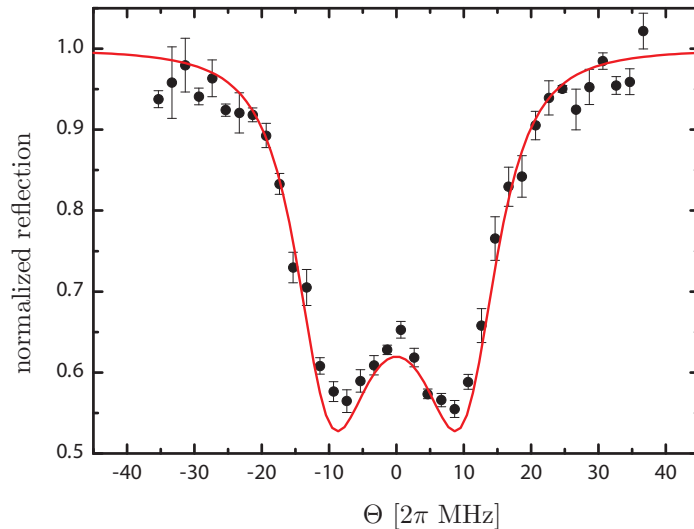
Figure 10.13: Measured cavity spectrum for $\Theta = \Delta = \Delta_c$ for the same crystal as in fig. 10.9. The red line is a fit to the data based on eq. 10.7 with γ and κ fixed to the values found from fig. 10.9. The fit result gives $g\sqrt{N} = 2\pi \times (12.1 \pm 0.2)$ MHz.

Fig. 10.14 shows the result of the measurements where the cooperativity parameter C has been plotted versus the number of ions in the cavity modevolume N. Each point is the result of a measurement of the cavity HWHM κ on atomic resonance, as in the measurements of ch. 10.3.1. The atomic resonance was determined with high accuracy prior to these measurements from absorption and phase shift measurements.

The data confirms the expected linear scaling. The red line is a linear fit to the data and has a slope of $C/N = (5.05 \pm 0.05) \times 10^{-3}$. The highest measured value for the cooperativity was found for a crystal of about 1570 ions where a value of $C = 8.1$ was found.

Based on previous measurements of $g = 2\pi \times 0.53$ MHz and $\kappa = 2\pi \times 2.1$ MHz and with $\gamma = 2\pi \times 11.2$ MHz, the expected slope would be about 6×10^{-3} (dashed line) with perfect optical pumping. Taking the 97% optical pumping efficiency into account we would deduce a value for γ of $\gamma = 2\pi \times (12.7 \pm 0.2)$ MHz from this measurement. The higher value for γ could be due to less efficient cooling on the day of the measurement, giving rise to a larger temperature and, hence, Doppler broadening as described in appendix C.

A complementary measurement can be performed by measuring the Rabi splitting, as was done in the previous section, for different number of ions in the cavity modevolume. Fig. 10.15 shows examples of spectra obtained in this way. One clearly observes the splitting of the resonance for larger number of ions.

Fig. 10.16 summarizes these measurements, by showing the collective coupling strength versus the number of ions. Each point is the result of a fit based on eq. 10.7 to a spectrum such as those of fig. 10.15. As in the previous section, we fix the parameters for the cavity decay rate and the atomic decoherence rate to $\gamma = 2\pi \times 11.9$ MHz and
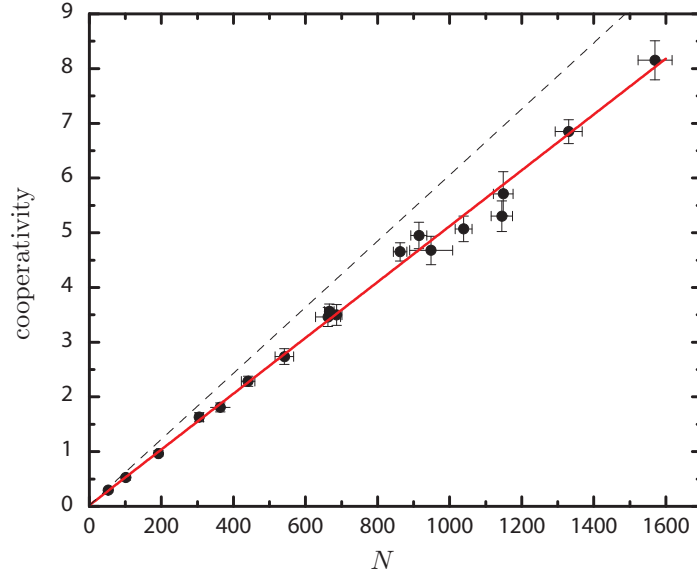
Figure 10.14: Measured cooperativity parameter versus number of ions in the cavity mod-evolume. The red line is a linear fit to the data and gives $C = (5.05 \pm 0.05) \times 10^{-3} \times N$ (not corrected for imperfect optical pumping).

$\kappa = 2\pi \times 2.2$ MHz, derived from the absorption spectrum (fig. 10.9), in order to have the fit converge. The plot shows the expected $g\sqrt{N}$ scaling and from a fit to this model (red line) we deduce a single ion coupling strength of $g = 2\pi \times (0.525 \pm 0.002)$ MHz after correcting for a optical pumping efficiency of 97%. Again, in agreement with the predicted value of $g = 2\pi \times (0.532 \pm 0.007)$ MHz (see appendix C, eq. C.12).

10.4 Optical pumping revisited

In ch. 9.3 we measured the optical pumping efficiency to find that about 97% of the ions were optically pumped into the $3D_{3/2}, m_J = +3/2$ state. This can also be tested by similar series of experiments as was done in ch. 9.3 but this time exploding the cavity QED interaction rather than the fluorescence as in the measurements of ch. 9.3. Specifically, we have performed measurements of the cooperativity C versus N in four different configurations by probing with both σ_-- and σ_+-polarized light, with and without prior optical pumping. The results are presented in fig. 10.14.

The experimental sequence in the experiments without optical pumping is un-changed except that the 866 nm optical pumping beam is not turned on during this part of the sequence. As discussed in ch. 9, the result is that the $4S_{1/2}, m_J = \pm 1/2$ states are depopulated by the 397 nm fields and due to the relative Clebsch-Gordan coefficients on the $3D_{3/2} \leftrightarrow 4P_{1/2}$ transition, the four magnetic sub-states of the $3D_{3/2}$ state are populated equally. In this case, the interaction is independent on the polarization being σ_- or σ_+ (if they are both on resonance), as both will probe half the ions of the $3D_{3/2}$ state. If optical pumping to prepare the ions in the $3D_{3/2}, m_J = +3/2$
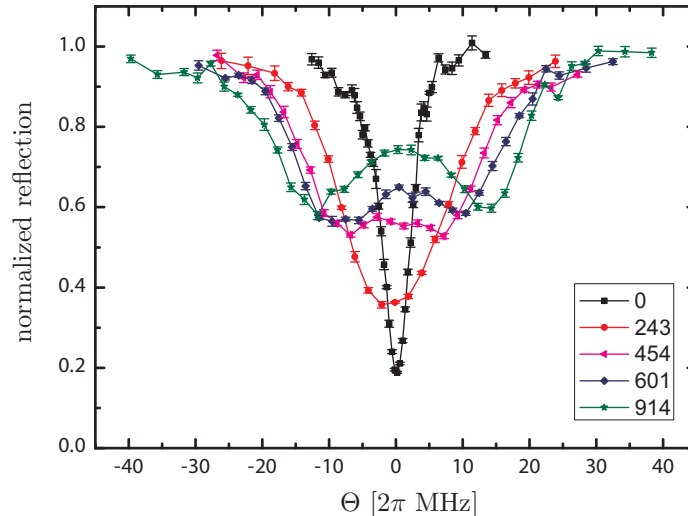
Figure 10.15: Measured cavity spectra for $\Delta = \Delta_c$ for crystals of different number of ions (see insert).

state is included in the sequence, then we will expect the cooperativity to be different for the two polarizations and the ratio to scale according to the optical pumping efficiency. This measurement scheme thus relies on comparing the scaling of the cooperativity parameter for measurements with and without prior optical pumping.

Fig. 10.17 shows plots of the measured cooperativity versus the number of ions in the cavity modevolume for σ_+- and for σ_--polarized probe, with and without prior optical pumping to the $3D_{3/2}, m_J = +3/2$ state. The level diagrams on the right indicates the probing scheme and the state preparation with the frame color corresponding to the respective data. The lines are linear fit to the data, fixed through zero, and the slopes C/N derived from the fits are listed in table 10.1. The results of probing with a σ_--polarized probe with prior optical pumping is shown by the red data and the value of C/N deduced from the fit is consistent with the measurements of the previous section. When probing the ions after optical pumping with a σ_+-polarized probe (purple data) we observe almost negligible coupling. Both these observations show that the optical pumping efficiency is indeed close to 100%.

As in the previous measurements, we find a slightly lower value for C/N than the

color in fig. 10.17	OP	pol	C/N $[10^{-3}]$
red	yes	σ_-	4.93 ± 0.07
green	yes	σ_+	0.08 ± 0.01
blue	no	σ_-	1.64 ± 0.03
purple	no	σ_+	1.44 ± 0.03

Table 10.1: Measured cooperativity slopes C/N from linear fits to the data of fig. 10.17. OP: optical pumping, pol: probe polarization.
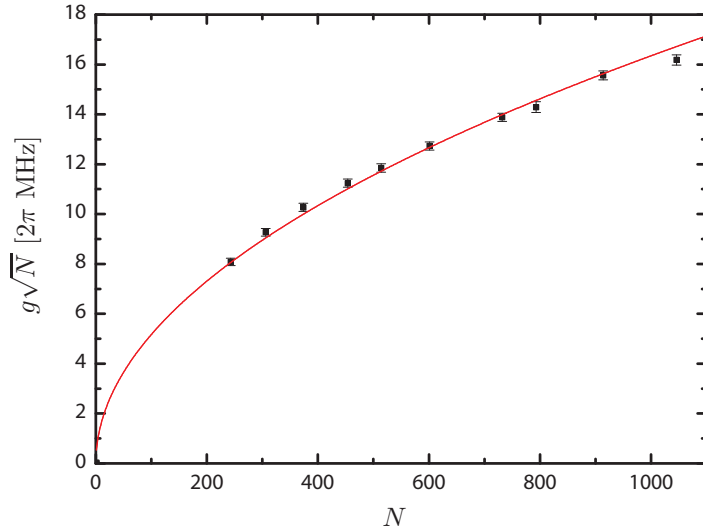
Figure 10.16: Collective coupling strength $g\sqrt{N}$ versus number of ions in the cavity mode. The red line is a fit to the data and gives $g = 2\pi \times (0.525 \pm 0.002)$ MHz when corrected for the optical pumping efficiency.

optimal. With $g = 2\pi \times 0.53$ MHz and $\kappa = 2\pi \times 2.1$ MHz this measurement corresponds to an effective atomic width of $\gamma = 2\pi \times 13.6$ MHz. As before we subscribe this to a higher temperature of the ions, caused by less efficient cooling. Note that the data has not been corrected for imperfect optical pumping as the objective of this section is to deduce this number from the data.

Due to the magnetic field necessary in our experiments there is a contribution from the Zeeman shift that needs to be taken into account when comparing signals based on different transitions. As we have adjusted the frequency of the 866 nm probe to be perfectly resonant with the $3D_{3/2}, m_J = +3/2 \leftrightarrow 4P_{1/2}, m_J = +1/2$ transition it will not be so, for the other transitions. This explains why the values deduced for the scaling of the cooperativity parameter are not identical for the two different probes in the case of no optical pumping.

Before proceeding we will analyze the effect of the magnetic field in the case of no optical pumping (green and blue data) in which case the probe, regardless of its polarization, will probe $\frac{1}{4}$ of the total $3D_{3/2}$ state population on either of the two transitions. We begin by recalling that the Clebsch-Gordon coefficients on the $3D_{3/2}, m_J = \pm 3/2 \leftrightarrow 4P_{1/2}, m_J = \pm 1/2$ and the $3D_{3/2}, m_J = \pm 1/2 \leftrightarrow 4P_{1/2}, m_J = \mp 1/2$ transitions are $\frac{1}{\sqrt{2}}$ and $\frac{1}{\sqrt{6}}$, respectively (see appendix A). Combined with the state-dependent detuning due to the magnetic field and assuming the probe laser is tuned to resonance with the $3D_{3/2}, m_J = +3/2 \leftrightarrow 4P_{1/2}, m_J = +1/2$ transition, we can calculate the scaling of the cooperativity parameter C/N as

$$\left(\frac{C}{N}\right)_{\text{noOP},\sigma_-} \propto \frac{1}{4} \times \frac{1}{2} + \frac{1}{4} \times \frac{1}{6} \times \frac{\gamma^2}{\gamma^2 + \Delta^2}, \tag{10.9}$$
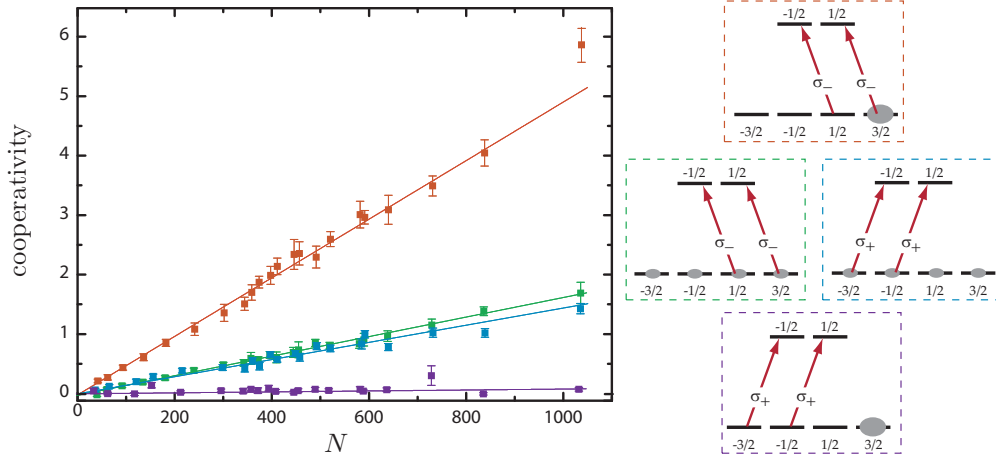
Figure 10.17: Measured cooperativity parameter versus number of ions in the cavity mod-evolume for σ_+- and for σ_--polarized probe, with and without prior optical pumping (OP) to the $m_J = +3/2$ state. Red data: σ_- probe with OP. Green data: σ_- probe without OP. Blue data: σ_+ probe without OP. Purple data: σ_+ probe with OP. The lines are linear fit to the data. The level schemes on the right indicate the state preparation by OP and the probe polarization with the frame color corresponding to the respective data.

for the σ_--polarized probe and

$$\left(\frac{C}{N}\right)_{\text{noOP},\sigma_+} \propto \frac{1}{4} \times \frac{1}{2} \times \frac{\gamma^2}{\gamma^2 + (3\Delta)^2} + \frac{1}{4} \times \frac{1}{6} \times \frac{\gamma^2}{\gamma^2 + (2\Delta)^2}, \qquad (10.10)$$

for the σ_+-polarized probe, where $\Delta = g_J \mu_B B/\hbar$ is the detuning induced by the Zeeman shift for a given magnetic sub-state (c.f. appendix A). Taking the ratio of the two, here denoted W_{noOP}, one finds after some algebra

$$W_{\text{noOP}} = \frac{\left(\frac{C}{N}\right)_{\text{noOP},\sigma_+}}{\left(\frac{C}{N}\right)_{\text{noOP},\sigma_-}} = \frac{\frac{3}{1+(3\beta)^2} + \frac{1}{1+(2\beta)^2}}{3 + \frac{1}{1+\beta^2}}, \qquad (10.11)$$

where we have defined $\beta = \Delta/\gamma$. Inserting the ratio W_{noOP} found from table 10.1 and solving for B one finds $B = 1.6 \pm 0.3$ G using $\gamma = 2\pi \times 13.6$ MHz. This is slightly below the value of $2 - 2.5$ G, that we infer from the dimensions of the magnetic field coils, the distance between the coils and the trap and the current in the coils for that experiment. The reason for this discrepancy is at present not known, however, more careful measurements and measurements taken at different magnetic field strengths might illuminate the issue. For now we merely wish to point to the fact that the magnetic field can in principle be determined from these measurements.

In the case where optical pumping prepares the ions in the $3D_{3/2}, m_J = +3/2$ state such that $\eta_{\text{OP}} N$ are in this state and $(1 - \eta_{\text{OP}}) N$ are in the other magnetic sub-states of the $3D_{3/2}$ state, one finds

$$\left(\frac{C}{N}\right)_{\text{OP},\sigma_-} \propto \eta_{\text{OP}} \times \frac{1}{2} + \frac{1 - \eta_{\text{OP}}}{3} \times \frac{1}{6} \times \frac{\gamma^2}{\gamma^2 + \Delta^2}, \qquad (10.12)$$

for the σ_--polarized probe and

$$\left(\frac{C}{N}\right)_{\mathrm{OP},\sigma_+} \propto \frac{1-\eta_{\mathrm{OP}}}{3} \times \frac{1}{2} \times \frac{\gamma^2}{\gamma^2+(3\Delta)^2} + \frac{1-\eta_{\mathrm{OP}}}{3} \times \frac{1}{6} \times \frac{\gamma^2}{\gamma^2+(2\Delta)^2}, \quad (10.13)$$

for the σ_+-polarized probe. In both expressions we have assumed that the residual population is equally distributed among the three "wrong" magnetic sub-states of the $3D_{3/2}$ state. As in the analysis of the magnetic field strength we may now take the ratio of the two expressions to compare this with our measurements

$$W_{\mathrm{OP}} = \frac{\left(\frac{C}{N}\right)_{\mathrm{OP},\sigma_+}}{\left(\frac{C}{N}\right)_{\mathrm{OP},\sigma_-}} = \frac{\frac{1-\eta_{\mathrm{OP}}}{3}\frac{3}{1+(3\beta)^2} + \frac{1-\eta_{\mathrm{OP}}}{3}\frac{1}{1+(2\beta)^2}}{3\eta_{\mathrm{OP}} + \frac{1-\eta_{\mathrm{OP}}}{3}\frac{1}{1+\beta^2}}. \quad (10.14)$$

Inserting the values given in table 10.1 and using $B = 1.6$ G and $\gamma = 2\pi \times 13.6$ MHz as found above, we find an optical pumping efficiency of $\eta_{\mathrm{OP}} = 96.5 \pm 0.5\%$ in agreement with the value found in ch. 9. Of cause, the values used for B and γ in this expression are associated with some uncertainty, however, in the case of near-perfect optical pumping this is not critical as the dominant term in eq. 10.14 will be the first term in the denominator, which is independent of these parameters.

10.5   Conclusion

In this chapter have studied our system of ion Coulomb crystals in the context of cavity QED.

We first made a brief analytic and numerical analysis of the system composed of an ensemble of ^{40}Ca$^+$ ions, prepared in the $3D_{3/2}, m_J$ state, interacting with a cavity field of a single photon. This analysis justified the two-level description of ch. 2 and, hence, allowed us to evaluate all measurements based on this formalism.

In the second part of this chapter, we presented results on the first realization of collective strong coupling with ions. In the most precise of these measurements, the single ion coupling strength was found to $g = 2\pi \times (0.530 \pm 0.018)$ MHz in excellent agreement with the expected value of $g = 2\pi \times (0.532 \pm 0.007)$ MHz, based on our knowledge of the cavity geometry (c.f. appendix C).

We also studied the scaling of the interaction strength with the number of ions, both via measurements of absorption and via analysis of the Rabi splitting spectra. In both cases the system exhibited the expected scaling with the number of ions. For the largest number of ions that has been probed thus far, the measured cooperativity was 8.1. Extrapolating the performance of this system as a tool for quantum information science, we note that it would potentially operate as a quantum memory for light [66] with a fidelity of 94% [50, 51].

In the last section we analyzed data on measurements of the cooperativity versus the number of ions, to extract information about the optical pumping efficiency. This concluded that $96.5 \pm 0.5\%$ of the ions where prepared in the right state by our optical pumping scheme, in agreement with the measurements of ch 9.

In all of our measurements we found a larger value for the atomic linewidth γ than expected. Although this requires further studies, we believe this to be related to the finite temperature of the ions and for one set of data we estimated the temperature to $T = 24^{+20}_{-14}$ mK, based on the model developed in appendix D.

Chapter 11

Summary and outlook

This thesis has covered several aspects of ion Coulomb crystals for the purpose of cavity QED. The journey toward the successful combination of large ion Coulomb crystals and a high finesse cavity for the realization of collective strong coupling has offered many technical challenges and has required the development and construction of a number of specific tools that now comprise the cavity QED experiment in the Ion Trap Group at the University of Aarhus. In the following we shall attempt to summarize the main constituents of this experiment that this thesis has covered.

Seven different laser systems have been used in the experiments (see ch. 5). Some had already been developed for other experiments in the group, while others had to be developed specifically for this project. Among these was a UV laser source at 272 nm, based on a CW distributed feedback fiber laser at 1088 nm that has recently become commercially available. The narrow linewidth and relatively high power of this type of laser make it ideal for frequency doubling into the visible part of the spectrum. We demonstrated that light at 544 nm could be generated stably and efficiently in an external enhancement cavity with a conversion efficiency of 55% and without deteriorating the Gaussian beam profile. These results allowed for further frequency doubling in a second enhancement cavity to produce light at 272 nm with a conversion efficiency of 16%. In total, the conversion efficiency from 1088 nm to 272 nm was about 8% corresponding to a maximum output of about 115 mW. The results of this work showed that a DFB fiber laser of this type may be used to access a range of wavelengths in both the visible and the UV that had hitherto been difficult to access with solid state based laser systems and it is our belief that DFB fiber lasers in combination with second harmonic generation will be used extensively in the future.

The development of the trap and cavity that would later become the cavity trap, did not begin on page 1 of this thesis. Several aspects, especially regarding the design, had already been initiated prior to this work [66] and, as described in ch. 6, these early studies formed the basis for the design of the cavity trap.

When characterizing the trap in ch. 8 we found very nice agreement with the theoretical predictions for the physical properties of the trapped ion Coulomb crystals. While this was encouraging for our confidence in the design and assembly of the trap it also led to the conclusion that the integration or mirror substrates into the linear Paul trap had been accomplished without perturbing the trapping fields.

The characterization also provided a precise calibration of the trapping parame-

ters, which has allowed for an evaluation of the number of ions interacting with the cavity field in the trapped ion Coulomb crystals with a precision of $2-4\%$ depending on the crystal size. Incidentally, the high precision in our calibration enabled us to claim a value for the prefactor in the expression for the inter-shell spacing of long ion Coulomb crystals (see eq. 8.16). The value determined by our mesurements was 1.484 ± 0.010, which should be compared to the best known previous measurement of 1.35 ± 0.15 [98] and thus strongly supports the value predicted by MD simulations of 1.48 [97].

Toward the end of ch.8 we described the results of an extensive empirical study launched with the purpose of mapping out the optimal trapping parameters for maximizing the coherent coupling to the cavity field. Our findings justified the effort and an optimum configuration was identified in which more than 2000 ions were expected to interact with the cavity field. This investigation also revealed what we described as a threshold-like behavior in the minimal attainable aspect ratio versus number of ions in the crystal. We believe the issue to be related to rf-heating in the crystal, however, no thorough study to illuminate the effect has been conducted thus far.

On the whole, the design and assembly of the cavity trap was successful, however, on three accounts we had unpleasant surprises. First, the immediate contamination of the cavity during the bake-out along with the following slow increase in the intra-cavity losses over time, that we described in ch. 6.6.1. Although this was not ideal and should be accounted for in future studies, the effect is not at a level where it poses any serious limitation to our experiment. Second, the susceptibility of the cavity to acoustic noise. This was a more serious problem that has, however, been worked around by schemes to filter and clean the data. Future versions of the experiment should incorporate some form of passive damping in the design to isolate the setup from outside vibrations as well as modify the design to result in higher, less harmful mechanical resonance frequencies. Third, the overlap between the cavity mode and the ion Coulomb crystal was imperfect to begin with. To address this issue we developed a general technique for moving the minimum of the quadrupole potential. We demonstrated that with this method, the ions could be moved by $\pm 100~\mu$m in the radial plane of the trap, which facilitated a near perfect overlap with the cavity mode. We note that this technique is generally applicable and may thus be a convenient technique in experiments where $\sim$micron positioning of ions without increased micromotion is critical.

In ch. 7 we presented results on loading of the cavity trap by resonance-enhanced photoionization of a beam of atomic calcium. By this method we were able to achieve loading rates of more than 3000 ions/s allowing for production of large ion Coulomb crystals of more than 10^5 ions in less than a minute. Furthermore, we demonstrated the ability of the 272 nm laser system used in the photoionization scheme to selectively load specific isotopes of Ca^+. While the issue of high loading rates is of general importance to the practicality of a cavity QED experiment with ensembles of ions, the isotope selectivity is especially relevant for the ability to perform such experiments with two-component crystals.

We also developed a novel, all-optical loading technique in which the beam of atomic calcium is produced through pulsed laser ablation of a calcium target. A key motivation factor for this loading scheme is the possibility of working with a lower atomic beam flux, which can be advantageous for loading of e.g. microtrap architectures where contaminants deposited on the trap electrodes may lead to unwanted

heating effects. In the context of the general theme of this thesis, the reduction of potentially contaminating material passing through the optical cavity would also be highly advantageous. Although, the loading rates obtained so far by this loading scheme do not promote the method as a viable technique for loading large ion Coulomb crystals, we have strong belief that further optimization will improve on this and increase the potential of this method.

Having successfully loaded the trap and optimized its performance we implemented a scheme to prepare all ions in the $3D_{3/2}, m_J = 3/2$ of ^{40}Ca$^+$ by optical pumping. This we described in ch. 9, where we estimated that 97^{+3}_{-5} % of the ions can be prepared in the correct state.

This series of developments lead us to what is to our knowledge the first realization of collective strong coupling with ions. In ch. 10 we presented results on the coherent coupling of our crystals to the cavity field, which we found in excellent agreement with the theoretical prediction for our system with a measured single ion coupling strength of $g = 2\pi \times (0.530 \pm 0.018)$ MHz. In our characterization of the system in this chapter, we also studied the scaling of the interaction with the number of ions by measurements of the cooperativity to find a value of $C \simeq 5 \times 10^{-3} \times N$ and a cooperativity of $C \sim 8$ for the highest number of ions of ~ 1600.

In all measurements we observed slightly higher values for the atomic linewidth γ than the natural linewidth, which we attribute to Doppler broadening induced by the thermal motion of the ions. The result is that the effective cooperativity of the system is lowered accordingly. However, the fact that the scaling of the cooperativity with the number of ions is still linear suggests that at least up to the crystals sizes that we have studied so far there are no size dependent heating effects. This observation gives hope that increasing the number of ions will increase the cooperativity further. Combined with optimized cooling we would extrapolate our present data to $C \sim 12$. Perhaps, with further optimization, even more ions can be confined in the trap, however, based on our measurements of ch. 8.3 where we systematically studied the maximization of ions in the cavity mode, we do not believe the system to be far from its optimal performance, already at this stage. One obvious way to increase the cooperativity, though, would be through a reduction in the cavity losses. For instance, with no intra-cavity losses in our present cavity, our extrapolations would go beyond $C \sim 15$.

For the sake of comparison, we mention that a cooperativity of around 8 is already in the vicinity of that used in neutral atom based quantum memories [25,33,52,58,59]. Moreover, as we have pointed out previously, the expected scaling of the fidelity in such applications is $\frac{2C}{1+2C}$ [50, 51], which potentially allows for 94% fidelity with a cooperativity of 8. By this measure, the system is, in its present state, already a promising candidate for efficiently realizing important quantum information protocols.

Besides venturing into the field of quantum information science, one might consider if rather than exploiting ion Coulomb crystals for cavity QED, one could make use of the cavity QED interaction to learn about the physics of ion Coulomb crystals. We have already mentioned the possibility of measuring the temperature of the ion Coulomb crystal via the single photon field probe of the cavity and in ch. 10 we quoted a temperature of $T = 24^{+20}_{-14}$ mK based on a model of the influence of Doppler broadening in such measurements. As a temperature measurement that experiment was quite preliminary, but with further studies on the subject it might become a viable method. The establishment of such a diagnostic would be of great value for exploring

the possibilities of observing effects of cavity mediated cooling in our system [179]. In such a scheme the fact that for our system $\kappa < \gamma$ would in principle allow for cooling below the Doppler limit. Other applications of cavity QED for ion Coulomb crystals could lie in the possibility of observing changes in the collective coupling strength as a result of structural phase transitions in the crystal.

Finally, we mention that the use of two-component crystals may further increase the potential of the system. As we have pointed out previously in this thesis, one advantage in this is the possibility of continuous cooling during the experiment and, hence, the prospect of working with even better controlled samples of ions.

Chapter 12

Acronyms

ar   anti-reflection

AOM   acousto-optic modulator

APD   avalanche photo detector

bcc   body-centered cubic

CCD   charge coupled device

CW   continuous wave

DFB   distributed feedback

EIT   electromagnetically induced transparency

EOM   electro-optic modulator

FSR   free spectral range

FWHM   full width at half the maximum

HWHM   half width at half the maximum

LBO   Lithium Triborate

MD   molecular dynamics

OI   optical isolator

PBS   polarizing beam splitter

PDH   Pound-Drever-Hall

PM   polarization maintaining

PMT   photo-multiplier tube

ppm   parts per million

PZT   piezo-electric transducer

rf   radio frequency

SHG   second harmonic generation

SM   single mode

Ti:Sapph Titanium Sapphire

UV   ultra violet

QED   quantum electrodynamics

Appendices

Appendix A

The Ca+ ion

A.1 Abundance of Ca-isotopes

The natural abundance of the stable isotopes of calcium is listed in Table A.1

Isotope	Abundance
40	96.941%
42	0.647%
43	0.135%
44	2.086%
46	0.004%
48	0.187%

Table A.1: Abundance of the stable isotopes of calcium [157].

A.2 Transitions in the ^{40}Ca$^+$ ion

Transition	Wavelength [nm]	$\Gamma/2\pi$ [MHz]	Sat. intensity [mW/cm^2]
$4S_{1/2}$-$4P_{1/2}$	396.847	20.7	43.3
$4S_{1/2}$-$4P_{3/2}$	393.366	21.5	46.2
$3D_{3/2}$-$4P_{1/2}$	866.214	1.69	0.34
$3D_{3/2}$-$4P_{3/2}$	849.802	0.177	0.038
$3D_{5/2}$-$4P_{3/2}$	854.209	1.58	0.33

Table A.2: Data for dipole-allowed transitions in ^{40}Ca$^+$, as shown in Fig. 4.3. Transition wavelengths are measured in air [178, 180]. $\Gamma/2\pi$ is the transition rate [178, 180]. Saturation intensities are calculated according to $I_{\text{sat}} = \frac{\hbar\Gamma\omega^3}{12\pi c^2}$, using the relevant transition rate Γ and transition frequency ω.

The isotope shifts for the $S \leftrightarrow P$ transitions (397nm, 393 nm) and the $D \leftrightarrow P$ transitions (850 nm, 854 nm, 866 nm) are listed here:

Transition	^{40}Ca$^+$	^{42}Ca$^+$	^{43}Ca$^+$	^{44}Ca$^+$	^{46}Ca$^+$	^{48}Ca$^+$
$S \leftrightarrow P$	0	425	688	842	1287	1696
$D \leftrightarrow P$	0	-2350	-3465	-4495	-6478	-8288

Table A.3: Isotope shifts in ^{40}Ca$^+$ in MHz. Values are taken from Ref. [140]

The coupling strengths for dipole-allowed transitions between the various sublevels are characterized by the values of Γ given in Table A.2 and the Clebsch-Gordan coefficients (see, e.g., Ref. [61] for a definition), which are listed in Tables A.4–A.6.

	$4S_{1/2}, -1/2$	$4S_{1/2}, +1/2$
$4P_{1/2}, -1/2$	$-\sqrt{1/3}$	$\sqrt{2/3}$
$4P_{1/2}, +1/2$	$-\sqrt{2/3}$	$\sqrt{1/3}$
$4P_{3/2}, -3/2$	1	-
$4P_{3/2}, -1/2$	$\sqrt{2/3}$	$\sqrt{1/3}$
$4P_{3/2}, +1/2$	$\sqrt{1/3}$	$\sqrt{2/3}$
$4P_{3/2}, +3/2$	-	1

Table A.4: Clebsch-Gordan coefficients for transitions between the $4S_{1/2}$ state and the $4P_{1/2}$ and $4P_{3/2}$ states.

	$3D_{3/2}, -3/2$	$3D_{3/2}, -1/2$	$3D_{3/2}, +1/2$	$3D_{3/2}, +3/2$
$4P_{1/2}, -1/2$	$\sqrt{1/2}$	$-\sqrt{1/3}$	$\sqrt{1/6}$	-
$4P_{1/2}, +1/2$	-	$\sqrt{1/6}$	$-\sqrt{1/3}$	$\sqrt{1/2}$
$4P_{3/2}, -3/2$	$-\sqrt{3/5}$	$\sqrt{2/5}$	-	-
$4P_{3/2}, -1/2$	$-\sqrt{2/5}$	$-\sqrt{1/15}$	$\sqrt{8/15}$	-
$4P_{3/2}, +1/2$	-	$-\sqrt{8/15}$	$\sqrt{1/15}$	$\sqrt{2/5}$
$4P_{3/2}, +3/2$	-	-	$-\sqrt{2/5}$	$\sqrt{3/5}$

Table A.5: Clebsch-Gordan coefficients for transitions between the $3D_{3/2}$ state and the $4P_{1/2}$ and $4P_{3/2}$ states.

	$4P_{3/2}, -3/2$	$4P_{3/2}, -1/2$	$4P_{3/2}, +1/2$	$4P_{3/2}, +3/2$
$3D_{5/2}, -5/2$	$\sqrt{2/3}$	-	-	-
$3D_{5/2}, -3/2$	$-\sqrt{4/15}$	$\sqrt{2/5}$	-	-
$3D_{5/2}, -1/2$	$\sqrt{1/15}$	$-\sqrt{2/5}$	$\sqrt{1/5}$	-
$3D_{5/2}, +1/2$	-	$\sqrt{1/5}$	$-\sqrt{2/5}$	$\sqrt{1/15}$
$3D_{5/2}, +3/2$	-	-	$\sqrt{2/5}$	$-\sqrt{4/15}$
$3D_{5/2}, +5/2$	-	-	-	$\sqrt{2/3}$

Table A.6: Clebsch-Gordan coefficients for transitions between the $3D_{5/2}$ state and the $4P_{3/2}$ state.

A.3 Zeeman-splitting in the ^{40}Ca$^+$ ion

The Zeeman-splitting of the magnetic sub-levels of ^{40}Ca$^+$ is given by:

$$\Delta E_{Zeeman} = m_J g_J \mu_B B, \tag{A.1}$$

where m_J is the magnetic quantum number, μ_B is the Bohr magneton, B is the magnetic field strength and g_J is the Landé g-factor,

$$g_J = 1 + \frac{J(J+1) + S(S+1) - L(L+1)}{2J(J+1)}. \tag{A.2}$$

Values of g_J are listed in Table A.7 for the lowest lying states of the ^{40}Ca$^+$ ion.

State	g_J
$4S_{1/2}$	2
$4P_{1/2}$	2/3
$4P_{3/2}$	4/3
$3D_{3/2}$	4/5
$3D_{5/2}$	6/5

Table A.7: Values of g_J for the lowest lying levels of the ^{40}Ca$^+$ ion.

For $B = 1$ Gauss, the Zeeman-splitting of the metastable $3D_{3/2}$ sub-states are $2\pi \times 1.1$ Mhz.

Appendix B

Extraction of crystal parameters

Fig. B shows an image of a crystal recorded with the camera along the y-axis (c.f. fig. 6.9). L' and $2R'$ denote the length and diameter of the crystal, respectively, both defined as the distance between the centers of the outermost shell on either side. To deduce the diameter $2R$ and the length L as defined within the zero temperature charged liquid model, one intershell spacing δr must be added. δr may be calculated from eq. 3.22 or measured as indicated in the figure below the crystal image, which shows the radial distribution of the ions along the white line in the image. The crystal aspect ratio as defined in this thesis, is thus derived from images such as that of fig. B using the relation

$$\alpha \equiv \frac{2R}{L} = \frac{2R' + \delta r}{L' + \delta r}. \tag{B.1}$$

The volume of the crystal, is defined through the equation for a spheroid, which
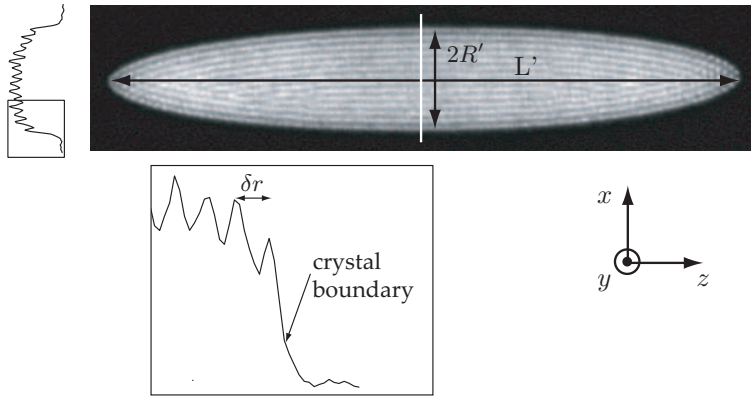
Figure B.1: Image of a crystal recorded with the camera along the y-axis (c.f. fig. 6.9). L' and $2R'$ denote the length and diameter of the crystal, respectively, both defined as the distance between the centers of the outermost shell on either side. To the left of the crystal is shown the radial density distribution of the ions along the white line in through the crystal. A part of this has been enlarged below the image, where also the intershell spacing δr and the crystal boundary, found by adding half an intershell spacing, are indicated.

169

in the prolate case ($\alpha < 1$) reads:

$$V = \frac{4}{3}\pi R^2 L/2 = \frac{4}{3}\pi(R' + \delta r/2)^2(L/2 + \delta r/2), \tag{B.2}$$

where again the intershell spacing is added to emulate the density distribution of the zero temperature charged liquid model. From crystal images such as the one in fig. B, we are typically able to determine L and $2R$ of the crystal to within a pixel ($\pm\frac{1}{2}$pix), which with our typical magnification of 5 corresponds to an uncertainty of $\delta x = 1\ \mu$m (c.f. ch. 6.4). Note that as the crystals are typically comprised of several shells, a considerably lower uncertainty in δr can generally be achieved. From eq. B.2 the uncertainty in the crystal volume can be found as

$$
\begin{aligned}
\delta V &= \sqrt{\left(\frac{\partial V}{\partial R}\delta R\right)^2 + \left(\frac{\partial V}{\partial L}\delta L\right)^2} = \sqrt{\left(\frac{4}{3}\pi RL\right)^2 + \left(\frac{2}{3}\pi R^2\right)^2}\,\delta x \\
&= \frac{\sqrt{4L^2 + R^2}}{RL}V\delta x = \sqrt{\frac{16}{\alpha^2} + 1}\frac{V}{L}\delta x,
\end{aligned}
\tag{B.3}
$$

which for low aspect ratio, prolate crystals as is typically the relevant case in this thesis, gives $\frac{\delta V}{V} \simeq \frac{4\delta x}{L\alpha}$. For a crystal such as the one of fig. B with an aspect ratio around 0.2 and a length of about 1 mm, the relative uncertainty in the volume is thus $\frac{\delta V}{V} \simeq 2$ %. For typical crystal sizes in the experiments, this uncertainty is around $1 - 3$ %.

Since the number of ions N is determined by the product of the crystal density ρ_0 and the volume V the relative uncertainty in N is thus

$$\frac{\delta N}{N} = \sqrt{\left(\frac{\delta\rho_0}{\rho_0}\right)^2 + \left(\frac{\delta V}{V}\right)^2}. \tag{B.4}$$

Based on the calibration of the density, made in ch. 8.2.1 (eq. 8.18) a conservative estimate for the relative uncertainty in the density is around 2 % and we thus find a relative uncertainty in the number of ions in the image of fig. B of about $\delta N/N \simeq 3$ %. Typically, this will be $2 - 4$ %. It is interesting to note that with $\delta N/N \simeq 3$ %, e.g., we are able to determine the number of ions to within $\sqrt{N}$ for up to about $N = 1100$ ions. This is illustrated in fig. B.2, where the black line is the $\sqrt{N}$ curve and the grayscale lines are for uncertainties of $2 - 3$ %.

When the uncertainty is less critical and large amounts of data need to be analyzed, we generally use computer software to deduce the crystal volume and, hence, the number of ions. Image analysis programs such as ImageJ[1] or alternatively, a MATLAB code, can be used to find the boundary of the projection image of the crystal. Assuming rotational symmetry about the z-axis, the volume can be found via

$$V[\text{pix}^3] = \sum_{i=1}^{n}\pi r_i^2 \times \text{pix}, \tag{B.5}$$

where r_i is the radial distance in pixels from the crystal center to the boundary at the ith pixel along z. With this method we generally have an uncertainty of $5 - 10$ %. This method is used for e.g. evaluation of the loading rate in ch. 7.

---

[1]available at e.g. http://rsbweb.nih.gov/ij/download.html
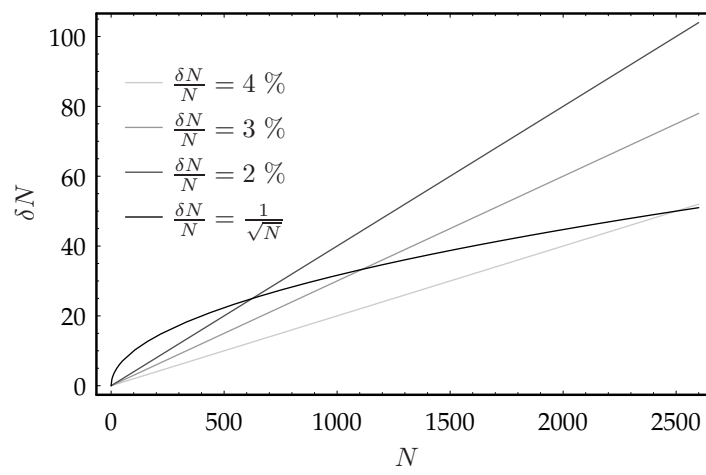
Figure B.2: Uncertainty in number of ions for various relative uncertainties. The black line shows the $\sqrt{N}$ curve.

Appendix C

Collective coupling strength

C.1 Single ion coupling strength

The coupling strength for a single ion at position $\mathbf{r}$ in the cavity is given by

$$g(\mathbf{r}) = g\Psi(\mathbf{r}) \; , \tag{C.1}$$

where $\Psi(\mathbf{r})$ is the modefunction of the standing wave TEM_{00} mode of the cavity field and where g is the coupling strength of a single ion at the waist and anti-node of this cavity field. Since g is the Rabi frequency corresponding to a single photon it can be found from eq. 2.17 with $|A|^2 = 1$

$$g^2 = \frac{\Gamma^2 I}{8 I_{\text{sat}}} = \frac{3\pi c^2 \Gamma I}{2\hbar\omega^3}, \tag{C.2}$$

where we have inserted the expression for the saturation intensity $I_{\text{sat}} = \frac{\hbar\Gamma\omega_{\text{eg}}^3}{12\pi c^2}$ [61]. The field intensity is given by eq. 2.4 as $I = 2\epsilon_0 c \mathcal{E}_0^2$, where the field strength $\mathcal{E}_0$ of a single photon can be found by equating the field energy within a volume V by the photon energy

$$2\epsilon_0 \mathcal{E}_0^2 V = \hbar\omega$$

$$\Downarrow$$

$$\mathcal{E}_0 = \sqrt{\frac{\hbar\omega}{2\epsilon_0 V}}. \tag{C.3}$$

Inserting into eq. C.2 we find

$$g^2 = \frac{3\pi c^3 \Gamma}{2\omega^2 V}, \tag{C.4}$$

where V is the modevolume of the TEM_{00} mode defined as $V = \int |\Psi(\mathbf{r})|^2 d\mathbf{r}$. The modefunction of the standing wave TEM_{00} Gaussian beam is given by

$$\Psi(\mathbf{r}) = \frac{w_0}{w(z)} e^{-(x^2+y^2)/w^2(z)} \sin(kz) \; , \tag{C.5}$$

where $k = 2\pi/\lambda$ is the wave number, w_0 is the minimal waist and $w(z)$ is the waist a distance z from the location of w_0. From this we evaluate the modevolume

$$
\begin{align}
V &= \int \frac{w_0^2}{w^2(z)} e^{-2(x^2+y^2)/w^2(z)} \sin^2(kz) d\mathbf{r} \tag{C.6}\\
&= \frac{\pi w_0^2}{2} \int_0^{l_{\text{cav}}} \sin^2(kz) dz \tag{C.7}\\
&= \frac{\pi w_0^2}{2} \left[\frac{z}{2} - \frac{\sin(2kz)}{4k} \right]_0^{l_{\text{cav}}} \tag{C.8}\\
&= \frac{\pi w_0^2}{2} \left[\frac{l_{\text{cav}}}{2} - \frac{\sin(4\pi l_{\text{cav}}/\lambda)}{4k} \right] \tag{C.9}\\
&= \frac{\pi w_0^2}{4} l_{\text{cav}} \;, \tag{C.10}
\end{align}
$$

where l_{cav} is the cavity length and where in the last step we used the fact that the cavity is resonant with the field. Combining eq. C.4 and C.10 we arrive at the following expression for the single ion coupling strength:

$$
g = \sqrt{\frac{3c\lambda^2\Gamma}{2\pi^2 w_0^2 l_{\text{cav}}}}. \tag{C.11}
$$

In our experiments we will use the $3D_{3/2}, m_J = +3/2 \leftrightarrow 4P_{1/2}, m_J = +1/2$ transition at 866 nm. Of the $3D_{3/2} \leftrightarrow 4P_{1/2}$ transitions, this has the highest Clebsch-Gordan coefficient, resulting in decay rate of $\Gamma = 2\pi \times 1.69/2$ MHz (c.f. appendix A). With a cavity waist of 37 μm and a cavity length of 11.8 ± 0.3 mm (measured in ch. 6.6.1) we find

$$
g = 2\pi \times (0.532 \pm 0.007) \text{ MHz}. \tag{C.12}
$$

C.2   Collective coupling strength

The collective coupling for an ion crystal of uniform density ρ_0 and length L is found analogously to the modevolume

$$
\begin{align}
g^2 N &= \int g^2(\mathbf{r}) \rho_0 d(\mathbf{r}) \tag{C.13}\\
&= g^2 \rho_0 \int \Psi^2(\mathbf{r}) d\mathbf{r} \tag{C.14}\\
&= g^2 \rho_0 \frac{\pi w_0^2}{2} \int_0^L \sin^2(kz) dz \tag{C.15}\\
&= g^2 \rho_0 \frac{\pi w_0^2}{4} L \;. \tag{C.16}
\end{align}
$$

By this we have basically defined the number of ions in the modevolume as

$$
N = \rho_0 \int \Psi^2(\mathbf{r}) d\mathbf{r} = \rho_0 \frac{\pi w_0^2}{4} L. \tag{C.17}
$$

This definition has been used when estimating the number of ions in the cavity mode in e.g. ch. 8.3.

This definition does not, however, take the spheroidal shape of the crystal into account and, hence, overestimates the number of ions for very prolate crystals. The correct number of ions within the cavity modevolume is found from a convolution of the crystal shape and the cavity modefunction. For a crystal of length L and diameter $2R$ the expression reads:

$$
\begin{aligned}
N &= \rho_0 \int_{\text{crystal}} \Psi^2(\mathbf{r} - \mathbf{r}_0) d\mathbf{r} \\
&= \rho_0 \int_{-x'}^{x'} \int_{-y'}^{y'} \int_{-z'}^{z'} \frac{w_0^2}{w^2(z)} e^{-2((x-x_0)^2 + (y-y_0)^2)/w^2(z)} \sin^2(kz) \; dx \; dy \; dz,
\end{aligned}
$$

(C.19)

where $x' = \sqrt{1 - \frac{y^2}{R^2} - \frac{z^2}{R^2}} R$, $y' = \sqrt{1 - \frac{z^2}{(L/2)^2}} R$ and $z' = L/2$. x_0 and y_0 are the offset between the center of the crystal and the cavity mode in the radial plane. This expression has been used when evaluating the number of ions interacting with the cavity field in ch. 10.

Appendix D

Cooperativity parameter for a Doppler broadened atomic medium in a standing wave cavity

Due to the finite temperature of the ions their velocities can not be completely neglected in the interaction with the cavity field. To account for this, we rewrite the atomic dipole for an ion inside the standing wave field of the cavity as,

$$\dot{P}_{\pm kv} = -\left(\frac{\Gamma}{2} + i(\Delta \pm kv)\right)P - igA\left(\Pi_e - \Pi_g\right), \qquad (D.1)$$

where we have made the substitution $\Delta \to \Delta \pm kv$ in eq. 2.12. Here v is the speed of the ion and k is the wave vector of the cavity field, which can be either co- or counter propagating with the motion of the ion. We consider the problem in one dimension, only, and will treat the field as two counter propagating plane waves each with a single k-vector. Note that, unlike the case for a traveling wave, where the atomic dipole is given simply by either P_{+kv} or P_{-kv}, depending on the velocity of ion with respect to the field, here, the total dipole is given by the sum $P = \frac{1}{2}(P_{+kv} + P_{-kv})$. Furthermore, we are ignoring the spatial variation of the standing wave field, which will give rise to an spatial variation in the coupling strength g. This issue is treated in appendix C, where the collective coupling strength $g\sqrt{N}$ is weighted by the cavity field modefunction. Here we shall therefore assume that any spatial dependence is absorbed into g.

In the low-saturation regime ($\Pi_e - \Pi_g \simeq -1$) the steady state value of the $P_{\pm kv}$ of an ion moving at the speed v becomes,

$$P_{\pm kv} = \frac{igA}{\Gamma/2 + i(\Delta \pm kv)}. \qquad (D.2)$$

Assuming the ions have velocities distributed according to a Maxwell-Boltzmann distribution,

$$df(v) = \sqrt{\frac{M}{2\pi k_B T}}\exp\left(\frac{-Mv^2}{2k_B T}\right)dv, \qquad (D.3)$$

177

where a fraction $df(v)$ of the ions occupy velocity classes between v and $v + dv$, then the total atomic dipole, averaged over all velocity classes, can be expressed as

$$P(\Delta) = \frac{1}{2}\sqrt{\frac{M}{2\pi k_B T}} \int_{-\infty}^{\infty} \exp\left(\frac{-Mv^2}{2k_B T}\right) [P(\Delta + kv) + P(\Delta - kv)] \, dv. \qquad (D.4)$$

Through the expression for Doppler width:

$$\delta\nu_D = \frac{2}{\lambda}\sqrt{\frac{2k_B T}{M}\ln 2}, \qquad (3.23)$$

we may define the dimensionless parameters,

$$\zeta = \frac{\sqrt{\ln 2}}{\pi}\frac{kv}{\delta\nu_D} \qquad \Gamma_D = \frac{\sqrt{\ln 2}}{\pi}\frac{\Gamma}{\delta\nu_D} \qquad \Delta_D = \frac{\sqrt{\ln 2}}{\pi}\frac{\Delta}{\delta\nu_D}, \qquad (D.5)$$

and write the real and imaginary parts of the atomic dipole as,

$$\begin{aligned}
\mathrm{Re}\,[P(\Delta_D)] &= -\frac{\sqrt{\ln 2}\,gA}{2\sqrt{\pi^3}\delta\nu_D} \int_{-\infty}^{\infty} e^{-\zeta^2}\left[\frac{(\Delta_D + \zeta)}{(\Gamma_D/2)^2 + (\Delta_D + \zeta)^2}\right.\\
&\quad + \left.\frac{(\Delta_D - \zeta)}{(\Gamma_D/2)^2 + (\Delta_D - \zeta)^2}\right]d\zeta, \qquad (D.6)\\
\mathrm{Im}\,[P(\Delta_D)] &= \frac{\sqrt{\ln 2}\,gA}{2\sqrt{\pi^3}\delta\nu_D} \int_{-\infty}^{\infty} e^{-\zeta^2}\left[\frac{(\Gamma_D/2)}{(\Gamma_D/2)^2 + (\Delta_D + \zeta)^2}\right.\\
&\quad + \left.\frac{(\Gamma_D/2)}{(\Gamma_D/2)^2 + (\Delta_D - \zeta)^2}\right]d\zeta. \qquad (D.7)
\end{aligned}$$

The cavity field equation is given by (c.f. 2.3)

$$\dot{A} = -(\kappa + i\Delta_c)A + igP + \sqrt{2\kappa_1}A^{\mathrm{in}}, \qquad (2.30)$$

in which the real part of the atomic dipole produces a phase shift and the imaginary part results in absorption, which gives rise to a broadening of the cavity resonance, as discussed in ch. 2.3.

On atomic resonance ($\Delta_D = 0$) the equations simplify somewhat. The real part of the dipole is of course zero, as expected for a phase shift, but the absorption is not and the effect of Doppler broadening will reflect on this. The imaginary part of the dipole can be written as,

$$\begin{aligned}
\mathrm{Im}\,[P(0)] &= \frac{\sqrt{\ln 2}\,gA}{\sqrt{\pi^3}\delta\nu_D} \int_{-\infty}^{\infty} e^{-\zeta^2}\frac{(\Gamma_D/2)}{(\Gamma_D/2)^2 + \zeta^2}d\zeta\\
&= \frac{\sqrt{\ln 2}\,gA}{\sqrt{\pi}\delta\nu_D}e^{(\Gamma_D/2)^2}\mathrm{erfc}(\Gamma_D/2), \qquad (D.8)
\end{aligned}$$

where $\mathrm{erfc}(\Gamma_D/2)$ is the complementary error function. In steady state, the resulting HWHM of the cavity $\tilde{\kappa}$ for N ions interacting with the cavity under the influence of Doppler broadening, will be given by

$$\tilde{\kappa} = \kappa\left(1 + \frac{g^2 N}{\kappa\delta\nu_D}\sqrt{\frac{\ln 2}{\pi}}e^{(\Gamma_D/2)^2}\mathrm{erfc}(\Gamma_D/2)\right). \qquad (D.9)$$

Note that since $\text{Im}\,[P(0)]$ is linear in A, and otherwise constant as a function of Δ_c, the cavity lineshape is still a Lorentzian and assigning a width $\tilde{\kappa}$ is therefore still meaningful in this sense. Comparison with the expression for the cavity width without the effect of Doppler broadening (eq. 10.8) suggests that we may treat the finite temperature of the ions as giving rise to an effective width $\tilde{\Gamma}$ and retain the form of the cooperativity parameter as,

$$\tilde{C} = \frac{g^2 N}{\kappa \tilde{\Gamma}}, \tag{D.10}$$

where

$$\begin{aligned}
\frac{1}{\tilde{\Gamma}} &= \frac{1}{2\delta\nu_D}\sqrt{\frac{\ln 2}{\pi}}e^{(\Gamma_D/2)^2}\text{erfc}(\Gamma_D/2) \\
&\simeq \frac{1}{\Gamma}\left(1 - \frac{1}{2(\Gamma_D/2)^2} + \frac{3}{(2(\Gamma_D/2)^2)^2} - \frac{15}{(2(\Gamma_D/2)^2)^3} + ...\right), \tag{D.11}
\end{aligned}$$

where we have expanded the complementary error function going to the second line. Keeping only the first two terms in the expansion and substituting eq. D.5 for Γ_D,

$$\tilde{\Gamma} \simeq \Gamma\left[1 + \left(\frac{2\pi}{\sqrt{\ln 2}}\frac{\delta\nu_D}{\Gamma}\right)^2\right], \tag{D.12}$$

which will be valid in the limit where $\Gamma \gg \delta\nu_D$, that is, for small temperatures. This is seen in fig. D.1, which shows the dependence of $\tilde{\Gamma}$ on the temperature, based on the full expression of eq. D.11 (solid line) as well as the first-order approximation of eq. D.12 (dashed line). Only for temperatures below ~ 20 mK is the approximate expression reasonably accurate.

So far we have only considered the resonant case, where $\Delta = 0$. In general we would like know how the finite temperature of the ions affect our system for all values of the atomic detuning. This requires solving eq. D.7 which we can only do numerically.
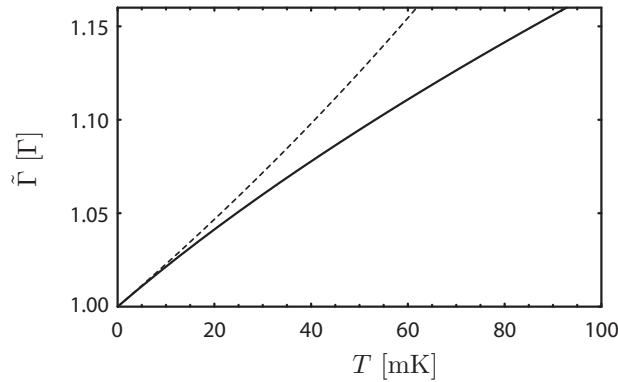
Figure D.1: $\tilde{\Gamma}$ in units of the natural width Γ as a function of temperature for $\Delta = 0$. The solid line is the full solution of eq. D.11, whereas the dashed line is based on eq. D.12 and only valid for small temperatures.

Fig. D.2 shows the resulting absorption and phase shift curves for $T = 0$ mK and $T = 100$ mK. Clearly one sees the effect of the inhomogeneous broadening, although the choice of temperature in this calculation was higher than expected for the ions to make the effect easily visible.

In ch. 10 where we study the interaction between the ions and the cavity field by measurements that produce such curves as those of fig. D.2, it will prove necessary to to take the effect of broadening into account to understand the data. In principle, to extract the physical parameters of the system from a fit to such data, one should use a Voigt profile and in this way isolate the effect of Doppler broadening in the Gaussian width of that profile. In practice we have often used a simpler Lorentzian fit with a width modified by the effect of Doppler broadening. To interpret such data, we made a numerical analysis, performing Lorentzian fits to curves such as that of fig. D.2a). Fig. D.3 shows the result, where the we have plotted the effective width $\tilde{\Gamma}'$, deduced from a Lorentzian fit, as a function of temperature.

(a)   (b)

Figure D.2: a) Absorption and b) phase shift in units of κC versus the detuning from atomic resonance. The solid line is based a temperature of 100 mK whereas the dashed line is based on a temperature of 0 mK.
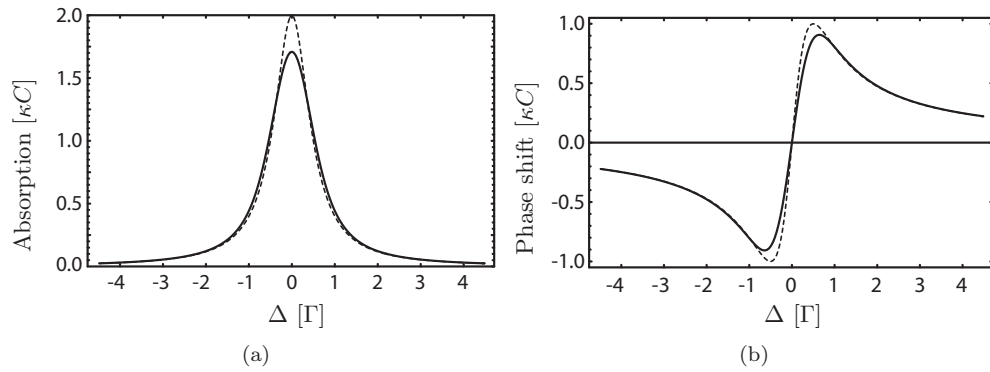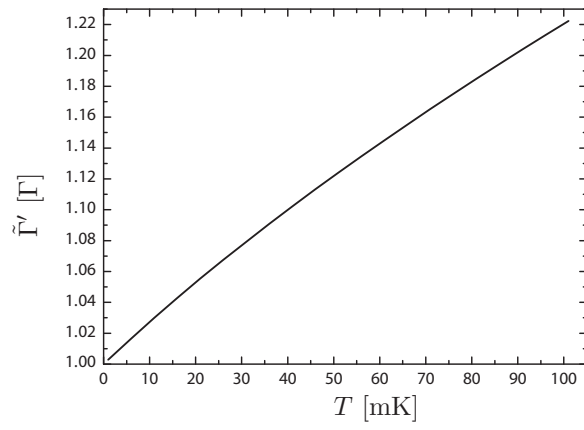
Figure D.3: $\tilde{\Gamma}'$ in units of the natural width Γ as a function of temperature. The curve is produced from Lorentzian fits to curves such as that of fig. D.2a) for various temperatures.

Appendix E

Optical pumping of Ca$^+$

Fig. E.1 shows the level scheme of the relevant levels and transitions for optical pumping of ^{40}Ca$^+$. In the optical pumping scheme we aim at accumulating all the population in the $3D_{3/2}, m_J = -3/2$ state ($|7\rangle$), which means that we should have $\Omega_-^{\mathrm{dp}} = 0$. Here we have included this field to allow for modeling of imperfections in the pumping scheme. As outlined in ch. 9.1, the equations of motion for the populations and coherences are derived from the Hamiltonian described by eq. 9.2, 9.3 and 9.4 using Hamilton's equation of motion. We then apply the rotating wave approximation and add terms accounting for spontaneous emission. In ch. 2.1 we went through the derivation for the case of a two-level system and the equations of motion for this eight-level system are found in similar fashion. The result is given here:

$$
\begin{aligned}
\dot{\Pi}_0 &= \Gamma_{20}\Pi_2 + \Gamma_{30}\Pi_3 - i(\Omega_0^{\mathrm{sp}} P_{02}^* - \Omega_0^{\mathrm{sp}} P_{02}) - i(\Omega_+^{\mathrm{sp}} P_{03}^* - \Omega_+^{\mathrm{sp}*} P_{03}) \\
\dot{\Pi}_1 &= \Gamma_{21}\Pi_2 + \Gamma_{31}\Pi_3 - i(\Omega_0^{\mathrm{sp}} P_{13}^* - \Omega_0^{\mathrm{sp}} P_{13}) - i(\Omega_-^{\mathrm{sp}} P_{12}^* - \Omega_-^{\mathrm{sp}*} P_{12}) \\
\dot{\Pi}_2 &= -\Gamma_2\Pi_2 - i(\Omega_0^{\mathrm{sp}} P_{02} - \Omega_0^{\mathrm{sp}} P_{02}^*) - i(\Omega_-^{\mathrm{sp}*} P_{12} - \Omega_-^{\mathrm{sp}} P_{12}^*) \\
&\quad + i(\Omega_0^{\mathrm{dp}} P_{25}^* - \Omega_0^{\mathrm{dp}} P_{25}) - i(\Omega_{+1}^{\mathrm{dp}*} P_{24}^* - \Omega_{+1}^{\mathrm{dp}} P_{24}) - i(\Omega_{-2}^{\mathrm{dp}*} P_{26}^* - \Omega_{-2}^{\mathrm{dp}} P_{26}) \\
\dot{\Pi}_3 &= -\Gamma_3\Pi_3 + i(\Omega_0^{\mathrm{sp}} P_{13}^* - \Omega_0^{\mathrm{sp}} P_{13}) + i(\Omega_+^{\mathrm{sp}} P_{03}^* - \Omega_+^{\mathrm{sp}*} P_{03}) \\
&\quad + i(\Omega_0^{\mathrm{dp}} P_{36}^* - \Omega_0^{\mathrm{dp}} P_{36}) - i(\Omega_{+2}^{\mathrm{dp}*} P_{35}^* - \Omega_{+2}^{\mathrm{dp}} P_{35}) - i(\Omega_{-1}^{\mathrm{dp}*} P_{37}^* - \Omega_{-1}^{\mathrm{dp}} P_{37}) \\
\dot{\Pi}_4 &= \Gamma_{24}\Pi_2 - i(\Omega_{+1}^{\mathrm{dp}} P_{24} - \Omega_{+1}^{\mathrm{dp}*} P_{24}^*) \\
\dot{\Pi}_5 &= \Gamma_{25}\Pi_2 + \Gamma_{35}\Pi_3 + i(\Omega_0^{\mathrm{dp}} P_{25}^* - \Omega_0^{\mathrm{dp}} P_{25}) + i(\Omega_{+2}^{\mathrm{dp}*} P_{35}^* - \Omega_{+2}^{\mathrm{dp}} P_{35}) \\
\dot{\Pi}_6 &= \Gamma_{26}\Pi_2 + \Gamma_{36}\Pi_3 + i(\Omega_0^{\mathrm{dp}} P_{36}^* - \Omega_0^{\mathrm{dp}} P_{36}) + i(\Omega_{-2}^{\mathrm{dp}*} P_{26}^* - \Omega_{-2}^{\mathrm{dp}} P_{26}) \\
\dot{\Pi}_7 &= \Gamma_{37}\Pi_3 + i(\Omega_{-1}^{\mathrm{dp}*} P_{37}^* - \Omega_{-1}^{\mathrm{dp}} P_{37}) \\
\dot{P}_{01} &= -i2\delta_s P_{01} - i\Omega_0^{\mathrm{sp}} P_{12}^* - i\Omega_+^{\mathrm{sp}} P_{13}^* + i\Omega_0^{\mathrm{sp}} P_{03} + i\Omega_-^{\mathrm{sp}*} P_{02} \\
\dot{P}_{02} &= -(\Gamma_2/2 + i(\delta_s - \delta_p + \Delta_{\mathrm{sp}}))P_{02} - i\Omega_0^{\mathrm{sp}}(\Pi_2 - \Pi_0) - i\Omega_+^{\mathrm{sp}} P_{23}^* + i\Omega_-^{\mathrm{sp}} P_{01} \\
&\quad + i\Omega_0^{\mathrm{dp}} P_{05} + i\Omega_{+1}^{\mathrm{dp}} P_{04} + i\Omega_{-2}^{\mathrm{dp}} P_{06} \\
\dot{P}_{03} &= -(\Gamma_3/2 + i(\delta_s + \delta_p + \Delta_{\mathrm{sp}}))P_{03} - i\Omega_+^{\mathrm{sp}}(\Pi_3 - \Pi_0) - i\Omega_0^{\mathrm{sp}} P_{23} + i\Omega_0^{\mathrm{sp}} P_{01} \\
&\quad + i\Omega_0^{\mathrm{dp}} P_{06} + i\Omega_{+2}^{\mathrm{dp}} P_{05} + i\Omega_{-1}^{\mathrm{dp}} P_{07}
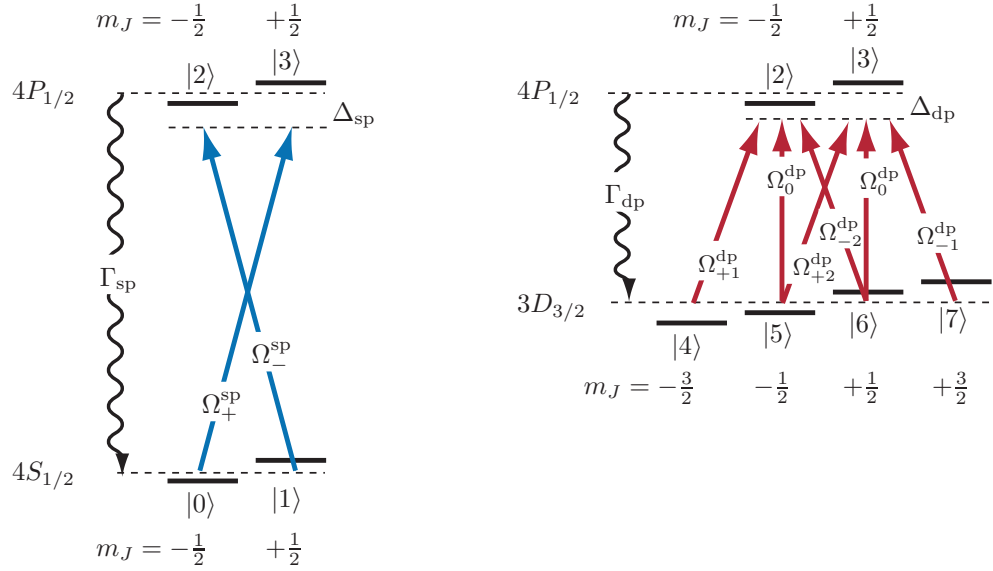\end{aligned}
$$

Figure E.1: Level scheme of the relevant levels and transitions for optical pumping of ^{40}Ca$^+$. Due to the Zeeman effect, the levels are shifted from their unperturbed configuration (dashed lines). Ω denotes the Rabi frequencies of the various transitions, Δ the detunings with respect to the unperturbed transitions and the decay rates Γ are distributed among the magnetic substates according to the Clebsch-Gordan coefficients of those transitions (see appendix. A). Γ_{ds} is set equal to zero due to the long life time ($\simeq 1$ s) of the $3D_{3/2}$ state. The state designation $|i\rangle$ where $i = 1, 2, 3, 4, 5, 6, 7$ is used in the equations of motion (see text).

$$
\begin{aligned}
\dot{P_{04}} &= -i(\delta_{\mathrm{s}} - 3\delta_{\mathrm{d}} + \Delta_{\mathrm{sp}} - \Delta_{\mathrm{dp}})P_{04} - i\Omega_0^{\mathrm{sp}}P_{24} - i\Omega_+^{\mathrm{sp}}P_{34} + i\Omega_{+1}^{\mathrm{dp}\,*}P_{02} \\
\dot{P_{05}} &= -i(\delta_{\mathrm{s}} - \delta_{\mathrm{d}} + \Delta_{\mathrm{sp}} - \Delta_{\mathrm{dp}})P_{05} - i\Omega_0^{\mathrm{sp}}P_{25} - i\Omega_+^{\mathrm{sp}}P_{35} + i\Omega_0^{\mathrm{dp}}P_{02} + i\Omega_{+2}^{\mathrm{dp}\,*}P_{03} \\
\dot{P_{06}} &= -i(\delta_{\mathrm{s}} + \delta_{\mathrm{d}} + \Delta_{\mathrm{sp}} - \Delta_{\mathrm{dp}})P_{06} - i\Omega_0^{\mathrm{sp}}P_{26} - i\Omega_+^{\mathrm{sp}}P_{36} + i\Omega_0^{\mathrm{dp}}P_{03} + i\Omega_{-2}^{\mathrm{dp}\,*}P_{02} \\
\dot{P_{07}} &= -i(\delta_{\mathrm{s}} + 3\delta_{\mathrm{d}} + \Delta_{\mathrm{sp}} - \Delta_{\mathrm{dp}})P_{07} - i\Omega_0^{\mathrm{sp}}p27 - i\Omega_+^{\mathrm{sp}}P_{37} + i\Omega_{-1}^{\mathrm{dp}\,*}P_{03} \\
\dot{P_{12}} &= -(\Gamma_2/2 + i(-\delta_{\mathrm{s}} - \delta_{\mathrm{p}} + \Delta_{\mathrm{sp}}))P_{12} - i\Omega_-^{\mathrm{sp}}(\Pi_2 - \Pi_1) - i\Omega_0^{\mathrm{sp}}P_{23}^* + i\Omega_0^{\mathrm{sp}}P_{01}^* \\
&\quad + i\Omega_0^{\mathrm{dp}}P_{15} + i\Omega_{+1}^{\mathrm{dp}}P_{14} + i\Omega_{-2}^{\mathrm{dp}}P_{16} \\
\dot{P_{13}} &= -(\Gamma_3/2 + i(-\delta_{\mathrm{s}} + \delta_{\mathrm{p}} + \Delta_{\mathrm{sp}}))P_{13} - i\Omega_0^{\mathrm{sp}}(\Pi_3 - \Pi_1) - i\Omega_-^{\mathrm{sp}}P_{23} + i\Omega_+^{\mathrm{sp}}P_{01}^* \\
&\quad + i\Omega_{+2}^{\mathrm{dp}}P_{15} + i\Omega_0^{\mathrm{dp}}P_{16} + i\Omega_{-1}^{\mathrm{dp}}P_{17} \\
\dot{P_{14}} &= -i(-\delta_{\mathrm{s}} - 3\delta_{\mathrm{d}} + \Delta_{\mathrm{sp}} - \Delta_{\mathrm{dp}})P_{14} - i\Omega_0^{\mathrm{sp}}P_{34} - i\Omega_-^{\mathrm{sp}}P_{24} + i\Omega_{+1}^{\mathrm{dp}\,*}P_{12} \\
\dot{P_{15}} &= -i(-\delta_{\mathrm{s}} - \delta_{\mathrm{d}} + \Delta_{\mathrm{sp}} - \Delta_{\mathrm{dp}})P_{15} - i\Omega_0^{\mathrm{sp}}P_{35} - i\Omega_-^{\mathrm{sp}}P_{25} + i\Omega_0^{\mathrm{dp}}P_{12} + i\Omega_{+2}^{\mathrm{dp}\,*}P_{13} \\
\dot{P_{16}} &= -i(-\delta_{\mathrm{s}} + \delta_{\mathrm{d}} + \Delta_{\mathrm{sp}} - \Delta_{\mathrm{dp}})P_{16} - i\Omega_0^{\mathrm{sp}}P_{36} - i\Omega_-^{\mathrm{sp}}P_{26} + i\Omega_0^{\mathrm{dp}}P_{13} + i\Omega_{-2}^{\mathrm{dp}\,*}P_{12} \\
\dot{P_{17}} &= -i(-\delta_{\mathrm{s}} + 3\delta_{\mathrm{d}} + \Delta_{\mathrm{sp}} - \Delta_{\mathrm{dp}})P_{17} - i\Omega_0^{\mathrm{sp}}P_{37} - i\Omega_-^{\mathrm{sp}}P_{27} + i\Omega_{-1}^{\mathrm{dp}\,*}P_{13}
\end{aligned}
$$

$$\dot{P_{23}} = -((\Gamma_2 + \Gamma_3)/2 + i2\delta_{\rm p})P_{23} - i\Omega_0^{\rm sp}P_{03} - i\Omega_-^{\rm sp*}P_{13} - i\Omega_0^{\rm dp}P_{35}^* - i\Omega_{+1}^{\rm dp*}P_{34}^*$$
$$- i\Omega_{-2}^{\rm dp*}P_{36}^* + i\Omega_0^{\rm sp}P_{12}^* + i\Omega_+^{\rm sp}P_{02}^* + i\Omega_0^{\rm dp}P_{26} + i\Omega_{+2}^{\rm dp}P_{25} + i\Omega_{-1}^{\rm dp}P_{27}$$

$$\dot{P_{24}} = -(\Gamma_2/2 + i(\delta_{\rm p} - 3\delta_{\rm d} - \Delta_{\rm dp}))P_{24} - i\Omega_{+1}^{\rm dp*}(\Pi_4 - \Pi_2) - i\Omega_0^{\rm sp}P_{04} - i\Omega_-^{\rm sp*}P_{14}$$
$$- i\Omega_0^{\rm dp}P_{45}^* - i\Omega_{-2}^{\rm dp*}P_{46}^*$$

$$\dot{P_{25}} = -(\Gamma_2/2 + i(\delta_{\rm p} - \delta_{\rm d} - \Delta_{\rm dp}))P_{25} - i\Omega_0^{\rm dp}(\Pi_5 - \Pi_2) - i\Omega_0^{\rm sp}P_{05} - i\Omega_-^{\rm sp*}P_{15}$$
$$- i\Omega_{+1}^{\rm dp*}P_{45} - i\Omega_{-2}^{\rm dp*}P_{56}^* + i\Omega_{+2}^{\rm dp*}P_{23}$$

$$\dot{P_{26}} = -(\Gamma_2/2 + i(\delta_{\rm p} + \delta_{\rm d} - \Delta_{\rm dp}))P_{26} - i\Omega_{-2}^{\rm dp*}(\Pi_6 - \Pi_2) - i\Omega_0^{\rm sp}P_{06} - i\Omega_-^{\rm sp*}P_{16}$$
$$- i\Omega_0^{\rm dp}P_{56} - i\Omega_{+1}^{\rm dp*}P_{46} + i\Omega_0^{\rm dp}P_{23}$$

$$\dot{P_{27}} = -(\Gamma_2/2 + i(\delta_{\rm p} + 3\delta_{\rm d} - \Delta_{\rm dp}))P_{27} - i\Omega_0^{\rm sp}P_{07} - i\Omega_-^{\rm sp*}P_{17} - i\Omega_0^{\rm dp}P_{57}$$
$$- i\Omega_{+1}^{\rm dp*}P_{47} - i\Omega_{-2}^{\rm dp*}P_{67} + i\Omega_{-1}^{\rm dp*}P_{23}$$

$$\dot{P_{34}} = -(\Gamma_3/2 + i(-\delta_{\rm p} - 3\delta_{\rm d} - \Delta_{\rm dp}))P_{34} - i\Omega_0^{\rm sp}P_{14} - i\Omega_+^{\rm sp*}P_{04} - i\Omega_0^{\rm dp}P_{46}^*$$
$$- i\Omega_{+2}^{\rm dp*}P_{45}^* - i\Omega_{-1}^{\rm dp*}P_{47}^* + i\Omega_{+1}^{\rm dp*}P_{23}^*$$

$$\dot{P_{35}} = -(\Gamma_3/2 + i(-\delta_{\rm p} - \delta_{\rm d} - \Delta_{\rm dp}))P_{35} - i\Omega_{+2}^{\rm dp*}(\Pi_5 - \Pi_3) - i\Omega_0^{\rm sp}P_{15} - i\Omega_+^{\rm sp*}P_{05}$$
$$- i\Omega_0^{\rm dp}P_{56}^* - i\Omega_{-1}^{\rm dp*}P_{57}^* + i\Omega_0^{\rm dp}P_{23}^*$$

$$\dot{P_{36}} = -(\Gamma_3/2 + i(-\delta_{\rm p} + \delta_{\rm d} - \Delta_{\rm dp}))P_{36} - i\Omega_0^{\rm dp}(\Pi_6 - \Pi_3) - i\Omega_0^{\rm sp}P_{16} - i\Omega_+^{\rm sp*}P_{06}$$
$$- i\Omega_{+2}^{\rm dp*}P_{56} - i\Omega_{-1}^{\rm dp*}P_{67}^* + i\Omega_{-2}^{\rm dp*}P_{23}^*$$

$$\dot{P_{37}} = -(\Gamma_3/2 + i(-\delta_{\rm p} + 3\delta_{\rm d} - \Delta_{\rm dp}))P_{37} - i\Omega_{-1}^{\rm dp*}(\Pi_7 - \Pi_3) - i\Omega_0^{\rm sp}P_{17} - i\Omega_+^{\rm sp*}P_{07}$$
$$- i\Omega_0^{\rm dp}P_{67} - i\Omega_{+2}^{\rm dp*}P_{57}$$

$$\dot{P_{45}} = -(i2\delta_{\rm d})P_{45} - i\Omega_{+1}^{\rm dp}P_{25} + i\Omega_0^{\rm dp}P_{24}^* + i\Omega_{+2}^{\rm dp*}P_{34}^*$$

$$\dot{P_{46}} = -(i4\delta_{\rm d})P_{46} - i\Omega_{+1}^{\rm dp}P_{26} + i\Omega_0^{\rm dp}P_{34}^* + i\Omega_{-2}^{\rm dp*}P_{24}^*$$

$$\dot{P_{47}} = -(i6\delta_{\rm d})P_{47} - i\Omega_{+1}^{\rm dp}P_{27} + i\Omega_{-1}^{\rm dp*}P_{34}^*$$

$$\dot{P_{56}} = -(i2\delta_{\rm d})P_{56} - i\Omega_0^{\rm dp}P_{26} - i\Omega_{+2}^{\rm dp}P_{36} + i\Omega_0^{\rm dp}P_{35}^* + i\Omega_{-2}^{\rm dp*}P_{25}^*$$

$$\dot{P_{57}} = -(i4\delta_{\rm d})P_{57} - i\Omega_0^{\rm dp}P_{27} - i\Omega_{+2}^{\rm dp}P_{37} + i\Omega_{-1}^{\rm dp*}P_{35}^*$$

$$\dot{P_{67}} = -(i2\delta_{\rm d})P_{67} - i\Omega_0^{\rm dp}P_{37} - i\Omega_{-2}^{\rm dp}P_{27} + i\Omega_{-1}^{\rm dp*}P_{36}^*$$

Not written are the complex conjugates of the equations of motion for the coherences and in total there are thus 64 coupled differential equations. In the above equations we have defined $\delta_{\rm s,p,d} = \frac{1}{2\hbar}g_{\rm s,p,d}\mu_B B$ and $*$ denotes complex conjugation as usual. All other parameters have been defined in ch. 9.1.

E.1 Polarization of $45°$ optical pumping beam

For the optical pumping to work, the 866 nm beam should only drive π and σ_+ transitions between the $3D_{3/2}$ and the $4P_{1/2}$ levels. With a magnetic field defining the quantization axis along the z-axis in the unprimed coordinate system (black axis of fig. E.2), the polarization of the electric field must only consist of linear and positive
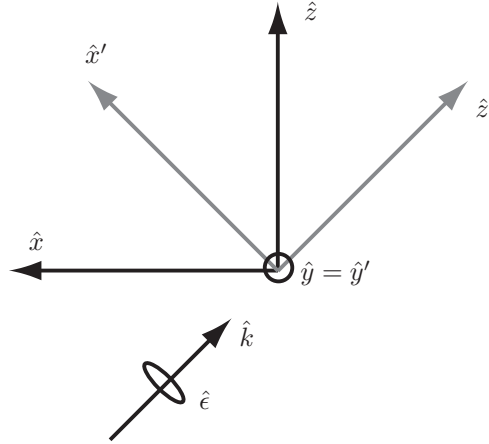
Figure E.2: Coordinate systems for transformation of polarization of 45° optical pumping beam with polarization $\hat{\epsilon}$ and propagation vector $\hat{k}$.

circular components. In the following we will show that this is possible to achieve for a beam propagating along the z'-axis.

In the primed coordinate system (gray axis of fig. E.2) the polarization of the field can be written as

$$\hat{\epsilon} = a_{x'}\hat{\epsilon}_{x'} + a_{y'}\hat{\epsilon}_{y'}, \tag{E.1}$$

where a_i and $\hat{\epsilon}_i$ are the polarization amplitudes and unit vectors, respectively. With the k-vector at 45° to the z-axis, transforming into the unprimed coordinate system gives

$$\hat{\epsilon} = a_{x'}\frac{\hat{\epsilon}_x + \hat{\epsilon}_z}{\sqrt{2}} + a_{y'}\hat{\epsilon}_y. \tag{E.2}$$

We then write the linear polarization components along x and y in terms of circular polarization vectors $\hat{\epsilon}_+, \hat{\epsilon}_-$ such that

$$
\begin{aligned}
\hat{\epsilon} &= \frac{a_{x'}}{\sqrt{2}}\left(\frac{\hat{\epsilon}_- - \hat{\epsilon}_+}{\sqrt{2}} + \hat{\epsilon}_z\right) + a_{y'}\frac{\hat{\epsilon}_- + \hat{\epsilon}_+}{i\sqrt{2}} \\
&= \frac{a_{x'}}{\sqrt{2}}\hat{\epsilon}_z - \left(\frac{a_{x'}}{2} + i\frac{a_{y'}}{\sqrt{2}}\right)\hat{\epsilon}_+ + \left(\frac{a_{x'}}{2} - i\frac{a_{y'}}{\sqrt{2}}\right)\hat{\epsilon}_-.
\end{aligned}
\tag{E.3}
$$

For the field not to contain any σ_- component of the polarization, the last term in eq. E.3 must vanish, which means that $a_{y'} = -i\frac{a_{x'}}{\sqrt{2}}$. In the unprimed coordinate system the expression for the polarization then reads

$$\hat{\epsilon} = a_{x'}\left(\frac{\hat{\epsilon}_z}{\sqrt{2}} - \hat{\epsilon}_+\right), \tag{E.4}$$

where $\hat{\epsilon}_z$ drives the π transitions and $\hat{\epsilon}_+$ drives the σ_+ transitions. This result shows that optical pumping can indeed be done using a single beam at 45° and that the field will drive π and the σ_+ transitions with a relative field strength of $\frac{1}{\sqrt{2}}$.

The actual ellipticity of the polarization can be calculated from the Stokes parameters defined as [181]

$$
\begin{align}
S_0 &= a_{x'}a_{x'}^* + a_{y'}a_{y'}^* \tag{E.5a}\\
S_1 &= S_0\cos(2\beta)\cos(2\alpha) = a_{x'}a_{x'}^* - a_{y'}a_{y'}^* \tag{E.5b}\\
S_2 &= S_0\cos(2\beta)\sin(2\alpha) = a_{x'}^*a_{y'} + a_{x'}a_{y'}^* \tag{E.5c}\\
S_3 &= S_0\sin(2\beta) = i(a_{x'}^*a_{y'} - a_{x'}a_{y'}^*), \tag{E.5d}
\end{align}
$$

where 2α is the azimuthal angle and 2β the angle with respect to the equatorial plane, when representing the polarization state on a Poincaré sphere. From the condition $a_{y'} = -i\frac{a_{x'}}{\sqrt{2}}$ eq. E.5 then gives

$$
\begin{align}
\cos(2\beta)\cos(2\alpha) &= \frac{1}{2} \tag{E.6a}\\
\cos(2\beta)\sin(2\alpha) &= 0 \tag{E.6b}\\
\sin(2\beta) &= \sqrt{2}, \tag{E.6c}
\end{align}
$$

which means that

$$
\begin{align}
\alpha &= \frac{\pi}{2}k \text{ , for } k = 0, \pm 1, \pm 2, ...\\
\tan(2\beta) &= \frac{1}{\sqrt{2}}\\
\Rightarrow 2\beta &\simeq 35°.
\end{align}
$$

The right polarization state can thus be produced starting from a perfectly linear polarization ($2\beta = 0$) and then changing the angle with respect to the equatorial plane on the Poincaré sphere by $35°$. In practice, it can be achieved by using a PBS followed by a $\lambda/4$-plate.

E.2 Rabi frequencies of optical pumping beams

The Rabi frequency is defined via eq. 2.17 as

$$
|\Omega|^2 = \frac{I\Gamma^2}{8I_{\text{sat}}},
$$

where Γ and I_{sat} are given in appendix A for the various transitions of Ca$^+$. In the current setup with beam waists of the 397 nm beam and of the 866 nm beam for optical pumping of ~ 1 mm and ~ 1.3 mm, respectively, we calculate the following expressions for the Rabi frequencies on the relevant transitions:

$$
\begin{align}
\Omega_+^{\text{sp}} &= \Omega_-^{\text{sp}} \simeq 2\pi \times 5 \times \sqrt{P_{397}}\,\frac{\text{MHz}}{\text{mW}}\\
\Omega_{+1}^{\text{dp}} &\simeq 2\pi \times 3 \times \sqrt{P_{866}}\,\frac{\text{MHz}}{\text{mW}}\\
\Omega_0^{\text{dp}} &= \Omega_{+2}^{\text{dp}} = \sqrt{\tfrac{1}{3}}\Omega_{+1}^{\text{dp}},
\end{align}
$$

where P_{397} and P_{866} denote the laser power of the 397 nm beam and of the 866 nm beam, respectively. The relationship between the Rabi frequencies on the $3D_{3/2} \leftrightarrow 4P_{1/20}$ transition is a result of eq. E.4 and of their relative Clebsch-Gordan coefficients (see appendix A). With the laser power that we have available with our present laser systems, Rabi frequencies of up to $2\pi\times \sim 20$ MHz can be achieved with both the 397 nm and the 866 nm beams.

Appendix F

Laser systems

Laser	Purpose	Max power	Typical power	Linewidth
272	Photoionization of Ca	50 mW	5-30 mW	~ 35 kHz
397 (Ti:Sapph)	Laser cooling / optical pumping	10 mW	0.1-10 mW	~ 100 kHz
397 (diode)	Laser cooling	3 mW	0.1-3 mW	<1000 kHz
866-1	Laser cooling / probe	20 mW	1-5 / 10^{-9} mW	~ 100 kHz
866-2	Laser cooling / optical pumping	20 mW	1-5 mW	~ 100 kHz
894	Cavity laser	20 mW	$10^{-3} mW$	~ 100 kHz

Table F.1: Data on various laser systems used in this work. The power level is that available for the experiment.

Appendix G

Properties of non-linear crystals used for the 272 nm laser

From the manufacturers (Castech [182] and Newlight Photonics) the following specifications were given:

crystal	wavelenghts	d_{eff}	n	l_c	α	ar-coating
LiNbO$_3$	1088 → 544 nm	5.1 pm/V	2.22	15 mm	0.15%	< 0.2%
BBO	544 → 272 nm	1.78 pm/V	1.67	8 mm	0.2%	< 0.2%

Table G.1: Specifications of non-linear crystal.

G.1 Phasematching temperature in LiNbO$_3$

The refractive index for a transparent medium is related to the wavelength of a light wave propagating in the medium through the so called Sellmeier equation. This empirical formula can be used to find the phasematching temperature for second harmonic generation for a given wavelength.

Including the temperature dependence to first order in the Sellmeier equations, the refractive index of LiNbO$_3$ with 7% Mg dopant, for the ordinary and the extraordinary axis, is given by [182]

$$n_0(\lambda, T) = 4.8762 + \frac{0.11554}{\lambda^2 - 0.04674} - 0.033119 \cdot \lambda^2 + (T - 25) \cdot (-0.874 \cdot 10^{-6}/°\text{C}) \, ,$$

$$n_e(\lambda, T) = 4.5469 + \frac{0.094779}{\lambda^2 - 0.04439} - 0.026721 \cdot \lambda^2 + (T - 25) \cdot 39.073 \cdot 10^{-6}/°\text{C} \, ,$$

where λ is in μm. With the fundamental wave propagating along the ordinary axis and the second harmonic wave along the extraordinary axis, the phasematching temperature is estimanted to $\sim 158°$C by solving $n_0(1.08898, T) = n_e(1.08898/2, T)$ for T. Fig. G.1 shows a graphic solution of this.
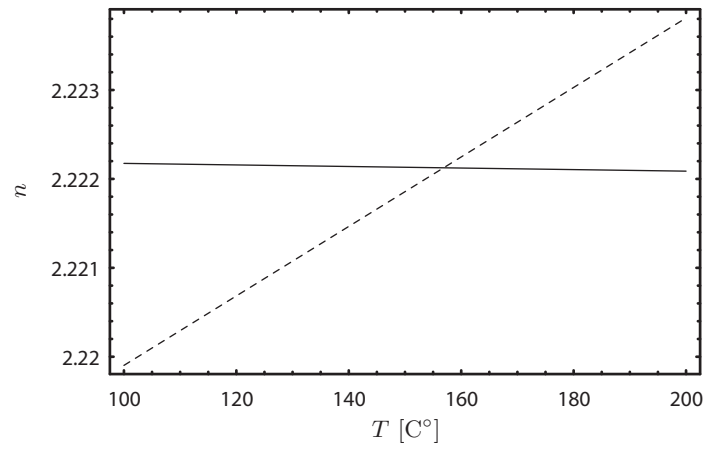
Figure G.1: Plot of the refractive index as a function of temperature for the fundamental wave propagating along the ordinary axis (solid line) and the second harmonic wave propagating along the extraordinary axis (dashed line).

.

Appendix H

Evaluation of uncertainty in measurements of the cavity width

Due to the acoustic noise in our cavity, the measured spectra are associated with some shot-to-shot fluctuations that give rise to a systematic uncertainty in our measurements. To evaluate the final error bars that we should give with our data, this has to be combined with the error which we obtain from each fit result. By a series of tests performed to measure the spread in the results of repeated measurements of the the empty cavity width, we have deduced that this uncertainty is about 7% of the measured mean value of the cavity width. To combine this with the statistical uncertainty obtained from fits to the data, we use a so-called unbiased estimator of weighted population variance, which is a model well-suited for our type of data with a limited number of measurements.

From n measurements of the width with outcomes x_i and associated errors σ_i, we define the mean value

$$\langle x \rangle = \frac{\sum_i^n w_i x_i}{\sum_i^n w_i}, \tag{H.1}$$

with $w_i = \frac{1}{\sigma_i}$. The total error is then given by

$$\sigma = \sqrt{\frac{\sigma_{\mathrm{stat}}^2 + \sigma_{\mathrm{sys}}^2}{n}}, \tag{H.2}$$

where $\sigma_{\mathrm{sys}} = 0.07 \times \langle x \rangle$ and

$$\sigma_{\mathrm{stat}} = \sqrt{\frac{\sum_i^n w_i}{\left(\sum_i^n w_i\right)^2 - \sum_i^n w_i^2} \sum_i^n w_i \left(x_i - \langle x \rangle\right)^2} \tag{H.3}$$

Bibliography

[1]   R. Loudon, *The quantum theory of light* (Oxford University Press, 2000).

[2]   E. M. Purcell, *Spontaneous Emission Probabilities At Radio Frequencies*, Physical Review **69**, 681 (1946).

[3]   K. H. Drexhage, *Progress in Optics, vol XII*, 165 (North Holland, Amsterdam, 1974).

[4]   P. Goy, J. M. Raimond, M. Gross and S. Haroche, *Observation Of Cavity-Enhanced Single-Atom Spontaneous Emission*, Physical Review Letters **50**, 1903 (1983),
URL link.

[5]   R. G. Hulet, E. S. Hilfer and D. Kleppner, *Inhibited Spontaneous Emission By A Rydberg Atom*, Physical Review Letters **55**, 2137 (1985),
URL link.

[6]   W. Jhe, A. Anderson, E. A. Hinds, D. Meschede, L. Moi and S. Haroche, *Suppression Of Spontaneous Decay At Optical Frequencies - Test Of Vacuum-Field Anisotropy In Confined Space*, Physical Review Letters **58**, 666 (1987),
URL link.

[7]   F. Demartini, G. Innocenti, G. R. Jacobovitz and P. Mataloni, *Anomalous Spontaneous Emission Time In A Microscopic Optical Cavity*, Physical Review Letters **59**, 2955 (1987),
URL link.

[8]   D. J. Heinzen, J. J. Childs, J. E. Thomas and M. S. Feld, *Enhanced And Inhibited Visible Spontaneous Emission By Atoms In A Confocal Resonator*, Physical Review Letters **58**, 1320 (1987),
URL link.

[9]   S. Haroche and J. M. Raimond, *Exploring the quantum: atoms, cavities, and photons* (Oxford University Press, 2006).

[10]   G. Nogues, A. Rauschenbeutel, S. Osnaghi, M. Brune, J. M. Raimond and S. Haroche, *Seeing a single photon without destroying it*, Nature **400**, 239 (1999),
URL link.

[11] H. J. Kimble, *Strong interactions of single atoms and photons in cavity QED*, Physica Scripta **T76**, 127 (1998),
URL link.

[12] S. Nussmann, M. Hijlkema, B. Weber, F. Rohde, G. Rempe and A. Kuhn, *Submicron positioning of single atoms in a microcavity*, Physical Review Letters **95**, 173602 (2005),
URL link.

[13] T. Aoki, B. Dayan, E. Wilcut, W. P. Bowen, A. S. Parkins, T. J. Kippenberg, K. J. Vahala and H. J. Kimble, *Observation of strong coupling between one atom and a monolithic microresonator*, Nature **443**, 671 (2006),
URL link.

[14] A. Badolato, K. Hennessy, M. Atature, J. Dreiser, E. Hu, P. M. Petroff and A. Imamoglu, *Deterministic coupling of single quantum dots to single nanocavity modes*, Science **308**, 1158 (2005),
URL link.

[15] G. Khitrova, H. M. Gibbs, M. Kira, S. W. Koch and A. Scherer, *Vacuum Rabi splitting in semiconductors*, Nature Physics **2**, 81 (2006),
URL link.

[16] A. Wallraff, D. I. Schuster, A. Blais, L. Frunzio, R. S. Huang, J. Majer, S. Kumar, S. M. Girvin and R. J. Schoelkopf, *Strong coupling of a single photon to a superconducting qubit using circuit quantum electrodynamics*, Nature **431**, 162 (2004),
URL link.

[17] J. K. Thompson, G. Rempe and H. J. Kimble, *Observation of normal mode splitting for an atom in an optical cavity*, Physical Review Letters **68**, 1132 (1992),
URL link.

[18] Y. Colombe, T. Steinmetz, G. Dubois, F. Linke, D. Hunger and J. Reichel, *Strong atom-field coupling for Bose-Einstein condensates in an optical cavity on a chip*, Nature **450**, 272 (2007),
URL link.

[19] F. Brennecke, T. Donner, S. Ritter, T. Bourdel, M. Kohl and T. Esslinger, *Cavity QED with a Bose-Einstein condensate*, Nature **450**, 268 (2007),
URL link.

[20] M. A. Nielsen and I. L. Chuang, *Quantum Computation and Quantum Information* (Cambridge University Press, 2000).

[21] C. H. Bennett, G. Brassard and A. K. Ekert, *Quantum Cryptography*, Scientific American **267**, 50 (1992).

[22] P. W. Shor, SIAM Journal of Computing **26**, 1484 (1997).

[23] L. K. Grover, *Quantum mechanics helps in searching for a needle in a haystack*, Physical Review Letters **79**, 325 (1997),
URL link.

[24] L. M. Duan, M. D. Lukin, J. I. Cirac and P. Zoller, *Long-distance quantum communication with atomic ensembles and linear optics*, Nature **414**, 413 (2001),
URL link.

[25] T. Chaneliere, D. N. Matsukevich, S. D. Jenkins, S. Y. Lan, T. A. B. Kennedy and A. Kuzmich, *Storage and retrieval of single photons transmitted between remote quantum memories*, Nature **438**, 833 (2005),
URL link.

[26] H. J. Kimble, *The quantum internet*, Nature **453**, 1023 (2008),
URL link.

[27] M. D. Lukin, *Colloquium: Trapping and manipulating photon states in atomic ensembles*, Reviews Of Modern Physics **75**, 457 (2003),
URL link.

[28] F. Schmidt-Kaler, H. Haffner, M. Riebe, S. Gulde, G. P. T. Lancaster, T. Deuschle, C. Becher, C. F. Roos, J. Eschner and R. Blatt, *Realization of the Cirac-Zoller controlled-NOT quantum gate*, Nature **422**, 408 (2003),
URL link.

[29] D. Leibfried, B. DeMarco, V. Meyer, D. Lucas, M. Barrett, J. Britton, W. M. Itano, B. Jelenkovic, C. Langer, T. Rosenband and D. J. Wineland, *Experimental demonstration of a robust, high-fidelity geometric two ion-qubit phase gate*, Nature **422**, 412 (2003),
URL link.

[30] C. Langer, R. Ozeri, J. D. Jost, J. Chiaverini, B. DeMarco, A. Ben-Kish, R. B. Blakestad, J. Britton, D. B. Hume, W. M. Itano, D. Leibfried, R. Reichle, T. Rosenband, T. Schaetz, P. O. Schmidt and D. J. Wineland, *Long-lived qubit memory using atomic ions*, Physical Review Letters **95**, 060502 (2005),
URL link.

[31] A. Kuhn, M. Hennrich and G. Rempe, *Deterministic single-photon source for distributed quantum networking*, Physical Review Letters **89**, 067901 (2002),
URL link.

[32] J. McKeever, A. Boca, A. D. Boozer, R. Miller, J. R. Buck, A. Kuzmich and H. J. Kimble, *Deterministic generation of single photons from one atom trapped in a cavity*, Science **303**, 1992 (2004),
URL link.

[33] K. S. Choi, H. Deng, J. Laurat and H. J. Kimble, *Mapping photonic entanglement into and out of a quantum memory*, Nature **452**, 67 (2008),
URL link.

[34] J. Benhelm, G. Kirchmair, C. F. Roos and R. Blatt, *Towards fault-tolerant quantum computing with trapped ions*, Nature Physics **4**, 463 (2008),
URL link.

[35] D. Leibfried, E. Knill, S. Seidelin, J. Britton, R. B. Blakestad, D. B. Chiaverini, J.and Hume, W. M. Itano, J. D. Jost, C. Langer, R. Ozeri, R. Reichle and D. J. Wineland, *Creation of a six-atom Schrödinger cat state*, Nature **438**, 639 (2005),
URL link.

[36] H. Häffner, W. Hänsel, C. F. Roos, J. Benhelm, D. Chek-al kar, M. Chwalla, T. Körber, U. D. Raipol, M. Riebe, P. O. Schmidt, C. Becher, O. Gühne, W. Dür and R. Blatt, *Scalable multiparticle entanglement of trapped ions*, Nature **438**, 643 (2005),
URL link.

[37] S. Gulde, M. Riebe, G. P. T. Lancaster, C. Becher, J. Eschner, H. Haffner, F. Schmidt-Kaler, I. L. Chuang and R. Blatt, *Implementation of the Deutsch-Jozsa algorithm on an ion-trap quantum computer*, Nature **421**, 48 (2003),
URL link.

[38] J. Chiaverini, J. Britton, D. Leibfried, E. Krill, M. D. Barrett, R. B. Blakestad, W. P. Itano, J. D. Jost, C. Langer, R. Ozeri, T. Schaetz and D. J. Wineland, *Implementation of the semiclassical quantum Fourier transform in a scalable system*, Science **308**, 997 (2005),
URL link.

[39] M. D. Barrett, J. Chiaverini, T. Schaetz, J. Britton, W. M. Itano, J. D. jost, E. Knill, C. Langer, D. Leibfried, R. Ozeri and D. J. Wineland, *Deterministic quantum teleportation of atomic qubits*, Nature **429**, 737 (2004),
URL link.

[40] M. Riebe, H. Häffner, C. F. Roos, W. Hänsel, J. Benhelm, G. P. T. Lancaster, T. W. Körber, C. Becher, F. Schmidt-Kaler, D. F. V. James and R. Blatt, *Deterministic quantum teleportation with atoms*, Nature **429**, 734 (2004),
URL link.

[41] T. Rosenband, D. B. Hume, P. O. Schmidt, C. W. Chou, A. Brusch, L. Lorini, W. H. Oskay, R. E. Drullinger, T. M. Fortier, J. E. Stalnaker, S. A. Diddams, W. C. Swann, N. R. Newbury, W. M. Itano, D. J. Wineland and J. C. Bergquist, *Frequency Ratio of Al+ and Hg+ Single-Ion Optical Clocks; Metrology at the 17th Decimal Place*, Science **319**, 1808 (2008),
URL link.

[42] J. I. Cirac, P. Zoller, H. J. Kimble and H. Mabuchi, *Quantum state transfer and entanglement distribution among distant nodes in a quantum network*, Physical Review Letters **78**, 3221 (1997),
URL link.

[43] G. R. Guthohrlein, M. Keller, K. Hayasaka, W. Lange and H. Walther, *A single ion as a nanoscopic probe of an optical field*, Nature **414**, 49 (2001),
URL link.

[44] A. B. Mundt, A. Kreuter, C. Becher, D. Leibfried, J. Eschner, F. Schmidt-Kaler and R. Blatt, *Coupling a single atomic quantum bit to a high finesse optical cavity*, Physical Review Letters **89**, 103001 (2002),
URL link.

[45] A. B. Mundt, A. Kreuter, C. Russo, C. Becher, D. Leibfried, J. Eschner, F. Schmidt-Kaler and R. Blatt, *Coherent coupling of a single Ca-40(+) ion to a high-finesse optical cavity*, Applied Physics B-Lasers And Optics **76**, 117 (2003),
URL link.

[46] M. Keller, B. Lange, K. Hayasaka, W. Lange and H. Walther, *Continuous generation of single photons with controlled waveform in an ion-trap cavity system*, Nature **431**, 1075 (2004),
URL link.

[47] P. Bushev, D. Rotter, A. Wilson, F. Dubin, C. Becher, J. Eschner, R. Blatt, V. Steixner, P. Rabl and P. Zoller, *Feedback cooling of a single trapped ion*, Physical Review Letters **96**, 043003 (2006),
URL link.

[48] M. Fleischhauer, S. F. Yelin and M. D. Lukin, *How to trap photons? Storing single-photon quantum states in collective atomic excitations*, Optics Communications **179**, 395 (2000),
URL link.

[49] M. Fleischhauer and M. D. Lukin, *Quantum memory for photons: Dark-state polaritons*, Physical Review A **65**, 022314 (2002),
URL link.

[50] A. Dantan and M. Pinard, *Quantum-state transfer between fields and atoms in electromagnetically induced transparency*, Physical Review A **69**, 043810 (2004),
URL link.

[51] A. V. Gorshkov, A. Andre, M. D. Lukin and A. S. Sorensen, *Photon storage in Lambda-type optically dense atomic media. I. Cavity model*, Physical Review A **76**, 033804 (2007),
URL link.

[52] J. Simon, H. Tanji, J. K. Thompson and V. Vuletic, *Interfacing collective atomic excitations and single photons*, Physical Review Letters **98**, 183601 (2007),
URL link.

[53] J. Simon, H. Tanji, S. Ghosh and V. Vuletic, *Single-photon bus connecting spin-wave quantum memories*, Nature Physics **3**, 765 (2007),
URL link.

[54] D. N. Matsukevich, T. Chaneliere, M. Bhattacharya, S. Y. Lan, S. D. Jenkins, T. A. B. Kennedy and A. Kuzmich, *Entanglement of a photon and a collective atomic excitation*, Physical Review Letters **95**, 040405 (2005),
URL link.

[55] F. Schmidt-Kaler, S. Gulde, M. Riebe, T. Deuschle, A. Kreuter, G. Lancaster, C. Becher, J. Eschner, H. Haffner and R. Blatt, *The coherence of qubits based on single Ca+ ions*, Journal Of Physics B-Atomic Molecular And Optical Physics **36**, 623 (2003),
URL link.

[56] C. F. Roos, G. P. T. Lancaster, M. Riebe, H. Haffner, W. Hansel, S. Gulde, C. Becher, J. Eschner, F. Schmidt-Kaler and R. Blatt, *Bell states of atoms with ultralong lifetimes and their tomographic state analysis*, Physical Review Letters **92**, 220402 (2004),
URL link.

[57] M. Keller, B. Lange, K. Hayasaka, W. Lange and H. Walther, *Deterministic coupling of single ions to an optical cavity*, Applied Physics B-Lasers And Optics **76**, 125 (2003),
URL link.

[58] B. Julsgaard, J. Sherson, J. I. Cirac, J. Fiurasek and E. S. Polzik, *Experimental demonstration of quantum memory for light*, Nature **432**, 482 (2004),
URL link.

[59] M. D. Eisaman, A. Andre, F. Massou, M. Fleischhauer, A. S. Zibrov and M. D. Lukin, *Electromagnetically induced transparency with tunable single-photon pulses*, Nature **438**, 837 (2005),
URL link.

[60] J. J. Sakurai, *Modern Quantum Mechanics* (Addison-Wesley, 1994).

[61] B. H. Bransden and C. J. Joachain, *Physics of Atoms and Molecules* (Prentice Hall, 2003), 2nd edition.

[62] C. Cohen-Tannoudji, *Atomic motion in laser light*, J. Dalibard, J.-M. Raimond and J. Zinn-Justin, editors, *Fundamental Systems in Quantum Optics, Proceedings of the Les Houches Summer School, Session LIII*, chapter 1 (Elsevier Science Publishers B.V., North-Holland, 1992).

[63] P. Milonni and J. Eberly, *Lasers* (John Wiley & Sons, Inc., New York, 1988).

[64] H. J. Metcalf and P. van der Straten, *Laser Cooling and Trapping* (Springer, 2002).

[65] H. J. Kimble, *Structure and dynamics in cavity quantum electrodynamics*, P. R. Berman, editor, *Cavity Quantum Electrodynamics* (Academic Press, Inc, 1994).

[66] A. Mortensen, *Aspects of Ion Coulomb Crystal based Quantum Memory for Light*, Ph.D. thesis, University of Aarhus (2005),
URL link.

[67] C. W. Gardiner, *Quantum noise* (Springer, Berlin, 1991).

[68] H. J. Kimble, M. Dagenais and L. Mandel, *Photon Anti-Bunching In Resonance Fluorescence*, Physical Review Letters **39**, 691 (1977),
URL link.

[69] F. Diedrich and H. Walther, *Nonclassical Radiation Of A Single Stored Ion*, Physical Review Letters **58**, 203 (1987),
URL link.

[70] R. H. Dicke, *Coherence In Spontaneous Radiation Processes*, Physical Review **93**, 99 (1954),
URL link.

[71] M. Gross and S. Haroche, *Super-Radiance - An Essay On The Theory Of Collective Spontaneous Emission*, Physics Reports-Review Section Of Physics Letters **93**, 301 (1982),
URL link.

[72] W. Paul, H. P. Reinhard and U. Vonzahn, *Das Elektrische Massenfilter Als Massenspektrometer Und Isotopentrenner*, Zeitschrift Fur Physik **152**, 143 (1958),
URL link.

[73] J. D. Prestage, G. J. Dick and L. Maleki, *New Ion Trap For Frequency Standard Applications*, Journal Of Applied Physics **66**, 1013 (1989),
URL link.

[74] E. Fischer, *Die Dreidimensionale Stabilisierung Von Ladungstragern In Einem Vierpolfeld*, Zeitschrift Fur Physik **156**, 1 (1959),
URL link.

[75] D. A. Church, *Storage-Ring Ion Trap Derived From Linear Quadrupole Radio-Frequency Mass Filter*, Journal Of Applied Physics **40**, 3127 (1969),
URL link.

[76] H. G. Dehmelt, *Radiofrequency spectrocopy of stored ions: I storage*, volume 3 of *Advances in Atomic and Molecular Physics*, 53–72 (Academic Press, New York, 1967).

[77] L. Hornekær, *Single- and Multi-Species Coulomb Ion Crystals: Structures, Dynamics and Sympathetic Cooling*, Ph.D. thesis, University of Aarhus (2000).

[78] P. K. Ghosh, *Ion Traps* (Oxford University Press, New York, 1995).

[79] M. Abramowitz and I. A. Stegun, *Handbook of Mathematical Functions With Formulas, Graphs, and Mathematical Tables* (National Bureau of Standards, 1964).

[80] T. Hasegawa and K. Uekara, *Dynamics Of A Single-Particle In A Paul Trap In The Presence Of The Damping Force*, Applied Physics B-Lasers And Optics **61**, 159 (1995),
URL link.

[81] M. Drewsen and A. Brøner, *Harmonic linear Paul trap: Stability diagram and effective potentials*, Physical Review A **6204**, 045401 (2000),
URL link.

[82] R. Hazeltine and F. Waelbroeck, *The Framework of Plasma Physics* (Perseus Books, Reading, Massachusetts, 1998).

[83] J. Jackson, *Classical Electrodynamics* (John Wiley & Sons, Inc., USA, 1999), 3rd edition.

[84] J. P. Hansen, *Statistical-Mechanics Of Dense Ionized Matter .1. Equilibrium Properties of the Classical One-Component Plasma*, Physical Review A **8**, 3096 (1973),
URL link.

[85] E. L. Pollock and J. P. Hansen, *Statistical-Mechanics Of Dense Ionized Matter .2. Equilibrium Properties And Melting Transition Of Crystallized One-Component Plasma*, Physical Review A **8**, 3110 (1973),
URL link.

[86] W. L. Slattery, G. D. Doolen and H. E. Dewitt, *Improved Equation Of State For The Classical One-Component Plasma*, Physical Review A **21**, 2087 (1980),
URL link.

[87] J. L. Barrat, J. P. Hansen and R. Mochkovitch, *Crystallization Of Carbon-Oxygen Mixtures In White-Dwarfs*, Astronomy And Astrophysics **199**, L15 (1988),
URL link.

[88] F. Diedrich, E. Peik, J. M. Chen, W. Quint and H. Walther, *Observation Of A Phase-Transition Of Stored Laser-Cooled Ions*, Physical Review Letters **59**, 2931 (1987),
URL link.

[89] D. J. Wineland, J. C. Bergquist, W. M. Itano, J. J. Bollinger and C. H. Manney, *Atomic-Ion Coulomb Clusters In An Ion Trap*, Physical Review Letters **59**, 2935 (1987),
URL link.

[90] L. Hornekær, N. Kjærgaard, A. M. Thommesen and M. Drewsen, *Structural properties of two-component Coulomb crystals in linear Paul traps*, Physical Review Letters **86**, 1994 (2001),
URL link.

[91] L. Turner, *Collective Effects On Equilibria Of Trapped Charged Plasmas*, Physics Of Fluids **30**, 3196 (1987),
URL link.

[92] J. P. Schiffer, M. Drewsen, J. S. Hangst and L. Hornekaer, *Temperature, ordering, and equilibrium with time-dependent confining forces*, Proceedings Of The National Academy Of Sciences Of The United States Of America **97**, 10697

(2000),
URL link.

[93] D. J. Berkeland, J. D. Miller, J. C. Bergquist, W. M. Itano and D. J. Wineland, *Minimization of ion micromotion in a Paul trap*, Journal Of Applied Physics **83**, 5025 (1998),
URL link.

[94] R. Blumel, C. Kappler, W. Quint and H. Walther, *Chaos And Order Of Laser-Cooled Ions In A Paul Trap*, Physical Review A **40**, 808 (1989),
URL link.

[95] J. N. Tan, J. J. Bollinger, B. Jelenkovic and D. J. Wineland, *Long-Range Order In Laser-Cooled, Atomic-Ion Wigner Crystals Observed By Bragg Scattering*, Physical Review Letters **75**, 4198 (1995),
URL link.

[96] W. M. Itano, J. J. Bollinger, J. N. Tan, B. Jelenkovic, X. P. Huang and D. J. Wineland, *Bragg diffraction from crystallized ion plasmas*, Science **279**, 686 (1998),
URL link.

[97] R. W. Hasse and J. P. Schiffer, *The Structure Of The Cylindrically Confined Coulomb Lattice*, Annals Of Physics **203**, 419 (1990),
URL link.

[98] M. Drewsen, C. Brodersen, L. Hornekær, J. S. Hangst and J. P. Schiffer, *Large ion crystals in a linear Paul trap*, Physical Review Letters **81**, 2878 (1998),
URL link.

[99] M. Drewsen, L. Hornekaer, N. Kjaergaard, K. Molhave, A. M. Tommesen, Z. Videsen, A. Mortensen and F. Jensen, *Ion Coulumb Crystals and Some Applications*, Non-Neutral Plasma Physics Conference IV, AIP Conference Proceedings **606**, 135 (2002).

[100] A. Mortensen, E. Nielsen, T. Matthey and M. Drewsen, *Observation of three-dimensional long-range order in small ion Coulomb crystals in an rf trap*, Physical Review Letters **96**, 103001 (2006),
URL link.

[101] A. Mortensen, E. Nielsen, T. Matthey and M. Drewsen, *Radio frequency field-induced persistent long-range ordered structures in two-species ion Coulomb crystals*, Journal Of Physics B-Atomic Molecular And Optical Physics **40**, F223 (2007),
URL link.

[102] R. Blatt, *Laser cooling of trapped ions*, J. Dalibard, J.-M. Raimond and J. Zinn-Justin, editors, *Fundamental Systems in Quantum Optics, Proceedings of the Les Houches Summer School, Session LIV* (Elsevier Science Publishers B.V., North-Holland, 1992).

[103] F. Diedrich, J. C. Bergquist, W. M. Itano and D. J. Wineland, *Laser Cooling To The Zero-Point Energy Of Motion*, Physical Review Letters **62**, 403 (1989),
URL link.

[104] R. J. Hendricks, J. L. Sorensen, C. Champenois, M. Knoop and M. Drewsen, *Doppler cooling of calcium ions using a dipole-forbidden transition*, Physical Review A **77**, 021401 (2008),
URL link.

[105] D. J. Larson, J. C. Bergquist, J. J. Bollinger, W. M. Itano and D. J. Wineland, *Sympathetic Cooling Of Trapped Ions - A Laser-Cooled 2-Species Nonneutral Ion Plasma*, Physical Review Letters **57**, 70 (1986),
URL link.

[106] P. Bowe, L. Hornekaer, C. Brodersen, M. Drewsen, J. S. Hangst and J. P. Schiffer, *Sympathetic crystallization of trapped ions*, Physical Review Letters **82**, 2071 (1999),
URL link.

[107] J. L. Hall and S. A. Lee, *Interferometric Real-Time Display Of Cw Dye-Laser Wavelength With Sub-Doppler Accuracy*, Applied Physics Letters **29**, 367 (1976),
URL link.

[108] A. M. Thommesen, *Optogalvanic effects in a Λ-level system of Ca^+ and application in laser cooling.*, Master's thesis, University of Aarhus (2000).

[109] R. Ohmukai, M. Watanabe, H. Imajo, K. Hayasaka and S. Urabe, *Doppler-Free Optogalvanic Spectroscopy Of Ca+ And Ca*, Japanese Journal Of Applied Physics Part 1-Regular Papers Short Notes & Review Papers **33**, 311 (1994),
URL link.

[110] P. Herskind, J. Lindballe, C. Clausen, J. L. Sorensen and M. Drewsen, *Second-harmonic generation of light at 544 and 272 nm from an ytterbium-doped distributed-feedback fiber laser*, Optics Letters **32**, 268 (2007),
URL link.

[111] N. Kjægaard, L. Hornekær, A. M. Thommesen, Z. Videsen and M. Drewsen, *Isotope selective loading of an ion trap using resonance-enhanced two-photon ionization*, Applied Physics B-Lasers And Optics **71**, 207 (2000),
URL link.

[112] Coherent Verdi
URL link.

[113] K. Schneider, S. Schiller, J. Mlynek, M. Bode and I. Freitag, *1.1-W single-frequency 532-nm radiation by second-harmonic generation of a miniature Nd:YAG ring laser*, Optics Letters **21**, 1999 (1996),
URL link.

[114] C. Czeranowsky, E. Heumann and G. Huber, *All-solid-state continuous-wave frequency-doubled Nd : YAG-BiBO laser with 2.8-W output power at 473 nm*, Optics Letters **28**, 432 (2003),
URL link.

[115] J. Sakuma, Y. Asakawa and M. Obara, *Generation of 5-W deep-UV continuous-wave radiation at 266 nm by an external cavity with a CsLiB6O10 crystal*, Optics Letters **29**, 92 (2004),
URL link.

[116] Koheras Boostik
URL link.

[117] R. Paschotta, J. Nilsson, A. C. Tropper and D. C. Hanna, *Ytterbium-doped fiber amplifiers*, Ieee Journal Of Quantum Electronics **33**, 1049 (1997),
URL link.

[118] G. P. Agrawal, *Nonlinear Fiber Optics* (Academic Press, San Diego, 2001), 3rd edition, chapter 9.

[119] D. A. Bryan, R. Gerson and H. E. Tomaschke, *Increased Optical-Damage Resistance In Lithium-Niobate*, Applied Physics Letters **44**, 847 (1984),
URL link.

[120] G. D. Boyd and D. A. Kleinman, *Parametric Interaction Of Focused Gaussian Light Beams*, Journal Of Applied Physics **39**, 3597 (1968),
URL link.

[121] H. Kogelnik and T. Li, *Laser Beams And Resonators*, Applied Optics **5**, 1550 (1966),
URL link.

[122] R. W. P. Drever, J. L. Hall, F. V. Kowalski, J. Hough, G. M. Ford, A. J. Munley and H. Ward, *Laser Phase And Frequency Stabilization Using An Optical-Resonator*, Applied Physics B-Photophysics And Laser Chemistry **31**, 97 (1983),
URL link.

[123] E. D. Black, *An introduction to Pound-Drever-Hall laser frequency stabilization*, American Journal Of Physics **69**, 79 (2001),
URL link.

[124] J. Lindballe, *Eksperimenter med resonant to-foton isotop-selektiv fotoionisation af calcium ved anvendelse af en frekvensfordoblet farvestoflaser*, Master's thesis, University of Aarhus (2003).

[125] T. W. Hänsch and B. Couillaud, *Laser Frequency Stabilization By Polarization Spectroscopy Of A Reflecting Reference Cavity*, Optics Communications **35**, 441 (1980),
URL link.

[126] J. Mes, E. J. van Duijn, R. Zinkstok, S. Witte and W. Hogervorst, *Third-harmonic generation of a continuous-wave Ti : Sapphire laser in external resonant cavities*, Applied Physics Letters **82**, 4423 (2003),
URL link.

[127] A. Friedenauer, F. Markert, H. Schmitz, L. Petersen, S. Kahra, M. Herrmann, T. H. Udem, T. W. Hänsch and T. Schatz, *High power all solid state laser system near 280 nm*, Applied Physics B-Lasers And Optics **84**, 371 (2006),
URL link.

[128] F. Markert, M. Scheid, D. Kolbe and J. Walz, *4W continuous-wave narrow-linewidth tunable solid-state laser source at 546nm by externally frequency doubling a ytterbium-doped single-mode fiber laser system*, Optics Express **15**, 14476 (2007),
URL link.

[129] B. J. Ainslie, S. P. Craig, S. T. Davey and B. Wakefield, *The fabrication, assessment and optical properties of high-concentration Nd3+- and Er3+-doped silica-based fibres*, Materials Letters **6**, 139 (1988),
URL link.

[130] S. Agger, J. H. Povlsen and P. Varming, *Single-frequency thulium-doped distributed-feedback fiber-laser*, Optics Letters **29**, 1503 (2004),
URL link.

[131] T. Okoshi, K. Kikuchi and A. Nakayama, *Novel Method For High-Resolution Measurement Of Laser Output Spectrum*, Electronics Letters **16**, 630 (1980),
URL link.

[132] C. D. Bruun, *Effektiv anden harmonisk generation i ekstern kavitet*, Master's thesis, Aarhus University (1998).

[133] D. Møller, *Adiabatic Processes in Quantum Computation - Experimental and theoretical studies*, Ph.D. thesis, University of Aarhus (2008).

[134] F. K. Jensen, *Laser frequency stabilization for use in stirap experiments*, Master's thesis, University of Aarhus (2004).

[135] A. Kreuter, C. Becher, G. P. T. Lancaster, A. B. Mundt, C. Russo, H. Haffner, C. Roos, J. Eschner, F. Schmidt-Kaler and R. Blatt, *Spontaneous emission lifetime of a single trapped Ca+ ion in a high finesse cavity*, Physical Review Letters **92**, 203002 (2004),
URL link.

[136] A. von Hippel, editor, *Dielectric materials and applications* (M.I.T. Technology press and John Wiley & Sons., 1954).

[137] E. Hecht, *Optics* (Addison-Wesley, 1998), 3rd edition.

[138] D. N. Madsen, S. Balslev, M. Drewsen, N. Kjaergaard, Z. Videsen and J. W. Thomsen, *Measurements on photo-ionization of 3s3p P-1(1) magnesium atoms*, Journal Of Physics B-Atomic Molecular And Optical Physics **33**, 4981 (2000),
URL link.

[139] S. Gulde, D. Rotter, P. Barton, F. Schmidt-Kaler, R. Blatt and W. Hogervorst, *Simple and efficient photo-ionization loading of ions for precision ion-trapping experiments*, Applied Physics B-Lasers And Optics **73**, 861 (2001), URL link.

[140] D. M. Lucas, A. Ramos, J. P. Home, M. J. McDonnell, S. Nakayama, J. P. Stacey, S. C. Webster, D. N. Stacey and A. M. Steane, *Isotope-selective photoionization for calcium ion trapping*, Physical Review A **69**, 012711 (2004), URL link.

[141] U. Tanaka, H. Matsunishi, I. Morita and S. Urabe, *Isotope-selective trapping of rare calcium ions using high-power incoherent light sources for the second step of photo-ionization*, Applied Physics B-Lasers And Optics **81**, 795 (2005), URL link.

[142] R. J. Hendricks, D. M. Grant, P. F. Herskind, A. Dantan and M. Drewsen, *An all-optical ion-loading technique for scalable microtrap architectures*, Applied Physics B-Lasers And Optics **88**, 507 (2007), URL link.

[143] M. Brownnutt, V. Letchumanan, G. Wilpers, R. C. Thompson, P. Gill and A. G. Sinclair, *Controlled photoionization loading of Sr-88(+) for precision ion-trap experiments*, Applied Physics B-Lasers And Optics **87**, 411 (2007), URL link.

[144] K. Vant, J. Chiaverini, W. Lybarger and D. J. Berkeland, *Photoionization of strontium for trapped-ion quantum information processing*, (Preprint quant-ph/0607055 v1) URL link.

[145] L. Deslauriers, M. Acton, B. B. Blinov, K. A. Brickman, P. C. Haljan, W. K. Hensinger, D. Hucul, S. Katnik, R. N. Kohn, P. J. Lee, M. J. Madsen, P. Maunz, S. Olmschenk, D. L. Moehring, D. Stick, J. Sterk, M. Yeo, K. C. Younge and C. Monroe, *Efficient photoionization loading of trapped ions with ultrafast pulses*, Physical Review A **74**, 063421 (2006), URL link.

[146] A. V. Steele, L. R. Churchill, P. F. Griffin and M. S. Chapman, *Photoionization and photoelectric loading of barium ion traps*, Physical Review A **75**, 053404 (2007), URL link.

[147] C. Balzer, A. Braun, T. Hannemann, C. Paape, M. Ettler, W. Neuhauser and C. Wunderlich, *Electrodynamically trapped Yb+ ions for quantum information processing*, Physical Review A **73**, 041407 (2006), URL link.

[148] M. Cetina, A. Grier, J. Campbell, I. Chuang and V. Vuletic, *Bright source of cold ions for surface-electrode traps*, Physical Review A **76**, 041401 (2007), URL link.

[149] A. Mortensen, J. J. T. Lindballe, I. S. Jensen, P. Staanum, D. Voigt and M. Drewsen, *Isotope shifts of the 4s(2) S-1(0)-> 4s5p P-1(1) transition and hyperfine splitting of the 4s5p P-1(1) state in calcium*, Physical Review A **69**, 042502 (2004), URL link.

[150] L. Deslauriers, S. Olmschenk, D. Stick, W. K. Hensinger, J. Sterk and C. Monroe, *Scaling and suppression of anomalous heating in ion traps*, Physical Review Letters **97**, 103007 (2006), URL link.

[151] R. G. DeVoe and C. Kurtsiefer, *Experimental study of anomalous heating and trap instabilities in a microscopic Ba-137 ion trap*, Physical Review A **65**, 063407 (2002), URL link.

[152] J. E. Hansen, C. Laughlin, H. W. van der Hart and G. Verbockhaven, *Energy levels, wavefunction compositions and electric dipole transitions in neutral Ca*, Journal Of Physics B-Atomic Molecular And Optical Physics **32**, 2099 (1999), URL link.

[153] N. Beverini, E. Maccioni, F. Sorrentino, V. Baraulia and M. Coca, *Measurementof the 4s(2) S-1(0) -> 4s3d D-1(2) transition probability in calcium*, European Physical Journal D **23**, 223 (2003), URL link.

[154] G. Smith, *Oscillator-Strengths For Neutral Calcium Lines Of 2.9 Ev Excitation*, Journal Of Physics B-Atomic Molecular And Optical Physics **21**, 2827 (1988), URL link.

[155] A. K. Pulhani, G. P. Gupta and B. M. Suri, *Isotopic selectivity calculations for multi-step photoionization of calcium atoms using narrow-band lasers*, Journal Of Physics B-Atomic Molecular And Optical Physics **35**, 3677 (2002), URL link.

[156] P. Muller, B. A. Bushaw, K. Blaum, S. Diel, C. Geppert, A. Nahler, N. Trautmann, W. Nortershauser and K. Wendt, *Ca-41 ultratrace determination with isotopic selectivity > 10(12) by diode-laser-based RIMS*, Fresenius Journal Of Analytical Chemistry **370**, 508 (2001), URL link.

[157] J. Emsley, *The Elements* (Oxford University Press, New York, 1995).

[158] S. Seidelin, J. Chiaverini, R. Reichle, J. J. Bollinger, D. Leibfried, J. Britton, J. H. Wesenberg, R. B. Blakestad, R. J. Epstein, D. B. Hume, W. M. Itano, J. D. Jost, C. Langer, R. Ozeri, N. Shiga and D. J. Wineland, *Microfabricated surface-electrode ion trap for scalable quantum information processing*, Physical Review Letters **96**, 253003 (2006), URL link.

[159] D. Stick, W. K. Hensinger, S. Olmschenk, M. J. Madsen, K. Schwab and C. Monroe, *Ion trap in a semiconductor chip*, Nature Physics **2**, 36 (2006),
URL link.

[160] N. S. Nogar, R. C. Estler and C. M. Miller, *Pulsed Laser Desorption For Resonance Ionization Mass-Spectrometry*, Analytical Chemistry **57**, 2441 (1985),
URL link.

[161] M. N. R. Ashfold, F. Claeyssens, G. M. Fuge and S. J. Henley, *Pulsed laser ablation and deposition of thin films*, Chemical Society Reviews **33**, 23 (2004),
URL link.

[162] C. R. Phipps, editor, *Laser Ablation and its Applications* (Springer, Heidelberg, 2007).

[163] L. Balazs, R. Gijbels and A. Vertes, *Expansion Of Laser-Generated Plumes Near The Plasma Ignition Threshold*, Analytical Chemistry **63**, 314 (1991),
URL link.

[164] R. Kelly, A. Miotello, A. Mele and A. Giardini Guidoni, *Laser Ablation abd Desorption*, 225–289 (Academic Press, New York, 1998).

[165] A. Bolovinos, E. LucKoenig, S. Assimopoulos, A. Lyras, N. E. Karapanagioti, D. Charalambidis and M. Aymar, *4pnp J=0(e)-2(e) autoionizing series of calcium: Experimental and theoretical analysis*, Zeitschrift Fur Physik D-Atoms Molecules And Clusters **38**, 265 (1996),
URL link.

[166] M. Fleischhauer, A. Imamoglu and J. P. Marangos, *Electromagnetically induced transparency: Optics in coherent media*, Reviews Of Modern Physics **77**, 633 (2005),
URL link.

[167] C. Cohen-Tannoudji, J. Dupont-Roc and G. Grynbergt, *Atom-photon interactions* (John Wiley, New York, 1992).

[168] M. Knoop, M. Vedel and F. Vedel, *Lifetime, Collisional-Quenching, And J-Mixing Measurements Of The Metastable 3d Levels Of Ca+*, Physical Review A **52**, 3763 (1995),
URL link.

[169] M. Knoop, M. Vedel and F. Vedel, *Collisional quenching and j-mixing rate constants for the 3D levels of Ca$^+$*, Physical Review A **58**, 264 (1998),
URL link.

[170] P. A. Barton, C. J. S. Donald, D. M. Lucas, D. A. Stevens, A. M. Steane and D. N. Stacey, *Measurement of the lifetime of the 3d 2D5/2 state in 40Ca+*, Physical Review A **62**, 032503 (2000),
URL link.

[171] P. Staanum, I. S. Jensen, R. G. Martinussen, D. Voigt and M. Drewsen, *Lifetime measurement of the metastable 3d (2)D5(/2) state in the Ca-40(+) ion using the shelving technique on a few-ion string*, Physical Review A **69**, 032503 (2004),
URL link.

[172] M. Knoop, C. Champenois, G. Hagel, M. Houssin, C. Lisowski, M. Vedel and F. Vedel, *Metastable level lifetimes from electron-shelving measurements with ion clouds and single ions*, European Physical Journal D **29**, 163 (2004),
URL link.

[173] A. Dantan, A. Bramati and M. Pinard, *Atomic quantum memory: Cavity versus single-pass schemes*, Physical Review A **71**, 043801 (2005),
URL link.

[174] D. M. Lucas, B. C. Keitch, J. P. Home, G. Imreh, M. J. McDonnell, D. N. Stacey, D. J. Szwer and A. M. Steane, *A long-lived memory qubit on a low-decoherence quantum bus*,
URL link, arXiv:0710.4421v1.

[175] J. Benhelm, G. Kirchmair, C. F. Roos and R. Blatt, *Experimental quantum-information processing with 43Ca+ ions*, Physical Review A **77**, 062306 (2008),
URL link.

[176] T. Iversen, *Raman overgange mellem meta-stabile D-tilstande i små laserkølede 40Ca+ Coulomb krystaller*, Master's thesis, University of Aarhus (2007).

[177] K. J. Boller, A. Imamoglu and S. E. Harris, *Observation Of Electromagnetically Induced Transparency*, Physical Review Letters **66**, 2593 (1991),
URL link.

[178] D. F. V. James, *Quantum dynamics of cold trapped ions with application to quantum computation*, Applied Physics B-Lasers And Optics **66**, 181 (1998),
URL link.

[179] V. Vuletic and S. Chu, *Laser Cooling of Atoms, Ions, or Molecules by Coherent Scattering*, Physical Review Letters **84**, 3787 (2000),
URL link.

[180] NIST Atomic Spectra Database
URL link.

[181] M. Walker, *Matrix Calculus and the Stokes Parameters of Polarized Radiation*, American Journal Of Physics **22**, 170 (1954),
URL link.

[182] Fujian Castech crystals inc.
URL link.